NANYANG
TECHNOLOGICAL
UNIVERSITY

RARE EARTH DOPED NANOMATERIALS AS POTENTIAL CONTRAST AGENTS FOR OPTICAL/MAGNETIC RESONANCE IMAGING

GAUTOM KUMAR DAS

SCHOOL OF CHEMICAL AND BIOMEDICAL ENGINEERING

2010

RARE EARTH DOPED NANOMATERIALS AS POTENTIAL CONTRAST AGENTS FOR OPTICAL/MAGNETIC RESONANCE IMAGING

GAUTOM KUMAR DAS

2010

RARE EARTH DOPED NANOMATERIALS AS POTENTIAL CONTRAST AGENTS FOR OPTICAL/MAGNETIC RESONANCE IMAGING

GAUTOM KUMAR DAS

School of Chemical and Biomedical Engineering

A thesis submitted to the Nanyang Technological University
in partial fulfillment of the requirement for the degree of
DOCTOR OF PHILOSOPHY

2010

ABSTRACT

The research work presented in this thesis focuses on the fabrication of rare earth (RE) doped nanomaterials as potential contrast agents for optical and magnetic resonance imaging. Owing to the sharp and intense emission obtained over the range of visible to the near-infrared regions in a wide variety of hosts, RE-doped nanomaterials have attracted strong interests as contrast agents in bioimaging applications.

The current study has successfully demonstrated the fabrication of fluorescent, and bifunctional magnetic-fluorescent RE-doped nanomaterials as contrast agents for bioimaging. At first, doping of different RE ions in yttrium oxide (Y_2O_3) host was investigated to fabricate the down- and up-conversion fluorescent nanoparticles. Effect of different synthesis parameters and type of RE dopants was investigated, and optimum conditions in relation to synthesis temperature, time, and concentration of RE dopants were reported and discussed. Spherical nanocrystals and nanorods could selectively be produced by varying different synthesis conditions. An evolution mechanism has been proposed to elucidate the morphology transformation to nanorods from nanocrystals.

We further investigated the use of RE doping in different magnetic host such as γ-Fe_2O_3, Gd_2O_3, and Dy_2O_3 to fabricate novel bifunctional magnetic-fluorescent nanoparticles for bimodal optical/magnetic resonance imaging. The key feature of these nanomaterials is that they are *single-phase* and *bifunctional* materials. One of these nanomaterials, RE-doped Gd_2O_3, demonstrate both down- and up-conversion fluorescence, and show excellent T_1-image contrast, which closely resembles that of commercial Gadovist^{TM} for MRI applications.

We also proposed a new method for cytotoxicity evaluation of nanomaterials based on American National Standard ISO 10993-5 and evaluated the cytotoxic effects of the synthesized RE-doped nanoparticles. Two different cell lines (Hepatoma HepG2 and fibroblast NIH3T3 cells) were exposed to the nanoparticles and their extracts. We inferred the RE-doped nanomaterials possessed minimal toxicity compared to semiconductor quantum dots.

ACKNOWLEDGEMENTS

This thesis is an important milestone in my journey as a researcher. I could not have reached this milestone without the support of many caring people. These few words will not do justice to all those who have made this work possible.

I owe my deepest gratitude to my supervisor, Asst/Prof. Tan Thatt Yang Timothy, for his inexhaustible patience in providing help, supports and suggestions. I am very grateful for the latitude which he has given me to seek my own research project and taught me to be respectful for originality. I feel privileged to have had the opportunity to work under his prudent supervision in one of the most exciting projects in his lab.

I gratefully thank Prof. Tim White and Asst/Prof. Joachim Loo of School of Materials Science and Engineering, and Dr. S. T. Selvan of Institute of Materials Research and Engineering (IMRE) for the fruitful discussions we had on different occasions and assisting with different characterization facilities. I am also thankful to Asst/Prof. Hongyu Chen from School of Physical and Mathematical Sciences for allowing me to access the facilities of his laboratory.

I am grateful to Dr. Zhang Yunxia for her support in my first year of study when my footing was unsteady. I would also like to thank Miss Juo Gun, and Mr Patrick Lai from School of Materials Science and Engineering for their assistance in electron microscopy, and VSM analysis respectively. Thanks to Dr. Jeyagowry T. Sampanthar (Institute of Chemical and Engineering Sciences) for the assistance in XPS measurements, and Dr. Ong Teng Teng for her assistance in TGA analysis. A sincere thank to Miss Teo Ailing for her help in conducting cell viability experiments.

A very special thank to Dr. Poernomo Gunawan and all the members of my group for their kind help and supports. Most importantly, it is a pleasure for me to thank of all of my friends who have helped me to live my life outside of the graduate school during this period of study.

Lastly but not least, a heartfelt gratitude goes to my family for their omnipresent love, trust and enthusiastic supports.

List of Publications

Journal Publications

(1) **Das, G. K.;** Heng, B. C.; Ng. S. C.; White, T.; Loo, J. S. C; D'Silva, L.; Padmanabhan, P.; Bhakoo K. K.; Selvan, S. T. and Tan, T. T. T. Y. Gadolinium Oxide Ultranarrow Nanorods as Multimodal Contrast Agent for Optical/Magnetic Resonance Imaging. Langmuir **2010**, 26, 8959-8965. (*Chapter 6*)

(2) **Das, G. K.**; Chan, P. P. Y.; Teo, A.; Loo, J. S. C.; Anderson, J. and Tan, T. T. Y. *in vitro* Cytotoxicity Evaluation of Biomedical Nanoparticles and Their Extracts. Journal of Biomedical Materials Research **2010**, *93A*, 337-346. (*Chapter 7*)

(3) Zhang, Y.[†]; **Das, G. K.**[†]; Xu, R. and Tan, T. T. Y. Tb-doped Iron Oxide: Bifunctional Fluorescent and Magnetic Nanocrystals. Journal of Materials Chemistry **2009**, *19*, 3696-3703. ([†] denotes authors of equal contributions). (*Chapter 5*)

(4) **Das, G. K.** and Tan, T. T. Y. Rare-Earth-Doped and Codoped Y_2O_3 Nanomaterials as Potential Bioimaging Probes. Journal of Physical Chemistry C **2008**, *112,* 11211–11217. (*Chapter 4*)

(5) **Das, G. K**.; D'Silva, L.; Padmanabhan, P.; Bhakoo K. K.; Selvan, S. T. and Tan, T. T. T. Y. Dysprosium Oxide Nanoparticles: Multimodal Contrast Agent for Optical/Magnetic Resonance Imaging. In Preparation. (*Chapter 6*)

Conference Proceedings

(1) **Das, G. K.** and Tan, T. T. T. Y. Gadolinium Oxide as Multimodal Contrast Agent for Optical and Magnetic Resonance Imaging. The International Symposium on Exploring the Frontiers of Chemical and Biomedical Engineering, May 2010, Singapore.

(2) **Das, G. K.** and Tan, T. T. Y. Mechanistic Studies of Fluorescence and Morphology Evolution for Rare Earth Doped Gd_2O_3 and Dy_2O_3 Ultranarrow Nanorods, The International Symposium on Advanced Bio, Nano, and Pharmaceutical Science and Technology 2009, May 2009, Beijing, China.

(3) Zhang Y.; **Das, G. K.**; Selvan S. T. and Tan, T. T. Y. Reverse Micelles Synthesis and Characterization of Magnetic-Luminescent Bifunctional Core/Shell Nanocomposite, The International Symposium on Advanced Bio, Nano, and Pharmaceutical Science and Technology 2009, May 2009, Beijing, China.

(4) **Das, G. K.** and Tan, T. T. Y. Rare-Earth Doped and Co-Doped Y_2O_3 Nanomaterials as Potential Bio-Imaging Probe. American Institute of Chemical Engineers (AIChE) Annual Meeting, Nov 2008, Pennsylvania, USA.

(5) **Das, G. K.** and Tan, T. T. Y. Nanorod Formation and Upconversion Fluorescence Mechanism of Rare Earth Codoped Y_2O_3:Yb,Er. Trends in Nanotechnology (TNT), Sep 2008, Oviedo, Spain. (**Won a competitive travel grant to present this work at TNT2008**)

(6) Tan, T. T. Y. and **Das, G. K.** Luminescent Nanocrystals for Potential Bioimaging Applications, 17th International Conference on Photochemical Conversion and Storage of Solar Energy, July 2008, Sydney, Australia.

(7) **Das, G. K.** and Tan, T. T. Y. Investigation of Rare Earth Doping and Codoping in Y_2O_3 Nanocrystals, Regional Symposium on Chemical Engineering (RSCE), Dec 2007, Yogyakarta, Indonesia.

(8) **Das, G. K.** and Tan, T. T. Y. Investigation of Terbium and Europium Dopant Concentrations in Y_2O_3 Nanocrystals, International Conference on Cellular & Molecular Bioengineering (ICCMB), Dec 2007, Singapore.

(9) Teo, A.; **Das, G. K.**; Anderson, J. M.and Tan, T.T.Y. *in vitro* cytotoxicity Studies of Various Nanomaterials for Bio-imaging Applications via Direct Cell Contact Methods and Nanomaterials Leachate, International Conference on Cellular & Molecular Bioengineering (ICCMB), Dec 2007, Singapore.

TABLE OF CONTENTS

LIST OF FIGURES

LIST OF TABLES

NOMENCLATURE

θ	diffraction angle
φ	work function
λ	wavelength
ω_0	Larmor precession frequency
Å	angstrom
A	ampere
ANOVA	analysis of variance
APTMS	aminopropyl trimethoxysilane
B_0	external magnetic field
BE	binding energy
CT	computed X-ray tomography
DC	direct contact method
DLS	dynamic light scattering
DMEM	Dulbecco's modified eagle's medium
DTPA	diethylenetriaminepentaacetate
E_i	higher-energy singlet state (i^{th}) in energy level
EDS	energy dispersive X-ray spectroscopy
em	emission
ESA	excited state absorption
ETU	energy transfer up-conversion
ET	energy transfer
eV	electron volt
ex	excitation
FBS	fetal bovine serum
FFT	fast Fourier transformation
FTIR	Fourier transform infrared spectroscopy
G	ground-state energy level
GSA	ground state absorption
h	hour
H	applied magnetic field

H_0	null hypothesis
HepG2	human hepatocellular liver carcinoma cell
HRTEM	high resolution transmission electron microscope
ICP-AES	induction couple plasma-atomic emission spectroscopy
K_BT	thermal energy
K_{eff}	magnetic anisotropy constant
m	magnetic moment
M	magnetization
MRI	magnetic resonance imaging
NIR	near-infrared
nm	nanometer
nM	nanomolar
NIH3T3	mouse embryonic fibroblast cell
Oe	Oersted
P	the probability value of the test statistic
PBS	phosphate buffer saline
PET	positron emission tomography
PL	photoluminescence
pM	picomolar
QDs	quantum dots
r_1	longitudinal relaxivity
r_2	transverse relaxivity
RE	rare earth
RF	radio frequency
SAED	selected area electron diffraction
SD	standard deviation
SPIO	superparamagnetic iron oxide
T_1	longitudinal relaxation time of water proton
T_2	transverse relaxation time of water proton
TEM	transmission electron microscope
TGA	thermogravimetric analysis
TMAH	tetramethylammonium hydroxide

TOP	trioctylphosphine
UV	ultraviolet
VIS	visible
VSM	vibrating sample magnetometer
W	watt
XPS	X-ray photoelectron spectroscopy
XRD	X-ray diffraction

CHAPTER 1

Introduction

Nanoscience and nanotechnology have been one of the most popular research frontiers in the past decades. The trend of shrinking the dimensionality of materials is driven by the desire to explore the unique material properties and superior performances that appear in the transition from bulk to nanometer length scales. The distinct chemical and physical properties in nanomaterials often significantly differ from their corresponding bulk counterparts.[1-3] As size diminishes to the nano-scale, certain properties of matter become size dependent; for example optical property, conductivity, magnetism, surface energy, and reactivity. Many of these properties are extremely promising and have been studied for a wide range of applications such as optoelectronics, photovoltaics, communication, information storage, energy conversion, catalysis, environmental protection, sensors and detectors, and biomedical applications.[4]

In biomedical research, the quest for early detection and diagnosis of diseases, and more efficient treatment is ardently pursued. In recent years, nanomaterials have been investigated extensively for the potential use in non-invasive visualization of molecular markers in the early stages of diseases and targeted delivery of therapeutic agents with lower side effects.[5-16] The conventionally used imaging and therapeutic agents such as gadolinium complexes and anticancer chemical drugs suffer from a short blood circulation time, non-specific biodistribution and many unwanted side effects.[6] In comparison, nanomaterials can be engineered to overcome these limitations. For example, blood circulation time can be enhanced significantly by controlling size and modifying the surface of the nanoparticles; site specific targeting can be achieved by conjugating targeting molecules, such as peptides and antibodies, on the nanoparticle surface.[13, 16] In addition, nanomaterials enrich detection and diagnosis by providing better spatial resolution, enhanced signal sensitivity of biomedical imaging with special ability to provide information at the molecular and cellular level of biological systems.[10]

Biomedical imaging plays a critical role in modern medicine in both successful diagnosis and treatment of diseases. Imaging techniques such as magnetic resonance imaging (MRI), computed X-ray tomography (CT), positron emission tomography (PET), and optical imaging have been serving as diagnostic tools for decades. Each of these imaging modalities has its own advantages and limitations. For instance, PET gives good target sensitivity while MRI gives good spatial resolution; and therefore, a single technique does not possess comprehensive capabilities to understand and diagnose the fundamental biological process of diseases. However, the combination of imaging modalities that integrate the strengths and compensate deficiencies of individual modalities offers improved diagnostics at molecular and cellular level, therapeutic monitoring and preclinical research using imaging approach. As a result, significant efforts have been dedicated in past decades to develop multimodal imaging agents in an attempt to shift the paradigm from conventional imaging to multimodal imaging technologies.[17-36] For example, Weissleder group reported a trimodal imaging agent combining near infra-red (NIR) fluorescent dyes on an aminated dextran coating of cross-linked iron oxide (CLIO) and conjugated diethylenetriaminepentaacetate (DTPA) chelate to PET tracer ^{64}Cu, resulting in a PET, MRI, and NIR fluorescent detectable imaging agent.[36] At the forefront of the novel multimodal imaging contrast agents development, nanostructured materials offer great potential since they can be designed from bottom-up approach, offering numerous opportunities to tailor and combine functionalities to the requirement of the individual modal imaging system.

Magnetism and fluorescence in nanomaterials have been exploited in bioimaging applications over the years for MRI and optical imaging respectively. MRI and optical imaging are two powerful and non-invasive diagnostic techniques. MRI offers high spatial resolutions (i.e. 25-100 µm)[37] and the capacity to simultaneously obtain physiological and anatomical information while optical imaging allows rapid screening and molecular information. Current commercial MRI contrast agents are in the form of either superparamagnetic iron oxide nanoparticles or paramagnetic complexes.[38-39] Superparamagnetic iron oxide nanoparticles accelerate the transverse (T_2) relaxation of water protons and exhibit dark contrast. Paramagnetic complexes, which are typically gadolinium or manganese chelates, accelerate the longitudinal (T_1) relaxation of water protons and exhibit bright contrast.[40] Optical imaging agents include various dye molecules,[41] dye-doped silica materials,[9] quantum dots,[1-2, 42-44] lanthanide compounds with up- and down-conversion luminescent properties,[14, 45] and near infrared (NIR) emitting fluorophores.[46] Several strategies have been reported to combine magnetism and fluorescence in nanomaterials. Examples include embedment of optical and MR imaging agents in a nanostructured matrix,[23, 33] formation of heterodimer,[18, 22, 30, 47] and core-shell[29] nanocrystals for combined optical-MR imaging. However, in spite of some successful reports, the development of multimodal nanoparticle-based contrast agents is still in its early stage.[17] The majority of multimodal contrast agents reported in open literature is in the form of hetero-structured nanocomposites, of which two or more nanomaterials of different functionalities were combined by some means. In contrast, reports of single-phase multimodal contrast agents are scarce. The notion of single-phase contrast agents would be useful in terms of ease of large scale synthesis and functional homogenization for biomedical applications.[48] In addition, important issues such as the dispersity, stability and toxicity of the multifunctional nanomaterials in physiological environment need to be addressed.[7]

The work presented in this PhD thesis aims to engineer novel single-phase bifunctional magnetic-fluorescent nanostructures for bimodal optical/MR imaging. In addition, this work aims to demonstrate the potential applicability of the designed nanostructures by demonstrating down- and up-conversion fluorescence, T_1-weighted MRI contrast, and investigating their short term toxicity in cell models. With the above aims in mind, rare earth (RE) materials have been chosen as the working materials. RE materials such as RE fluorides and oxides have been reported to be good host structures for up- and down-conversion luminescence and extremely promising as bioimaging probes.[14, 45] RE^{3+} ions have long emission lifetimes (ranging from μs to ms), superior photostability, multicolor emission, and most importantly, are less toxic compared to common organic dyes and semiconductor quantum dots.[49] In addition, some RE nanomaterials such as gadolinium oxides and gadolinium phosphates have been reported to be very promising as contrast agents for MRI.[50-54]

This thesis has been subdivided into following sections. Following this introduction, a review will be presented in Chapter 2 on magnetic and fluorescent nanoparticles, state-of arts of multifunctional nanoparticles for multimodal imaging technologies, motivation behind choosing rare earth materials for multimodal imaging agents, their synthesis approaches, surface modification techniques, and toxicity concerns of nanomaterials for bioapplications.

The basic principles of different materials characterization techniques used throughout the study, some key features of the American National Standard ISO 10993-5 and the one-way analysis of variance (ANOVA) are presented in Chapter 3.

Chapter 4 demonstrates the use of yttrium oxide (Y_2O_3) as the host and other RE^{3+} ions, such as terbium (Tb^{3+}), europium (Eu^{3+}), erbium (Er^{3+}), and ytterbium (Yb^{3+}), as dopant(s) to fabricate down- and up-conversion luminescent nanomaterials. Spherical nanocrystals, and nanorods can be selectively produced by varying synthesis conditions. The overall aims of this study are to: (I) understand various synthesis parameters, (II) investigate the impact of different RE dopant(s) concentration on down- and up-conversion luminescence, and lastly (III) functionalize the nanomaterials to render them biocompatible and suitable for further bioconjugation. It was observed that synthesis parameters such as reaction temperature, time, amount of surfactant, and type of liganding solvent have a significant influence on the morphology and the fluorescence emission process of the Y_2O_3 nanomaterials. In addition, different dopant ions and dopant concentrations were observed to produce emission at different wavelengths (colors) and intensities respectively.

Chapter 5 describes the synthesis and characterizations of a new class of bifunctional superparamagnetic-fluorescent nanocrystal using iron oxide (γ-Fe_2O_3) as the host and RE ion terbium (Tb^{3+}) as the dopant. The key feature of this study is to bring magnetism and fluorescence into a single-phase nanocrystal for multimodal imaging instead of fabricating nanocomposites by assembling different functional entities. A fluorescence enhancement technique has been demonstrated through passivating the nanocrystal surface with a higher bandgap material (ZnS) which resulted in improved photoluminescence (PL). Surface functionalization of the nanocrystals with a thin layer of silica (to render them water-dispersible, suitable for further bioconjugation and cytotoxicity studies) has also been discussed in this chapter.

Chapter 6 presents fabrication of bifunctional paramagnetic-fluorescent Tb^{3+}-doped, and Yb^{3+}/Er^{3+}-codoped Gd_2O_3, and Dy_2O_3 nanocrystals and nanorods. The key feature of these bifunctional nanomaterials is: they are RE-based single-phase nanocrystals where both fluorescence and paramagnetism originate from RE ions. One of these bifunctional nanomaterials Gd_2O_3 show good T_1-weighted MRI contrast, and demonstrate both down- and up-conversion fluorescence. The nanorod formation mechanism has been investigated and elucidated in this chapter. The nanomaterials are highly promising as contrast agent for multimodal optical/MR imaging.

Since all the nanomaterials synthesized are envisioned to be used as probes for bioimaging, their cytotoxicity needed to be evaluated. Chapter 7 presents a new, comprehensive approach of evaluating *in vitro* cytotoxicity of nanoparticles based on American National Standard ISO 10993-5. The cell viability was evaluated based on the detection of metabolic activities and observing Hepatomoa HepG2 and fibroblasts NIH3T3 cell morphological changes in the presence of the nanoparticles and their extracted products. In general, RE nanomaterials were found to have minimal toxicity towards these cell lines.

Lastly, Chapter 8 summarizes the major findings of this study, followed by the recommendations for further works.

CHAPTER 2

Literature Review

2.1 Introduction

Specific targetability, non-invasiveness, high spatial resolution, three-dimensional tomography, and real time imaging are some of the important requirements for next generation biomedical imaging technologies.[17, 37, 55] Therefore, the development of target-specific and real-time imaging agents is essential not only to understand the fundamental biological process but also to successfully diagnose various diseases. A number of non-invasive imaging modalities such as magnetic resonance imaging (MRI), positron emission tomography (PET), computed tomography (CT), single photon emission computed tomography (SPECT), ultrasound and optical imaging have been used in the diagnosis of various diseases. In general, the imaging modalities are complementary rather than competitive, yet each differs in terms of resolution, sensitivity, and data acquisition time (Table 2.1).[37] Hence, a specific imaging modality alone does not possess all the necessary capabilities to meet all the requirements. For example, MRI and CT have the advantages of being non-invasive and showing three-dimensional tomography, but they are limited by low target sensitivity. On the other hand, radioactive imaging techniques such as PET have very high target sensitivity but of poor spatial resolution. Other optical imaging methods such as fluorescence imaging have relatively good sensitivity but suffer from low tissue penetration depths. In brief, each imaging modality has its own advantages and disadvantages, but combination of different modalities into a single platform can compensate the deficiencies of a single

Table 2.1 Comparison of imaging modalities[37]

Imaging Technique	Detection	Tissue penetration depth	Spatial resolution	Sensitivity [a]
Magnetic resonance imaging (MRI)	radiowave	No limit	25-100 μm	mM to μM (low)
Positron emission tomography (PET)	high energy γ-rays	No limit	1-2 mm	pM (high)
Single photon emission computed tomography (SPECT)	low-energy γ-rays	No limit	1-2 mm	nM to pM
Computed tomography (CT)	X-rays	No limit	50-200 μm	Not well characterized
Optical imaging	visible or near-infrared light	< 1 cm	2-3 μm in vivo sub-μm in vitro	nM to pM (medium)
Ultrasonography	ultrasonic waves	mm - cm	50–500 μm	Not well characterized

[a] sensitivity of the detecting probe is relative to background

imaging modality. The development of multifunctional nanomaterials as multimodal contrast agents is a step further in the same direction. Reported multimodal contrast agents include the combination of MRI-optical, PET-near-infrared (NIR) optical fluorescence, PET-CT modalities, and MRI-PET-NIR optical fluorescence.[30, 34, 36, 56-57]

Since the main focus of the thesis is to engineer novel multifunctional magnetic-fluorescent contrast agent for multimodal imaging, we will focus our review on the properties of magnetic and fluorescent nanoparticles, and highlight the latest development of magnetic-fluorescent contrast agents. A good portion of the review is dedicated to rare earth materials since they are the materials of choice as multifunctional agents in the current thesis. Lastly, a brief discussion on the cytotoxicity issues of nanoparticles for bioapplications will be presented.

2.2 Magnetic Nanoparticles

Magnetic nanoparticles have been studied and employed in a wide range of disciplines ranging from data storage, biotechnology, magnetic resonance imaging, catalysis, and environmental remediation.[58-64] In most of the envisaged applications, the nanoparticles of some critical size range performs better than others. The critical size limit depends on materials but usually falls in the range of few tens of nm.[5] Usually, each nanoparticle of this size range becomes a single magnetic domain and shows superparamagnetism above the blocking temperature. Such individual nanoparticles have large magnetic moment and behave like a giant paramagnetic atom with a fast response to applied magnetic fields with negligible remanence and coercivity. Remanence and coercivity are two important characteristic parameters of magnetic materials. The former measures the residual magnetism left behind in the magnetic materials after removal of magnetic field and the later measures the field required to bring the magnetization to zero. Because of very low remanence and coercivity, the superparamagnetic nanoparticle have negligible risk of forming nanoparticle aggregates at room temperature and, therefore, is attractive choices for a broad range of biomedical applications.

2.2.1 Origin of Magnetism

Spin angular moment generally dominates orbital angular momentum in determining the magnetic properties of a material. Materials in which all spins are paired are diamagnetic and generate a weak moment that opposes the direction of an applied field. When there are unpaired spins present that do not interact with those on adjacent atoms, the sample is paramagnetic (PM), and the unpaired spins give rise to a moment that aligns parallel to the direction of an applied field (Figure 2.1). Paramagnetic effects dominate diamagnetic effects in magnitude. When unpaired spins on adjacent atoms interacts, they may have alignments of ferromagnetic (FM), antiferromagnetic (AFM), or ferrimagnetic type. In the ferromagnetic case, the spins align parallel to one another, and their moments add. If the spins align antiparallel to each other, the moments cancel, and the material is antiferromagnetic (AFM). If there are two different sublattices aligned antiparallel to each other, the material is ferrimagnetic. Ferromagnets (FMs) have a magnetic ordering temperature called Curie temperature, above which they are paramagnetic.

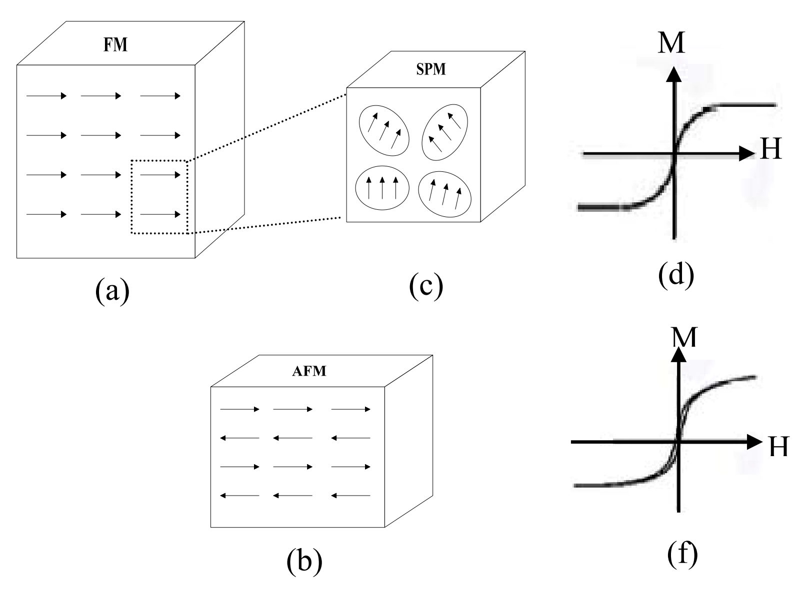

Figure 2.1 The different magnetic effect occurs in magnetic nanoparticles. All the figures presented here are rather simplistic view of the phenomena present in small magnetic particles. Spin arrangement in (a) a ferromagnet (FM), (b) an antiferromagnet (AFM), (c) An illustration of the magnetic moment in a superparamagnet (SPM). An SPM is defined as an assembly of giant magnetic moments which are not interacting; (d) Superparamagnetic particle exhibit no remanence or coercivity, hence no hysteresis in magnetization curve. (f) Pure antiferromagnetic nanoparticle could exhibit superparamagnetic relaxation.

Antiferromagnets and ferrimagnets also have an analogous temperature, the Néel temperature, above which they are paramagnetic. All different magnetic effects are shown schematically in Figure 2.1.[5]

2.2.2 Field-dependent Magnetization

Magnetization (M) vs applied field (H) measurements are useful for characterizing magnetic materials. A typical M vs H curve for ferromagnetic materials is shown schematically in Figure 2.2. The field is usually adjusted to the highest available field in the magnetometer. A ferromagnetic material that has never been previously magnetized or has been thoroughly demagnetized will follow the dashed line as H is increased. If the curve flattens at high field, the magnetization has reached a maximum value, called saturation magnetization (M_S). As the field is decreased to zero, the magnetization decreases to the remanence (M_R). When the field is applied in the negative direction, the

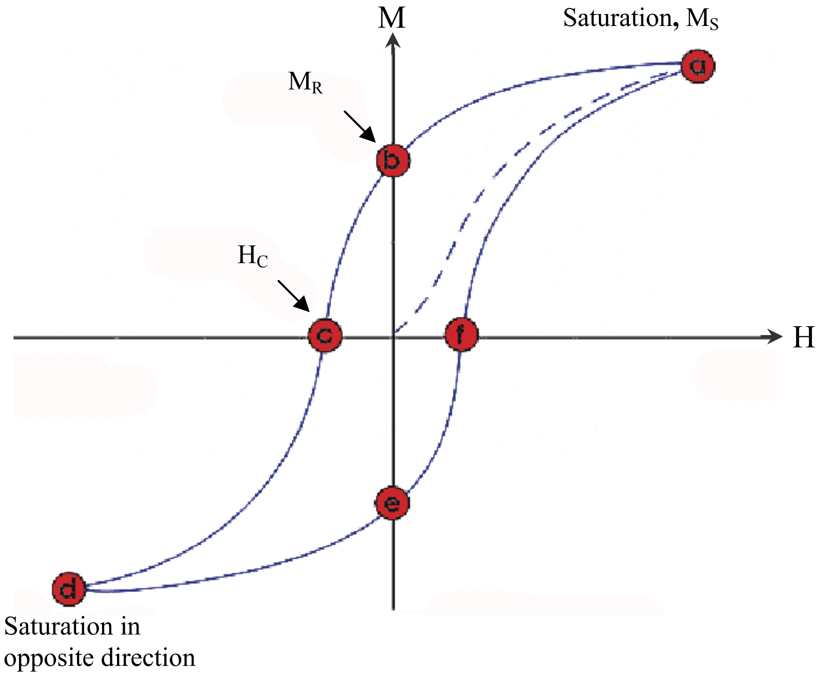

Figure 2.2 Schematic curve of magnetization (M) as function of magnetic field strength (H).

magnetization eventually decreases to zero. The magnitude of the field at which this occurred is called the coercive field or coercivity (H_C). As the applied field is increased in the negative direction, the material will again become magnetically saturated in the opposite direction (point "d"). Reduction of H to zero will result in a level of residual magnetism equal to the same value in other direction (point "e"). Further, increasing H in the positive direction will return M to zero (point "f") while further increment will lead the curve back to the saturation point (point "a") to complete the loop. If we choose a field and wish to know magnetization, we must also know the history of the sample, since each field values in the plot corresponds to two magnetizations. This property is called hysteresis (i. e. the loop abcd-defa). As the sample is heated up, H_C decreases, and the two curves collapse into one. That happens when the sample becomes paramagnetic because the thermal fluctuations erase the memory of its history of each nanoparticle.[5]

2.2.3 Superparamagnetism

A region in ferromagnetic materials where all magnetic moments points in the same direction is called a magnetic domain. Large magnetic particles are generally multi-domain structure and regions of uniform magnetization are separated by domain walls. Domain wall formation process is driven by the balance between the domain-wall energy, and magnetostatic energy. Domain-wall energy is directly proportional to the volume of the material while magnetostatic energy are proportional to the interfacial area among the domains.[5] If the size of a material reduces below a critical volume, it demands more energy to create a domain wall than to support the external magnetostatic energy of the single-domain state. Therefore, below a critical size magnetic particles usually form single-domain state. Typically, the single-domain limit is material-dependent but lies in the range of a few tens of nanometers.[65]

Superparamagnetism is a form of magnetism which usually occurs in single-domain nanoparticles. Single-domain particles are uniformly magnetized and have all its spins lined up in the same direction. Essentially, single-domain particles have no domain wall and magnetization will change with the rotation of the spins. The magnetic anisotropy energy per particle, which is responsible for holding the magnetic moments along a certain direction, can be expressed as:[5]

$$E(\theta) = K_{eff} V \sin^2\theta \qquad \text{(Eq. 2.1)}$$

where K_{eff}, V, and θ are the anisotropy constant, the particle volume, and the angle between the magnetization and the easy axis respectively. The energy barrier $K_{eff}V$ separates the two energetically equivalent easy directions of magnetization. In small enough particles, the thermal energy (K_BT) exceeds the energy barrier $K_{eff}V$, and the magnetization can easily flip. Thus for ferromagnetic materials, at few tens of nanometer the system behaves like a paramagnet due to formation of giant moment inside each particle (Figure 2.1c).[5] Such system should ideally have no hysteresis and coercivity. This system is called as superparamagnetism.

Nanoscale materials generally fall in the region of well-isolated single-domain. Despite material dependence, the sizes of the magnetic nanoparticles studied in this PhD work are sufficiently small to assume single-domain nanoparticles which are superparamagnetic or paramagnetic.

2.3 Luminescent Nanoparticles

The application of the luminescence and the luminescent materials in science and technology is ubiquitous, ranging from biological labeling to information technology and beyond. The excellent spatial and temporal resolutions, and the high signal-to-noise ratios inherent in luminescent analysis, make luminescent nanomaterials the ideal candidates as luminescent probes. Currently, several classes of materials have been employed as fluorescent emitters/probes, which includes fluorescent proteins, organic and metallorganic dye molecules, semiconductor nanoparticles (commonly known as quantum dots), lanthanide-doped inorganic materials, polymer/dye-based nanoparticles and silica/dye hybrid particles.[66] These materials have their distinct advantages and disadvantages. A comparison of currently employed fluorophores is shown in Table 2.2. It is seen that the commonly used dyes have good fluorescence quantum yield (QY) but are susceptible to photobleaching. They also have broad emission spectrum which often overlaps with tissue autofluorescence. On the other hand, inorganic nanoparticle based fluorophores have relatively good fluorescence QY and are photostable. However, their application in bioimaging, especially quantum dots, is constrained by cytoxicity and biocompatibility issues.

2.3.1 Luminescence Mechanism

When a fluorophore is excited by quanta of specific energy, electrons are transferred from a ground state (G) to a higher energy singlet state (i.e. E_1, E_2). Upon relaxation to the ground state, the excited state electrons release the energy either by non-radiative energy decay (thermal decay) or by emitting as photons of lower energy. In the later case, fluorescence takes place. The excitation and emission process can be described as:

Table 2.2 Comparison of properties among organic dyes and inorganic nanoparticles[66]

Type of fluorescent agent	Advantages	Limitations
Organic Dyes		
Fluoresceins and Rhodamines (examples FITC)	High absorptivity. High fluorescence QY. Good aqueous solubility.	Very much susceptible to photobleaching and pH sensitivity. Low photostability. Broad emission spectrum.
Cyanine dyes (example Cy5)	High photostability. Relatively efficient QY. Good aqueous solubility.	Susceptible to photobleaching. Generally have narrow excitation spectra so that can only be excited within a very limited range of wavelength
Alexa dyes	High photostability and pH insensitivity over a broad range.	Nonspecific interactions with cell due to net negative charge carrying with them.
Inorganic nanoparticles		
Semiconductor quantum dots (QDs)	Great assay sensitivity and stability over conventional organic fluorophores. Stable against photobleaching. About one-third spectral line width compare to organic fluorophores. Multicolor emission. Low autofluorescence.	Major drawback is QDs are generally toxic to cellular environment. QDs themselves are not biocompatible and need surface modification for bioapplications.
Rare earth doped nanoparticles	Multicolor emission. Low toxicity. Can readily synthesized in water. Capable of producing up-conversion luminescence at NIR excitation which is the best window for deep tissue imaging. Large wavelength separation between excitation and emission. Long fluorescence lifetime. Sharp emission spectra.	Applications of RE-doped nanoparticles are still in early stages and an open area of investigation.

QY-Quantum Yield; FITC-fluorescein-5-isothiocyanate; NIR-Near-infrared

Excitation: $G + h\nu_{ex} \rightarrow E_i (i = 1,2,3...)$ (Eq. 2.2)

Emission (luminescence): $E_i \rightarrow G + h\nu_{em}$ (Eq. 2.3)

Where, hν is a generic term for photon energy, h is Planck's constant, and ν is the frequency of light. State G and E_i are called the ground and electronically excited states of the fluorophores respectively.

In addition to luminescence and non-radiative relaxation, the excited state electrons can also relax via conversion to a triplet state which may subsequently relax via phosphorescence or by a secondary non-radiative relaxation step. Relaxation from an excited E_i state can also occur via a second molecule through fluorescence quenching, a phenomenon results in the decrease of fluorescence intensity. For example, molecular oxygen (O_2) is an extremely efficient fluorescence quencher. A schematic illustration of fluorescence process is shown in Figure 2.3.

2.3.2 Down- and Up-conversion Fluorescence Emission

The difference between the position of the band maxima of the excitation and emission spectra of the same electronic transition is known as the Stoke's shift. A fluorescence emission can be either of Stoke's or anti-Stoke's type.

Down-conversion fluorescence emission occurs when the energy of the emitting photon is lower than that of an exciting photon, which follows the principle of the Stoke's law. In other words, output photon energy is lower than input photon energy. This principle is valid only when one excited ion system is considered. On the other hand, up-conversion

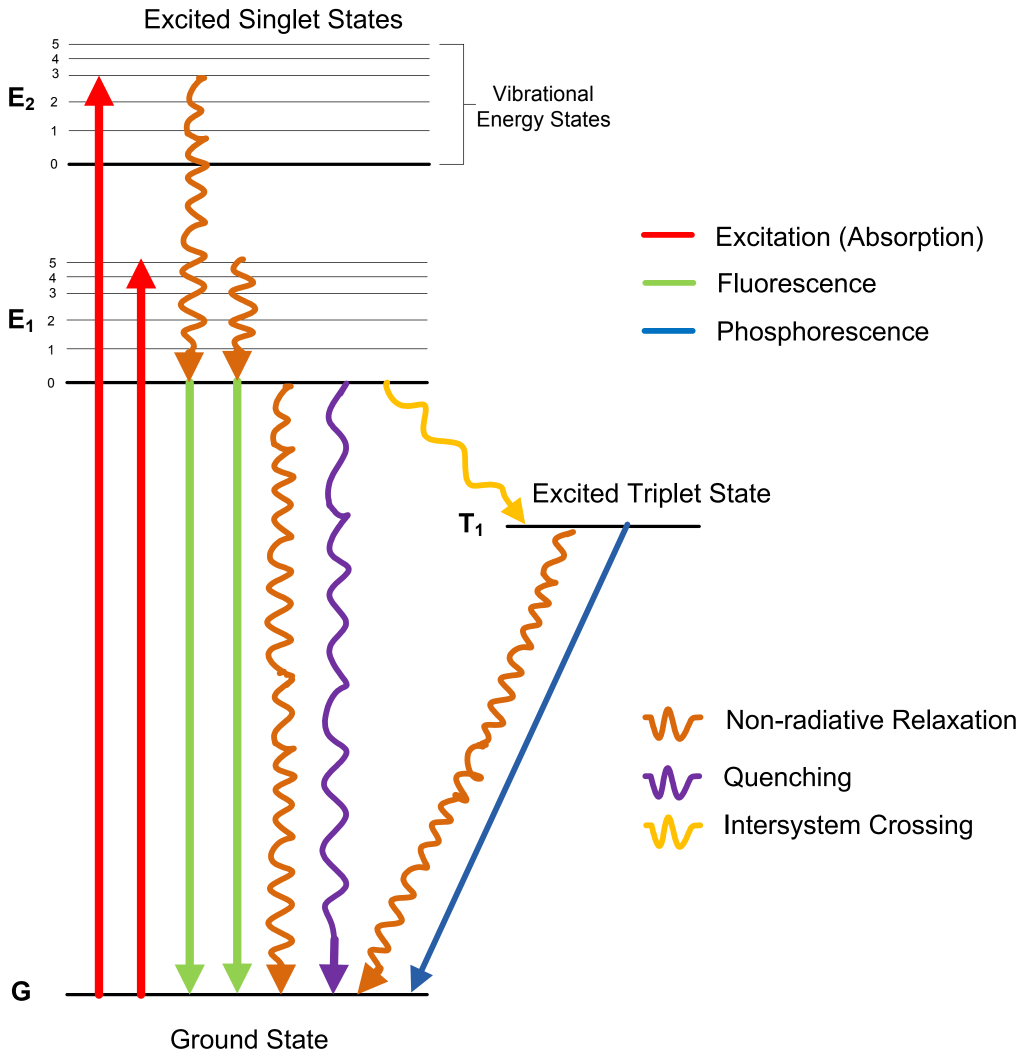

Figure 2.3 A schematic illustration of fluorescence process.

fluorescence contradicts Stoke's law and emits photon of higher energy than that of excitation. It has been shown in lanthanide, uranide and transition-metal ions systems, when embedded in a solid or host, produce up-conversion emission of anti-Stoke's types. In anti-Stoke's emissions or up-conversion process, emission energy exceeds excitation energy even by 10-100 times thermal energy (K_BT).[67] A number of different mechanisms have been recognized to be involved in up-conversion, either being a stand alone mechanism or in combinations such as excited state absorption (ESA), energy transfer up-conversion (ETU), and photon avalanche (PA). This will be further reviewed in section 2.5.2.

2.3.3 Interaction of Light with Tissues

The fundamental hurdles of tissue imaging using optical means are autofluorescence, high absorption and light scattering by e.g. hemoglobin (Hb). In tissues, absorption coefficient of light depends on the wavelength employed and absorbers such as water, hemoglobins, and lipids. Based on the wavelength of the light employed, different penetration depths can be achieved. For example, ultraviolet (UV) - visible (VIS) photons are strongly absorbed by deoxy- and oxyhemoglobin (HbO_2), and tissue

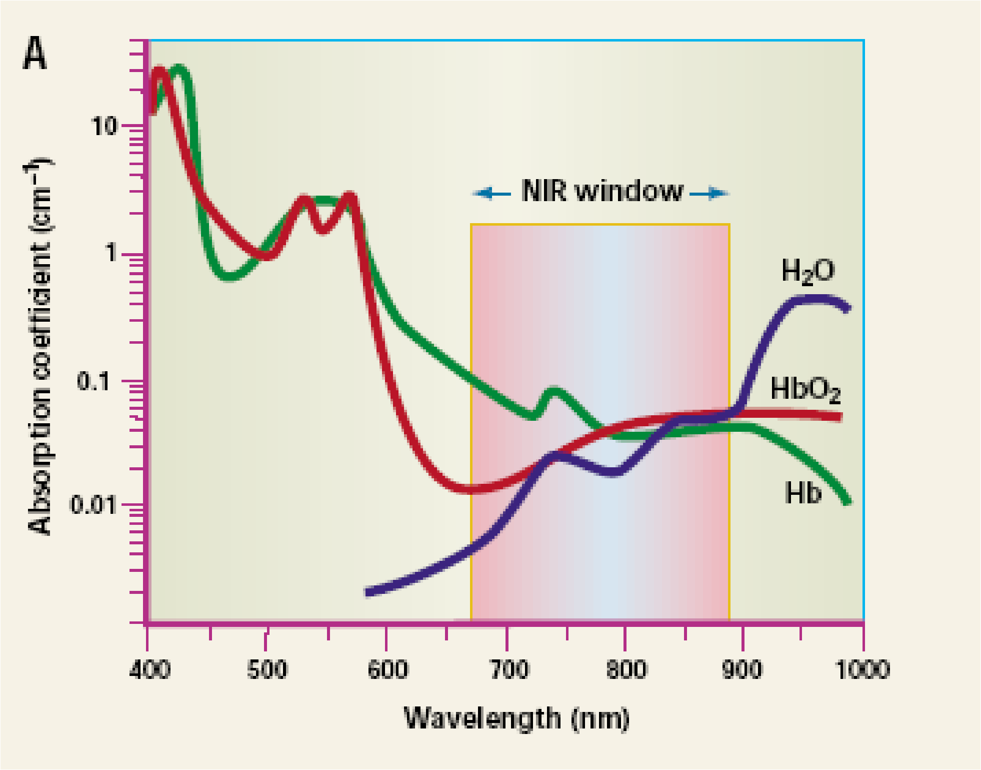

Figure 2.4 Interaction of light with tissue. The graph is calculated assuming normally oxygenated tissue (saturation of 70%), a hemoglobin concentration of 50 mM, and a composition of 50% water and 15% lipids. (Reprinted with permission from ref. [68]. Copyright 2001, Nature Publishing Group).

chromophores within the first few micrometers to a millimeter of tissue thickness. These possess serious limitation in terms of tissue penetration depth. On the other hand, near-infrared (NIR) light of 650 to 900 nm have minimal absorbency as hemoglobin (the primary absorber of visible light), water and lipids (the primary absorber of infrared light) have their lowest absorption coefficients in the NIR region (Figure 2.4).[68-69] Therefore, NIR fluorophores remains the best choice for deep tissue imaging and tomographic display.

2.4 Contrast Agents for Bioimaging

2.4.1 Conventional Contrast Agents

Contrast agents for bioimaging can be broadly categorized into two classes: endogenous agents and exogenous agents. Endogenous agents typically use an enzyme-mediated process inside the body to generate visible light when a substrate is degraded. Example of endogenous agent is green fluorescent protein (GFP).[70-72] GFP offers good potential in extracting information at cellular and molecular level but they have some critical intrinsic limitations which inhibit their widespread application in clinical phase.[69, 73] For example, GFP emission at ~510 nm overlaps with autofluorescence of many tissues which restricts its application in cellular labeling. GFP with red shifting has been engineered to overcome this problem but maximum shift attained was only ~25 nm.[69] In contrast, exogenous imaging agents are more advantageous. Examples of this type of agents include different organic/inorganic fluorophores, gadolinium chelates, and superparamagnetic iron oxides. Some of the critical limitations associated with conventional organic contrast agents are:[74]

I. Fluorescence emission from organic dyes is not continuous for longer period of time (due to photobleaching). Therefore, they are not suitable for longer period of bioimaging observations.

II. Generally, the emission spectra of most of the organic fluorophores are relatively broad which may overlap with the emission wavelengths of other fluorophores. Hence, they are not suitable for simultaneous multicolor imaging applications.

III. Local chemical environment such as change in pH, ions are often very sensitive to emission.

IV. Emission from fluorescent dyes sometimes overlaps with tissue-autofluorescence.

V. Lanthanide chelates such as Gd-based chelates Gd-DTPA (diethyltriaminepentaacetic acid) have been used in MRI. But the non-specific uptake by intravascular and extravascular space limits their applications.

VI. Besides, Gd in its ionic form has been reported to be toxic with a half-life of several weeks.[75] Though Gd is administrated as complex form, its stability is influenced by concentrations of surrounding ions, pH, temperature, and capping ligands.

2.4.2 Nanoparticle-based Contrast Agents

Example of nanoparticle based contrast agents includes gold nanoparticles, organic dye doped silica, quantum dots, superparamagnetic iron oxide nanoparticle and lanthanide based phosphors. In comparison to conventional fluorophores discussed above, nanoparticle-based contrast agents consist of a number of desired properties. Table 2.2 has summarized briefly major advantages and limitations of QDs and rare-earth based contrast agents. However, with proper surface modification, the nanoparticle-based contrast agents generally have the following advantages over conventional organic contrast agents:[74]

I. Relatively superior resistant to photobleaching.
II. High absorbency and quantum yield.
III. Better resistance to metabolic degradation resistant.
IV. Emission tuning in the NIR 700-900 window for good tissue penetration.
V. Good dispersibility in biological environment.
VI. *in vivo* and *in vitro* stability.

A single contrast agent in conventional imaging techniques usually provides limited information of the organs. Hence, the current research trend in bioimaging has been directed towards the integration of multimodal imaging techniques and concurrently the development nanoparticle based multifunctional contrast agents.[76-77] The significance of medical imaging contrast agents research could be assessed from sales of medical imaging contrast agents, which were $1.41 billion in 2004 but are expected to go up to $2.58 billion by 2009 in US market only.[78] One of the advantages of nanoparticle based probes is their flexibility in conjugation with various moieties such as DNAs, peptides, and antibodies, whichever is needed for monitoring special molecular events and biological process. In the following section, we will focus on the review of recent development of multifunctional nanoparticles as contrast agents.

2.4.3 Multimodal Contrast Agents

In general, imaging modalities can be broadly classified into two groups: (I) modalities providing structural information (e.g. MRI, CT, and ultrasound), and (II) modalities providing functional or molecular information (e.g. optical imaging, SPECT, and PET).[76] Therefore, in the development of multimodal contrast agents, considerable efforts have been devoted toward integrating one modality from each group, which should enable function and structure to be examined within the same individual and at the same time. A variety of nanoparticle based contrast agents have been developed combining the modalities from two groups, such as the combination of MRI-optical, PET-CT, PET-NIR optical fluorescence, MRI-PET-NIR optical fluorescence.[36, 57, 79] However, we will limit our discussion to the advancement and recent efforts made on fabrication of magnetic-fluorescent nanoparticles as multifunctional contrast agents for MRI-optical imaging. As reviewed by Corr *et al.*,[35] on the basis of fabrication strategy, there are few types of magnetic-fluorescent nanocomposites that have been reported in the literature such as (I) a magnetic core coated with a silica shell containing fluorescent components, (II) polymer-coated magnetic nanoparticles functionalized with a fluorescent moiety, (III) ionic aggregates consisting of a magnetic core and fluorescent ionic compounds, (IV) fluorescent labeled bilipid-coated magnetic nanoparticles, (V) a magnetic core covalently bound to a fluorescent entity via a spacer, (VI) a magnetic core directly coated with a semiconducting shell, (VII) magnetically doped QDs, and (VIII) nanocomposites, which consists of magnetic nanoparticles and QDs encapsulated within a polymer or silica matrix (Figure 2.5). Superparamagnetic iron oxide (SPIO), or paramagnetic gadolinium (Gd)-based chelates or nanoparticles have been mostly used as the magnetic entity of the multifunctional contrast agent, while the fluorescent entity

Table 2.3 Comparison of various SPIO and Gd based multimodal imaging contrast agents

Multimodal nanoparticles	Particle Size	Emission wavelength	Relaxivity r_1	Relaxivity r_2	Magnetic Field strength, B_0
	(nm)	(nm)	($mM^{-1}s^{-1}$)		(T)
BASED ON SPIO					
CLIO-SS-R4-Cy5.5 [80]	~70	695	27.8	91.2	9.4
CLIO-Cy5.5-EPPT [81]	35.8	695	26.42	53.44	9.4
Fe_3O_4-SiPEG-Cltx-Cy5.5[82]	~10.5	695			4.7
Fe_3O_4-SiPEG-TCL-Cy5.5[83]	~33	695			1.5
$CoFe_2O_4$@SiO_2(FITC)[84]	60	518			4.7
Fe_3O_4@SiO_2(FITC)[85]	50			128	1.5
$DySiO_2$-(Fe3O4)n[86]	46	580		397	9.4
Fe_3O_4@mesoporous silica(FITC)[23]	Length ~154	518		153	4.7
Fe_2O_3/CdSe@silica[30]	11~14	600			
Au–Fe_3O_4 [87]	8 (Au)-20(Fe_3O_4)	530		105	3
FePt–Au [22]	6 (FePt)-10(Au)	530		58.7	9.4
Fe_2O_3-SWNT[88]	>1000	NIR			14.1
BASED ON GD^{3+} IONS					
Gd-DTPA-phospholipid stabilized QD[89]	5	560	12		
Gd-TSPETE-QD@silica[90]	10-20	590	20.5	151	4.7
Gd-TSPETE-silica nanoparticle-$[Ru(bpy)_3]^{2+}$[91]	100	600	9	116	4.7
Gd-DTPA-PAMAM G6 dendrimer-Cy5.5[92]	5-6	699	13.9	36.5	3
Gd-Si-DTTA-silica nanoparticle-$[Ru(bpy)_3]^{2+}$[93]	40	615	19.7	60.0	
Gd-LbL(3 layers)-silica nanoparticle-$[Ru(bpy)_3]^{2+}$[94]	40-50	615	19.0	55.0	
Gd-DTTA-mesoporous silica nanoparticle-RITC[95]	60-120	575	28.8	65.5	3
Gd-DTTA-mesoporous silica nanorod-FITC[96]	Length 320-540	520	22.0	41.0	0.47
Gd_2O_3@Cy5-doped silica[50]	3.3	690	8.8	11.4	7

r_1-longitudinal relaxivity; r_2-transverse relaxivity , CLIO-Crosslinked iron oxide nanoparticles; EPPT-a peptide, PEG-poly(ethylene glycol), FTIC-fluorescein isothiocyanate, DTPA-diethylenetriamineoentaacetate, SWNT-single wall nano tube, TSPETE- n-(trimethoxysilylpropyl)ethyldiame triacetic acid trisodium salt, PAMAM-polyamidoamine dendrimers, DTTA-diethylenetriaminetetraacetate comprises of organic dyes, QDs, and rare-earth doped materials. Most multifunctional nanostructure fabrication techniques involve combining fluorescent and magnetic entities into a nanocomposite (as exemplified in Table 2.3). In comparison, the fabrication of single-phase multifunctional nanocomposites would be more advantageous since all the functionalities would come from a single crystal which is easy to fabricate, functionalize and apply to biological systems. The synthesis process of fabricating multifunctional nanoparticles (such as those shown in Figure 2.5) often involves multiple steps. Therefore, single phase contrast agents would potentially be superior either in the view point of synthesis feasibility or functional homogenization compared to the

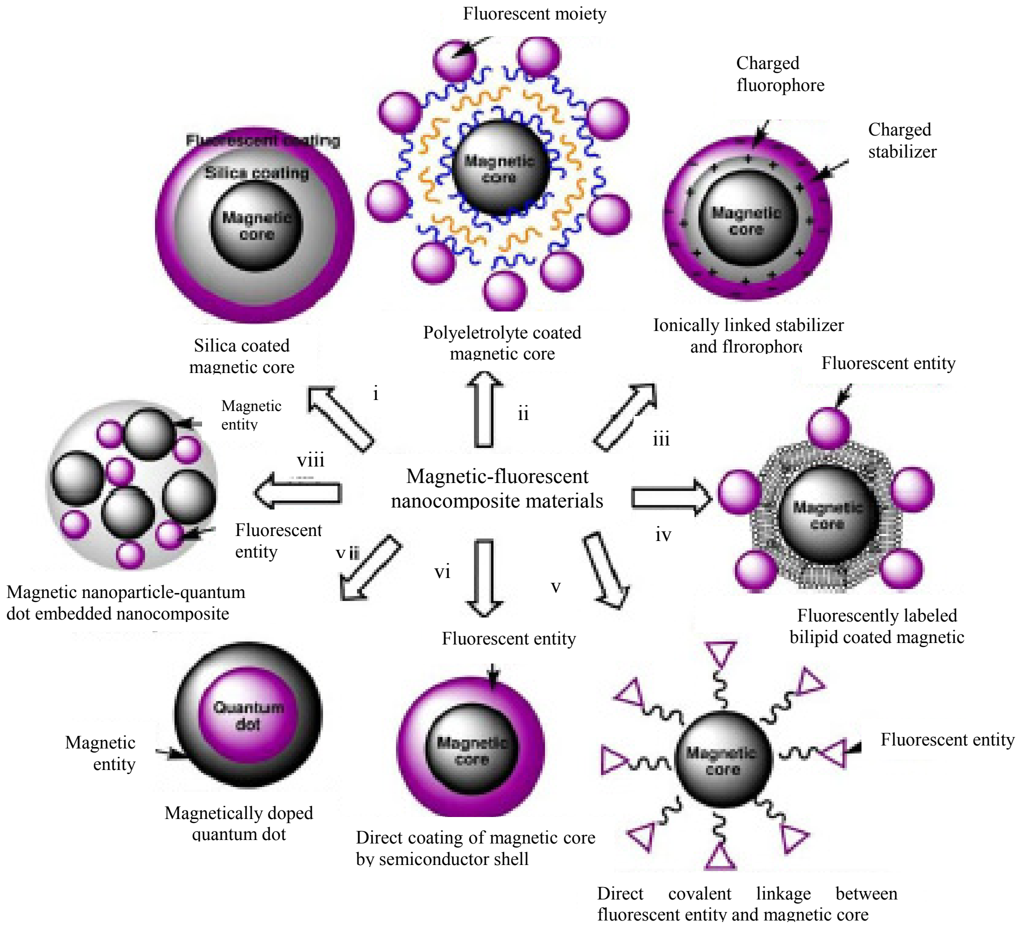

Figure 2.5 Magnetic-fluorescent nanocomposites on basis of fabrication strategy. (Reprinted with permission from ref. [35]. Copyright 2008, Springer).

heterostructured multifunctional nanocomposites.[48] To some extent, these benefits have motivated us to fabricate multimodal contrast agents in the form of single-phase nanostructures. The working material for this dissertation, rare earths, will be reviewed in detail in section 2.5.

2.4.4 Imaging Modalities

There are various imaging modalities that are currently used for non-invasive imaging (as shown in Table 2.1). However, we will focus our discussion on MRI and optical imaging in this section.

2.4.4.1 Magnetic Resonance Imaging (MRI)

MRI is a non-invasive imaging technique that works on the fundamental principles of nuclear magnetic resonance (NMR). Water, which consists of two hydrogen nuclei or protons, is the most abundant fluid in body. MRI generates two-dimensional images of tissues or internal organs based on the response of these protons to magnetic field. When an external magnetic field (B_0) is applied, a fraction of the proton nuclei aligns in the B_0 direction (Figure 2.6), and subsequently the aligned nuclei start to gyroscopically precess with a net magnetic moment of m and a Larmor precession frequency of ω_0 ($\omega_0 = \gamma B_0$), where $\gamma = 2.67 \times 10^8$ rad.s^{-1}.T^{-1} for ^{1}H.[97] When a resonant radio frequency (RF) transverse pulse is applied perpendicular to B_0, it causes resonant excitation of the magnetic moment procession into the perpendicular plane. Upon removal of the RF, the magnetic moment gradually relaxes to equilibrium by realigning to B_0. The relaxation process involves two pathways: longitudinal relaxation, accompanying loss of energy from excited state to its surroundings, and transverse relaxation from the loss of phase coherence of the precessing nuclei spins. The longitudinal and the transverse relaxation times are known as T_1 and T_2 respectively. The values of T_1 and T_2 are tissue-dependent and responsible for different image contrast from tissue to tissue. For example, in cancer diagnosis, due to difficulties in distinguishing tumor from healthy tissues, contrast agents are often injected during MR imaging. The fabrication of MRI contrast agent is hence critical as it changes the T_1 and/or T_2 of the protons in the surrounding area of the agent which produce different image contrasts (bright/dark).

Relaxation of water protons by contrast agent is a multifaceted phenomenon. Water molecules in close proximity to the contrast agents are relaxed and then rapidly exchanges relaxivity with the bulk water. Thus, water molecules surrounding the contrast agents are generally classified into three categories: (I) inner sphere water, where the water oxygen is directly coordinated to the contrast agents; (II) second-sphere water, which describes the water molecules that hydrate the contrast agent and have a finite residency time that is longer than the translation diffusion time of bulk water; (III) outer-sphere water, where the interaction of the water with the contrast agents is governed solely by translation diffusion.[38] Positive contrast agents such as Gd-based agents

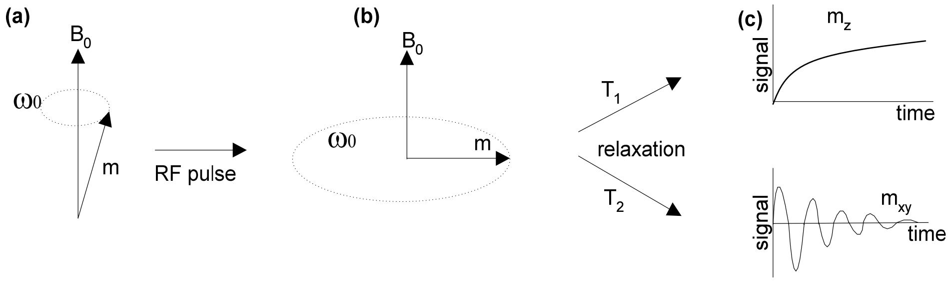

Figure 2.6 Schematic of the magnetic resonance (MR) principle; (a) net magnetic spins (m) of water protons precess with a Larmor frequency (ω_0); (b) upon application of a RF pulse, m begins precessing perpendicular to B_0; (c) m relaxes back to its original equilibrium states through longitudinal (T_1, m_z) and transverse in-planar (T_2, m_{xy}) modes.

primarily shorten the T_1 relaxation time through the inner sphere water and second-sphere water while negative contrast agents such as iron oxide exert their effect though bulk water.

2.4.4.2 Optical Imaging

Light can create contrast by its properties such as nonlinear effects, intensity, interference lifetime, polarization, wavelength, and coherence.[98-100] Different physical parameters of light interaction with tissues are used in various optical imaging techniques as shown in Table 2.4. For example, surface and multispectral images have been used for assessing brain function,[101] epithelial tissue structure and physiology.[102] Reflectance imaging[103] or diffuse optical tomography[104] have been used in probing of hemoglobins deeper in tissue. Other techniques which exploit the properties of light are light interference[100] and polarization.[98] For these techniques, image signal is primarily a function of 'internal contrast', and sometimes is limited in information content.[69]

In contrast, fluorescence imaging can impart molecular specificity to *in vivo* imaging technologies.[69] In fluorescence imaging, the energy from an external source of light is absorbed and almost immediately re-emitted at a lower- or higher-energy wavelength depending on whether up- or down-conversion fluorophores are used respectively. Fluorescence imaging can be done at different resolutions and tissue penetration depths, ranging from micrometers (intravital microscopy) to centimeters (fluorescence molecular tomography, FMT). In section 2.3.1, a detail mechanism of fluorescence emission has been described. As discussed, fluorescence depends much on the inherent properties of the fluorophores used.

Table 2.4 Optical imaging techniques [69]

Imaging Techniques	Contrast	Depth	Commonly used wavelength
Microscopic resolution			
Epi	A, Fl	20 µm	Visible
Confocal	Fl	500 µm	Visible
Two-photon	Fl	800 µm	Visible
Mesoscopic resolution			
Optical projection tomography	A, Fl	15 mm	Visible
Optical coherence tomography	S	2 mm	Visible, NIR
Laser speckle imaging	S	1 mm	Visible, NIR
Macroscopic resolution, intrinsic contrast			
Hyperspectral imaging	A, S, Fl	<5 mm	Visible
Endoscopy	A, S, Fl	<5 mm	Visible
Polarization imaging	A, S	<1.5 cm	Visible, NIR
Fluorescence reflectance imaging (FRI)	A, Fl	<7 mm	NIR
Diffuse optical tomography (DOT)	A, Fl	<20 cm	NIR
Macroscopic resolution, molecular contrast			
Fluorescence resonance imaging (FRI)	A, Fl	<7 mm	NIR
Fluorescence molecular tomography (FMT)	Fl	<20 cm	NIR
Bioluminescence imaging (BLI)	E	<3 cm	500–600 nm

A –absorption, E-emission, S-scattering, Fl-Fluorescence, NIR-near infra-red.

The bifunctional nanoparticles synthesized in this PhD work are aimed to be applied as contrast agent for fluorescent imaging.

2.5 Rare Earth (RE) Materials

2.5.1 Magnetic-Fluorescent RE Inorganic Nanomaterials

The rare earths (RE), otherwise referred to as the lanthanides, include a series of elements in the sixth row of the periodic table stretching from lanthanum (La) to ytterbium (Yb). The trivalent RE materials have partially filled 4f electron shell shielded by $5s^2$ and $5p^6$ electrons. Therefore, the energy levels of these elements are not very sensitive to external influences when incorporated in amorphous or crystalline hosts. In the host materials, the RE materials may exist as trivalent (RE^{3+}), or occasionally divalent (RE^{2+}) ions. Generally, the trivalent (RE^{3+}) ions exhibit intense narrow-band intra-4f luminescence in a wide variety of hosts owing to the strong shielding provided by the $5s^2$ and $5p^6$ electrons, electron–phonon coupling is weak and radiative transitions of RE ions in solid hosts resemble those of the free ions. The positions of the RE electronic levels are influenced more by spin–orbit interactions than by applied crystal field. The intra-4f transitions are generally parity forbidden and are partially allowed by crystal field interactions mixing opposite parity wavefunctions.[105] For these reasons, RE ion produces long luminescence lifetimes (usually in micro to millisecond range), and narrow emission line-widths. By choosing appropriate RE ions, sharp and intense emission can be obtained over the range of visible to the near-infrared regions. Figure 2.7 shows energy level diagrams for the individual RE^{3+} ions of each of the 13 lanthanides from cerium (Ce) to ytterbium (Yb) with partially filled 4f orbitals.[106] A conventional way to denote energy levels of rare-earth ions is ${}^{2S+1}L_j$, which is labeled according to their angular momentum and spin quantum numbers. In symbol, the letter L refers to the total orbital angular momentum of the ion obtained by combining the orbital angular momenta of the individual electrons in the ion according to the Clebsch–Gordan series. The left superscript, presented as $2S+1$, is the number of possible orientations of the total spin of the ion, where S is the total spin of the ion. The right subscript j represents the total angular momentum of the ion and is determined using the Russell–Saunders coupling scheme.[107]

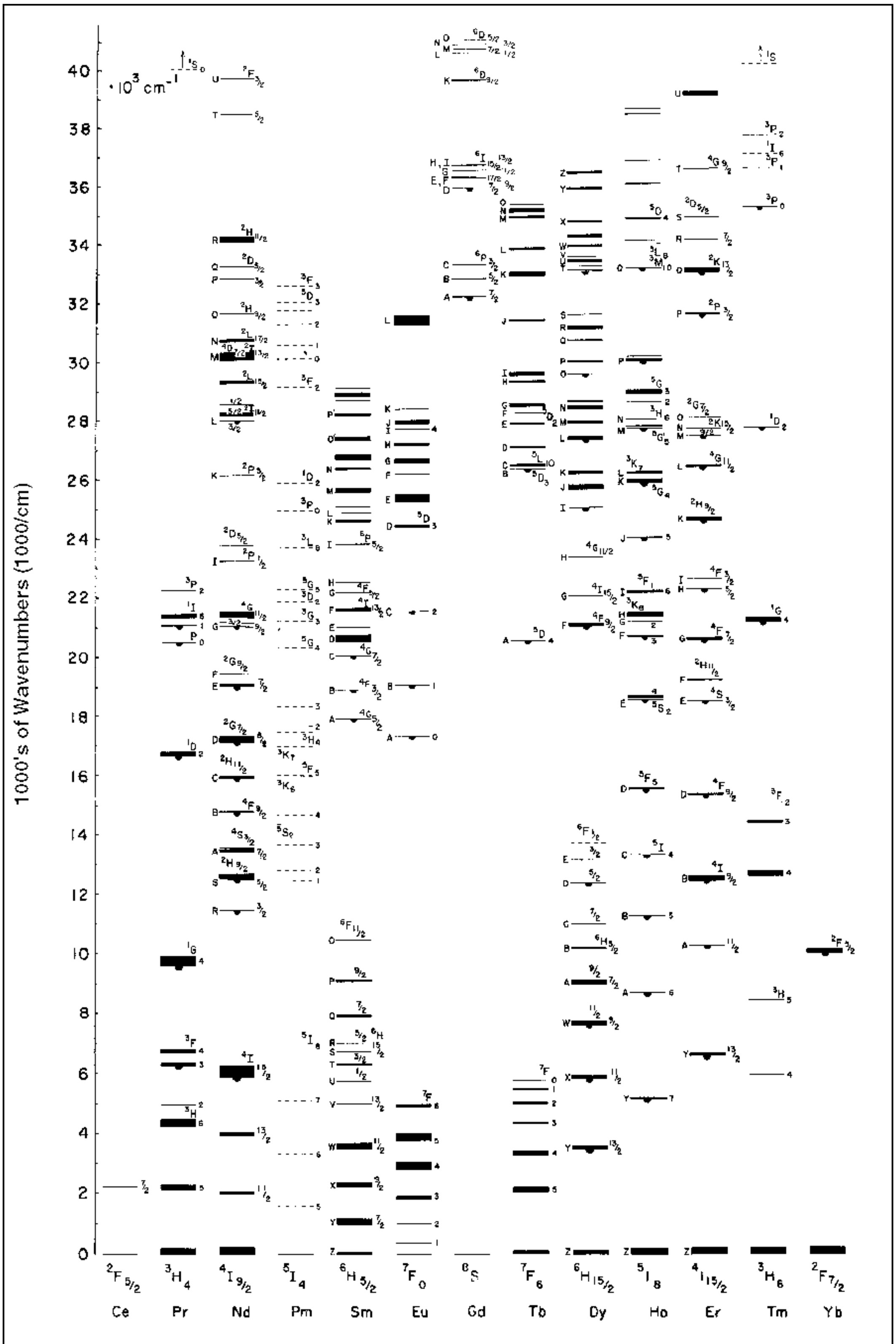

G. H. Dieke. Spectra and energy levels of rare earth ions in crystals
(Interscience Publishers. New York. 1968)

Figure 2.7 Energy level diagram of the rare earth materials (Dieke diagram).[106]

In recent years, rare earth (RE)-doped nanomaterials have been emerging as a new class of luminescent optical labels that appears to be very promising alternatives to organic fluorophores and quantum dots for bio-related applications such as biological assays and medical imaging. This type of fluorophores offer low autofluorescence background, large Stoke's and anti-Stoke's shifts, sharp emission bandwidths, high resistance to photobleaching, and high temporal resolution. The RE ions exhibit up-conversion luminescence which could achieve high tissue penetration and therefore are more effective for deep tissue imaging. In addition, some recent studies reported rare-earth materials as potential MRI contrast agent.[51-54, 108-111] In this work, we will present the results of fabricating single-phase bifunctional nanoparticles by combining the intrinsic magnetic and fluorescent properties of RE materials to engineer bifunctional contrast agents for bimodal optical/MR imaging.

2.5.2 Fluorescence Mechanism in Rare Earth Materials: Ion-ion Interactions

In rare earth doped materials (doped with one or more RE species), a number of ion-ion interactions could occur which leads to different electronic transition pathways. Simple schematic diagrams are presented in Figure 2.8 to illustrate the most important interactions.

2.5.2.1 Co-operative Up-conversion

Co-operative up-conversion is a special type of luminescence in which two interacting ions in the excited state return to the ground state simultaneously, exciting one ion to an energy state which is the sum of the energies of the two interacting ions.[112] The first observation of co-operative luminescence was reported by Nakazawa *et al.*[113] for Yb^{3+}

pairs in $YbPO_4$. A simple schematic for the co-operative up-conversion mechanism is presented in Figure 2.8a.

2.5.2.2 Energy Migration

An ion 1 in the metastable state can interact with a nearby ground state ion 2, promoting it to the higher energy level (Figure 2.8b). Although radiative emission may still occur from ion 2, the probability of non-radiative decay is increased with each successive transfer.

2.5.2.3 Cross-relaxation

In a cross-relaxation process, excitation energy from an ion decaying from a highly excited state promotes a nearby ion from the ground state to the metastable state. For example, the energy gap between two consecutive the energy levels E_2 to E_1 is close to energy gap between E_1 to G (Figure 2.8c). At sufficiently high concentrations of excited ions in level E_2, the population of the metastable state E_1 could increase by the decay of ions from the E_2 level which transfer its equivalent energy to promote nearby ions from the ground state G to metastable state E_1. This process is called cross relaxation.

2.5.2.4 Excited State Absorption (ESA) and Ground State Absorption (GSA)

ESA takes the form of successive absorption of pump photons by a single ion. The general energy diagram of the ESA process is shown in Figure 2.8d. If excitation energy is resonant with the transition from ground level G to excited level E_1, phonon absorption occurs and populates E_1 from G in a process known as ground state absorption (GSA). A second pump photon then promotes the ion from E_1 to higher-lying state E_2. During relaxation from E_2 to ground level G, the ion may result in emission (shown as red arrow), or relaxes non-radiatively.

2.5.2.5 Energy Transfer Up-conversion (ETU)

ETU is similar to ESA in that both processes utilize sequential absorption of two photons to populate the metastable level. The essential difference between ETU and ESA is that the excitation in ETU is realized through energy transfer between two neighboring ions. In an ETU process, each of two neighboring ions can absorb a pump phonon of the same

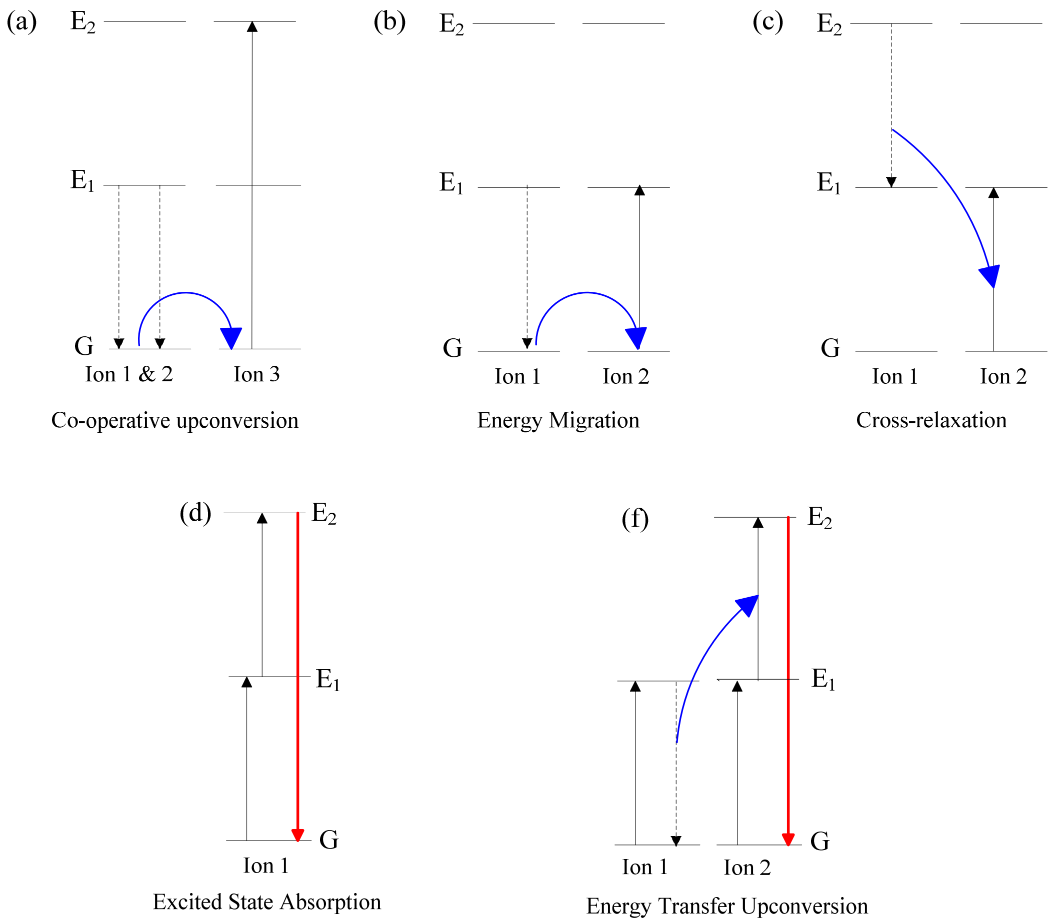

Figure 2.8 Ion-ion interactions are shown using a simple three-level system energy level diagram. The black solid line, and dashed lines represents photon excitations, and relaxations respectively, the blue arrow shows energy transfer process between ions and the red arrow represents emissions.

energy, thereby populating the metastable level E_1 (Figure 2.8f). A non-radiative energy transfer process promotes one of the ions to upper emitting state E_2 while the other ion relaxes back to ground state G. The dopant concentration that determines the average distance between the neighboring dopant ions has a strong influence on the efficiency of the up-conversion process.

2.5.3 Factors Affecting Choice of RE Host/dopant

Inorganic nanocrystals in most cases do not exhibit fluorescence at room temperature. Therefore, care has to be taken in choosing right crystalline host and dopants especially in preparation of new nanomaterials of well defined optical properties. The dopants are usually in the form of localized luminescent centers within the hosts. The dopants ions radiate upon excitation. The ion emitting the radiation is called an activator ion and the ion transferring the energy is called the sensitizer. Sensitized luminescence often takes place in up-conversion fluorescence where two or more RE ions are doped in host. In single doped nanocrystals, the distances between two neighboring activator ions and the absorption cross-section of the ions are important in the fluorescence process. High doping level may lead to deleterious cross-relaxation which results in quenching of excitation energy. A sensitizer with a sufficient absorption cross-section in the NIR region is usually codoped along with the activator to allow efficient ETU process between the sensitizer and the activator. The concentrations of the activator and sensitizer often require careful adjustment to avoid fluorescence quenching. For example, the trivalent Yb^{3+} possesses an extremely simple energy level scheme with only one excited 4f level of ${}^2F_{5/2}$ (refer to Figure 2.7) with absorption band located around 980 nm due to the ${}^2F_{7/2} \rightarrow {}^2F_{5/2}$ transition which is larger than other rare-earth ions. Beside the

$^2F_{7/2} \rightarrow {}^2F_{5/2}$ transition, Yb^{3+} is resonant to the f → f transition of other up-converting rare earth ions like erbium (Er), thulium (Tm), holmium (Ho) which makes it very effective up-conversion codopant pair in different host.[14]

Selection of host material is also important for favorable optical properties. The host materials require close lattice matches to dopant ions and should have low phonon energies. Heavy halides like bromides, chlorides, and iodides generally exhibit low phonon energies but they are hygroscopic which quenches fluorescence. Oxides have relatively higher phonon energies but show higher chemical stability. Fluorides show lower phonon energies and good chemical stabilities. In addition, crystal size, symmetry of host also affects luminescence of the rare earth nanocrystals.[114-115] The most extensively explored rare-earth host nanomaterials for doping are different forms of oxides, fluorides, and phosphates.[116] Yttrium oxide (Y_2O_3) is one of very widely investigated hosts among them. Y_2O_3 has similar crystal structure to other lanthanide oxides, and the ionic radii of Y^{3+} is similar to other lanthanide ions. Besides, lanthanide doped Y_2O_3 have been fabricated using a wide range of synthesis method. Morphology of Y_2O_3 can be tuned; few different morphologies of lanthanide Y_2O_3 such as nanoparticles, hollow spheres, and disks have been reported.[117-120] Yttrium ortho-vanadate (YVO_4) is also a very good host for doping lanthanides. Doping of Eu^{3+}, and Er^{3+}, Dy^{3+}, and samarium (Sm^{3+}) in YVO_4 have been reported to produce high intensity multicolor emitting phosphors.[119, 121-122] Some other RE doped hosts have also been reported as potential contrast agents for optical imaging as well as MR imaging such as $LaPO_4$,[123] $GdPO_4$,[51, 53] Gd_2O_3,[52, 108-109] and Dy_2O_3[54], and fluorides like GdF_3,[110] $NaGdF_4$.[111] Gadolinium (Gd^{3+}) ions are paramagnetic and their chelate forms are used as clinical paramagnetic relaxation agents in nuclear magnetic resonance (NMR) and MRI.[38, 124]

In our work, we started our investigation with Y_2O_3 host with a number of RE^{3+} dopants which includes Tb^{3+}, Eu^{3+}, Er and codopant Yb^{3+}/Er^{3+}. Y_2O_3 was chosen as the host because it has broad transparency range (0.2- 8 μm) and relatively low phonon energy,[125] which makes it one of the better choices for fluorescent study by doping RE^{3+} ions. Based on the knowledge from the $Y_2O_3:RE^{3+}$ system, we have further developed Tb^{3+} ion-doped superparamagnetic host (γ-Fe_2O_3) to fabricate single-phase bifunctional superparamagnetic-fluorescent nanocrystals. Finally, we extended our study by choosing paramagnetic RE oxides (Gd_2O_3 and Dy_2O_3) as hosts for doping different RE^{3+} ions, forming single-phase bifunctional paramagnetic-fluorescent nanoparticles as potential contrast agent for the bimodal optical/magnetic resonance imaging.

2.5.4 Rare Earth Nanomaterials Synthesis

Different synthesis techniques for rare earth nanomaterials have been reported, which include coprecipitation, hydrothermal synthesis, sol-gel processing, thermal decomposition, and combustion synthesis. Optimization of synthesis process and parameters are very critical in tailoring nanoparticles with desired phase, size, morphology, chemical composition, surface functional groups, and optical properties. Depending on the applications, different synthesis process can be adopted. For example, narrow size distribution and high aqueous dispersity are very important for biomedical application. In the following section, summary of the key features of the above mentioned synthesis techniques are presented in Table 2.5, and is followed by short description of the commonly used methods for synthesizing fluorescent nanocrystals.

Table 2.5 Typical synthetic routes to several fluorescent nanocrystals[14]

Method	Hosts	Key Features
Coprecipitation	$NaYF_4$ $LuPO_4$ $YbPO_4$ LaF_3	Fast growth rate without the need for costly equipment and complex procedures. Post-heat treatment typically required.
Thermal decomposition	$NaYF_4$ LaF_3 GdOF	Expensive, air-sensitive metal precursors. High quality, monodisperse nanocrystals, toxic by-products.
Hydro(solvo)thermal synthesis	LaF_3 $NaYF_4$ YVO_4	Cheap raw materials. No post-heat treatment. Good control over particle size and shape. Specialized reaction vessels required.
Sol–gel method	ZrO_2 TiO_2 $Lu_3Ga_5O_{12}$ YVO_4	Cheap raw materials. Calcinations at high temperatures required.
Combustion synthesis	Y_2O_3 Gd_2O_3 La_2O_2S	Time and energy saving. Considerable particle aggregation.
Flame synthesis	Y_2O_3	Time saving and readily scalable.

2.5.4.1 Coprecipitation Method

Coprecipitation is one of the convenient techniques that usually produce small nanocrystals with narrow size distribution. The synthesis condition of this method is less stringent, low-cost, and less time consuming compare to others. In most of the cases the nanocrystals synthesized by coprecipitaiton method need post heat treatment to obtain better crystallinity. In many occasions, commercially available ligands such as di-n-octadecyldithiophosphate,[126] polyvinylpyrrolidone (PVP),[127] and polyethylamine (PEI)[128] have been used in the synthesis process to control particle growth, prevent agglomerates, and render water dispersity property. RE doped fluorescent nanocrystals synthesized using this method includes LaF_3,[126, 129] $NaYF_4$,[115] $LuPO_4$, and $YbPO_4$.[130]

2.5.4.2 Thermal Decomposition Method

This method is a very effective route to synthesize high crystalline, highly monodisperse, and uniform nanoparticles. Generally, the metal precursor is thermally decomposed at very high temperature using a high boiling point (bp) liganding solvent (e.g. octadecene; bp 317 °C) and a surface passivating ligand (e.g. oleic acid) to passivate the nanoparticle surface and prevent aggregation. This method produces nanoparticles with very small size distribution and nanoparticle size can be tuned very precisely. Some of the uniform RE-doped fluorescent nanocrystals with narrow size distribution reported using this method are $NaYF_4$:Yb,Er(Tm),[131-132] LaF_4.[133] One of the limitations of this method is that the synthesized nanoparticles are not readily dispersible in polar solvent such as water, despite being well-dispersible in non-polar solvent like cyclohexane. Hence, post synthesis surface modification of the nanoparticles with hydrophilic groups is often needed to render them water dispersible.

2.5.4.3 Hydrothermal Method

The hydrothermal method offers an alternative of synthesizing nanoparticles with good dispersibility in solvents including water. This method utilizes the supercritical condition of the solvent. At an elevated pressure and temperature above the critical value, the solubility increases and the reactivity among the reactants are enhanced. As a result, highly crystalline nanomaterials can be produced at much lower temperature using this method. The reaction is carried out in a specially designed reaction vessel known as the autoclave which can sustain high temperature and pressure for a prolonged period of time. But generally the synthesized nanocrystals are not as monodisperse as the nanocrystals produced by thermal decomposition method. Reported RE doped nanocrystals using this method are $NaYF_4$:Tb(Eu/Yb,Er),[134] LaF_3:Yb,Er(Tm/Ho).[135] Like thermal decomposition method, surfactant have also been used in this method to tailor morphology and crystal size of the nanoparticles.[134, 136]

2.5.4.4 Sol-gel Method

Sol-gel technique is a wet-chemical method which is characterized by the hydrolysis and polycondensation of metal alkoxide/halide based precursors. This method works well for the fabrication of nanocrystals for applications like thin film coating. Though there has been some reports of synthesizing different RE doped fluorescent material using this method, the method is not particularly suitable for bioapplications due to difficulty in particle size control and nanoparticle aggregation in aqueous solutions. Example of RE doped nanoparticles includes TiO_2:Er, $Lu_2Ga_5O_{12}$:Er, $BaTiO_3$:Er, YVO_4:Yb,Er.[137-139]

Beside these methods, some other methods such as combustion synthesis[140] and flame synthesis[141] have been reported for RE doped fluorescent nanocrystals. However, in this PhD work, we have chosen to use thermal decomposition method. The choice of thermal decomposition method is motivated by its ability to tailor various nanoparticles morphology and yet produce highly monodisperse, uniform nanoparticles, which is one of the key prerequisites for bioapplications.

2.6 Surface Modification

Surface modification of the fluorescent nanoparticles may provide improved photostability, colloidal stability, and platform for attaching biological molecules. The surface phenomena at nanoscale materials are very pronounced compare to their bulk counterparts due to their higher surface to volume ratio. For nanomaterial-based fluorophores, the presence of surface defects often significantly influences their luminescent properties. For RE doped fluorescent nanoparticles, the presence of any surface dopant ions in incomplete coordination may quench the luminescence. Quenching may take place due to high energy oscillators arise from weakly bound surface impurities, ligands, and solvent due to lack of effective protection by the host lattice.[14] Introduction of an inert crystalline shell around the doped nanoparticles can passivate the surface defect (Figure 2.9) and improve luminescent efficiency. For example Mai *et al.*[142] reported a two fold increase of luminescence efficiency for $NaYF_4$:Yb,Er, while Yi *et al.*[143] reported 30 times increment of $NaYF_4$:Yb,Tm nanocrystals coated with a 1.5 nm thick $NaYF_4$ shell. Amorphous shells have also been reported to surface passivate and improve luminescence. For example, amorphous silica shell has been reported to improve the up-conversion luminescence for Y_2O_3:Tb,Tm nanocrystals with the ability to vary the luminescence by varying thickness of the silica shell.[144]

Beside surface passivation, the nanocrystals intended for bioapplications often require surface functionalization with different ligands to render them biocompatible. Nanocrystals prepared by high-temperature routes, such as thermal decomposition, lack functional moieties for dispersion in aqueous media. Hydrophilic ligands are commonly

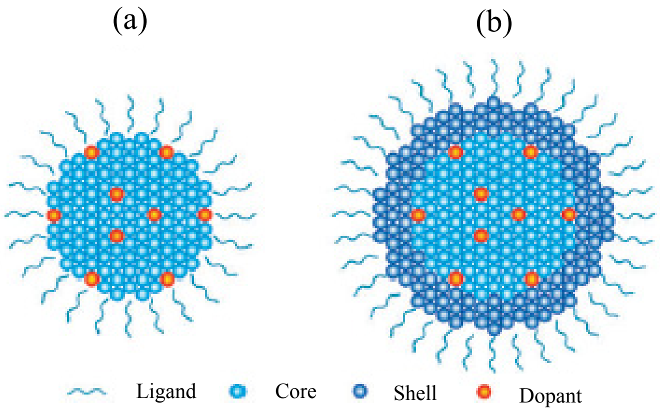

Figure. 2.9 Proposed distributions of lanthanide dopants in (a) a nanocrystal without the protection of a shell and (b) a core–shell type nanocrystal. (Reprinted with permission from ref. [14]. Copyright 2009**,** The Royal Society of Chemistry (RSC).

used to functionalize the nanocrystals surface prior to disperse in aqueous media or attachment with biomolecules. Different strategies have been explored to provide nanocrystal with properties such as water dispersity and, biomolecule conjugation for biomedical applications and biodetection schemes. Table 2.6 shows some of the major strategies reported in the literature which include ligand exchange, ligand oxidation, ligand attraction, layer by layer assembly, and surface silanization.

Ligand exchange has been demonstrated by Yi *et al.*[145] for up-converting $NaYF_4$ nanocrystals where they used polyethylene glycol 600 diacid (HOOC-PEG-COOH) to replace the surface amine ligand (oleylamine) with carboxyl-functional groups. The carboxyl-functional groups on the nanoparticle surface render them to water-dispersible. Chen *et al.*[146] developed ligand oxidation technique alternative to ligand exchange. Lemieux-von Rudloff reagent was used to oxidize the surface oleic acid to azelaic acid. The oxidized ligands have carboxyl groups on the surface which provide them water dispersity. The same group later reported a strategy based on epoxidation of the double bond followed by the reaction with PEG-amines to render the nanocrystals water dispersible.[147] A limitation of this process is that it can only be applied to ligands containing unsaturated carbon-carbon bonds and not applicable to all ligands in general. A ligand attraction process was reported by Yi *et al.*[148] where they coat the core-shell nanocrystals with 25% octylamine and 40% isopropylamine modified poly(acrylicacid) (PAA). Wang et al[149] reported layer-by-layer assembly technique which is based on the adsorption of alternatively charged polyions on the nanocrystals surface. They reported sequential adsorption of poly(allylamine hydrochloride) and negatively charged poly(sodium 4-styrenesulfonate) onto the $NaYF_4$ surface to generate water-dispersible nanocrystals.

In comparison, the surface silanization technique is versatile and applicable for both hydrophobic and hydrophilic nanocrystals. The Stöber method [150] is a popular silanization technique for hydrophilic nanoparticles while reverse-microemulsion technique has been adopted for silanization of hydrophobic nanoparticles. The silanization process is based on the hydrolysis and polycondensation of silica precursor (e.g. tetraethoxysilane, TEOS) in presence of alkali hydroxide (e.g. ammonium hydroxide, NH_4OH). In the surface silanization process, organosilanes with amine functional groups are assembled onto nanoparticles surface, making the nanoparticles water-dispersible and biocompatible. This method is attractive because silica coating is very much biocompatible and can be conjugated to a wide range of biomolecules conveniently.[9] Some example of silanization include silica coating of PVP-stabilized $NaYF_4$:Yb,Er,[127] a thin layer of silica formation on Fe_2O_3-CdSe magnetic quantum dots,[30] and encapsulation of magnetic and fluorescent nanocrystals in silica shell.[24, 151]

Table 2.6 Some of the generic strategies for solubilization and functionalization of nanoparticles. Reprinted with permission from ref. [14]. Copyright 2009, The Royal Society of Chemistry (RSC).

Type of Strategies	Scheme of strategies	Representative reagents
Ligand Exchange	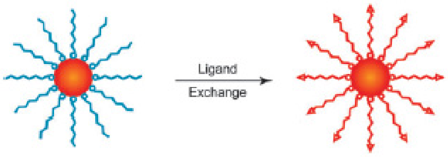	
Ligand Oxidation	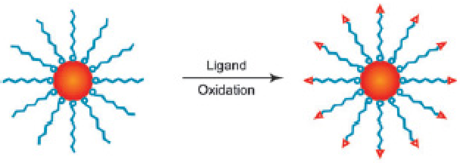	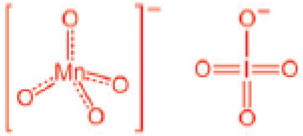
Ligand Attraction	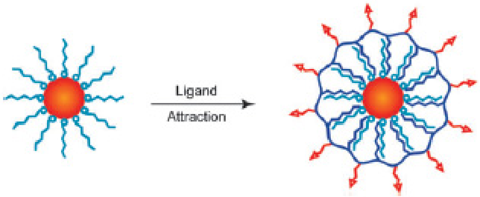	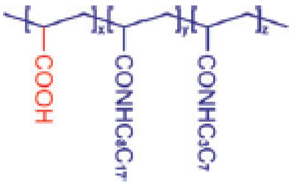
Layer by layer Assembly	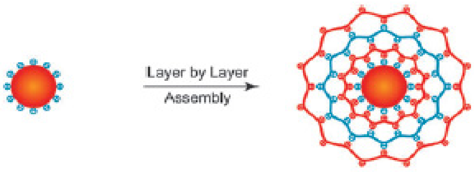	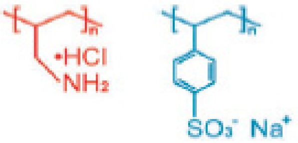
Surface Silanization	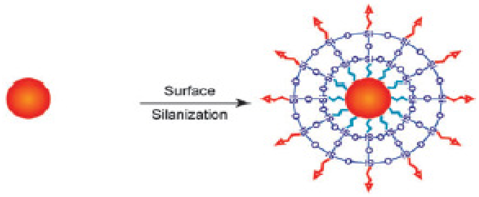	

Considering the above advantages, we have adopted surface silanization technique in our work for making a thin layer of silica coating using aminopropyl trimethoxysilane (APS) as silica precursor, and tetramethylammonium hydroxide (TMAH) as the alkali hyroxide.

2.7 Shape Control of Nanoparticles

Size, shape and composition play critical roles in determining the properties of the nanomaterials. For example, the electronic band of quantum dots has been revealed to be gradually quantized with size reduction of the nanocrystal (i.e. decrease in crystal-size increase the band-gap energy). The ability to control and manipulate the size and shape of the nanoparticles is one of the challenges in chemistry and materials science research due to poor understanding of nucleation and growth process of the nanocrystals.[152] In the last decade, successful syntheses of various metal nanocrystals with different morphologies have been reported.[116, 152-155] On the basis of dimensionality, basic motifs of the inorganic nanocrystals fabricated can be categorized as 0-dimensional cubes, spheres, polyhedrons; 1-D wires and rods; 2-D prisms, plates, discs; and some complex structures such as stellations and tetrapods. Figure 2.10 shows the schematics of the basic motifs. As described by Xia *et al.*[152] the nucleation and growth mechanisms behind different shape formation is extremely complicated and current perceptive is far from being able to present atomistic details for the evolution pathways that a precursor compound may take to form metal atoms, nuclei, and then well-defined nanocrystals. However, typical nanocrystal formation mechanism can be broken down into three distinct phases: (I) nucleation, (II) evolution of nuclei into seeds which are something larger than nuclei, and (III) growth of seeds into nanocrystals. The final shape of the nanocrystals depends primarily on the inherent crystal structure of the corresponding seed crystal. Many other factors also play significant roles in forming different shapes such as inherent anisotropy of the crystal structure, crystal surface reactivity, dipolar interactions, and binding affinity of the capping ligands. The internal structures of the intermediate seeds and nanocrystals end products are usually analyzed by techniques such as electron microscopy and X-ray diffraction.

In our experiments, we achieve controlled synthesis of 1-D nanorods of rare earth oxides which evolve from their spherical nanocrystals. Evolution of nanorods from the nanocrystals can be selectively controlled. The synthesis and formation mechanism have been investigated using high resolution transmission electron microscope which will be discussed in chapter 5.

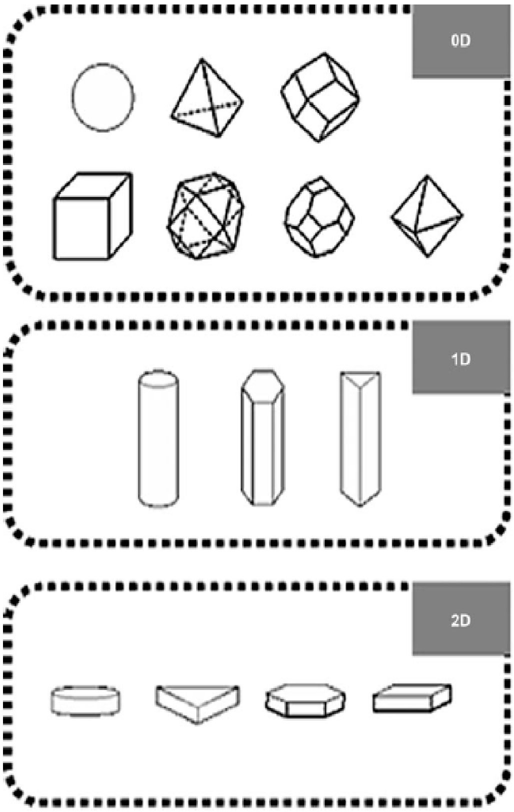

Figure 2.10 Basic motifs of inorganic nanocrystals: 0D spheres, cubes, and polyhedrons; 1D rods and wires; 2D discs, prisms, and plates. Reprinted with permission from ref. [153]. Copyright 2006, Wiley-VCH Verlag GmbH & Co. KGaA).

2.8 Toxicity Concern of Nanoparticles

Toxicity is a critical consideration in evaluating nanomaterials intended for biomedical applications. There are number of literatures reporting potential toxic effects of nanoparticles in cellular environment.[156-159] Toxicity depends on many factors which include constituent materials, materials dosage, surface charge of the nanomaterial, surface molecules of nanomaterials, incubation time with cells, and cell types. Due to their small size, nanoparticles can readily enter the cells, the cell nuclei, and other subcellular compartments. Nanoparticle toxicity, both *in vitro* and *in vivo*, is thus important characteristics for defining and limiting their applications.

In cellular environment, nanoparticles are reported to generate reactive oxygen species (ROS) such as free radicals both *in vivo* and *in vitro*. ROS are reactive, are capable of degenerating biomacromolecules such as DNA and proteins, leading to deterioration of cellular function. ROS can influence oxidative signaling in cells, resulting in alteration of gene expression, cell proliferation, differentiation, and cell death. [160] The nanoparticles reported to produce ROS includes fullerene (C60),[161] TiO_2,[162] CdTe Qds,[163] CdSe QDs,[164] CdSe@ZnS Qds,[165-166] single wall carbon nanotubes (SWCNT),[167] and silver nanoparticles.[168]

Mitochondria, the redox active organelles in the cytoplasm of the cell, play a critical role in cell biology not only as the producer of adenosine triphosphate (ATP), but also in the sequestration of calcium ions (Ca^{2+}) and generation of free radicals. They are also repositories of several proteins that regulate apoptosis.[169] Studies on intracellular localization show that some nanoparticles such as fullerenes could cross the external cellular membrane and preferentially relocate in mitochondria.[170-171] Perturbations in normal functions of mitochondria will inevitably disturb cell functions, may sensitize cells to neurotoxic insults, and may initiate cell death.[160] Different mechanisms of cell deaths have been proposed, among which changes in nucleus is an important one. Nuclear condensation with DNA fragmentation is typical for apoptotic cell deaths, while the nucleus is swollen for necrotic cell death. Mitochondrial damage and intracellular metabolism of the nanoparticles may generate free electrons which also induce ROS production.[162] Up till now, the mechanism of which nanoparticles trigger cellular responses is not well understood. However, ROS and Ca^{2+} seem to be involved in eliciting nanoparticle-induced cytotoxicity while ROS generation has been a dominating explanation for the biological reactivity of the nanoparticles.

The cytotoxicity studies of the nanoparticles have been conducted for: (I) carbon based nanomaterials such as fullerene, single and multi-walled carbon nanotubes;[172-175] (II) metal-based nanoparticles such as gold nanoparticles,[176] nanoshells,[177] nanorods,[18, 178-179] superparamagnetic iron oxide nanoparticles,[168, 180-181] and (III) semiconductor-based nanoparticles such as quantum dots.[182-184] In contrast, cytotoxicity studies of rare-earth doped inorganic nanoparticles or rare-earth based nanoparticles are very few. In this work, we have conducted cytotoxicity study of RE-doped fluorescent inorganic nanocrystals and compared the results with iron oxides and CdSe QDs using a new approach based on American National Standard ISO 10993-5. This approach of conducting cytotoxicity studies for rare earth nanomaterials, as presented in chapter 6, should be useful for the evaluation of all the nanoparticles in general.

2.9 Motivation behind the Research Conducted

The development of multifunctional nanoscale platforms for integrated imaging is still in its early stage.[17] In an effort to fabricate nanoparticle-based multifunctional contrast agents, many different materials and integration strategies have been reported. In most cases, they are fabricated by combining two or more functional entities. In addition, potential short-term and long-term toxicity effect, degradation, and metabolism of nanoparticle based agents are not well studied.[185] Our contribution to the field is through the realization of single-phase bifunctional nanomaterials as bimodal contrast agent via a simple synthetic strategy, and to demonstrate their potential application in optical imaging and MRI. Their *in vitro* cytotoxicities were also evaluated using a new method proposed by us. Such multimodal contrast agents may be extended to therapeutic applications by functionalizing drug molecules with the probes, or by using the magnetic component in hyperthermia or as a guiding vector to the targeted area.

CHAPTER 3

Materials Characterization and Analysis Techniques

This chapter describes the characterization techniques used throughout the study and illustrates their basic principles, operating conditions and methods of sample preparation. In addition, some of the key features of the American National Standard ISO 10993-5, which was used to evaluate *in vitro* cytotoxicity of the nanomaterials, will be presented. The last section will include a brief introduction of the one-way analysis of variance (ANOVA), a statistical analysis method which was used to analyze the cytotoxicity data.

3.1 Transmission Electron Microscopy (TEM)

The transmission electron microscope (TEM) is a microscopy technique which operates on the same basic principles as the light microscope but uses electrons instead of light. The use of electrons makes it possible to get a resolution a thousand times higher than that of a light microscope.

An electron gun at the top of the microscope ejects the electrons that travel through a vacuum in the column of the microscope towards the specimen. Instead of using glass lenses to focus the light in the light microscope, a TEM uses electromagnetic lenses to focus the electrons into a very fine beam. Depending on the density of the material present, some of the electrons are scattered while some penetrates through the sample. At the bottom of the microscope the unscattered electrons hit a fluorescent screen, which give rise to a shadow image that provides morphological features at low resolution and lattice/atomic arrangements at high resolution for the nanostructured materials.[186] The image can be studied directly or photographed with a charge coupled device (CCD) camera. A simple schematic diagram of a TEM is presented in Figure 3.1.

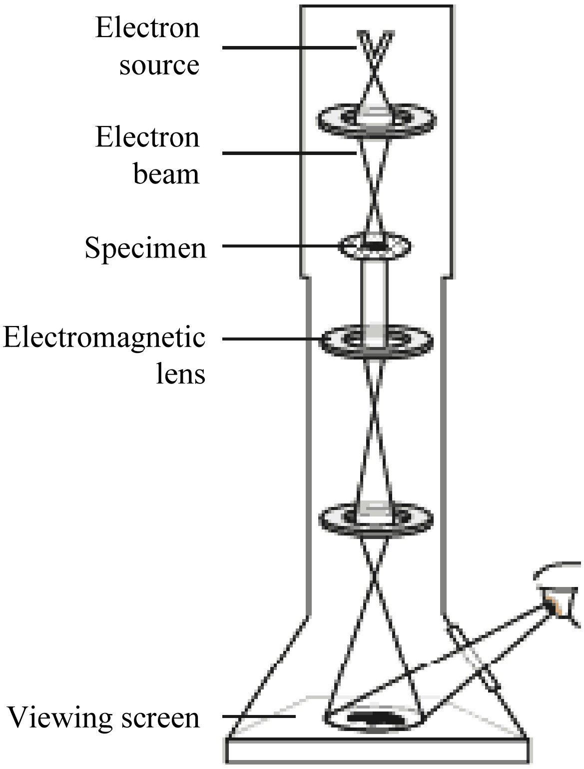

Figure 3.1 Schematic of a transmission electron microscope[186]

In addition, this technique can be very powerful in providing electron diffraction patterns, and elemental information of the specimen. The electron diffraction X-ray spectroscopy (EDS) data can be collected with a nanometer resolution, which enables the construction of detailed elemental maps of the nano-object under study.[187]

For the specimen preparation in current study, a few drops of nanoparticle were dispersed onto a holey carbon film supported on a 200 mesh copper grid (3 mm in diameter) and allowed to dry in air at room temperature. The carbon grid with sample was then mounted into the vacuum chamber for imaging and selected area electron diffraction (SAED) The observation was carried out in JEOL 3010 and JEOL JEM-2100F microscopes, operated at an accelerating voltage of 200 kV.

3.2 Powder X-ray Diffraction (XRD)

Powder X-ray diffraction (XRD) is an analytical technique primarily used for phase identification of a crystalline material and can provide information about unit cell dimensions. X-ray diffraction is based on constructive interference of monochromatic X-rays and a crystalline sample. These X-rays are generated by a cathode ray tube, filtered to produce monochromatic radiation, collimated to concentrate and direct toward the sample. The interaction of the incident X-rays with the sample produces constructive interference (and a diffracted ray) when conditions satisfy Bragg's law:[188]

$$n\lambda = 2d \sin \theta \qquad \text{(Eq. 3.1)}$$

where λ is the wavelength of incident X-ray, d is the crystal plane distance, and θ is the diffraction angle. Bragg's law (Figure 3.2) relates the wavelength of electromagnetic radiation to the diffraction angle and the lattice spacing in a crystalline sample. These diffracted X-rays are then detected, processed and counted. By scanning the sample through a range of 2θ angles, all possible diffraction directions of the lattice should be attained due to the random orientation of the powdered material. Conversion of the diffraction peaks to d-spacings allows identification of the materials because each material has a set of unique d-spacings. Typically, this is achieved by comparison of d-spacing with standard reference patterns.

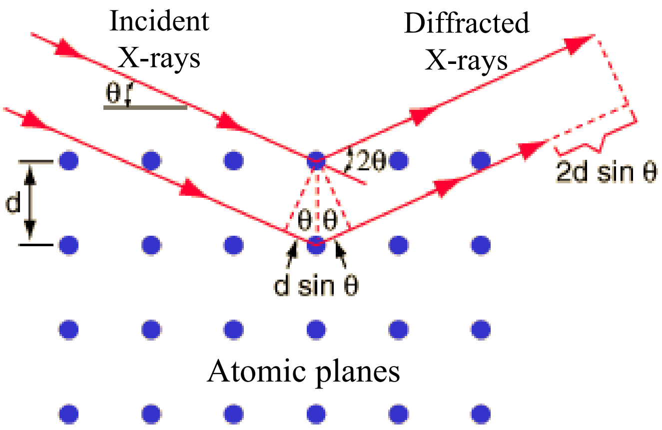

Figure 3.2 Bragg's law and the interaction of the X-rays with the atoms in a crystal.

In a powder XRD, the sample is prepared in the form of fine homogeneous powder. As a result, the sample contains a large collection of vary small crystals which could be orientated in every possible direction relative to the beam of radiation. For the specimen preparation in this study, approximately, 40-50 mg of a sample was stirred gently in an agate mortar to break up lumps. The powdery samples of the nanoparticles were then spread evenly onto a zero-background holder. Step-scan X-ray powder diffraction data were collected over the range of 2θ range of 10-85° on a D8 Advance Bruker powder X-ray diffractometer with Cu Kα (operated at 40 kV, 40 kA) radiation (λ = 0.15406 nm) with 6 mm divergence slit, 1 mm scattering slit, and 0.2 mm receiving slit. The scanning step size was 0.015° in 2θ with a counting time of 1 s per step.

The diffraction peaks can be used to calculate the average crystallite size, Dp, by Scherrer formula:[189]

$$Dp = \frac{K\lambda}{\mathrm{FWHM}\cos\theta} \qquad \text{(Eq. 3.2)}$$

where k is the Scherrer constant that falls in the range 0.87-1.0 (in this study 0.89 has been chosen), λ is the wavelength of X-ray; and FWHM is full width at half maximum of the diffraction peaks.

3.3 X-ray Photoelectron Spectroscopy (XPS)

X-Ray Photoelectron Spectroscopy (XPS) is an analysis technique used to obtain chemical information about the surfaces of solid materials. Both composition and the chemical states of surface constituents can be determined by XPS. The sample is placed in an ultrahigh vacuum environment and exposed to a low-energy, monochromatic X-ray source. The incident X-ray causes the ejection of core-level electrons from sample atoms. The energy of a photoemitted core electron is a function of its binding energy and is characteristic of the element from which it is emitted (Eq. 3.3). Energy analysis of the emitted photoelectrons (Figure 3.3a) is the primary data used for XPS. When the core electron is ejected by the incident x-ray, an outer electron fills the core hole. The energy of this transition is balanced by the emission of an Auger electron (Figure 3.3b) or a characteristic X-ray. Analysis of Auger electrons can be used in XPS, in addition to emitted photoelectrons. The photoelectrons emitted from the sample are detected by an electron energy analyzer, and their energy is determined as a function of their velocity entering the detector. By counting the number of photoelectrons as a function of their energy, a spectrum representing the surface composition is obtained. The energy corresponding to each peak is characteristic of an element present in the sample volume. The area under a peak in the spectrum is a measure of the relative amount of the element represented by that peak. The peak shape and precise position indicates the chemical state for the element. XPS is a surface sensitive technique because only those electrons

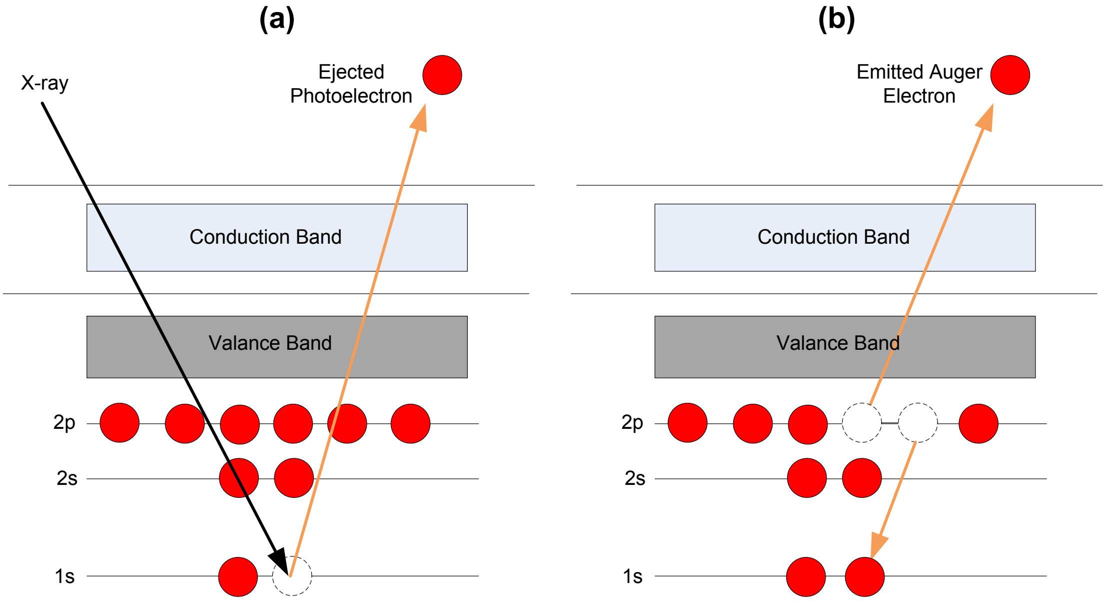

Figure 3.3 A scheme showing the principles of X-ray photoelectron spectroscopy.

generated near the surface escape and are detected. The photoelectrons of interest have relatively low kinetic energy. Due to inelastic collisions within the sample's atomic structure, photoelectrons originating more than 20 to 50 Å below the surface cannot escape with sufficient energy to be detected.

Mathematically, bombarding a sample in vacuum with x-rays gives rise to the emission of electrons. If monochromatic X-rays are used with a photon energy hν, the kinetic energy (KE) of the emitted electrons is given by:[190]

$$KE = h\nu - BE - \varphi \qquad \text{(Eq. 3.3)}$$

where, BE is the binding energy of the atomic orbital from which the electron originates and φ is the work function. The work function is the minimum amount of energy an individual electron needs to escape from the surface. Each element produces a unique set of electrons with specific energies. By measuring the number of these electrons as a function of kinetic (or binding) energy, an XPS spectrum is obtained.

The XPS spectra presented in this report were collected from a VGESCALAB 250 spectrometer using a monochromatic Al Kα X-ray source (1486.6 eV) operating at 15 kV and a pressure of 10^{-9} torr. Samples were finely ground before being mounted onto the adhesive tape. BEs of all elements were corrected by referring to the C 1s peak (BE of 284.6 eV) that was sputtered on the samples under study.

3.4 Fourier Transform Infrared (FTIR) Spectroscopy

Qualitative infrared spectroscopy is one of the most powerful tools for the analysis of compounds or moieties in a sample. This is achieved by recognizing characteristic shapes and patterns within the spectrum. The generated spectrum is formed as a consequence of the absorption of electromagnetic radiation at frequencies that correlate to the rotational and vibrational motions of specific chemical bonds within a molecule.[191] Molecular bonds vibrate at various frequencies depending on the elements and the type of bonds. For a given bond, there are several specific frequencies at which it can vibrate. According to quantum mechanics, these frequencies correspond to the ground state (lowest frequency) and several excited states (higher frequencies). One way to increase the frequency of a molecular vibration is to excite the bond by absorption. By interpreting the infrared absorption spectrum, the chemical bonds in a molecule can be determined. The FTIR spectra of pure compounds are generally unique and therefore can be used as molecular fingerprints.

The potassium bromide (KBr) pellet technique is widely used for solid sample analysis. In this work, a few milligrams of finely ground sample was mixed with KBr powder with a mass ratio of about 1:100. The mixture was then palletized before the measurement. The measurement was conducted in a Digilab FTS 3100 instrument by collecting 64 scans with a resolution of 4 cm^{-1} at the mid-infrared region (400-4000 cm^{-1}). In this work, FTIR was used to analyze the chemical bonding information of metal-oxygen, the surfactants adsorbed, and silica coating layer on the surface of the nanoparticles.

3.5 Thermogravimetric Analysis (TGA)

Thermogravimetric analysis (TGA) is a technique in which the mass of a sample is monitored as a function of temperature while the sample is subjected to heating under a controlled atmosphere.[188] This analysis is used to study the physical or chemical changes that occur in the sample upon heating. In this work, TGA study was carried out in a Diamond TG/TGA (Perkin Elmer) with a heating rate of 10 °C/min and an air flow rate of 200 ml/min from room temperature up to 800 °C.

3.6 Inductive Coupled Plasma-Atomic Emission Spectroscopy (ICP-AES)

The principle of this analytical technique is based on the excitation of electrons of the element by electronically generated plasma to the higher level of energies above the ground state. A plasma is an electrically neutral, highly ionized gas that consists of ions, electrons, and atoms.[192] When an electron returns to ground state, a photon with a particular wavelength corresponding to the difference in the energy levels is emitted.

There is an empirical correlation between the power of the emitted radiation to the quantity of the corresponding element in the sample. Such information is then used to generate a mass spectrum for the quantitative analysis of inorganic components in a solution. In this work, the solid samples were first dissolved in 2% nitric acid solutions to obtain clear solutions containing metal cations of the samples. The measurement was conducted in a Teledyne Prodigy ICP-AES using Argon plasma as an excitation source.

3.7 Particle Size Analysis using Dynamic Light Scattering (DLS)

A colloidal dispersion is known to be able to scatter a beam of light. The light scattering behavior, in turn, offers an opportunity for the determination the size of colloidal particles as the intensity of the scattered light has a proportional correlation with particle size.[193] The method of dynamic light scattering (DLS) has been widely used, especially to determine particle sizes below 1 μm. It utilizes a coherent, monochromatic, and intense laser as the light source for detecting a wide range of particle shapes and size at high accuracy. In our study, dispersion of the nanoparticles was analyzed with a Brookhaven 05-LHP-928 laser (Brookhaven Instruments Corporation) light scattering system fitted with a He-Ne laser (35 mW).

3.8 Vibrating Sample Magnetometer (VSM)

A vibrating sample magnetometer (VSM) is used to measure the magnetic behavior of magnetic materials as a function of magnetic field, temperature, and time. A VSM operates on Faraday's law of induction which states that a changing magnetic field will produce an electric field. Thus by measuring the electric field, information about the magnetic field can be obtained. If a material is placed within a uniform magnetic field, a magnetic moment will be induced in the sample. In VSM, a sample is placed within suitably placed sensing coils. The resulting magnetic flux changes induce a voltage in the sensing coils that is proportional to the magnetic moment of the sample. In the case of a typical recording medium, the hysteresis loop gives the relationship between the magnetization (M) and the applied field (H). A hysteresis loop of a magnetic recording medium is illustrated schematically in Figure 2.2. The parameters extracted from the hysteresis loop are the saturation magnetization (M_S), the remanence (M_R), the coercivity (H_C).

In this study, the magnetization values of the samples were acquired at room temperature with a LakeShore 7400 vibrating sample magnetometer (VSM) using an applied magnetic field from 0 to 10 KOe. Approximately 10 mg dry powder samples were used for the magnetization measurements.

3.9 Fluorescence Studies

Luminescence arises from the emission of photons from a substance that is at electronically excited states as discussed earlier in section 2.3.1 and section 2.5.2. In this study, down- and up-conversion fluorescence of the RE-doped nanoparticles has been investigated. Nanoparticle samples were dispersed in cyclohexane in a standard suare quartz cuvette at room temperature. Up-conversion fluorescence spectra were obtained using a Fluoromax-4, Horiba Jobin Yvon Spectrofluorometer, which employs a photon-counting detection system for the detection of fluorescence emission. To obtain the emission spectra, sample excitation was accomplished using a diode laser, BWF-2 (980 nm, P_{max}=2.0 W at 3.0 A, B&W TEK Inc.) coupled to a 100 μm (core) optical fiber. The emission spectra in the visible region were obtained with a resolution of 1 nm and a laser power of 0.75W. Down-conversion fluorescence spectra were obtained using a Shimadzu RF-5301PC Spectrofluorometer fitted with a 150 W xenon lamp as the excitation source with a resolution of 1 nm.

3.10 Magnetic Resonance Imaging (MRI)

MRI is a widely used non-invasive diagnostic tool which has an excellent spatial resolution and delivers no radiation burden. The basic principle of MRI is based on nuclear magnetic resonance (NMR) together with the relaxation of proton spins in a magnetic field. In MRI, contrast agents have been frequently used to enhance image contrast. The basic principles of MRI have been discussed early in section 2.4.4.1.

In this study, we conducted *in vitro* MRI for RE^{3+}-doped Gd_2O_3 nanoparticles. The T_1-weighted images were obtained on a Varian 9.4T MRI system. All samples were dissolved in double distilled water. The repetition time (TR) and echo time (TE) values were optimized for T_1-weighting while using the spin echo sequence. Other parameters used for imaging are: number of acquisitions = 25, field of view = 35 mm, slice thickness = 3 mm, and acquisition time ~ 6 min/sample. All experiments were performed in 1% agarose medium.

3.11 American National Standard ISO 10993-5

3.11.1 Introduction

ISO (International Organization for Standardization) is a worldwide federation of national standards bodies. ISO 10993 with a general title - “Biological evaluation of medical devices” have 20 different parts for evaluation and testing of medical devices. The part 5 (ISO 10993-5) is for the test of *in vitro* cytotoxicity of medical devices. This part was adopted for the evaluation of *in vitro* cytotoxicity of the nanomaterials synthesized in this study. Some of its key features are given in the following sections.

3.11.2 Scope

The ISO 10993-5 describes test methods to assess the *in vitro* cytotoxicity of medical devices. These methods specify the incubation of cultured cells in contact with a device and/or extracts of a device either directly or through diffusion. These methods are designed to determine the biological response of mammalian cells *in vitro* using appropriate biological parameters.

3.11.3 Principle of Extraction

Extracting conditions should attempt to simulate or exaggerate the clinical use conditions so as to determine the potential toxicological hazard without causing significant changes in the test sample, such as fusion, melting or any alteration of the chemical structure, unless this is expected during clinical application.

One or more of the following vehicles can be used for mammalian cell assays: (a) culture medium with serum; (b) physiological saline solution; (c) other suitable vehicle.

Considerations will be given to the use of both a polar and a non-polar vehicle. Culture medium with serum is the preferred extraction vehicle. The use of culture medium with serum is preferred for extraction because of its ability to support cellular growth as well as extract both polar and non-polar substances. In addition to culture medium with serum, use of medium without serum should be considered in order to specifically extract polar substances (e.g. ionic compounds). Other suitable vehicles include purified water and dimethyl sulfoxide (DMSO).

Fetal Bovine Serum was used as the medium in our experiments.

3.11.4 Sample and Control preparation

Due to the general applicability of *in vitro* cytotoxicity tests and their widespread use in evaluating a large range of devices and materials, the ISO 10993-5 define a scheme for testing rather than to specify a single test for decision making. Three categories of test are listed: (I) extract test, (II) direct contact test, and (III) indirect contact test.

The choice of one or more of these categories depends upon the nature of the sample to be evaluated, the potential site of use and the nature of the use. This choice then determines the details of the preparation of the samples to be tested, the preparation of the cultured cells, and the way in which the cells are exposed to the samples or their extracts. Controls should be selected so that they can be prepared by the same procedure as the test sample.

In the cytotoxicity experiments, we have used direct contact tests and extracts test of the nanoparticles exposed at different time and temperature.

3.11.5 Extraction Conditions

The extraction shall be conducted at one of the following conditions and shall be applied according to the device characteristics and specific conditions for use:

a) (24 ± 2) h at (37 ± 1) °C;

b) (72 ± 2) h at (50 ± 2) °C;

c) (24 ± 2) h at (70 ± 2) °C;

d) (1 ± 0.2) h at (121 ± 2) °C.

Extraction conditions described above, which have been used to provide a measure of the hazard potential for risk estimation of the device or material, are based on historical precedent. Other conditions such as prolonged or shortened extraction times at 37 °C simulate the extraction that occurs during clinical use or provide an adequate measure of the hazard potential. A minimum of three replicates shall be used for test samples and controls.

In this study, nanoparticles extract were collected at 37, 50, 70, and 121 °C with a maximum nanoparticle concentration of 0.25 mg/ml and exposure time of 24, 48, and 72 h. More detail of sample preparation will be discussed in section 7.2.3.

3.12 Analysis of Variance (ANOVA)

One-way analysis of variance (ANOVA) has been used to statistically analyze the toxic response of the cells to nanoparticles. One-way ANOVA is an exploratory test designed to detect evidence of any difference among a set of group means. The analysis provides a set of formulas that enable to compute test statistics and confidence intervals required to make inferences. The analysis tests the null hypothesis (H_0) that samples in two or more groups are drawn from the same population.[194] The ANOVA produces an F statistic, the ratio of the variance calculated among the means to the variance within the samples, which help to determine the acceptance or rejection of H_0.[195]

There are some assumptions upon which the test is developed which are as follows:

1. The probability distributions of the populations of responses associated with each treatment must be normal.
2. The probability distributions of the populations of responses associated with each treatment must have equal variances.
3. The samples of experimental units selected for the treatments must be random and independent.

3.12.1 P-Value

Once the test statistic F is calculated, a measure is obtained of how unusual that observed value is relative to what would be expected for its value if H_0 is true. To calculate such a measure, we consider the collection of possible values for the test statistic that give at least as much evidence in favor of the alternative hypothesis as the observed test statistic. The P-value is defined to be the probability that the test statistic would occur in this collection of values, if H_0 were true.[194]

The P-value is used as a measure of the weight of evidence supporting the null hypothesis (H_0). A moderate to large P-value means that the data are consistent with H_0. On the other hand, the smaller the P-value, the more contradictory the sample results are to H_0. In practice, researcher usually requires very small P-value, such as $P< 0.05$, in order to conclude that the data contain sufficient evidence to reject H_0.

In the cytotoxicity studies of this thesis, all the cell viability data has been statically analyzed by one-way ANOVA and P-value lower than 0.05 was considered statistically significant.

CHAPTER 4

Investigation of RE Doping in Y_2O_3 Host as Potential Contrast Agent in Optical Imaging

4.1 Introduction

The endeavor to develop novel fluorescent nanomaterials in the fields of nanobiotechnology, photonics and optoelectronics has been burgeoning in the past decade.[9, 66, 196] As reviewed in chapter 2, several classes of nanomaterials including organic, metallorganic and polymer based dye, fluorescent proteins and semiconductor nanocrystals have been investigated or operational as fluorescent emitters. These fluorescent nanomaterials have their respective advantages and disadvantages. In brief, dye molecules have good quantum yield but often undergoes photobleaching and fluorescence quenching due to interactions with solvent molecules and reactive species such as oxygen or ions dissolved in solution.[9] Another class of nanomaterial, colloidal II-VI semiconductor nanocrystals, more commonly known as quantum dots (QDs),[44, 197-200] were the subject of intense study as light-emitting materials for biological labeling. However, their translation to clinical application is hindered by their potential toxic effects in cell environment.[11, 163] QDs consist of metals such as, Pb^{2+} or Cd^{2+}, which are toxic and therefore not suitable for bioapplications without proper surface modifications.[201-202] In comparison, rare-earth (RE) doped nanophosphors offer an alternative for biological labeling due to their large Stoke's shift, sharp emission spectra,

---

Much of this chapter has appeared in print in *Journal of Physical Chemistry C*, 2008, *112*, 11211-11217. Reproduced with permission. Copyright 2008 American Chemical Society.

long lifetime, multiphoton and up-conversion excitation, reduced photobleaching, and lower toxicity over semiconductor nanocrystals like quantum dots and organic phosphors molecule.[14, 49, 203-204] The RE^{3+} ions have the ability to emit intensely at various wavelengths by an appropriate choice of color-center elements instead of varying particle size.[205] In RE-doped nanophosphors, the RE^{3+} ions 4f electronic levels are spatially localized to dimensions much smaller than the size of the nanoparticles and thus are not affected by the dimensions of the nanostructure.

Yttrium oxide (Y_2O_3) has been widely investigated as the host for RE^{3+} ions for optical application.[120, 125, 206-208] Its combination of favorable properties such as broad transparency range (0.2 – 8 μm), a wide band gap of 5.6 eV, high refractive index, good thermal conductivity and low phonon energy makes it an attractive choice as the host material.[125] The bulk of Y_2O_3:RE research has been focused primarily on their luminescence properties. In contrast, few works have addressed their morphological characteristics. Some recent works have reported different morphologies of Y_2O_3:RE. Wang *et al.*[120] showed self-assembly of Y_2O_3:Eu nanocrystals to nanodisks, Si *et al.*[209] reported the formation of Y_2O_3 nanoplates, while other morphologies like a flower-like,[210] wire-like[211] nanostructure of RE-doped Y_2O_3 has also been reported.

In this work, we principally aimed to study the photoluminescence (PL) properties of Y_2O_3 nanomaterials when doped with different RE^{3+} ions including terbium (Tb^{3+}), europium (Eu^{3+}), erbium (Er^{3+}), and codoping with ytterbium (Yb^{3+}) and erbium (Er^{3+}). In addition, we achieved controlled morphological evolution from nanocrystals to nanorods for all RE^{3+} doped and codoped Y_2O_3. We herein present the results in two subsections: (I) The synthesis conditions affecting the morphology of RE^{3+} (RE = Tb, Eu, Er, Yb/Er) doped yttrium oxide ($Y_2O_3:RE^{3+}$) nanomaterials, and (II) The effect of different RE dopant concentrations on the photoluminescence properties of the $Y_2O_3:RE^{3+}$ materials. Lastly, a silanization process will be shown to render the nanomaterials water dispersible and suitable for further bioconjugation.

4.2 Experimental Section

4.2.1 Chemicals

Terbium (III) chloride hexahydrate (99.9%), ytterbium (III) chloride hexahydrate (99.99%), europium (III) chloride hexahydrate (99.9%), erbium (III) chloride hexahydrate (99.9%), tetramethylammoniumhydroxide (TMAH) 25wt% in methanol, Igepal CO-520 (Polyoxyethylene(5)nonylphenylether), oleylamine (tech., 70%), and 1-dodecylamine (98%) were purchased from Aldrich and used without further purifications. Yttrium oxide (99.99%), HNO_3 (analytical reagents, 70%) and oleic acid (tech., 90%) were purchased from Alfa Aesar. NaOH (reagent grade, 97%, beads), hexadecylaine (puriss ≥ 99%) 3-aminopropyltrimethoxysilane (APS) (97%) were purchased from Fluka. Ethanol, hexane, cyclohexane and chloroform were of analytical reagent grade and were used as received.

4.2.2 Synthesis of $Y_2O_3:RE^{3+}$ Nanocrystals and Nanorods

Yttrium (RE)-oleate complex was first prepared by reacting Y_2O_3 powder, oleic acid, sodium hydroxide and RE chlorides hexahydrates (i.e. $TbCl_3.6H_2O$, $EuCl_3.6H_2O$, $ErCl_3.6H_2O$, $YbCl_3.6H_2O$). Typically, 10 mmol of Y_2O_3 was dissolved in 4 ml of HNO_3 (70%), and *x* mmol of RE chlorides hexadydrates (varied from 0.05 to 2 mmol) was then added. To this precursor, 21 ml of oleic acid, 100 ml of hexane, 80 ml of ethanol and 60 ml of H_2O was added and then stirred for 1 h. Then, 2.65 g of NaOH was added and aged in a silicon oil bath at 70 °C in oven for 4 h. After that, the upper organic layer containing Y(RE)-oleate complex was collected using a seperatory funnel, washed with 30 ml of distilled water and dried overnight at 70 °C to evaporate off the water and hexane. Y_2O_3:RE^{3+} nanocrystals or nanorods were then synthesized by the thermal decomposition of Y(RE)-oleate complex in the presence of the long-chain alkyl amines. In a typical synthesis process for nanocrystals and nanorods, 1 mmol of Y(RE)-oleate complex was dissolved in x mmol (x varied from 10 to 40) of oleylamine (or dodecylamine, hexadecylamine) in a three-neck flask. The mixture solution was then heated to the crystallization temperature at 5°C/min under N_2 environment. Nanocrystals and nanorods were grown in the solution by varying the reaction time at fixed temperature 280 °C. Reaction was halted by cooling the reaction solution to room temperature and precipitating with excess ethanol. The precipitate was collected by centrifugation and the supernatant decanted. This washing process was repeated several times and the purified nanomaterials then dispersed in hexane.

4.2.3 Silica-coating and Amine Functionalization

Silica coating of the nanoparticles was performed according to the process described by Selvan *et al.*[30] At first, micelles were prepared by dissolving 0.2 g of Igepal CO-520 in 4 ml of cyclohexane, followed by stirring vigorously for 30 min. Meanwhile, nanoparticles were redispersed in chloroform at a concentration of 4 mg/ml. Next, 0.5 ml of nanoparticles in chloroform was added to the micelle solution and stirred for 15 min. Subsequently, 20 µl of APS was added and the mixture was stirred for another 1 h. Then, 20 µl of TMAH in methanol was added. After 1 more h of stirring, 20 µl of deionized water was added and stirred for 30 min. At this stage, some globules were formed and settled at the bottom of the flask, leaving the upper solution transparent. The globules of $Y_2O_3:RE^{3+}$ (RE = Tb, Eu, Er, Yb/Er) nanoparticles were then collected and the transparent organic phase was discarded. After this the functionalized nanoparticles were washed with chloroform and ethanol for the complete removal of excess surfactant and other reactants. The silica-coated $Y_2O_3:RE^{3+}$ nanoparticles were then dispersed in deionized water.

4.2.4 Characterization

Transmission electron microscope (TEM) images were obtained on a JEOL 3010 electron microscope operating on 200 kV. High resolution transmission electron microscope (HRTEM) images were obtained on a JEOL JEM-2100F electron microscopy operating on 200 kV. The X-ray diffraction patterns of the as-synthesized nanomaterials were collected using a D8 ADVANCE X-ray diffractometer with Cu Kα is used as X-ray source (λ=1.5406 Å). Photoluminescence (PL) spectra were collected on a Shimadzu RF-5301 PC Spectrofluorophotometer using 150 W Xenon lamp as an excitation source. Up-conversion fluorescence spectra were recorded using a Fluoromax-4, Jobin Yvon spectrofluorometer. All $Y_2O_3:RE^{3+}$ (RE = Tb, Eu, Er, Yb/Er) nanomaterials were dispersed at a concentration of 0.25 mg/ml in hexane in standard quartz cuvettes at room temperature for all the luminescence spectra measurement. Fourier Transform Infrared (FTIR) spectra were recorded using a Digilab FTS3100 spectrometer with a resolution of 4 cm^{-1}.

4.3 Results and Discussions

4.3.1 Morphology

We observed a morphological evolution from nanocrystals to self-assembled nanorods of all RE^{3+} doped and codoped Y_2O_3. It was found that process parameters such as reflux time, reaction temperature, and the type of liganding solvent influence the morphology of Y_2O_3:RE^{3+} (RE = Tb, Eu, Er, Yb/Er), within the scope of our investigation. The effects of the parameters are summarized in Table 4.1 and discussed in the subsequent sections.

Table 4.1 Effect of different experimental parameters in morphology change

Name of the Liganding Solvent	Liganding solvent: Y(RE)-complex ratio (mole)	Reaction Temperature (°C)	Growth Time (h)	Morphology
Oleylamine	30:1	280	0.16	Nanocrystals
Oleylamine	30:1	280	0.5	Nanocrystals and few Nanorods
Oleylamine	30:1	280	2.0	Nanorods
Oleylamine	10:1	280	2.0	Nanocrystals
Oleylamine	40:1	280	2.0	Nanorods
Oleylamine	30:1	250	2.0	Nanocrystals
Dodecylamine	30:1	260	2.0	Nanocrystals
Hexadecylamine	30:1	280	2.0	Nanorods of different type

4.3.1.1 Effect of Reflux Time: Crystal Structure and Composition Analysis

To investigate effect of reflux time, all other conditions were kept fixed. At 280 °C, and oleylamine to Y(RE)-oleate complex ratio of 30:1, a longer reflux time was observed to cause morphological changes of Y_2O_3:RE^{3+} nanocrystals to nanorods. The typical observation of as-formed Y_2O_3:RE^{3+} nanocrystals and nanorods are shown in the TEM images in Figure 4.1. After 10 min of reflux, reaction mixture produced monodisperse quasi-spherical nanocrystals of 2.5 ± 0.3 nm (Figure 4.1a). Refluxing the solution to 30 min yielded a mixture of nanocrystals and nanorods (Figure 4.1b), while extending the reflux time to 2 h resulted in the formation of nanorods of length in the range of 20 ± 5.3 nm (Figure 4.1c). This trend of morphological evolution was observed for all RE^{3+}-doped (i.e Tb^{3+}, Eu^{3+}, Er^{3+}) and co-doped (Yb^{3+}/Er^{3+}) Y_2O_3 nanomaterials. We attribute this observation to small amount of RE^{3+} dopants used, which are of similar ionic diameter of the host Y^{3+} ion, and therefore the type or amount of dopant did not exert significant influence on the nanoparticle morphology.[212] The HRTEM images (Figure 4.1d) show high magnification view of parallel nanorods while the clear lattice stripes (Figure 4.1e) suggest the nanorods are single crystalline with an interplanar distance of 0.19 nm, corresponding to the (440) planes of a cubic Y_2O_3. Selected area electron diffraction (SAED) from a bunch of nanorods (Figure 4.1f) can be indexed as cubic Y_2O_3 with (222), (440) and (622) diffraction rings at real space interplanar distances of 0.329 nm, 0.19 nm, and 0.163 nm respectively. The corresponding fast Fourier transformation (FFT) pattern (Figure 4.1g) further characterizes the cubic structure of $Y_2O_3:RE^{3+}$.

The crystal structure of the as-synthesized nanocrystals and nanorods was analyzed by powder X-ray diffraction (XRD). Figure 4.2a shows the powder XRD pattern of as-prepared RE-doped $Y_2O_3:RE^{3+}$ nanomaterials. The diffraction peaks obtained from XRD confirmed the crystallinity of the as-prepared $Y_2O_3:RE^{3+}$ nanomaterials. The peaks can be assigned to cubic Y_2O_3 (JCPDS file no. 89-5592). Broadening of the peaks suggests small crystalline size. The intense peaks at (440) in Figure 4.2a(i) indicate the anisotropic growth due to formation of nanorods at longer heating time. XRD analysis further

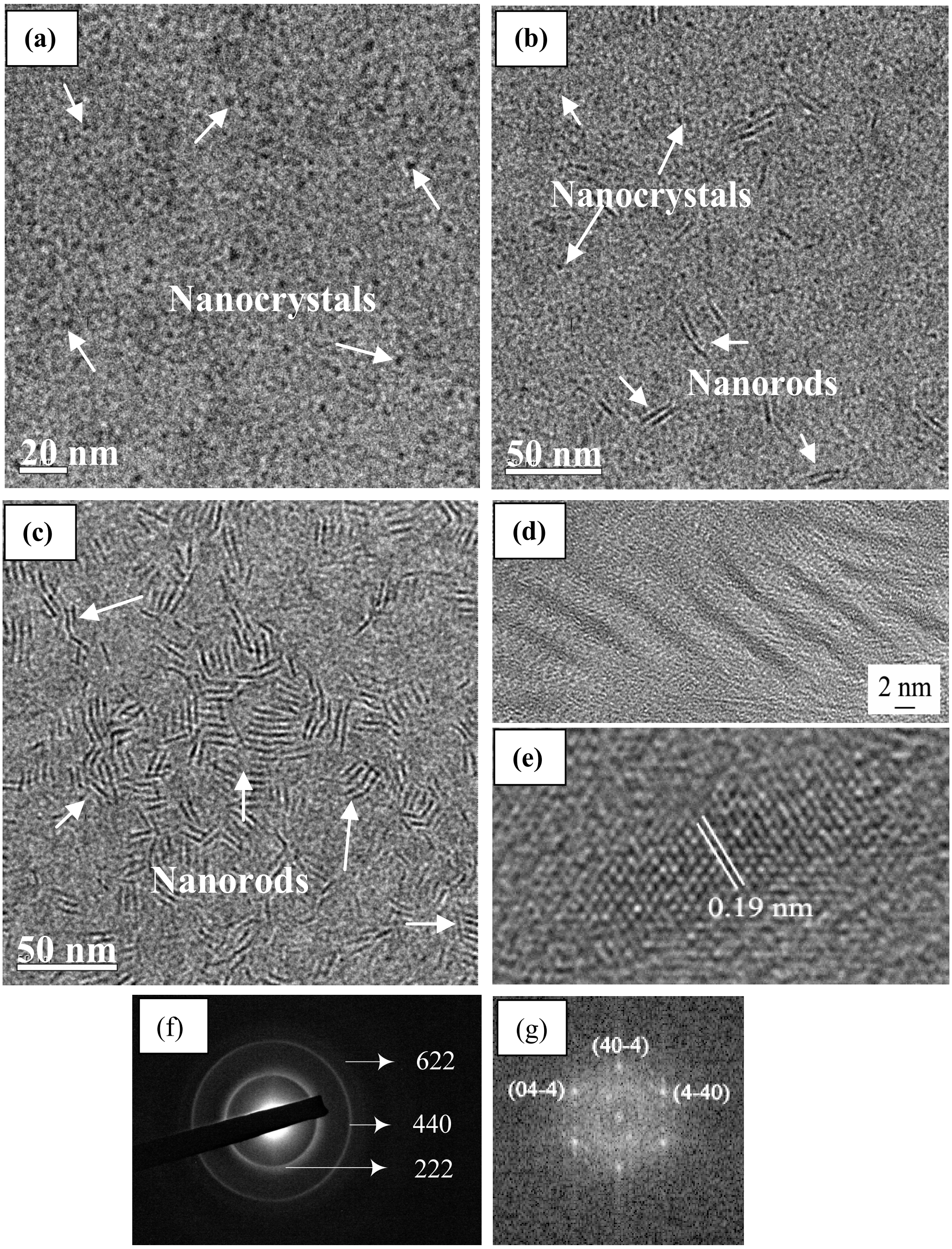

Figure 4.1 Typical TEM images of Y_2O_3:RE^{3+} obtained at 280°C (a): after 10 min, indicating the formation of nanocrystals; (b): after 30 min, indicating the formation of mixture of nanocrystals and nanorods; and (c): after 2 hour, indicating the formation of nanorods only. (d) HRTEM image of several nanorods; (e) HRTEM image of a single nanorod; (f) SEAD pattern of the nanorods; (e) the corresponding FFT pattern.

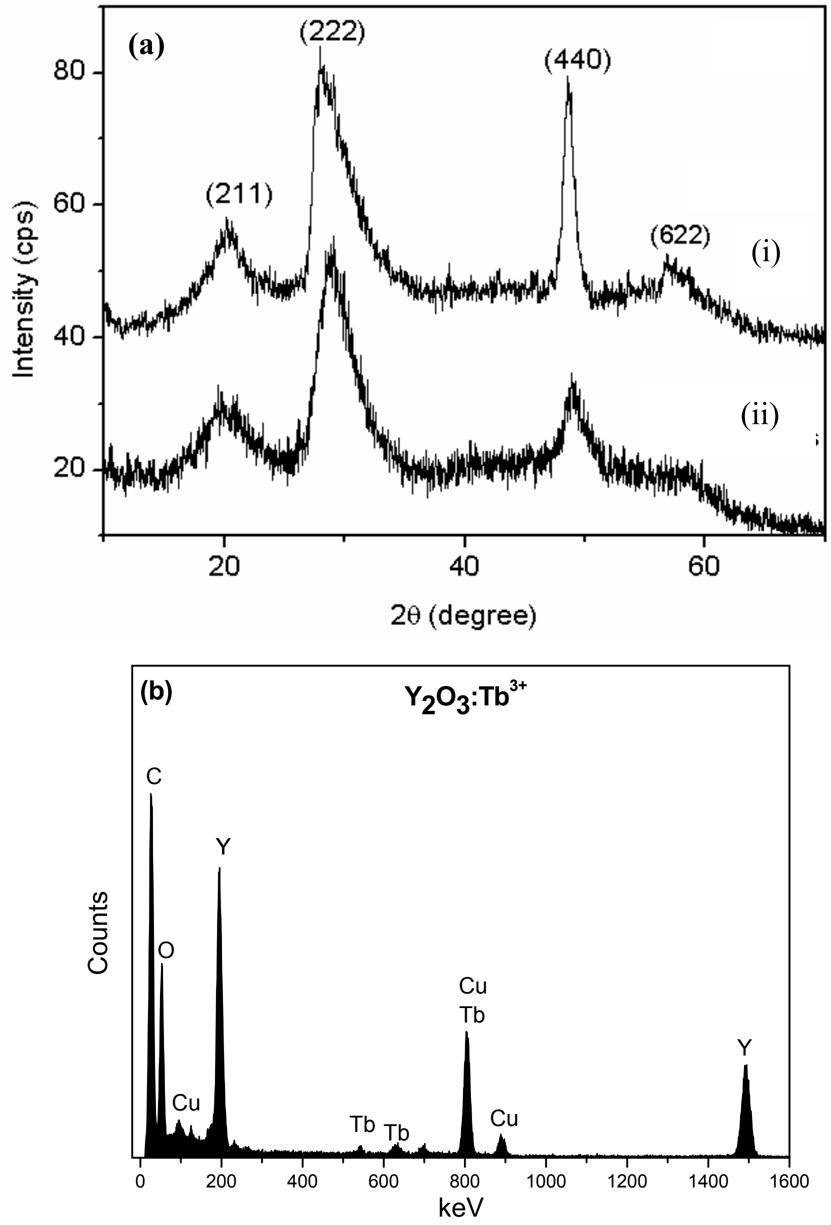

Figure 4.2 (a) Typical XRD patterns of as-prepared Y_2O_3:RE^{3+} (RE = Tb, Eu, Er, Yb/Er) (i) nanorods; (ii) nanocrystals; (b) EDX spectrum of the as-synthesized Y_2O_3:Tb^{3+} nanorods.

provides support that Y_2O_3:RE^{3+} crystal growth is independent on the type and concentration of RE dopant. Energy dispersive X-ray (EDX) spectrum (Figure 4.2b) of Y_2O_3:Tb^{3+} sample was obtained as the representative, which shows that the samples are composed of Y, O, and Tb. The peaks of C, and Cu originated from the surfactants capped the nanorods and the carbon film of the copper TEM grid. The formation of the nanorods was identified as the self-assembly of the nanocrystals along the longitudinal axis due to dipole-dipole interactions. Owing to self-assembly along the longitudinal axis, the diameters of the nanorods were similar to that of the nanocrystals. Detailed investigation of the self assembly phenomenon will be provided in Chapter 6 in section 6.3.2.

4.3.1.2 Effect of Reaction Temperature

A fixed reflux time (2 h), and oleylamine to Y-complex ratio (30:1) were used to study the effect of temperature on the morphology of Y_2O_3:RE^{3+}. It was observed that only a few nanocrystals were formed at 230 °C while increased number of nanocrystals nuclei was observed at an elevated temperature 250 °C. However, no nanorods were formed until the reaction temperature reached to 280 °C or above. The highest number of nanocrystals formation was observed at 280 °C. It was anticipated that high number of nanocrystals would favor nanorods formation due to their self-assembly, and henceforth this temperature was chosen for the study of nanorods formation. The above observation suggests that temperature influences the growth kinetics, and therefore the morphology. At higher temperature, growth rate is increased and formation of the anisotropic nanorods is favored. The temperature dependent nanorod evolution phenomenon is due to change in surface energy of nanocrystals at higher temperature. A possible nanorod evolution mechanism is that at a higher temperature, the nanocrystals with high surface energy approached each other and lowered their surface energy by elimination of the curved surfaces by fusing end-to-end longitudinally. [213-214] This enthalpy favorable process resulted in self-assembly of nanocrystals to the nanorod structures.

4.3.1.3 Effect of Liganding Solvent

A number of liganding solvents have been reported to be used for controlling shape and size of different semiconductors and metal nanoparticles.[120, 215-219] Liganding solvents play the important role of stabilizing the nanoparticles and providing the spacing among them. Appropriate choice of liganding solvents can afford tailoring anisotropically grown nanostructures such as nanorods, arrow-like, tetrapods and so forth.[215, 220] Here, we investigated two aspects of the liganding solvents on the nanoparticles morphology: (I) molar ratio of the liganding solvent with respect to the reactant precursor, and (II) different type of amine-based liganding solvents (summarized in Table 4.1).

When a molar ratio of 10:1 (oleylamine to Y(RE)-complex) was used, only nanocrystals were formed after 2 h of reaction at 280 °C. However, the 30:1 and 40:1 molar ratio were found to be favorable for producing uniform, monodispersed nanorods. Hence, molar ratio of 30:1 was chosen for the subsequent experiments involving the use of hexadecylamine and dodecylamine as solvents. Figure 4.3 shows the typical TEM images of the nanoparticles formed in hexadecylamine and dodecylamine respectively. The TEM images show that some non-uniform and random nanorods were obtained for hexadecylamine (Figure 4.3a) while no nanorods were formed using dodecylamine after 2 h of reflux at 280 °C (Figure 4.3b). The result implies that the liganding solvent oleylamine favors the formation of uniform nanorods while other two amines (hexadecylamine and dodecylamine) do not produce similar results. This could be attributed to different nanocrystals-surface energies associated with different types of solvents. During thermal decomposition of the precursor complex, the liganding solvent together with the surfactants (i.e. oleic acids) adsorbed onto the crystal surface. The adsorption process depend on the type and concentration of the solvents.[216] Besides, the chemical nature of the liganding solvents significantly affects the surface energy of the nanocrystals.[215] Thus at 30:1 molar ratio, the surface energy and the lateral spacing provided by the adsorbed oleylamine on nanocrystals surface offered the most favorable surface conditions for fusion of nanocrystals as compared to that of dodecylamine and hexadecylamine.

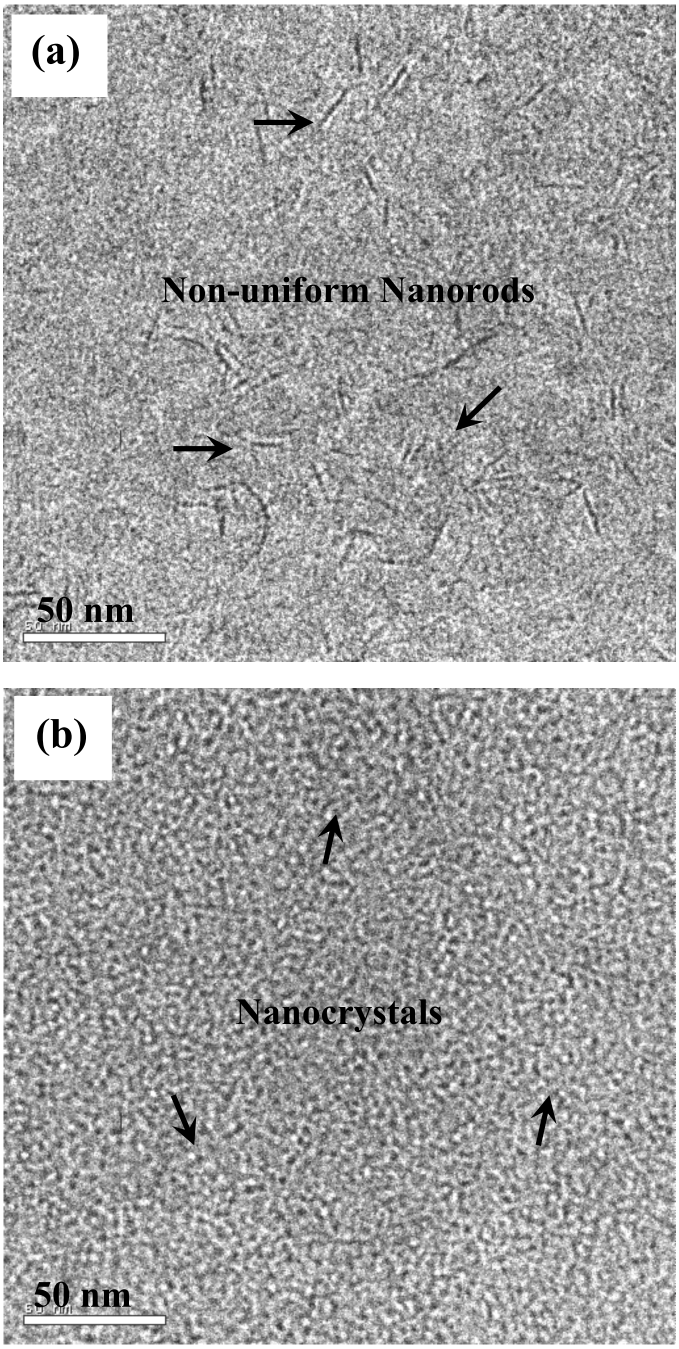

Figure 4.3 Typical TEM images of effect of liganding solvent on the morphology of Y_2O_3;RE^{3+} (RE = Tb, Eu, Er, Yb/Er). (a) hexadecylamine; (b) dodecylamine as ligating solvent produces few non-uniform nanorods and nanocrystals respectively.

4.3.2 Optical Properties

4.3.2.1 Room Temperature Down-conversion Photoluminescence (PL) Spectra of $Y_2O_3:RE^{3+}$ (RE = Tb, Eu, Er)

The room temperature photoluminescence (PL) spectra of single RE^{3+} (RE = Tb, Eu, Er) doped Y_2O_3 nanomaterials dispersed in hexane are shown in Figure 4.4. Emission peaks at different wavelengths correspond to the electronic transitions between energy levels in the respective RE^{3+} ions. Figure 4.4a shows photoluminescence excitation and emission spectra of $Y_2O_3:Tb^{3+}$ nanomaterials. The emission spectrum of $Y_2O_3:Tb^{3+}$ nanomaterials under 235 nm excitation displays four emission bands at 490, 545, 585 and 620 nm, which can be assigned to 4f → 4f transitions within Tb^{3+} ions. The most intense peak at 545 nm corresponds to $^5D_4 \rightarrow {}^7F_5$ transition, while the peaks at 490, 585 and 620 nm correspond to $^5D_4 \rightarrow {}^7F_6$, $^5D_4 \rightarrow {}^7F_4$ and $^5D_4 \rightarrow {}^7F_3$ transitions respectively.[207, 221] PL excitation and emission spectra of $Y_2O_3:Eu^{3+}$ nanomaterials is shown in Figure 4.4b. Three emission peaks were observed at 590, 612 and 625 nm at 255 nm excitation. The most intense peak at 612 nm corresponds to $^5D_0 \rightarrow {}^7F_2$ transition within Eu^{3+} ions while the other peaks at 590 and 625 nm corresponds to $^5D_0 \rightarrow {}^7F_1$ and $^5D_0 \rightarrow {}^7F_3$ transition respectively.[120, 208] Figure 4.4c shows excitation and emission spectra of $Y_2O_3:Er^{3+}$. Two emission peaks at 525 and 553 nm were found at 245 nm excitation. The intense peak at 525 nm corresponds to $^2H_{11/2} \rightarrow {}^4I_{15/2}$ transition and the other at 553 nm corresponds to $^4S_{3/2} \rightarrow {}^4I_{15/2}$ transition.[222]

4.3.2.2 Investigation of the Dopant Concentration on the PL of $Y_2O_3:RE^{3+}$

To investigate the effect of the RE^{3+} (RE = Tb, Eu, Er) dopant concentration on Y_2O_3 photoluminescence (PL), doped RE^{3+} concentration were varied in a range of 0.5 to 20

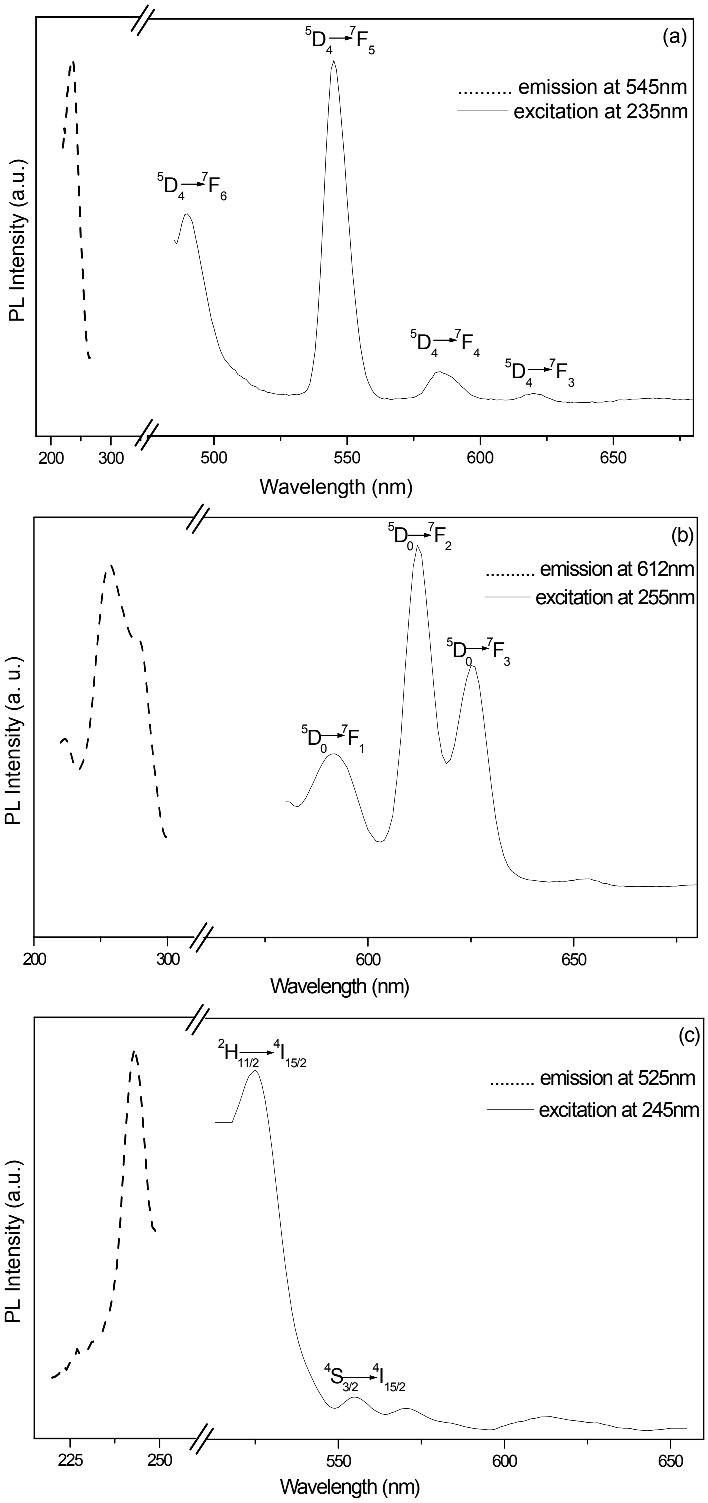

Figure 4.4 Room temperature photoluminescence emission and excitation spectra of (a) $Y_2O_3:Tb^{3+}$; (b) $Y_2O_3:Eu^{3+}$; and (c) $Y_2O_3:Er^{3+}$ nanomaterials. All PL measured at a concentration of 0.25 mg sample/ml in hexane.

mol%. As shown in Figure 4.5, no shift in the peaks position was observed by varying Tb, Eu and Er dopant concentration but intensity of the PL emission varied considerably. The inset of Figure 4.5a shows PL intensity as a function of Tb concentration (mol%) at 545 nm for $^5D_4 \rightarrow {}^7F_5$ transition, while insets of Figure 4.5b and Figure 4.5c shows PL intensity as a function of Eu concentration at 612 nm for $^5D_0 \rightarrow {}^7F_2$ transitions and Er concentration at 525 nm corresponds to $^2H_{11/2} \rightarrow {}^4I_{15/2}$ transition respectively. By varying Tb, Eu and Er concentrations in the range of 0.5 – 20 mol%, the highest PL intensity was observed at 5 mol% for all three RE dopant concentrations. The trend of the dopant concentration dependence luminescence is consistent with the trends reported in literatures. Park *et al.*[223] reported 8% Tb dopant to be the highest PL intensity while Muenchausen *et al.*[207] reported optimum Tb concentration was 1.8% in Y_2O_3 host. For Eu dopant, Zeng *et al.*[210] reported that the highest PL was obtained at 4% Eu dopant in Y_2O_3 while Pang *et al.*[224] reported that at 6% in Y_2O_3 host. Yet in another report, Yi *et al.*[222] found that 4% Er-doped Y_2O_3 resulted in the highest luminescence. Thus, the luminescence property is not only dependent on dopant concentration but also on other factors such as synthesis process, host material, crystal size, and temperature.[225-226] This is because luminescence property is related to the exact energy level positions, absorption cross sections, dielectric constant and typical phonon energy of the host material. The general trend is an initial increase of the PL intensity up to a critical concentration, at which photoluminescence intensity is the maximum. Higher PL intensity is attributed to the larger number of luminescent centers in the respective emitting level. With the increment of doped RE^{3+} ions, more excited ions are transited to respective emitting level (for example, $^5D_4$ for Tb, $^5D_0$ for Eu, $^2H_{11/2}$ for Er). Therefore, increasing RE ions concentration will increase the intensity of photoluminescence up to a critical concentration of which the luminescence is the maximum. However, photoluminescence decreases beyond the critical concentration. At too high RE^{3+} concentrations, interaction among RE^{3+} ions causes an output-limiting effect. Studies on Tb-[207, 227-228] and Eu-[225, 229-230] doped systems suggested that concentration quenching beyond a optimal dopant concentration is due to energy transfer between adjacent luminescence centers via cross-relaxation. For Er-doped system, Lei at al.[231] explained the concentration quenching in terms of a cooperative up-conversion process. At too high Er^{3+} ions concentration when two erbium ions come to very close proximity, an excited Er^{3+} ion de-excites the neighboring excited Er^{3+} ion by energy transfer, and itself returns to ground state by non-radiative relaxation. Hwang *et al.*[232] investigated cooperative up-conversion for Er-doped phosphate glasses and reported similar de-excitation mechanism. Thus, at too high Er dopant concentrations, neighboring excited Er^{3+} ions depopulates $^4I_{11/2}$ level which in turn lowers the number of excited ions and hence photoluminescence intensity.

4.3.2.3 Effect of Liganding Solvent on the PL

In addition to other factors, liganding solvents were found to influence the PL of Y_2O_3:RE^{3+}. Tb^{3+}-doped Y_2O_3, taken as the representative sample, were synthesized in three different amine-based liganding solvents (oleylamine, hexadecyl- amine, and dodecylamine) to investigate the influence of liganding solvents on the PL. The PL spectra of the nanomaterials synthesized in three different solvents are shown in Figure 4.6. Similar to the dopant concentration study, we obtained all four Tb^{3+}-ion characteristics emission peaks with different intensity for the nanomaterials synthesized at three different solvents. It can be observed that the nanocrystals synthesized in oleylamine manifest the most intense luminescence followed by hexadecylamine and by

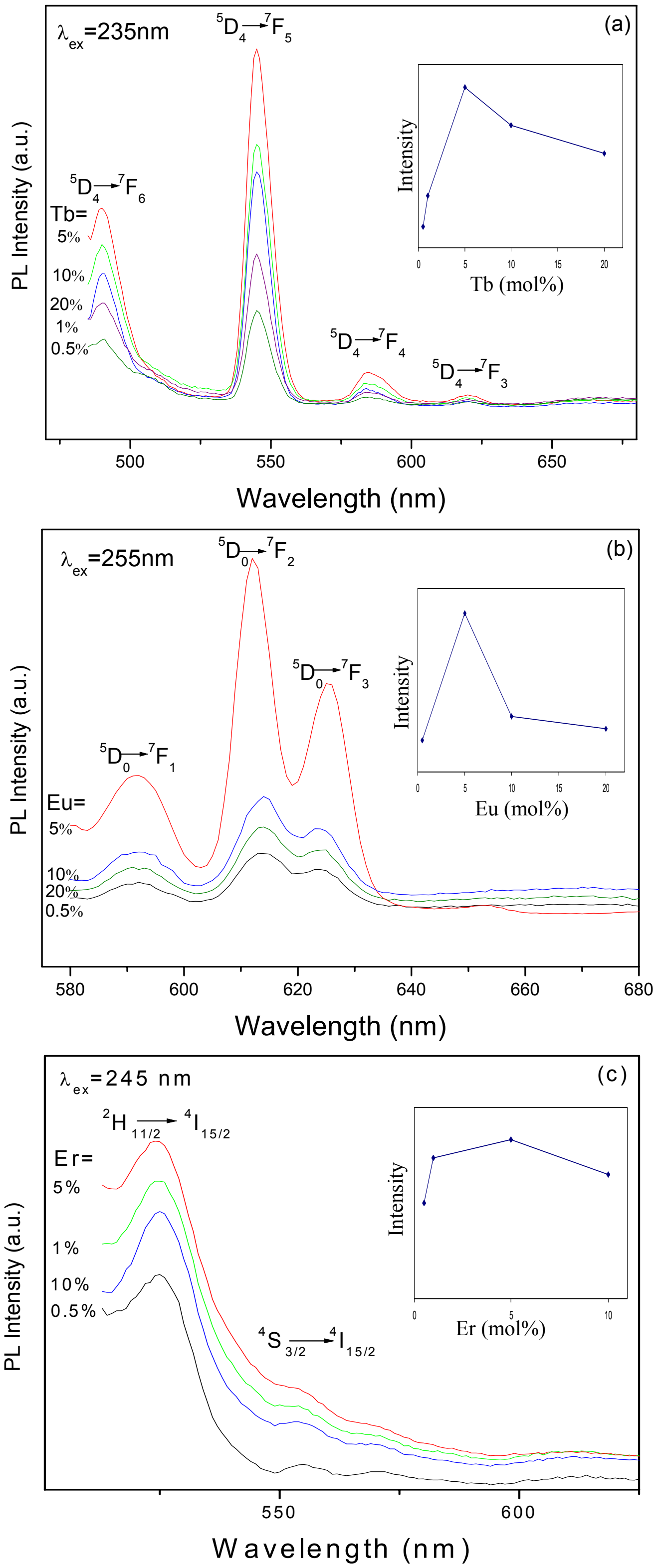

Figure 4.5 Effect of dopant concentration on photoluminescence for (a) Tb^{3+}-doped and (b) Eu^{3+}-doped (c) Er^{3+}-doped Y_2O_3 nanomaterials.

dodecylamine. At 545 nm emission the nanocrystals in oleylamine is almost five times more intense than that of dodecylamine.

The above data inferred that the photoluminescence of the RE^{3+}-doped nanocrystals is sensitive to the type of liganding solvents. Wuister *et al.*[233] reported the influence of alkyl chain length on the luminescence of CdSe QDs where they observed the organic surface passivation layer play significant roles both in passivating dangling lone pairs and in surface reconstruction which influence the luminescence considerably. In addition, overall surface state of the nanocrystals, quantum confinement effects, and difference in crystal structures are reported to be the factors affecting the luminescence properties.[233-235] As discussed earlier, the affinity of different liganding molecules on the nanocrystal surface is not the same. Thus, different surface-bound liganding molecules are likely to produce photoluminescence emission of different intensity.

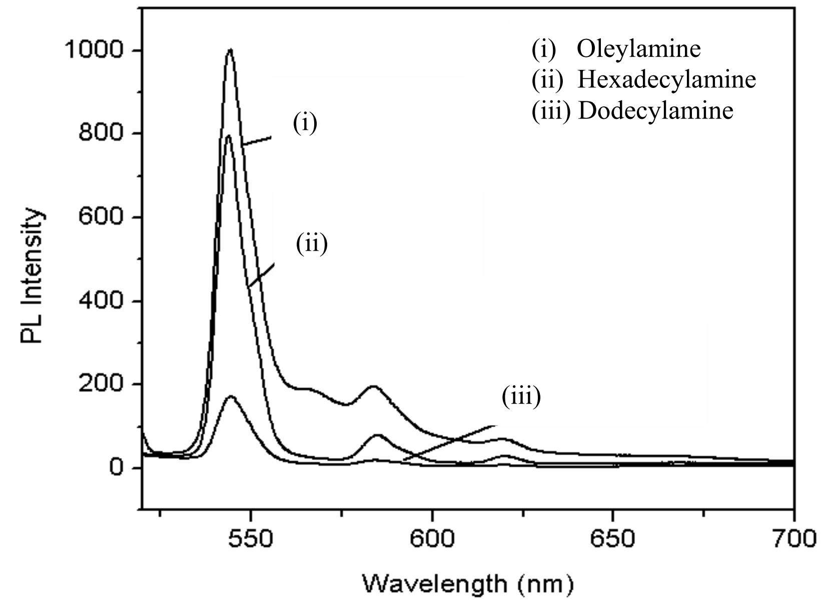

Figure 4.6 Effect of liganding solvent on the PL of $Y_2O_3:Tb^{3+}$. PL measured at a concentration of 0.25 mg of sample/ml in cyclohexane.

4.3.2.4 Up-conversion Luminescence for Yb^{3+}/Er^{3+}-codoped Y_2O_3

While photoluminescence has been investigated for single RE^{3+}-doped systems, it has also been studied for codoped system of which two different RE^{3+} ions were doped in the same host material. Codoping can increase the efficiency of the luminescence with the help of a sensitizer ion and in some cases can induce up-conversion luminescence which is not possible in the single ion doped materials.[236] In our experiment, Yb^{3+} was codoped with Er^{3+} and their room temperature photoluminescence was studied. Yb^{3+} was chosen as codopant because it can act as a sensitisier. Its $^2F_{5/2}$ level is nearly resonant to the $^4I_{11/2}$ level of Er^{3+}, therefore capable of inducing energy transfer to the Er^{3+} ion. In addition, Yb^{3+} has a much longer excited state lifetime.[125] The up-conversion luminescence spectra of the Yb^{3+}/Er^{3+}-codoped Y_2O_3 are shown in Figure 4.7. Figure 4.7a shows the up-conversion emission spectra of 2 mol% Er^{3+}/1 mol% Yb^{3+} codoped Y_2O_3 excited at 980 nm. The bands centered at 525 and 535 nm in the green emission region corresponds to $^2H_{11/2} \rightarrow {}^4I_{15/2}$ transition and $^4S_{3/2} \rightarrow {}^4I_{15/2}$ transition respectively while the other peak appears at 652 nm correspond to $^4F_{9/2} \rightarrow {}^4I_{15/2}$ transition.[222]

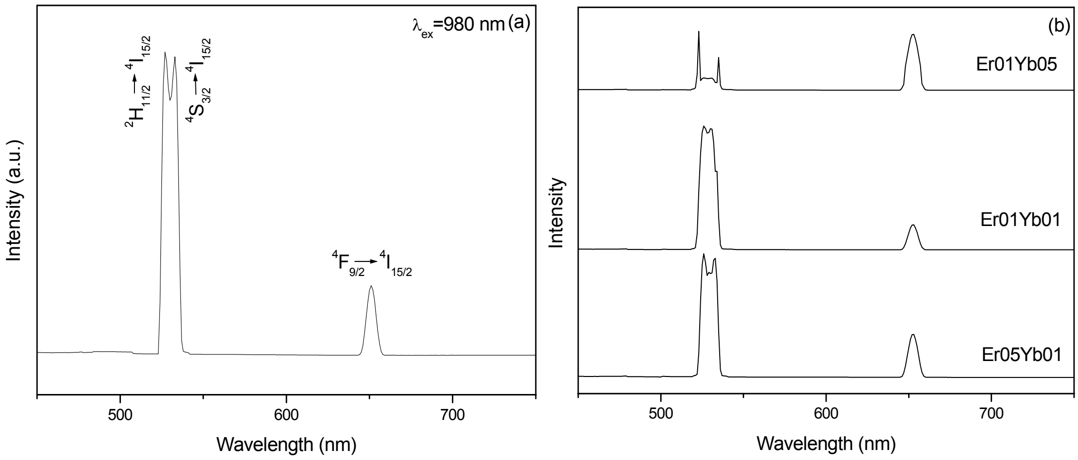

Figure 4.7 (a) Up-conversion spectra of Yb^{3+}-Er^{3+} (1:2 mol%) co-doped Y_2O_3 at 980 nm excitation; (b) Concentration dependence up-conversion spectra at 980 nm excitation.

4.3.2.5 Investigation of Dopant Concentration on Up-conversion Luminescence of Yb^{3+}/Er^{3+}-codoped Y_2O_3

The concentration dependence of up-conversion spectra of Yb^{3+}/Er^{3+}-codoped Y_2O_3 was investigated and is shown in Figure 4.7b. Using a fixed Er concentration (1 mol%) and increasing Yb concentration (from 1% to 5 mol%), it was found that green emission intensity decreased while red emission intensity increased. When Yb concentration was fixed at 1 mol% and Er concentration was increased from 1 mol% to 5 mol%, red emission intensity increases while green emission intensity was almost unchanged. The observed phenomenon is consistent with that reported by Guo *et al.*[237] and Vetrone *et al.*[140] for Yb^{3+}/Er^{3+} codoped up-conversion. The up-conversion mechanism in Yb^{3+}/Er^{3+} co-doped systems is very well studied and occurs via two successive energy transfers from Yb to Er ion.[132, 140, 145, 206, 237] Figure 4.8 shows the schematic of the up-conversion mechanism. At 980 nm excitation, the Er^{3+} ions can be excited to the $^4I_{11/2}$ excited state via two processes: ground-state absorption (GSA: $^4I_{15/2} \rightarrow {}^4I_{11/2}$) and energy transfer (ET) from excited Yb^{3+} ions ($^2F_{5/2} + {}^4I_{15/2} \rightarrow {}^2F_{7/2} + {}^4I_{11/2}$). The latter process is particularly dominant in codoped samples with higher Yb concentrations because Yb^{3+} ions have larger absorption cross section than Er^{3+} ions around 980 nm.[140] Upon absorbing 980 nm photons, the Er^{3+} ions in the $^4I_{11/2}$ level can be further excited to $^4F_{7/2}$ level by excited-state absorption (ESA) process. The ions then undergo multi-photon relaxation to $^2H_{11/2}$, $^4S_{3/2}$ and $^4F_{9/2}$ luminescent levels.

Considering the first case where red emission was enhanced with increasing Yb concentrations. The red emission enhancement is certainly due to more population of Er^{3+} ions at red emitting level $^4F_{9/2}$. One of the most likely reason is the higher efficiency of the cross relaxation (ET1: $^4F_{7/2} + {}^4I_{11/2} \rightarrow {}^4F_{9/2} + {}^4F_{9/2}$) which can directly populate the

$^4F_{9/2}$ level.[140] Another possible route is the populated $^4I_{13/2}$ level was excited to the $^4F_{9/2}$ level by energy transfer from excited Yb^{3+} ions (ET2: $^4I_{13/2} + {}^2F_{5/2} \rightarrow {}^4F_{9/2} + {}^2F_{7/2}$).[237] However, unlike the red emission enhancement, the green emission of the co-doped sample was decreased with increased Yb concentration. Guo *et al.*[237] proposed that the energy-transfer process of (ET3: $^4F_{7/2} + {}^2F_{7/2} \rightarrow {}^4I_{11/2} + {}^2F_{5/2}$) depopulates the excited $^4F_{7/2}$ level at higher Yb concentrations. This results in less population of the $^2H_{11/2}$ and $^4S_{3/2}$ green emitting levels and causes a decrease in green emission intensity. In the second case when Er^{3+} concentrations are five-fold higher than Yb^{3+} concentrations, it is more likely that the up-conversion is occurring via Er^{3+} ions. At first, Er^{3+} ions are excited to $^4I_{11/2}$ level via ground-state absorption. One ion subsequently transfers it energy to its neighboring Er^{3+} ion and returns to $^4I_{15/2}$ ground state while the second ion further excited to $^4F_{7/2}$ level by a energy-transfer process (ET4: $^4I_{11/2} + {}^4I_{11/2} \rightarrow {}^4F_{7/2} + {}^4I_{15/2}$). Hence, more Er^{3+} ions are excited to the $^4F_{7/2}$ level and relax non-radiatively to the $^2H_{11/2}$, $^4S_{3/2}$ and $^4F_{9/2}$ luminescent levels. In addition, Lin et al[238] proposed an energy transfer

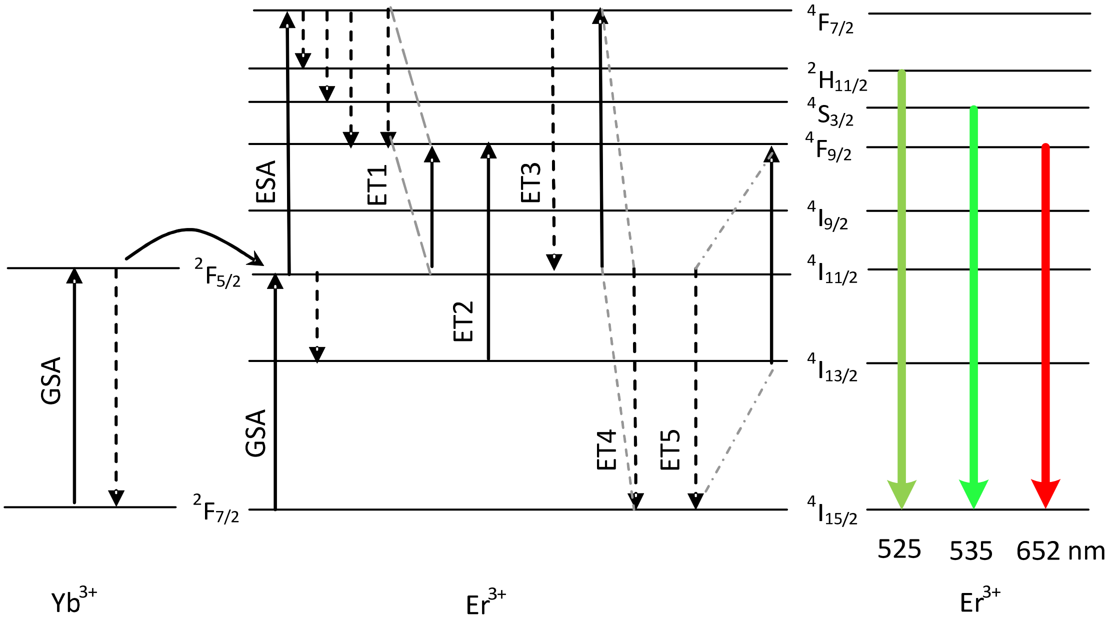

Figure 4.8 Schematic of the different up-conversion mechanism of Yb^{3+}/Er^{3+}-codoped Y_2O_3 excited at 980 nm.

mechanism (ET5: $^4I_{13/2} + {}^4I_{11/2} \rightarrow {}^4F_{9/2} + {}^4I_{15/2}$) which may populate $^4F_{9/2}$ level at high Er^{3+} concentration. The combined effect of ET4 and ET5 results in red emission enhancement while green emission intensity remains relatively unchanged in the observed up-conversion spectra.

Figure 4.9 shows the digital photographs of the fluorescent RE^{3+} (RE=Tb, Er, and Eu) doped and Yb^{3+}/Er^{3+} codoped Y_2O_3 samples. Green emission is visible from the Tb^{3+}- and Er^{3+}-doped Y_2O_3 nanorods due to their dominant green emission peaks at 545 and 525 nm respectively while red emission is observed from Eu^{3+}-dope Y_2O_3 nanorods due to the Eu^{3+} ions' strong emission at 612 nm. Figure 3.9b shows the photographs of up-

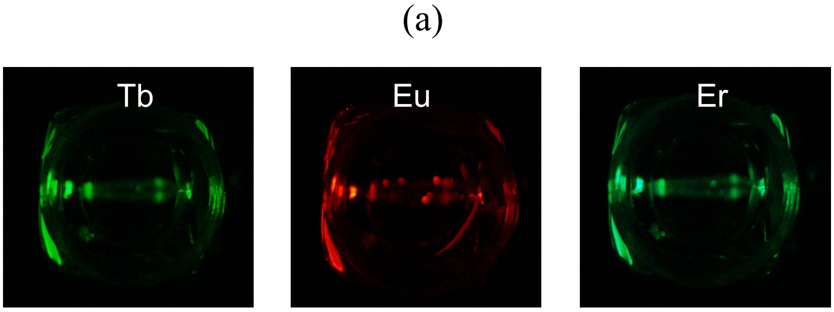

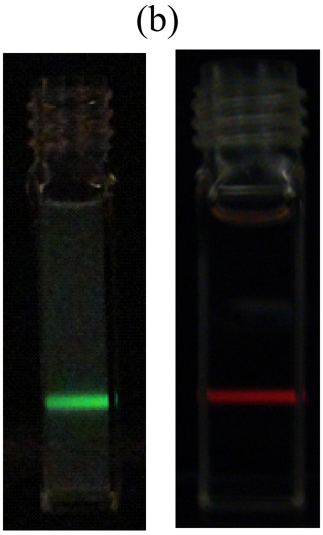

Figure 4.9 (a) Digital photographs (top view) of the cuvettes containing luminescent Tb^{3+}-, Eu^{3+}-, Er^{3+}-doped Y_2O_3 nanomaterials excited at 235, 255, and 245 nm respectively; (b) Side-view of up-conversion luminescent green and red emitting Y_2O_3:Yb^{3+},Er^{3+} excited at 980 nm.

conversion emission of $Y_2O_3:Yb^{3+},Er^{3+}$ samples. The up-converting Y_2O_3 samples (Er05Yb01 and Er01Yb05 samples shown in Figure 4.7b) produce green and red emissions at 980 nm excitation from external diode laser as expected due to different concentration of codopants.

4.3.3 Surface Functionalization of the Nanomaterials

To render these nanoparticles water dispersible and afford them with surface functional groups for further derivatization, a silanization procedure was carried out using a reverse microemulsion technique. The diagram of a silanized nanocrystal is presented in Figure 4.10a. These amine groups can afford easy biomolecule functionalization. The existence of silica- framework and amine (NH_2) groups on surface was confirmed by Fourier transform infrared (FTIR) spectroscopy. The FTIR spectrum in Figure 4.10b(i) was obtained for the typical as-synthesized $Y_2O_3:Tb^{3+}$ nanoparticles capped with oleic acid. The peaks at 3018, 2915 and 2850 cm^{-1} are due to =C-H stretching, asymmetric and symmetric C-H stretching respectively.[191] The peaks at 1549 and 1454 cm^{-1} are attributed to C=C stretching and C-O-H in plane bending band. The peak at 570 cm^{-1} is assigned to Y-O vibration bands.[239] The FTIR spectrum of amine-functionalized $Y_2O_3:Tb^{3+}$ nanoparticles is shown in Figure 4.10b(ii). The peak at 685 cm^{-1} is identified as N-H bending band. The relatively strong peak at 1109 cm^{-1} is due to the overlay of C-N stretching vibration, normally observed at 1000-1200 cm^{-1}, and IR absorption of Si-O-Si bond at the range of 1000-1130 cm^{-1}.[240-241] The peaks at 1570 and 1663 cm^{-1} are due to NH_2 symmetric bending and N-H bending respectively. The peak at 3635 cm^{-1} is assigned to N-H stretching for terminal amine (NH_2) group.[240] Amine-functionalization renders hydrophilic groups on the nanoparticle surface and enhances the dispersity of

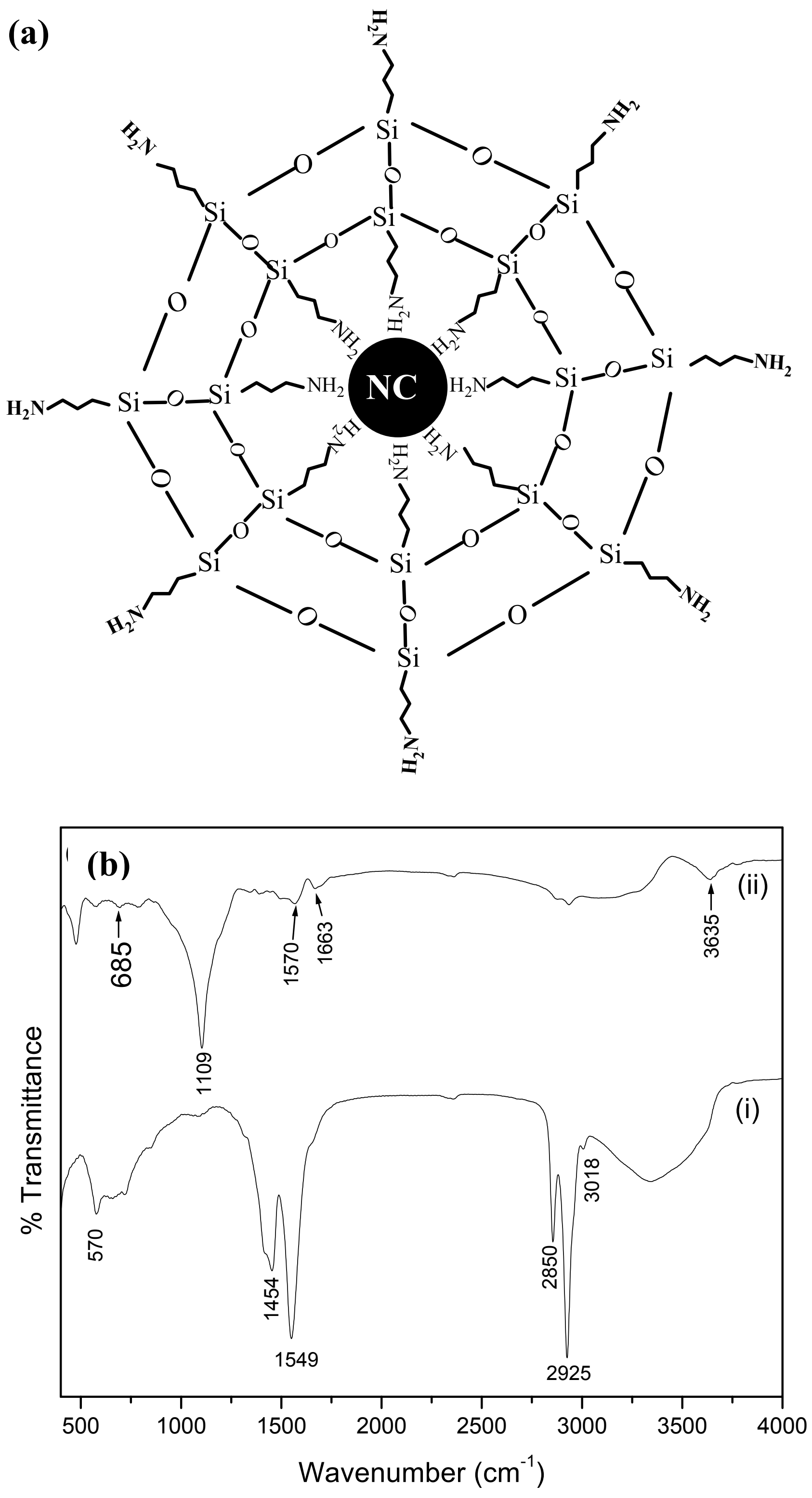

Figure 4.10 (a) A diagram of silanized nanocrystals (NC) with exposed amine ($-NH_2$) functional groups (b) FTIR spectra of (i) as-synthesized Y_2O_3:Tb^{3+}; (ii) silanized Y_2O_3:Tb^{3+}.

these nanoparticles in water. These waster-dispersible, amine functionalized nanoparticles can be potentially exploited for further bioconjugation. Amine surface functional group is reported to be less cytotoxic[242] and hence suitable for cytotoxicity studies.

4.4 Conclusion

Nanocrystals and nanorods of various doped and codoped $Y_2O_3:RE^{3+}$ (RE = Tb, Eu, Er, Yb/Er) have been synthesized in the presence of long-chain alkyl amines by adjusting the experimental parameters. The nanorods are formed from spherical nanocrystals by oriented attachment. The type of alkyl amine solvents has influence on the morphology of the nanoparticles as well as on the photoluminescence (PL) properties. It has been observed that the longer the chain length of alkyl amines, the stronger the PL emission intensity. The type of dopant had little or no effect on the morphology of the nanomaterials formed. Tb^{3+}, Eu^{3+}, Er^{3+}-doped and Er^{3+}/Yb^{3+}-codoped Y_2O_3 nanomaterials exhibit photoluminescence at room temperature. Under 980 nm excitation, green and red up-conversion emissions of Er^{3+}/Yb^{3+}-codoped Y_2O_3 have been observed. The dopant concentration plays an important role in tuning the green and red up-conversion intensities. In the first case, when Yb^{3+} concentration was increased five-fold, the red emission enhancement was attributed to enhanced population of the $^4F_{9/2}$ level via ET1 ($^4F_{7/2} + {}^4I_{11/2} \rightarrow {}^4F_{9/2} + {}^4F_{9/2}$) and ET2 ($^4I_{13/2} + {}^2F_{5/2} \rightarrow {}^4F_{9/2} + {}^2F_{7/2}$), while green emission diminishment was attributed to ET3 ($^4F_{7/2}+ {}^2F_{7/2} \rightarrow {}^4I_{11/2} + {}^2F_{5/2}$) which depopulates the excited $^4F_{7/2}$ level at higher Yb^{3+} concentrations. In the second case, when Er^{3+} concentration was 5 times higher than Yb^{3+} concentration, the combined effect of ET4 ($^4I_{11/2} + {}^4I_{11/2} \rightarrow {}^4F_{7/2} + {}^4I_{15/2}$) and ET5 ($^4I_{13/2} + {}^4I_{11/2} \rightarrow {}^4F_{9/2} + {}^4I_{15/2}$)

resulted in red emission enhancement while green emission intensity remains relatively unchanged. Surface functionalization with amine groups via a silanization process renders the nanomaterials water soluble and the ability to afford further functionalization by other biomolecules.

The rare-earth doped and codoped oxide synthesis method reported herein could be applied broadly to other RE oxide materials. This provides a general synthetic strategy for tailoring functional properties in rare earth oxide nanomaterials for potential applications such as bioimaging. Up-conversion fluorophores are envisioned to have potential in deep-tissue imaging.

CHAPTER 5

Tb^{3+}-Doped γ-Fe_2O_3: Novel Bifunctional Superparamagnetic-Fluorescent Nanocrystals

5.1 Introduction

Multifunctional nanomaterials that combine different useful functionalities offer a new platform for both diagnostics and treatment of disease.[6-7, 17] As briefly reviewed in chapter 2 (section 2.4), significant efforts have been made in recent years towards fabricating multifunctional nanomaterials for different biomedical applications. One of the most popular research focuses is to fabricate nanoparticle-based probes for combined optical/magnetic resonance imaging. Individually, both magnetism and fluorescence in materials have been exploited extensively in the biomedical research.[13, 66] Magnetic materials have been found in a variety of applications which includes magnetic data storage, ferrofluid technology, magnetorheological polishing, and energy storage.[5] Recent advancement in superparamagnetic colloidal synthesis has enhanced their potential for many other fields related to biology, pharmacy, and diagnostic, including magnetic fluids, magnetic bioseparation of labeled cells and biological entities,[243-244] magnetic resonance imaging (MRI) contrast agents,[245-246] targeted drug delivery,[247] radio frequency induced destruction of cells and tumors via hyperthermia,[248-249] and biosensing.[250] On the other hand, fluorescent nanomaterials have been exploited mostly for detection and sensing of cells and intracellular molecular events in the biomedical

---

Much of this chapter has appeared in print in *Journal of Materials Chemistry*, 2009, *19*, 3696-3703. Reproduced by permission of The Royal Society of Chemistry (RSC).

field.[74] The conventional fluorescent probes such as organic dyes, organic/inorganic fluorophores, have their respective advantages and shortcomings (details review has been presented in section 2.4). However, combining fluorescent with other properties like magnetism in nanomaterial has been considered as an effective mean of compensating the shortcomings and adding up the advantages of each.[7, 17-18, 35, 251] The combination strategies (a scheme is provided in section 2.4.3) includes magnetic and fluorescent nanocrystals incorporated into silica shells,[44, 200] magnetic nanocrystals attached to fluorescent nanocrystals by means of ligand molecules,[252] or magnetic and luminescent nanoparticles encapsulated into silica spheres,[24, 28] to produce hybrid nanostructures by colloidal syntheses. However, tailoring multifunctional nanocomposites by assembly of desired functional nanomaterials are rather tedious which involve multiple synthesis steps and potentially less attractive for large scale production. In comparison, the notion of engineering a single-phase multifunctional nanoparticle would be more advantageous, both in terms of ease of synthesis and applications.[48]

In chapter 4, we have presented the investigation of rare earth (RE) ions doping and co-doping into an oxide host (Y_2O_3) to fabricate fluorescent nanomaterials for bioimaging. The rare-earth ions exhibited intense, narrow-band intra-4f luminescence. In this work, by adopting the RE doping strategy, we doped terbium (Tb) ion in a superparamagnetic oxide host (γ-Fe_2O_3) to fabricate a novel single-phase bifunctional nanocrystal which combine two useful functionalities, superparamagnetism and luminescence, into the same crystal. The luminescence of the nanocrystals was further improved by affording a surface-passivating ZnS shell. Amine surface-functionalization of the Tb^{3+}-doped γ-Fe_2O_3 has also been demonstrated to render the bifunctional nanocrystals water dispersible, hence suitable for *in vitro* cytotoxicity studies and for further bioconjugations. The synthesized bifunctional nanocrystals are envisioned to be useful as negative contrast agents in T_2-weighted MRI as well as in optical imaging.

5.2 Experimental Section

5.2.1 Chemicals

All chemicals were used as received without further purifications. Terbium (III) chloride hexahydrate (99.9%), 1-octadecene (tech. 90%), diethylzinc (1.0M solution in hexanes), tetramethylammoniumhydroxide (25 wt% in methanol) (TMAH) and Igepal CO-520 (Polyoxyethylene(5)nonylphenylether) were purchased from Aldrich. Iron (III) chloride hexahydrate (98%) and oleic acid (tech. 90%) were purchased from Alfa Aesar. NaOH (reagent grade, 97%, beads), 3-aminopropyltrimethoxysilane (APS) (97%) trioctylphosphine (TOP), hexamethyl disilthiane were purchased from Fluka. Ethanol, hexane, cyclohexane and chloroform were of analytical reagent grade.

5.2.2 Synthesis of Tb^{3+}-doped γ-Fe_2O_3 Nanocrystals

Single-phase magnetic-fluorescent Tb^{3+}-doped γ-Fe_2O_3 nanocrystals were synthesized based on a modified method developed by Hyeon *et al.*[218] In a typical synthesis process, 2 mmol of $FeCl_3 \cdot 6H_2O$ and 0.2 mmol of $TbCl_3 \cdot 6H_2O$ (99.9%, Aldrich) was dissolved in 3 ml of deionized water. 1.9 ml of oleic acid, 7 ml of hexane and 4 ml of ethanol were added and stirred at room temperature for 30 min. Then, 6.25 mmol of NaOH was added to the reaction mixture and refluxed the reaction mixture at 70 ^{o}C for 4 h. The resultant solution was allowed to form two different layers in a separatory funnel. The top organic layer containing Fe(Tb)-oleate complex was collected, washed with 30 ml of water and then heated at 70 ^{o}C overnight in order to remove the hexane. The sticky iron(Tb)-oleate precursor was dispersed in 1.5 ml of oleic acid and 12 ml 1-octadecene. The mixture solution was degassed with N_2 for 30 min at room temperature. After that, the mixture was heated to 320 °C at 3 °C/min and maintained at that temperature for 30 min under N_2 flow. Afterwards, the solution was cooled to room temperature and precipitated by excess ethanol. The precipitate was collected by centrifugation and the supernatant decanted. The isolated solid was redispersed in hexane and then precipitated with ethanol. The precipitation-redispersion process was repeated for several times to purify the as-prepared Tb^{3+}-doped iron oxide nanocrystals.

5.2.3 ZnS Coating of Tb^{3+}-doped γ-Fe_2O_3 Nanocrystals

The as-prepared Tb^{3+}-doped iron oxide nanocrystals were dried at 70 °C overnight. A method similar to the literatures[253-254] was adopted to form ZnS coating onto Tb^{3+}-doped γ-Fe_2O_3 nanocrystals. 30 mg of dried Tb^{3+}-doped iron oxide nanocrystals was dispersed in 2 g of trioctylphosphine (TOP). The solution mixture was then degassed with N_2 for 30 min at room temperature and slowly heated up to 280°C under N_2 flow. A solution of 250 µl of hexamethyl disilathiane and 1 ml of diethylzinc premixed in 2 g of TOP was injected very slowly drop-wise into the hot reaction mixture and the reaction was kept at that temperature for 1 h under N_2.

5.2.4 Amine Functionalizations

Silanization and amine functionalization were carried out in a similar process described in chapter 4 which was adopted from method developed by Selvan *et al.*[30] In a typical process, γ-Fe_2O_3:Tb^{3+} nanocrystals dispersed in hexane were separated by centrifugation and 4 mg of the nanocrystals were re-dispersed in chloroform. Micelles were prepared by dissolving 0.2 g of Igepal CO-520 in 4 ml of cyclohexane and the mixture was stirred vigorously for 1 h. Next, 200 μl of nanocrystals in chloroform was added to the mixture and stirred for 15 min. Subsequently 50 μl of aminopropyl trimethoxysilane (APTMS) was added and the mixture was stirred for another 1 h. Then, 20 μl of tetramethylammonium hydroxide (TMAH) in methanol was added. After 1 h of stirring, 10 μl of deionized water was added and stirred for another 30 min. At this stage, some globules were formed and settled at the bottom of the flask leaving a transparent organic phase at the top. The transparent organic phase was then discarded and globules of γ-Fe_2O_3:Tb^{3+} nanocrystals were washed with chloroform and ethanol for the complete removal of excess surfactant and other reactants from the surface. The amine-functionalized γ-Fe_2O_3:Tb^{3+} nanocrystals were then dispersed in deionized water.

5.2.5 Characterizations

The as-prepared samples were characterized by powder X-ray diffraction (XRD) (D8 ADVANCED X-ray diffractometer), transmission electron microscopy (TEM), high resolution TEM (HRTEM) (JEOL JEM-3010) and Energy Dispersive X-ray Spectroscopy (EDS) supported by TEM. X-ray photoelectron spectroscopy (XPS) investigation was conducted on a VGESCALAB 250 spectrometer using a monochromatic Al Kα X-ray source (1486.6 eV). All binding energies (BEs) were referenced to the C 1s peak (BE = 284.6 eV) arising from surface hydrocarbons. Photoluminescence spectra were collected on a Shimadzu RF-5301 PC Spectrofluorophotometer using 150 W Xenon lamp as an excitation source. The magnetic properties of the iron oxide nanocrystals were studied using a vibrating sample magnetometer (VSM) (Lake Shore, 7300). Thermogravimetric analysis was performed using a Diamond TG/DTA (Perkin Elmer). Dynamic light scattering (DLS) experiments were performed with a Brookhaven 05-LHP-928 laser light scattering system (He-Ne laser, 35 mW).

5.3 Results and Discussion

5.3.1 Morphology, Size, and Crystal Structure of the Nanocrystals

Figure 5.1a shows a typical TEM image of as-synthesized Tb^{3+}-doped γ-Fe_2O_3 nanocrystals. It is observed that almost all the nanocrystals are spherical in shape and highly monodispersed with an average diameter of 13 ± 0.2 nm. The clear lattice fringes (Figure 5.1b) show the highly crystalline nature of the γ-Fe_2O_3:Tb^{3+} nanocrystals. The distance between two adjacent planes was measured to be about 0.29 nm, corresponding to (220) lattice planes in the spinel-structured γ-Fe_2O_3.

The X-ray powder diffraction (XRD) pattern of the as-prepared sample shown in Figure 5.2a which confirms that all the peaks match very well with XRD pattern of γ-Fe_2O_3 (maghemite) nanocrystals (PDF no.# 04-0755). The diffraction peaks at 30.3, 35.5, 43.1, 53.5, 57.1, 62.5 and 74.6° can be indexed as (220), (311), (400), (422), (511), (440), and (533) planes of γ-Fe_2O_3. The broadening of the peaks indicates small crystalline size of the resulting iron oxide particles. As calculated using Scherrer's formula,[255] the average size of these iron oxide nanoparticles is about 12.8 nm, which is quite consistent with the result obtained from TEM analysis. XRD patterns for Tb^{3+}-doped and undoped γ-Fe_2O_3 nanocrystals were compared (Figure 5.2c). Comparing these two patterns, it is observed that there is a slight shift towards the lower angles for the Tb-doped sample which is probably ascribed to a larger ionic radius of doped Tb^{3+} cation compared to that of host

Fe^{3+} cation. Such a phenomenon indicates that solid solution was likely formed by incorporating Tb^{3+} into the structure of γ-Fe_2O_3.The hydrodynamic size of the colloidal suspension was also obtained using dynamic light scattering (DLS). According to the particle size distribution plot, the average particle size is about 12.7 nm (as shown in Figure 5.2b), which is close to the results from TEM and XRD.

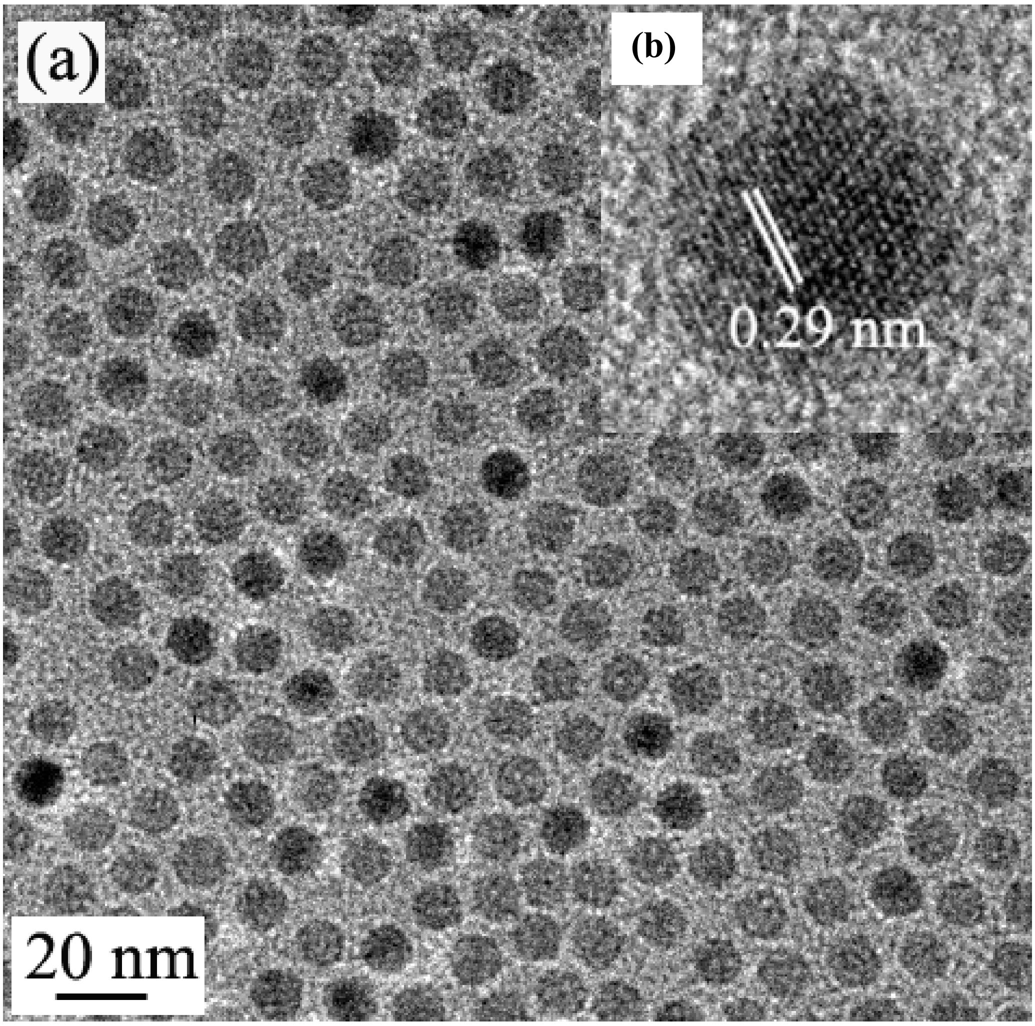

Figure 5.1 (a) A typical TEM image of Tb^{3+}-doped γ-Fe_2O_3 nanocrystals; (b) The inset shows HRTEM image of a single nanocrystal.

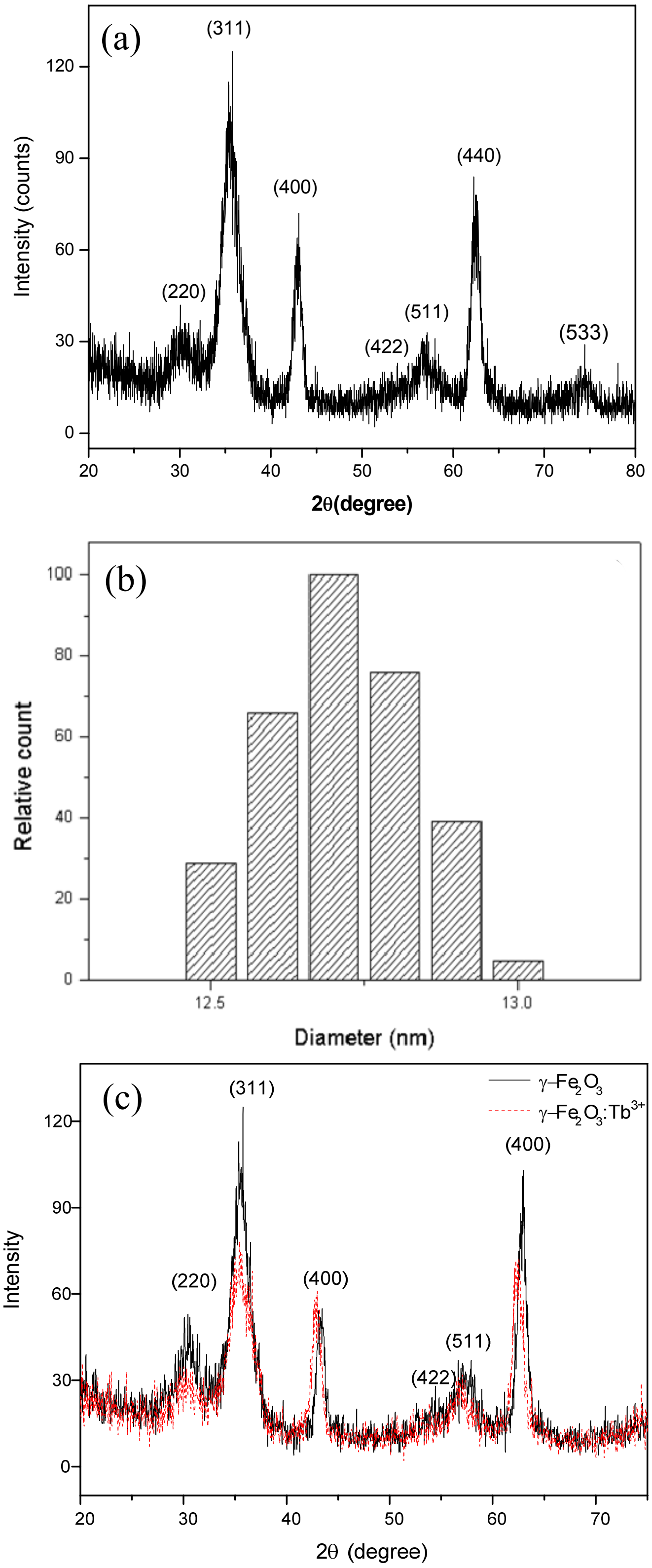

Figure 5.2 (a) XRD pattern of as-prepared iron oxide nanocrystals, showing the cubic spinel structures; (b) Particle size distribution of Tb^{3+}-doped iron oxide nanocrystals. (c) XRD pattern of Tb^{3+}-doped and undoped γ-Fe_2O_3 nanocrystals.

5.3.2 Composition Analysis of the Nanocrystals

The composition of these nanocrystals was analyzed by energy dispersive X-ray spectroscopy (EDS) by a JEOL JEM-3010 TEM. Figure 5.3 shows that these nanocrystals are composed of C (from the surfactant and carbon film on TEM copper grid), Fe, O and Tb. The peaks of Cu element are from the copper TEM grid. Quantitative analysis shows that the atomic ratio of Fe to Tb is about 10.5: 1.

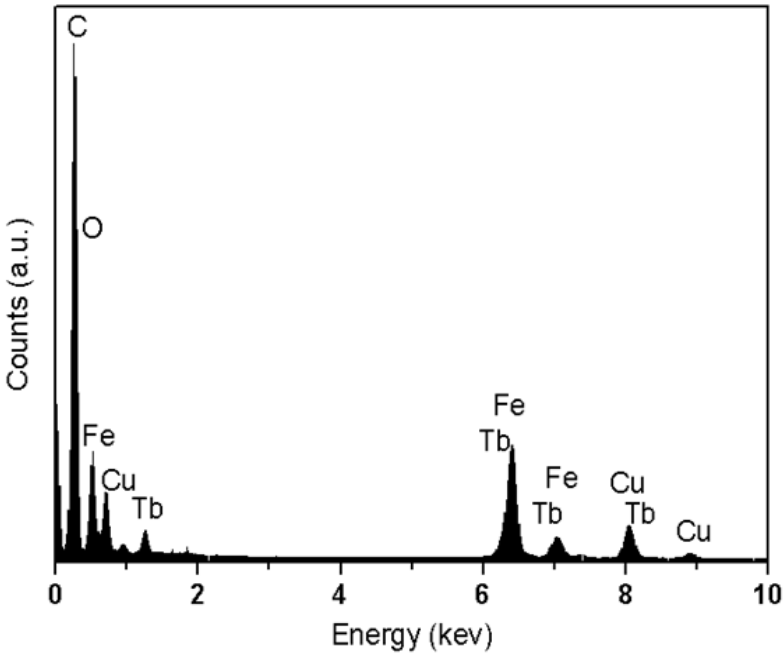

Figure 5.3 Energy dispersive X-ray spectra (EDS) of Tb^{3+}-doped γ-Fe_2O_3

X-ray photoelectron spectroscopy (XPS) was used to examine the oxidation states of the iron and Tb on the surface of these nanocrystals. The representative XPS survey spectrum is shown in Figure 5.4. The peaks of the C 1s, O 2p and Fe 2p observed indicate the organic coating (oleic acid) on the surface of iron oxide nanoparticles. The binding energies at 710.9 and 724.7 eV are attributed to Fe $2p_{3/2}$ and Fe $2p_{1/2}$ core-level electrons, respectively, in good agreement with the values reported for γ-Fe_2O_3 but not for Fe_3O_4.[256-257] The XPS spectrum of the Tb $4d_{5/2}$ of the as-prepared sample is shown in Figure 5.4d. A single peak at 149.5 eV corresponds to Tb in the trivalent state.[258]

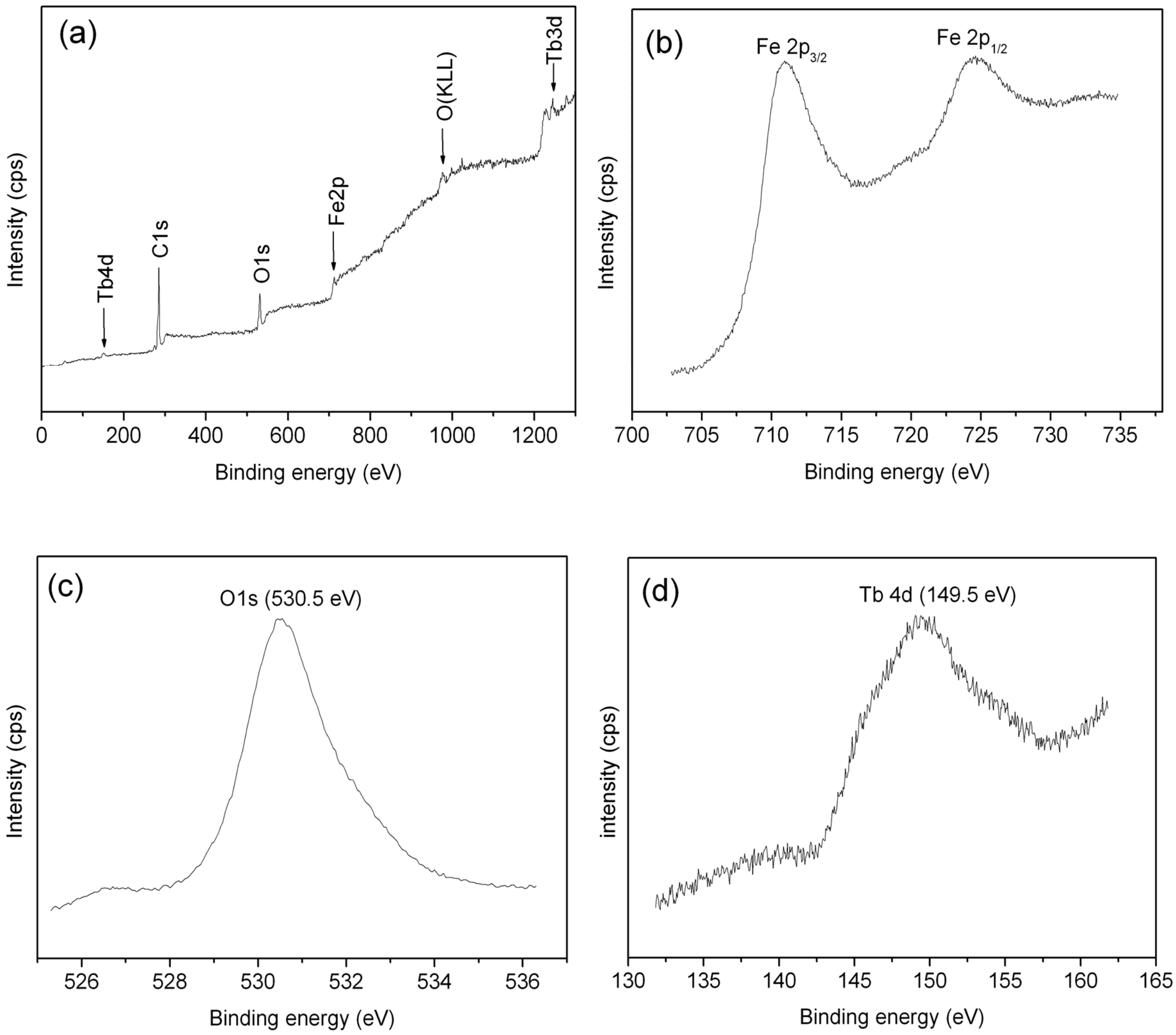

Figure 5.4 XPS spectra of the as-prepared: (a) survey; (b) Fe 2p; (c) O1s; (d) Tb 4d.

5.3.3 Optical Properties

5.3.3.1 The Room Temperature Photoluminescence (PL)

The room temperature PL spectra of Tb^{3+}-doped γ-Fe_2O_3 nanocrystals dispersed in hexane are shown in Figure 5.5. The emission spectrum at 235 nm excitation display four sharp but relatively weak emission bands which can be assigned to 4f → 4f transitions within Tb^{3+} ions. The most intense peak at 545 nm corresponds to the $^5D_4 \rightarrow {}^7F_5$ transition. The other emission peaks at 490, 585, and 620 nm correspond to transitions from $^5D_4$ to $^7F_6$, $^7F_4$ and $^7F_3$ respectively.[221]

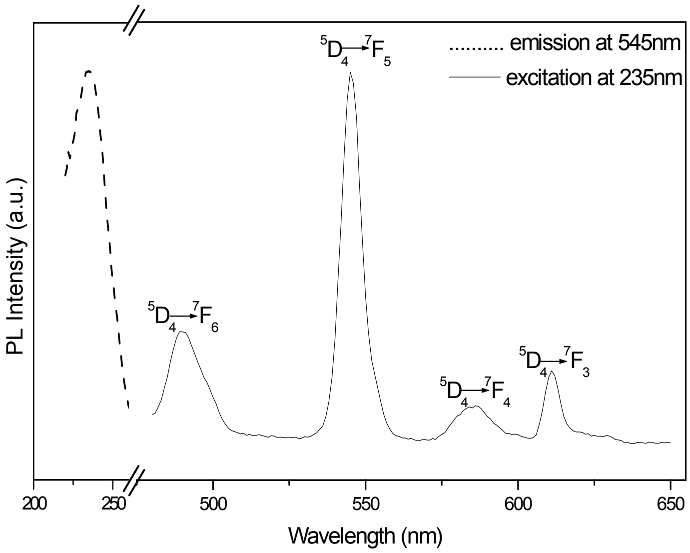

Figure 5.5 Excitation and emission spectra of as-obtained Tb^{3+}-doped γ-Fe_2O_3 nanocrystals in hexane at room temperature.

5.3.3.2 ZnS Surface Passivation

Although the emission bands suggest the presence of Tb^{3+} ions in γ-Fe_2O_3 nanocrystals, the possibility of Tb^{3+} ions adsorbed at the surface and bound to organic ligands rather than doped in the γ-Fe_2O_3 matrix cannot be ruled out completely. Considering this possibility, a surface passivation was carried out. The Tb^{3+}-doped γ-Fe_2O_3 nanocrystals were surface-coated with a thin layer of ZnS. Figure 5.6a shows the TEM image a thin layer of ZnS shell forms over the nanocrystals while the inset shows uniform dispersity of the ZnS coated nanocrystals in the solution. EDS analysis (Figure 5.6b) of the ZnS coated nanocrystals was also carried out. It confirms the presence of Zn and S on the nanocrystals surface which suggests that the nanocrystals are composed of C, Fe, O, Tb,

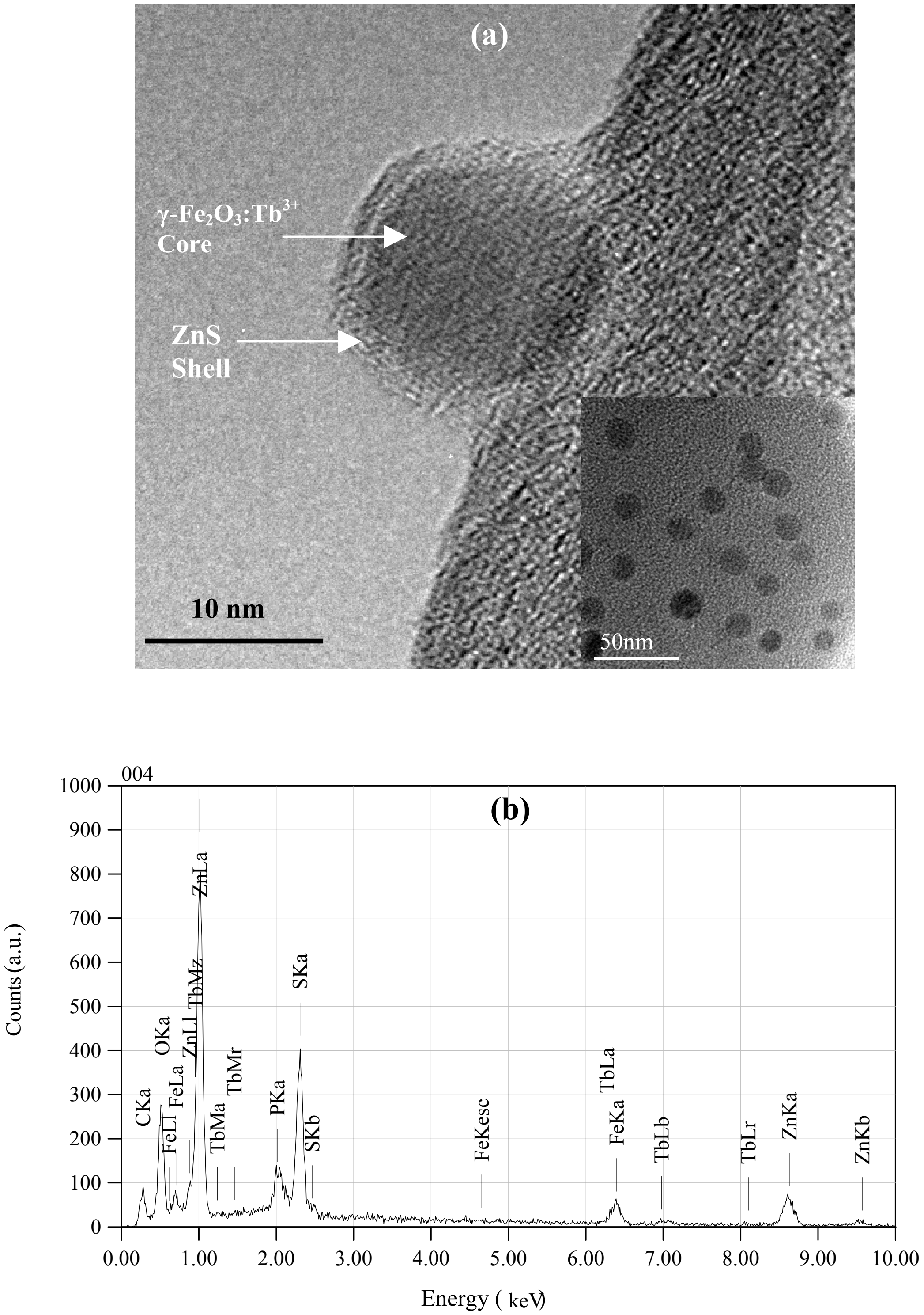

Figure 5.6 (a) HRTEM image of a single Tb^{3+}-doped γ-Fe_2O_3 nanocrystal coated with ZnS layer. Inset showing the uniform dispersity of the ZnS coated nanocrystals; (b) EDS analysis of ZnS coated Tb^{3+}-doped γ-Fe_2O_3 nanocrystals.

Zn, S and P. Carbon (C) and phosphorous (P) peaks appears from the surfactants oleic acid and trioctylphosphine (TOP) used in the synthesis process.

The PL spectra of the nanocrystals (Figure 5.7) before and after ZnS coating suggest that ZnS-coating enhances the PL intensity of the nanocrystals. The difference in luminescence properties can be ascribed to passivation of nanocrystals surface. Previous studies elucidated that surface states play a key factor for the occurrence of band-gap states that quench the excitation luminescence.[234-235] ZnS is a higher bandgap material which may help to enhance the fluorescence through the passivation of the nanocrystalline surface.[252] The ZnS shell can reduce luminescence quenching at the nanocrystal surface and increase the stability of nanocrystal to photochemical corrosion, which improve the PL. Yet, the increase of PL after ZnS coating is not very significant. The PL spectrum of ZnS-coated Tb^{3+}-doped γ-Fe_2O_3 also evidences the incorporation of Tb^{3+} ions in the γ-Fe_2O_3 matrix instead of present as adsorbates on the nanocrystal surface.[259]

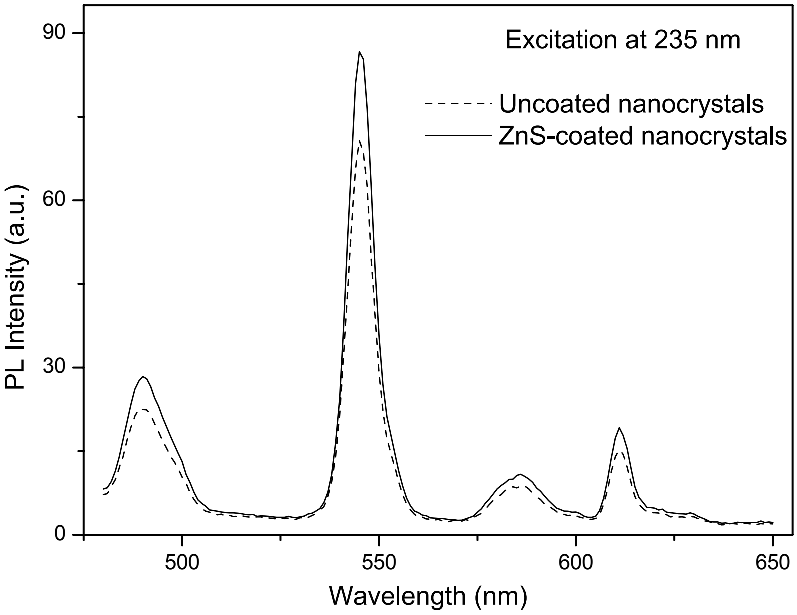

Figure 5.7 PL spectra of Tb^{3+}-doped γ-Fe_2O_3 nanocrystals before and after ZnS coating.

5.3.4 Magnetic Properties

Figure 5.8a shows the room-temperature magnetization curves of undoped, Tb^{3+}-doped and silanized γ-Fe_2O_3 nanocrystals. The coercivity values of undoped and Tb^{3+}-doped γ-Fe_2O_3 nanocrystals at room temperature are almost negligible at 8.52 G and 3.53 G respectively, which is a typical characteristic of superparamagnetic materials.[260] This also indicates that the thermal energy can overcome the anisotropy energy barrier of a single particle at room temperature, and that the net magnetization of the particle assemblies in the absence of an external magnetic field is almost zero. The saturation magnetization of Tb^{3+}-doped γ-Fe_2O_3 was 30.51 emu/g, which is slightly lower than those of similar size nanoparticles prepared by other methods.[261] The saturation magnetization of undoped γ-Fe_2O_3 was found to be similar at 30.39 emu/g. The lower saturation magnetization value of the as-synthesized iron oxides is most likely attributed to the existence of surfactants on the surface of γ-Fe_2O_3 nanoparticles. Kodama *et al.*'s studies suggested that noncollinear spin structure, which originated from the pinning of the surface spins and coated surfactant at the interface of iron oxide, results in the reduction of magnetic moment in such nanoparticles.[262] The amount of weight loss due to the surfactant layer on the as-prepared nanocrystals was estimated. Based on TGA analysis conducted in air with a heating rate of 10 °C/min (Figure 5.8b), it was estimated that the percentage loss due to the removal of oleate was around 27%, indicating that our nanocrystals are covered by oleate groups which may reduce the magnetization of the nanocrystals.

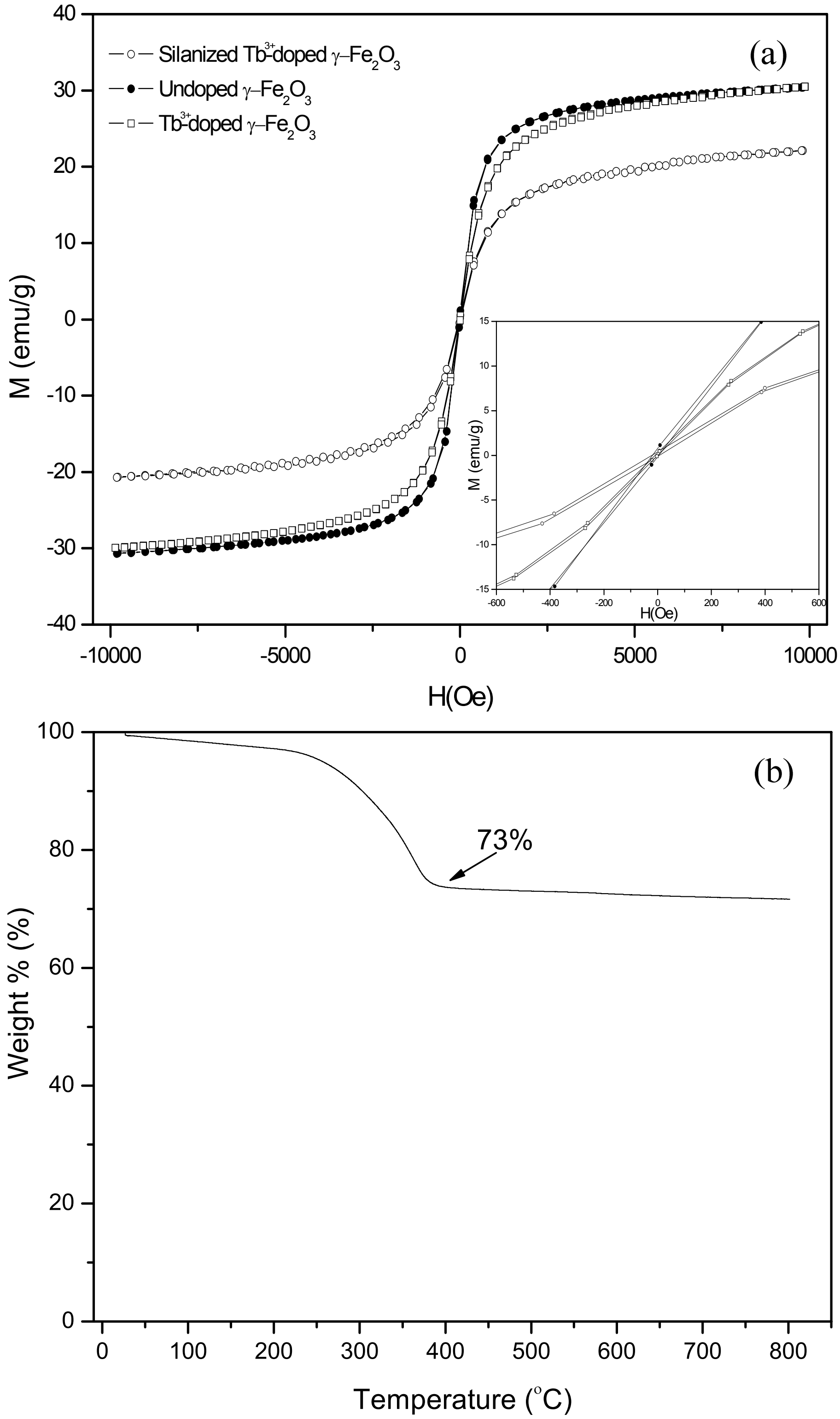

Figure 5.8 (a) Room temperature magnetic hysteresis curves for Tb^{3+}-doped, undoped γ-Fe_2O_3, and silanized Tb^{3+}-doped γ-Fe_2O_3. Insert: Magnified values at low fields; (b) Percentage of weight loss of the as-prepared Tb^{3+}-doped γ-Fe_2O_3 using TGA method.

5.3.5 Amine Surface Functionalization

Surface functionalization via silanization was carried in a reverse microemulsion to render the bifunctional nanocrystals water dispersible and ease of further functionalization for bio-conjugation. A thin layer of silica was produced on Tb^{3+}-doped γ-Fe_2O_3 with surface NH_2 groups after silanization using aminopropyl trimethoxysilane (APS). The silanized nanoparticles were well-dispersed in deionized water at pH 6.95. Proposed structure of the amine-functionalized nanocrystals is similar to that shown in Figure 4.10a (in chapter 4). FTIR spectroscopy was conducted to confirm the presence of silica layer and surface amine (NH_2) group. The FTIR spectrum in Figure 5.9a(i) was obtained for as-synthesized Tb^{3+}-doped γ-Fe_2O_3 capped with oleic acid. The peaks at 2923 cm^{-1} and at 2852 cm^{-1} are due to asymmetric and symmetric C-H stretches in oleic acid. Peaks at 1709 cm^{-1}, 1562 cm^{-1}, 1450 cm^{-1}, 1132 cm^{-1} are attributed to C=O stretching, C=C stretching, C-O-H in plane bending and C-O stretching band respectively.[191] A relatively small peak at 580 cm^{-1} is due to Fe-O vibration band. The spectrum for amine functionalized nanocrystals is shown in Figure 5.9a(ii). The incorporation of silica framework and amine groups can be qualitatively confirmed by this spectrum. A relatively strong peak at 630 cm^{-1} is due to bending of N-H bonds indicating the existence of amine groups. The C-N stretching vibration, normally observed in the range of 1000-1200 cm^{-1}, is overlaid with the IR absorptions of Si-O-Si in the range of 1130-1200 cm^{-1} and of Si-CH_2-R in range 1250-1200 cm^{-1} producing a wide peak at 1109 cm^{-1}.[240-241] Peaks at 1560 cm^{-1} and 1632 cm^{-1} are attributed to N-H bending and –NH_2 scissoring band respectively while the peak at 3416 cm^{-1} is due to N-H stretching band for terminal amine groups. Silanized magnetic nanoparticles show decreased saturation magnetization of 22.11 emu/g (Figure 5.8a). The coercivity was

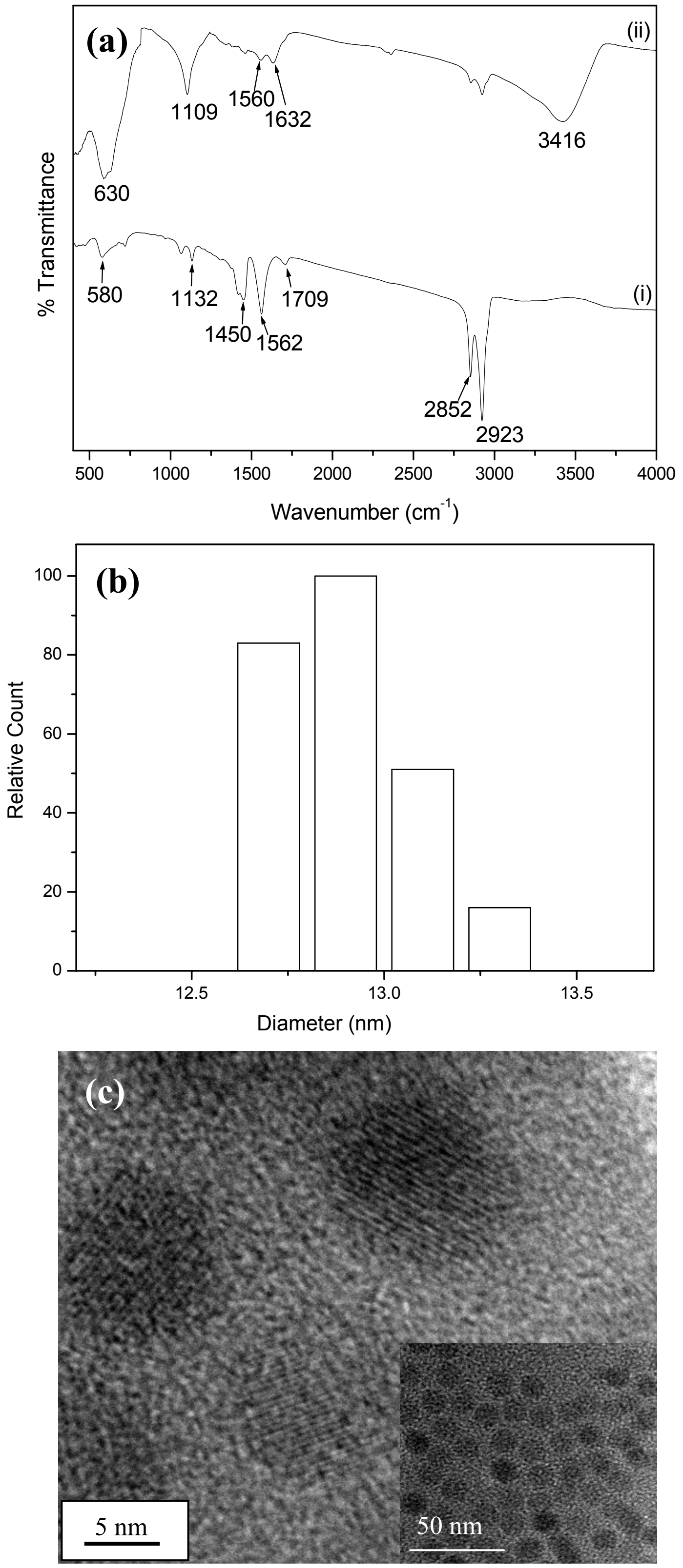

Figure 5.9 (a) FTIR spectra of (i) as-synthesized Tb^{3+} doped γ-Fe$_2$O$_3$; (ii) APS-modified Tb^{3+} doped γ-Fe$_2$O$_3$ nanocrystals; (b) Particle size distribution of Tb^{3+}-doped γ-Fe$_2$O$_3$ nanocrystals after silica silanization; (c) HRTEM image of amine functionalized Tb^{3+}-doped γ-Fe$_2$O$_3$ nanocrystals; Inset: Well-dispersed amine functionalized nanocrystals in water.

estimated to be 14.1 G. The mean hydrodynamic size after silanization and the particle size distribution is presented in Figure 5.9b. There is a small increase in mean particle size and a shift in particle size distribution. The mean size has increased from about 12.7 nm to 12.9 nm after silanization. The silanization process only yields a thin layer of silica coating. TEM image of the silanized nanoparticles (Figure 5.9c) shows that the layer owing to silanization is too thin to be visible under TEM. The silanized water-dispersible nanocrystals were further used for *in vitro* cytotoxicity studies.

A photograph of green emitting fluorescent Tb^{3+}-doped γ-Fe_2O_3 at 235 nm excitation is shown in Figure 5.10a. The green fluorescence emission line is visible along the excitation path. Figure 5.10b shows the as-synthesized nanocrystals kept in a sample vial while Figure 5.10c shows the nanocrystals being attracted to a magnet due to its superparamagnetism.

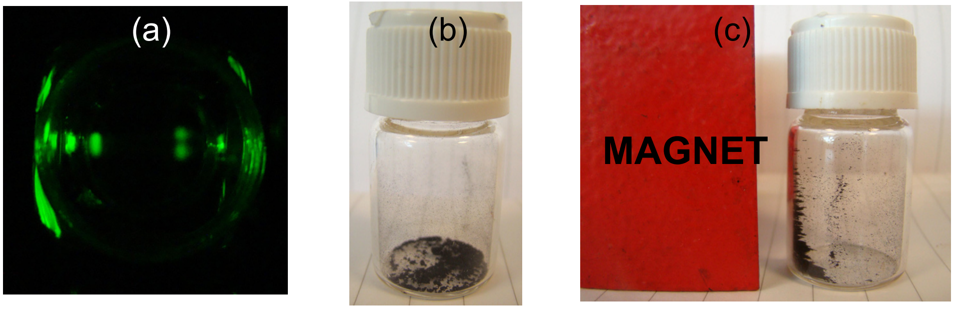

Figure 5.10 (a) Digital photograph (top view) of the Tb^{3+}-doped γ-Fe_2O_3 showing emission (green color); (b) the as-synthesized Tb^{3+}-doped γ-Fe_2O_3 in a sample vial; (c) sample attracted by a magnet.

5.4 Conclusions

In summary, a facile method has been developed to synthesize single-phase bifunctional magnetic-fluorescent Tb^{3+}-doped γ-Fe_2O_3 nanocrystals. These iron oxide nanocrystals are highly monodispersed and around 13 nm in diameter. The as-obtained nanocrystals are superparamagnetic (saturation magnetization strength of 30 emu/g) and exhibit room temperature photoluminescence emission at 235 nm excitation. We have also shown that the nanocrystals can be amine-functionalized. The reported single-phase bifunctional nanocrystals are envisioned to have potential in integrated imaging technology, of which T_2-weighted MRI and florescence microscopy can be combined to provide better resolution in tissue and cellular imaging.

CHAPTER 6

RE-Doped Gd_2O_3 & Dy_2O_3: Multimodal Contrast Agents for Optical/Magnetic Resonance Imaging

6.1 Introduction

Development of contrast agents for cellular and molecular imaging has been thriving in the past decades (as reviewed in section 2.4), particularly in areas of improving detection limits, incorporating functionalities and imaging modalities.[74, 76] Of these, MRI and optical imaging probes draws substantial interest. In particular, superparamagnetic iron oxides (SPIO) prevailed among inorganic nanoparticle-based MRI contrast agents, but they have been used to provide negative contrast only.[40, 263-266] As a result, simultaneous efforts have been made over the years to develop positive contrast agents. Generally, metal ion chelates such as Gd^{3+}- and Mn^{2+}-based chelates have been used as positive (T_1) contrast agents in MRI.[6, 40] For example, Gd-based chelate gadolinium diethylenetriaminepentaacetate (Gd-DTPA) has been used clinically for detecting the breakage of the blood-brain barrier (BBB) and changes in vascularity, flow dynamics, and perfusion.[267] However, the metal ion chelates are limited by quick removal by renal excretion, non-specificity to target, and short accumulation time.[50, 268] In comparison, rare-earth based inorganic nanoparticles agents such as gadolinium oxide[50, 108-109] and gadolinium fluorides[110] show very good potential in T_1-weighted MR imaging. For example, small Gd_2O_3 (20-40 nm) was reported to show comparable relaxivity to Gd-

---

Much of this chapter has appeared online in *Langmuir*, 2010, 26, 8959-8965. Reproduced with permission. Copyright 2010 American Chemical Society.

DTPA chelates by Alexander *et al.*[108] while Fortin *et al.*[109] showed poly(ethylene) glycol coated ultrasmall Gd_2O_3 (~3 nm) demonstrated relaxivity twice as high as for Gd-DTPA chelate. Other rare earths such as dysprosium oxide (Dy_2O_3) has also been reported as potential T_2-weighted MRI contrast agent by Norek *et al.*[54] Furthermore, rare earth oxides have been fabricated as bimodal imaging probes by Bridot *et al.*[50] They integrated paramagnetic Gd_2O_3 with fluorescent organic fluorophores by an encapsulation technique and manifested the applicability of the bifunctional nanomaterials to combined optical/MR imaging.

In chapter 5, rare earth (i.e. Tb^{3+}) doping in γ-Fe_2O_3 hosts has been demonstrated which resulted in single-phase bifunctional superparamagnetic-fluorescent nanocrystals. In this work, we extended our quest of fabricating single-phase multimodal contrast agent by choosing two paramagnetic RE oxide hosts gadolinium oxide (Gd_2O_3) and dysprosium oxide (Dy_2O_3) doped and codoped with RE^{3+} ions (i.e. Tb, and Yb/Er). Adopting similar synthesis strategy, single-phase bifunctional paramagnetic-fluorescent Gd_2O_3:RE^{3+} and Dy_2O_3:RE^{3+} nanocrystals and nanorods have been synthesized. It is observed that the nanorods (with uniform diameters of 2.5 ± 0.3 nm and lengths of 18.8 ± 5.7 nm) evolve from the quasi-spherical nanocrystals (2.5 ± 0.3 nm). The nanocrystals and nanorods demonstrate both down- and up-conversion fluorescence, and are paramagnetic, and one of these nanorods (Gd_2O_3:RE^{3+}) demonstrates good positive contrast in T_1-weighted MRI.

6.2 Experimental Section

6.2.1 Chemicals

All chemicals were used as received without further purifications. Gadolinium (III) oxide (99.99%), and dysprosium (III) oxide (99.99%), terbium (III) chloride hexahydrate (99.9%), ytterbium (III) chloride hexahydrate (99.99%), erbium (III) chloride hexahydrate (99.9%), tetramethylammoniumhydroxide (25 wt% in methanol) (TMAH) and Igepal CO-520 (Polyoxyethylene(5)nonylphenylether), oleylamine (tech., 70%), were purchased from Aldrich. HNO_3 (analytical reagents, 70%), and oleic acid (tech. 90%) were purchased from Alfa Aesar. NaOH (reagent grade, 97%, beads), 3-aminopropyltrimethoxysilane (APS) (97%) were purchased from Fluka. Ethanol, hexane, cyclohexane and chloroform were of analytical reagent grade.

6.2.2 Synthesis of RE^{3+}-doped Gd_2O_3 and Gd_2O_3 Nanocrystals and Nanorods

Typically, to synthesize RE^{3+}-doped Gd_2O_3 (or Dy_2O_3) nanocrystals and nanorods, 2 mmol Gd_2O_3 (or Dy_2O_3) were dissolved in 0.8 ml HNO_3 (70%) to which 0.22 mmol of $TbCl_3.6H_2O$ was added. To this precursor, 6 ml H_2O, 9 ml ethanol, 15 ml hexane, and 2 ml oleic acid were introduced in sequence and the mixture stirred in a closed vessel at 70 °C for 2 h. A second solution, prepared by dissolving 0.24 g NaOH (reagent grade, 97%, beads) in 6 ml H_2O was then added dropwise very slowly and heating with stirring at 70 °C continued for another 4 h. After reaction, the mixture separated into two transparent layers. The upper organic layer containing the doped RE-oleate complex was collected, washed with 30 ml of distilled water and dried overnight at 70 °C to evaporate water and hexane. The waxy complex obtained after drying, was dissolved in 20 ml oleylamine (tech., 70%) in a three-neck flask and purged with N_2. The solution was then heated at a rate of 5 °C/min to 300 °C under N_2. At this temperature, first nanocrystals and then nanorods were grown in the solution with different reflux times. The mixture was cooled to room temperature before precipitation and extensive washing with ethanol by centrifugation. The nanorods were finally redispersed in cyclohexane for further characterization. For Yb^{3+}/Er^{3+} codoped samples, 0.18 mmol $YbCl_3.6H_2O$ and 0.04 mmol $ErCl_3.6H_2O$ were used, instead of $TbCl_3.6H_2O$.

6.2.3 Silanization of the Gd_2O_3 Nanomaterials

Washed $Gd_2O_3:Yb^{3+},Er^{3+}$ nanomaterials were silanized using aminopropyl trimethoxysilane (APS) in a similar process described in section 4.3.3 and used for T_1-weighted MR imaging and cytotoxicity studies.

6.2.4 MRI Sample Preparations

T_1-weighted images were obtained on a Varian 9.4T MRI system. The sample concentrations were 0.015, 0.030, 0.06, 0.125, and 0.25 mM (shown in Figure 6.12). All samples were dissolved in (double distilled) water. TR and TE values were optimized for T_1-weighting while using the spin echo sequence. Other parameters used for imaging are: number of acquisitions = 25, field of view = 35 mm, slice thickness = 3 mm, acquisition time ~ 6 min/sample. In order to avoid susceptibility effects, all experiments were performed in 1% agarose medium. The image of the water sample was taken for reference.

6.2.5 Characterization

The high resolution transmission electron microscopy (HRTEM) and selected area electron diffraction (SAED) were obtained using a JEOL JEM-2100F high resolution transmission electron microscope operated at 200 kV. The X-ray diffraction (XRD) patterns were collected with a D8 ADVANCE X-ray diffractometer with Cu Kα radiation ($\lambda = 0.15406$ nm). Down-conversion luminescence spectra were obtained using a Shimadzu RF-5301 PC spectrofluorophotometer fitted with a 150 W xenon lamp as the excitation source. Up-conversion luminescence spectra were recorded using a Fluoromax-4, Horiba Jobin Yvon spectrofluorometer equipped with an adjustable laser (980 nm, maximum power 2W, B & W TEK Inc.) as the excitation source with a fiber-optic accessory. The room temperature magnetization properties of the nanorods were studied using a vibrating sample magnetometer (VSM) (Lakeshore, 7300). MRI images were obtained on a Varian 9.4T MRI system.

6.3 Results and Discussion

6.3.1 Morphology and Growth of the Nanorods

The doped RE-oleate complexes were decomposed at a fixed reaction temperature of 300 °C with morphological evolution compositionally independent. The nucleation and growth phenomena of Gd_2O_3:RE^{3+} (RE= Tb, Yb/Er) and Dy_2O_3:RE^{3+} (RE= Tb, Yb/Er) are broadly similar, and the results of Gd_2O_3:RE^{3+} are shown as representative in some cases. Typically, monodisperse quasi-spherical crystals of 2.5± 0.3 nm in diameter are produced after refluxing for 10 min (Figure 6.1a). The crossed lattice is clearly visible (upper inset of Figure 6.1a) and the interplanar distance was measured to be 0.31 nm, which corresponds to the (222) planes of cubic Gd_2O_3. The X-ray diffraction (XRD) pattern (Figure 6.2a) is consistent with the body-centered cubic structure of gadolinium oxide (JCPDS File No. 00-011-0604). However, it is noted that the symmetry is probably pseudocubic as the peak shape of the (222) reflection is anisotropic. The wide diffraction peaks are consistent with nanocrystallite size, with Scherrer line-width analysis yielding a domain diameter of 2.6 nm, in agreement with TEM. As refluxing progresses, nanocrystals evolve into nanorods and after 30 min, a few nanosized oligomers and nanorods are observed (Figure 6.3). After 1 h, most of the nanocrystals are fused into nanorods (Figure 6.4) and after 2 h the evolution is essentially complete (Figure 6.1b). The Gd_2O_3:RE^{3+} (RE= Tb, Yb/Er) nanorods display preferred growth on (222) planes (right inset of Figure 6.1b) that matches well with XRD (Figure 6.2b), where the (222) reflection is enhanced compared to the nanocrystals. Selected area electron diffraction (SAED) from nanorod agglomerates (lower inset of Figure 6.1a) can be indexed as cubic Gd_2O_3:RE^{3+} with (222), (440) and (622) diffraction rings at real space interplanar distances of 0.31 nm, 0.19 nm, and 0.16 nm respectively. The strongest intensity of (222) diffraction ring may provide further evidence of a preferred orientation to that direction as well. For Dy_2O_3:RE^{3+} (RE= Tb, Yb/Er), the preferential growth direction of the nanorods is found on (440) planes. The HRTEM, XRD, and SAED results for the Dy_2O_3:Tb^{3+} nanorods are shown in Figure 6.5 as representative sample. Energy dispersive X-ray (EDX) analysis was conducted for Tb^{3+}-doped Gd_2O_3 and Dy_2O_3. The EDX results are shown in Figure 6.6. The C and Cu peaks are resulted from surfactant oleic acid and copper grid used for TEM, respectively. The analysis suggests molar ratio of Tb in Gd_2O_3, and Dy_2O_3 is 10.1 and 8.9 mol% respectively.

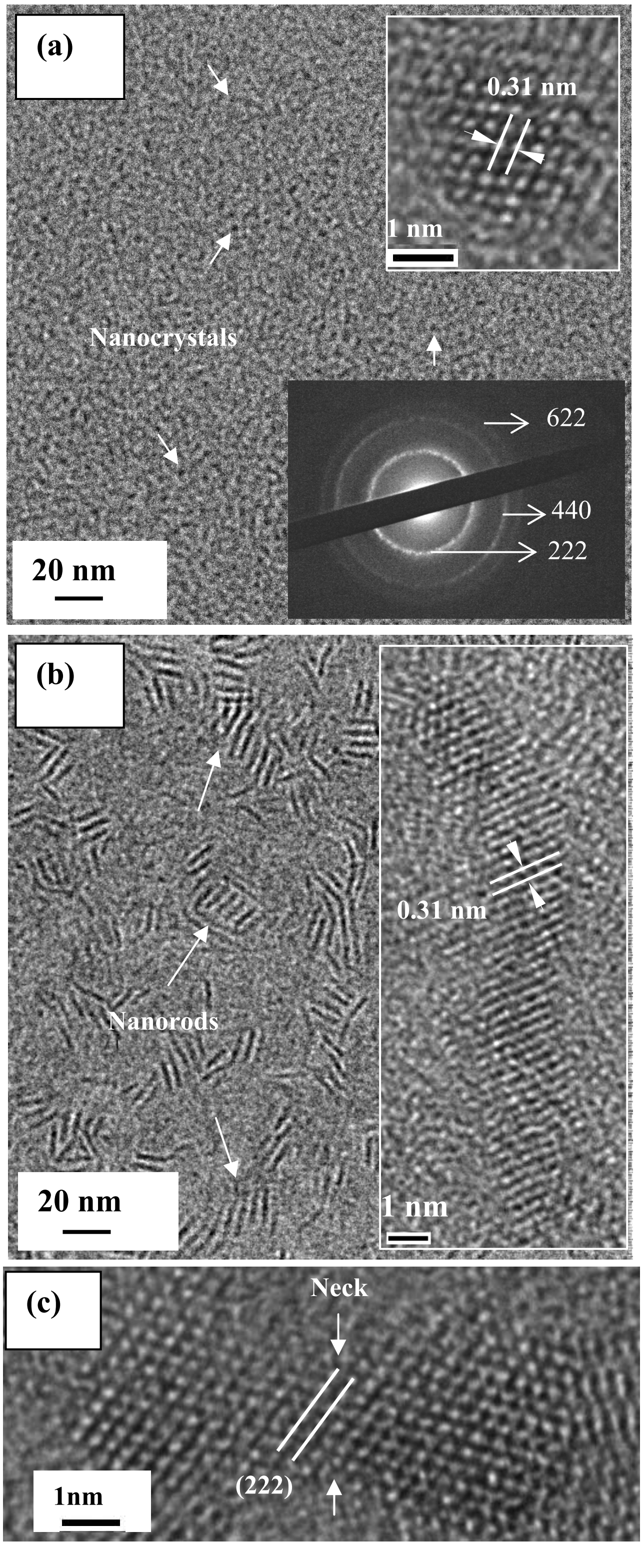

Figure 6.1 (a) Typical TEM images of monodispersed $Gd_2O_3:RE^{3+}$ (RE= Tb, Yb/Er) nanocrystals; Upper inset: HRTEM of a single nanocrystal; Lower inset: SAED pattern obtained for $Gd_2O_3:RE^{3+}$ nanorods; (b) Typical TEM image of monodispersed $Gd_2O_3:RE^{3+}$ (RE= Tb, Yb/Er) nanorods. Inset: HRTEM image of a single nanorod showing interplanar distance equivalent to (222) planes; (c) HRTEM image of a dimer fused together, creating a neck.

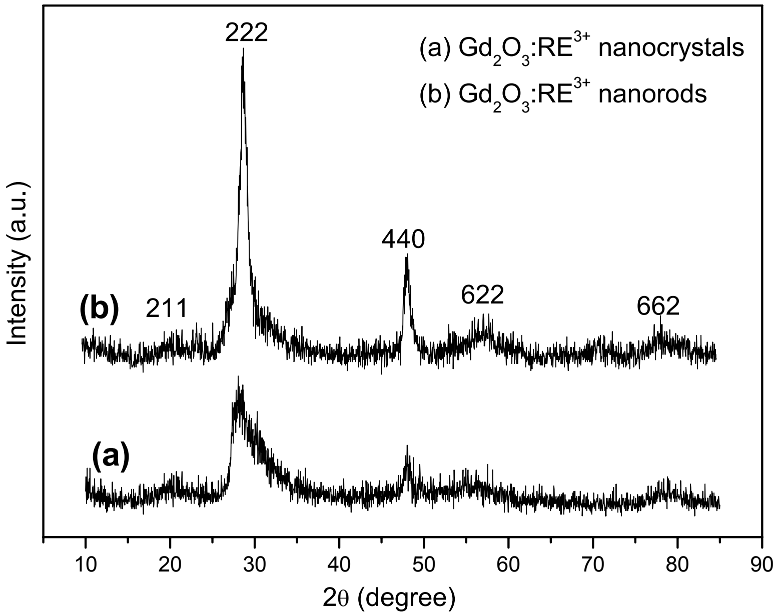

Figure 6.2 XRD patterns of $Gd_2O_3:RE^{3+}$ (RE= Tb, Yb/Er) (a) nanocrystals; (b) nanorods.

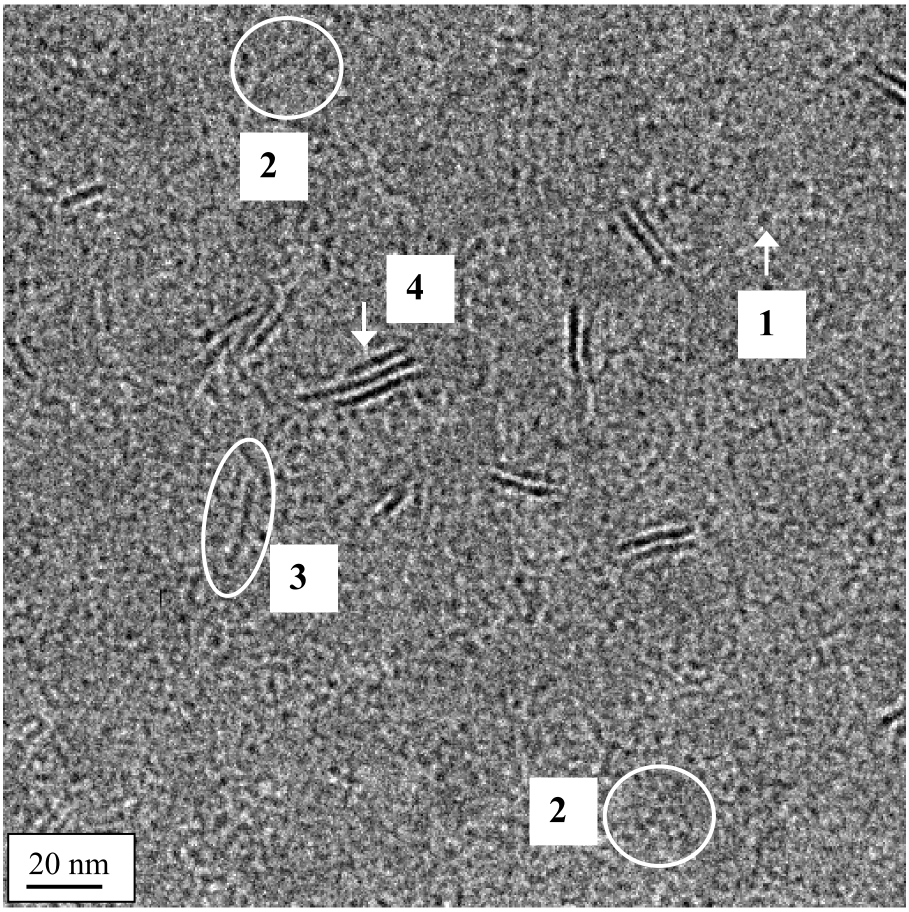

Figure 6.3 $Gd_2O_3:RE^{3+}$ samples after 30 min of reflux. Region (1): One of the many nanocrystals present in the solution; (2): A few nanocrystals fusing to form oligomer; (3): Oligomer produced after nanocrystals fusion, creating necks with adjacent nanocrystals; and (4) As-formed ultra-narrow nanorods.

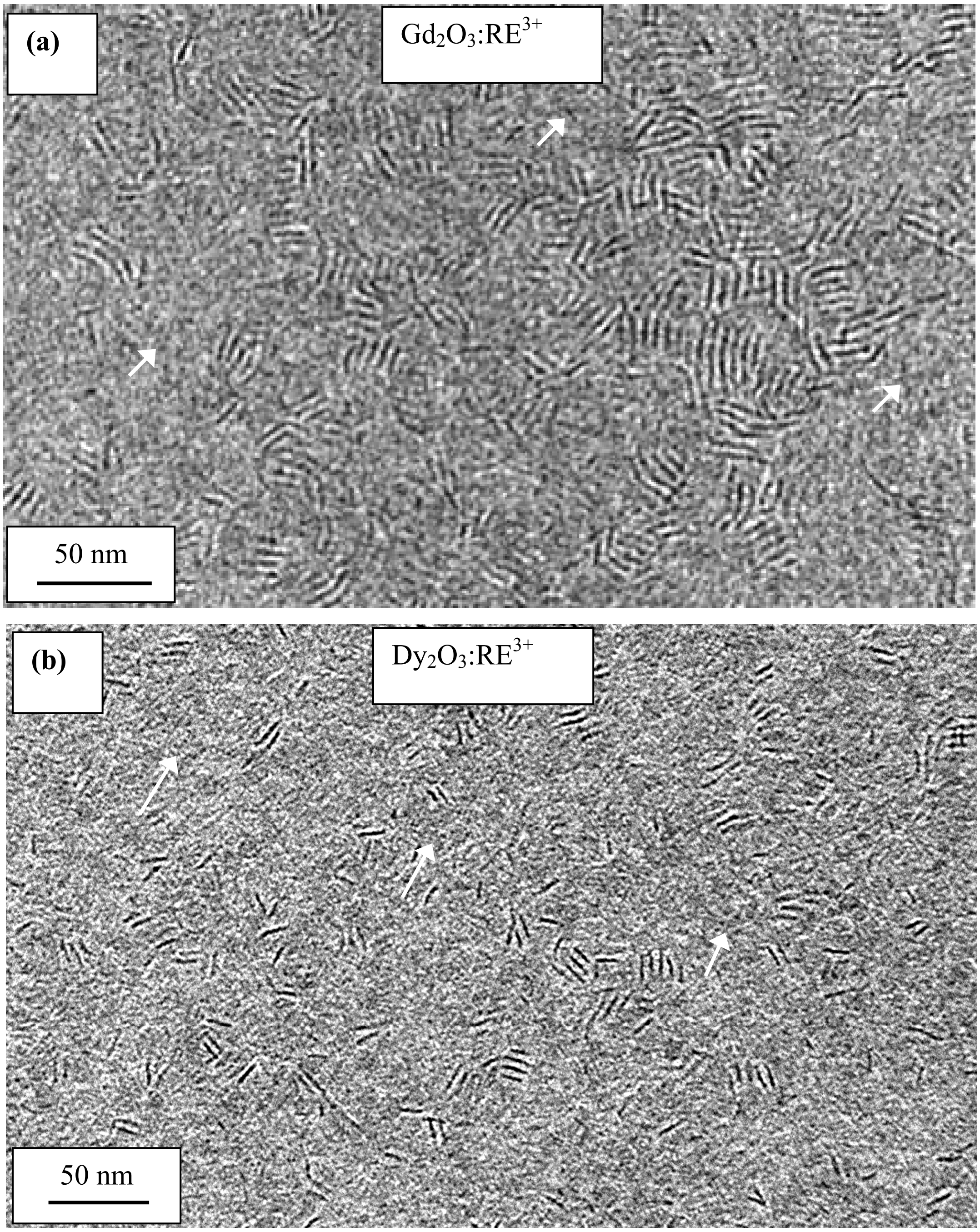

Figure 6.4 Typical TEM images of samples after 1 h of reflux (a) Gd_2O_3:RE^{3+} (RE= Tb, Yb/Er); (b) Dy_2O_3:RE^{3+} (RE= Tb, Yb/Er). The arrows indicate the presence of a few nanocrystals amongst the nanorods.

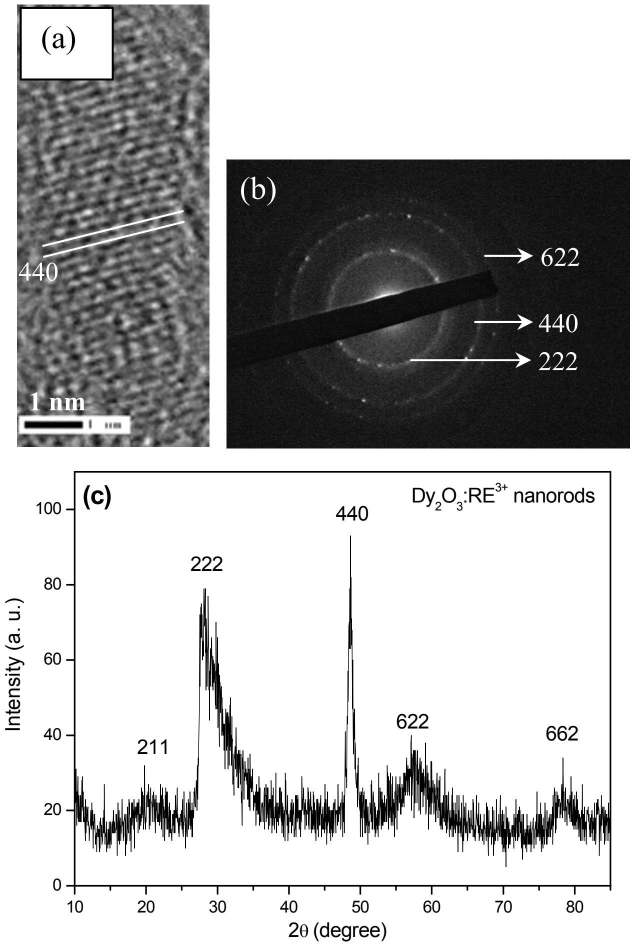

Figure 6.5 (a) HRTEM of a single $Dy_2O_3:Tb^{3+}$ nanorod showing interplanar distance equivalent to (440) planes; (b) SAED pattern obtained for $Dy_2O_3:Tb^{3+}$ nanorods; and (c) XRD pattern of $Dy_2O_3:Tb^{3+}$ nanorods (JCPDS File No. 00-022-0612).

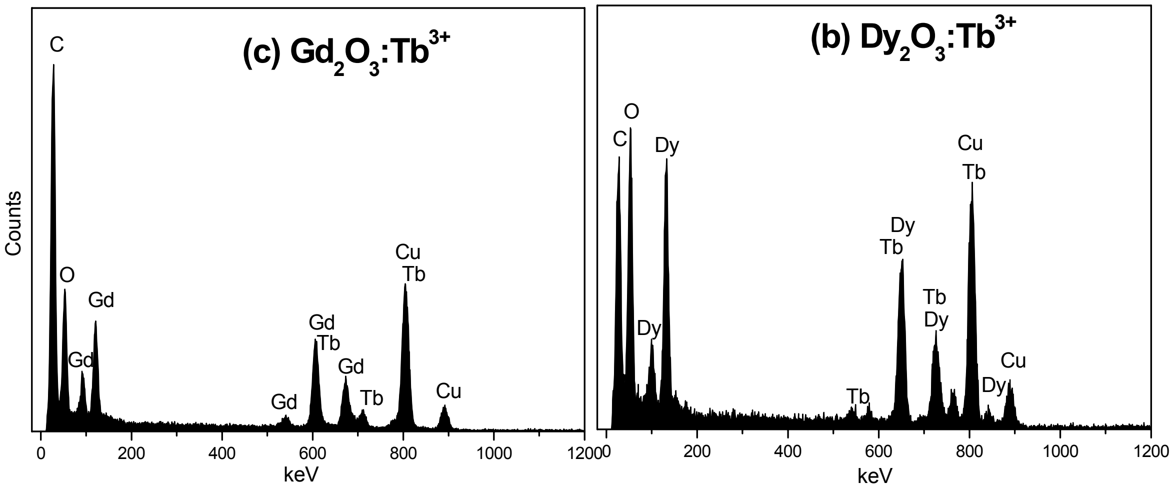

Figure 6.6 Energy dispersive X-ray (EDX) analysis of: (a) $Gd_2O_3:Tb^{3+}$; and (b) $Dy_2O_3:Tb^{3+}$ nanorods.

6.3.2 Study of Nanorods Formation Mechanism

The coalescence of two individual $Gd_2O_3:Tb^{3+}$ nanocrystals by crystallographical orientation and fusion is depicted in Figure 6.1c, where oriented attachment takes place on (222) planes. This topotaxial creates a neck with fusion along the <111> axis. When many nanocrystals fuse in this fashion, necklace-like chains are created (Figure 6.7). The formation of pearl necklace-like chains of diameter equal to that of a single nanocrystal evidenced the oriented attachment mechanism.[217] Oriented attachment is a mechanism for many different materials to form one-dimensional nanostructures.[215, 217, 269-271] Differences in crystal surface reactivity or dipolar interactions have been proposed as the main driving forces for 1D growth. For the current RE oxide nanocrystals, we believe the latter is the most probable cause of chain assembly. The dipole moments along the <111> and <110> axes induce the alignment of the nanocrystals in $Gd_2O_3:RE^{3+}$, and $Dy_2O_3:RE^{3+}$ respectively. The oleylamine ligands adsorbed on the nanocrystals surface, which provide steric stabilization and prevent aggregation, change the growth kinetics and surface energies of the crystal facets leading to anisotropic structures. [271] The role of dodecylamine and hexadecylamine as ligating solvents was also investigated, but they did not promote uniform nanorods formation as shown in Figure 4.3 for $Y_2O_3:RE^{3+}$ nanorods (section 4.3.1.3). Based on the analogous observations for all $Y_2O_3:RE^{3+}$, $Gd_2O_3:RE^{3+}$, and $Dy_2O_3:RE^{3+}$, a simple scheme has been devised to elucidate the pattern of the growth mechanism of these nanorods as shown in Figure 6.8. First, the nanocrystals form extended chains due to dipolar attractions are stabilized by oleyamine. Second, the chains fuse longitudinally and recrystallize into single crystal ultranarrow nanorods. The fusion of nanocrystals eliminates curved spheroid surfaces, which is an enthalpy favourable process.[213] Third, filling of the necks takes place by conventional dissolution and growth of monomers.[270]

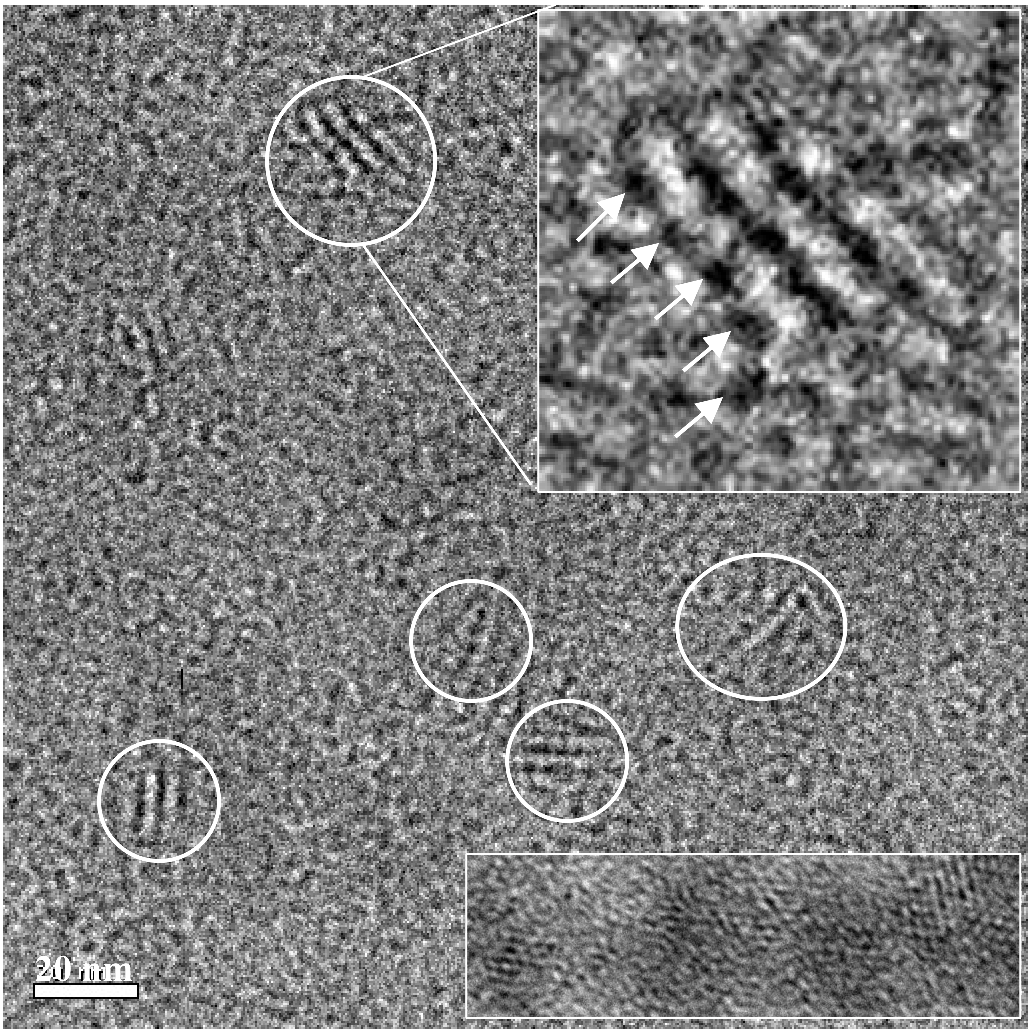

Figure 6.7 TEM images of samples at early stage of growth showing formation of pearl necklace-like chains. The marked circles show regions where chains of nanocrystals are observed. Upper inset: The magnified portion of the indicated region. Each arrow indicates individual nanocrystal forming into chain. Lower inset: Fusion of nanocrystals.

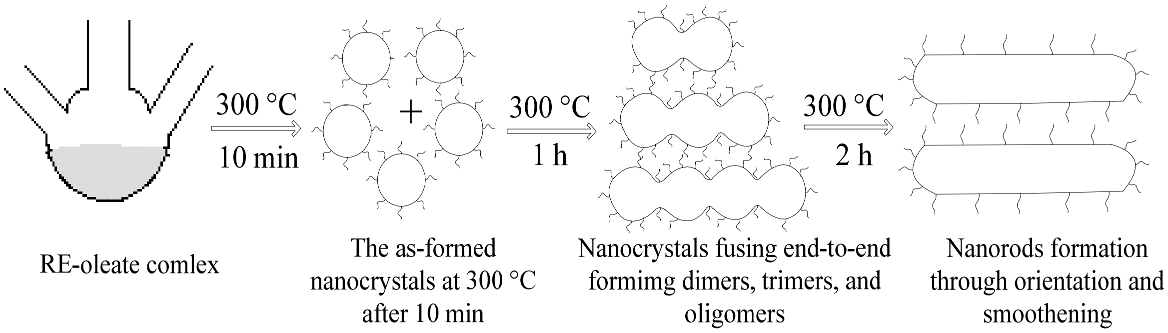

Figure 6.8 Proposed mechanism of the nanorods formation by oriented attachment.

6.3.3 Room Temperature Down- and Up-conversion Fluorescence of the Doped RE Oxides

The room temperature photoluminescence (PL) spectra of the Tb^{3+}- doped Gd_2O_3 and Dy_2O_3 nanorods excited at 235 nm shows down-conversion emission for both RE oxides (Figure 6.9a). The characteristic emission peaks of Tb ions appear at 489, 545, 585, and 619 nm from $^5D_4 \rightarrow {}^7F_j$ (j = 6, 5, 4, 3) transitions respectively;[221] the strongest green emission at 545 nm corresponds to the $^5D_4 \rightarrow {}^7F_5$ transition. To demonstrate the versatility of RE doping approach for up-conversion emission, we codoped the nanorods with Yb^{3+} and Er^{3+} ions. The up-conversion luminescence of Yb^{3+}/Er^{3+}-codoped Gd_2O_3 nanorods at 980 nm excitation is shown in Figure 6.9b. The up-conversion spectrum shows characteristic Er^{3+} green emissions at 520 and 539 nm which can be assigned to $^2H_{11/2} \rightarrow {}^4I_{15/2}$ and $^4S_{3/2} \rightarrow {}^4I_{15/2}$ transitions respectively. The dominant red emission appears between 651 and 667 nm is due to $^4F_{9/2} \rightarrow {}^4I_{15/2}$ transitions.[222] No up-conversion luminescence was observed for Yb^{3+}/Er^{3+}-codoped Dy_2O_3 as Dy^{3+} ions are reported to behave as poisonous centers in the Yb-Er, Yb-thulium(Tm), or Yb-holmium(Ho) up-converting codopants.[272]

Figure 6.10a shows a digital photograph of a Tb^{3+}-doped RE oxides solution emitting green color at the point of excitation which is due to its dominant green emission while Figure 6.10b shows a photograph of the up-conversion luminescence of the nanorods which appears red due to dominant red emission over green.

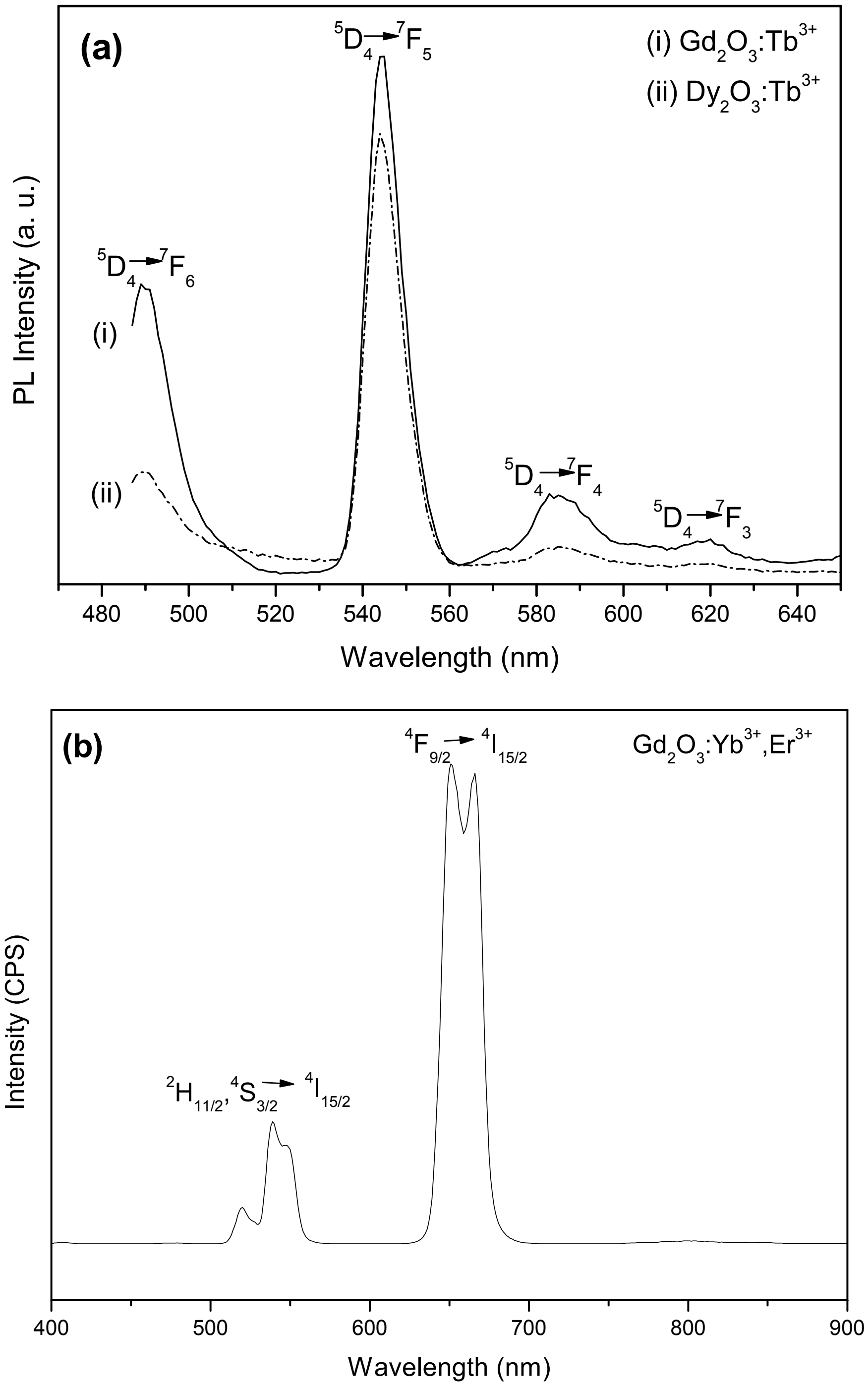

Figure 6.9 Room temperature (a) down-conversion luminescence spectra of Tb^{3+}-doped Gd_2O_3, and Dy_2O_3; (b) up-conversion luminescence spectra of Yb^{3+}/Er^{3+} codoped Gd_2O_3.

(a)

(b)

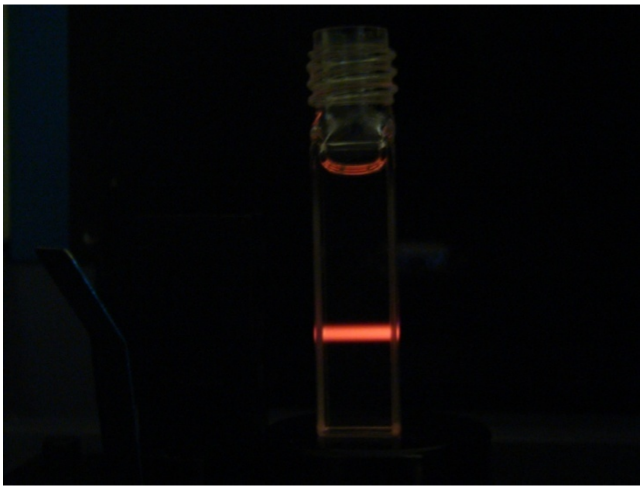

Figure 6.10 Digital photograph of (a) a down-converting Tb^{3+}-doped Gd_2O_3 solution emitting green color at the point of 235 nm excitation; (b) a up-converting Yb^{3+}/Er^{3+}-codoped Gd_2O_3 solution emitting red color at 980 nm excitation.

6.3.4 Magnetic properties

6.3.4.1 The Room Temperature Magnetization Curve

The room temperature magnetization (M) plots of $Gd_2O_3:RE^{3+}$ (RE = Tb, Yb/Er), and $Dy_2O_3:RE^{3+}$ (RE = Tb, Yb/Er) as a function of applied field (H) (-10 to +10 kOe) shows a linear correlation that suggests both are paramagnetic (Figure 6.11). The magnetization is 2.46 and 2.15 emu/g for the $Gd_2O_3:RE^{3+}$, and $Dy_2O_3:RE^{3+}$ nanorods respectively at 10 kOe. As a comparison, the room temperature magnetization value reported by Huang *et al.*[52] is ~1.25 emu/g (at 10 kOe) for 200 nm porous Gd_2O_3 while magnetization of 0.75 emu/g (at 300 K , and at 15 kOe) for polyethylene glycol-covered 3 nm Gd_2O_3 is reported by Fortin *et al.*[109]

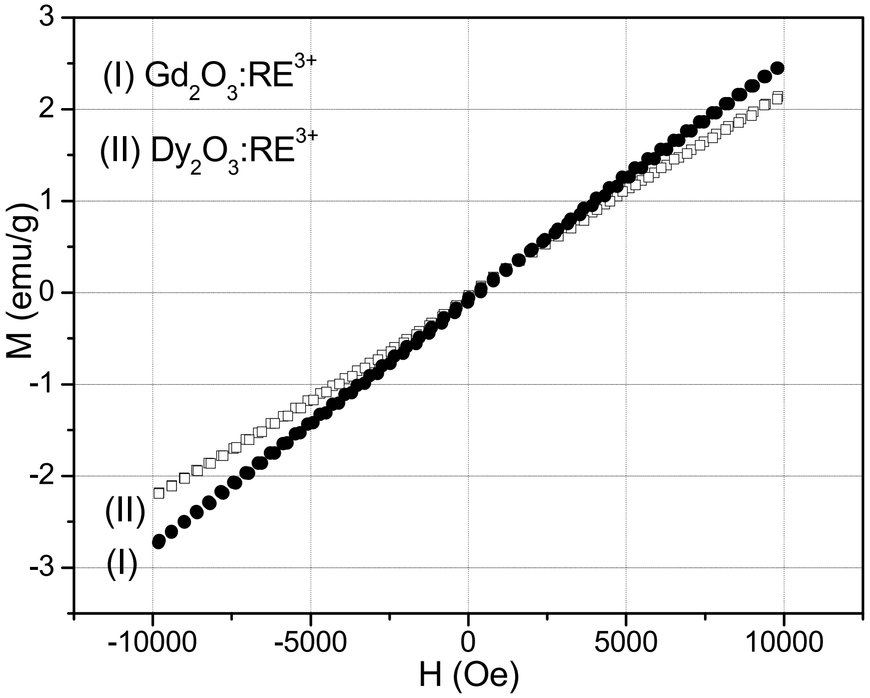

Figure 6.11 Typical room temperature magnetization plots of (i) $Gd_2O_3:RE^{3+}$ (RE = Tb, Yb/Er); and (ii) $Dy_2O_3:RE^{3+}$ (RE = Tb, Yb/Er).

6.3.4.2 T_1-weighted MRI Imaging

To examine the potential application of nanorods as MRI contrast agents, T_1-weighted images were acquired, and T_1-relaxation times measured *in vitro* for $Gd_2O_3:Yb^{3+},Er^{3+}$ nanorods on a Varian 9.4T MRI system in 1% agarose gel. As shown in Figure 6.12, the T_1-weighted MR images of $Gd_2O_3:Yb^{3+},Er^{3+}$ showed signal enhancement with increasing concentration. In addition, the longitudinal relaxation time (T_1) and the specific relaxivity (change in relaxation rate per unit concentration of an agent, r_1) was determined to be 665 ms and 1.5 $s^{-1}mM^{-1}$, respectively (Figure 5.13a). These values were compared with Gadovist^{TM}, a commercial Gd-based contrast agent. The observed T_1-weighted images (Figure 6.12) for Gadovist^{TM} reveals that the image contrasts of the nanorods closely mimic that of the Gadovist^{TM}. The longitudinal relaxation time (T_1) and relaxivity (r_1) of Gadovist^{TM} obtained are 230 ms and 4.34 $s^{-1}mM^{-1}$, respectively (Figure 6.13b). These results suggest that the nanorods are good T_1 contrast agents.

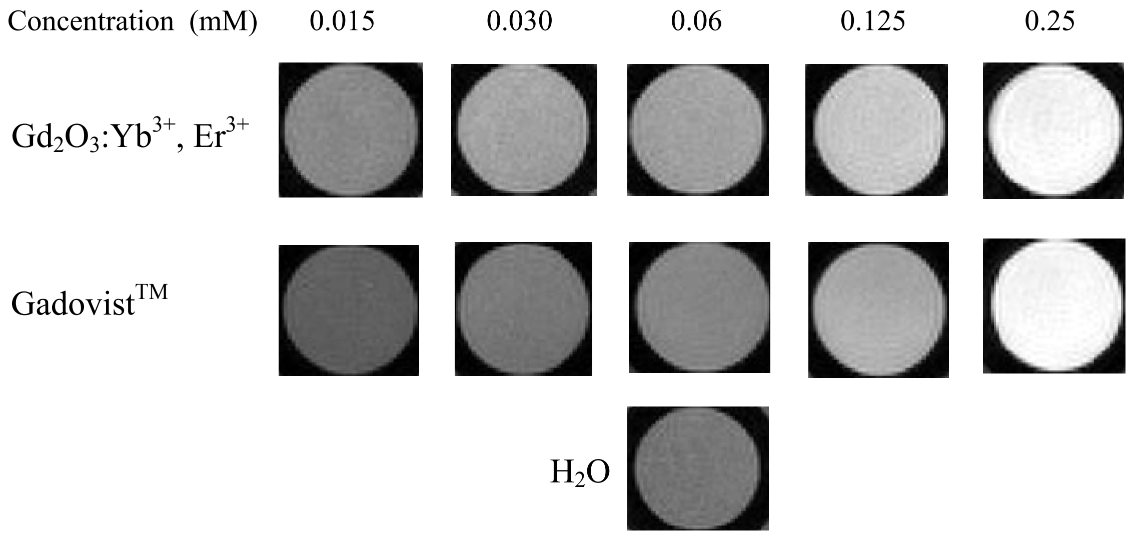

Figure 6.12 T_1-weighted images of $Gd_2O_3:Yb^{3+},Er^{3+}$ and Gadovist^{TM} at various Gd^{3+}concentrations. T_1-weighted image of water sample is shown for reference.

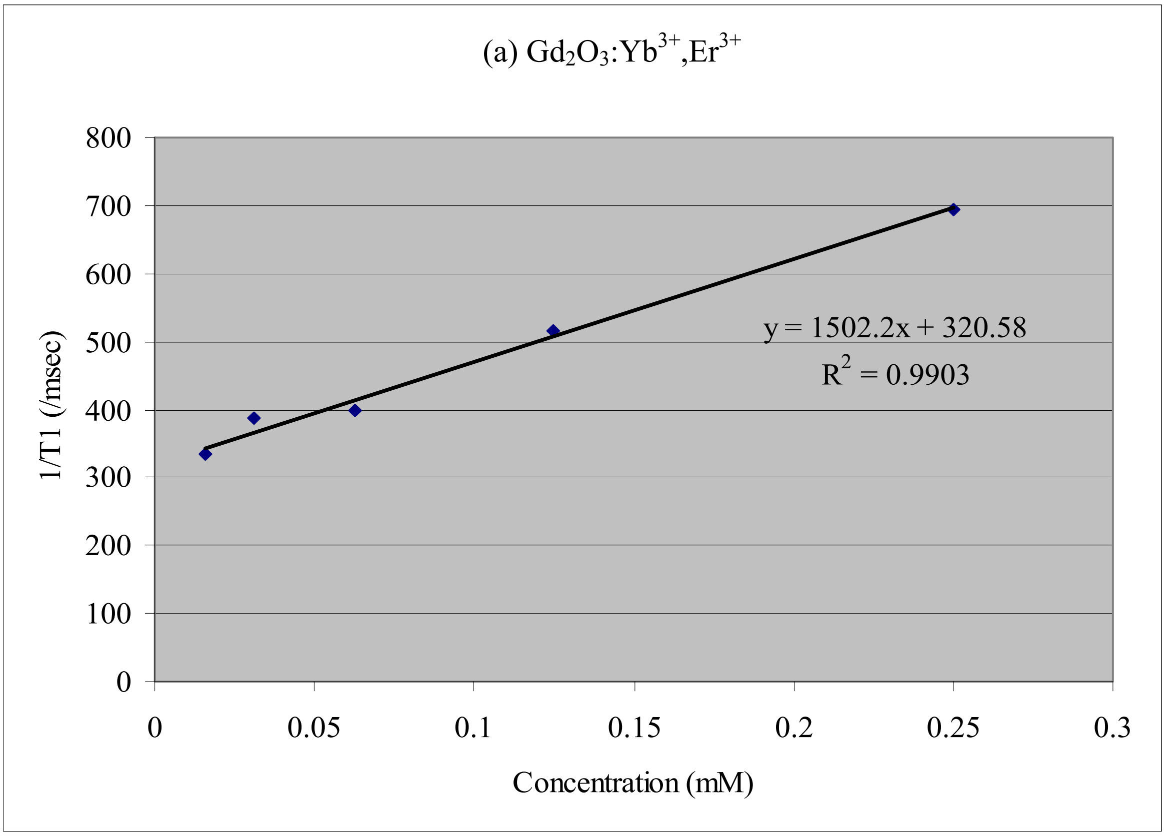

(a) $Gd_2O_3:Yb^{3+},Er^{3+}$

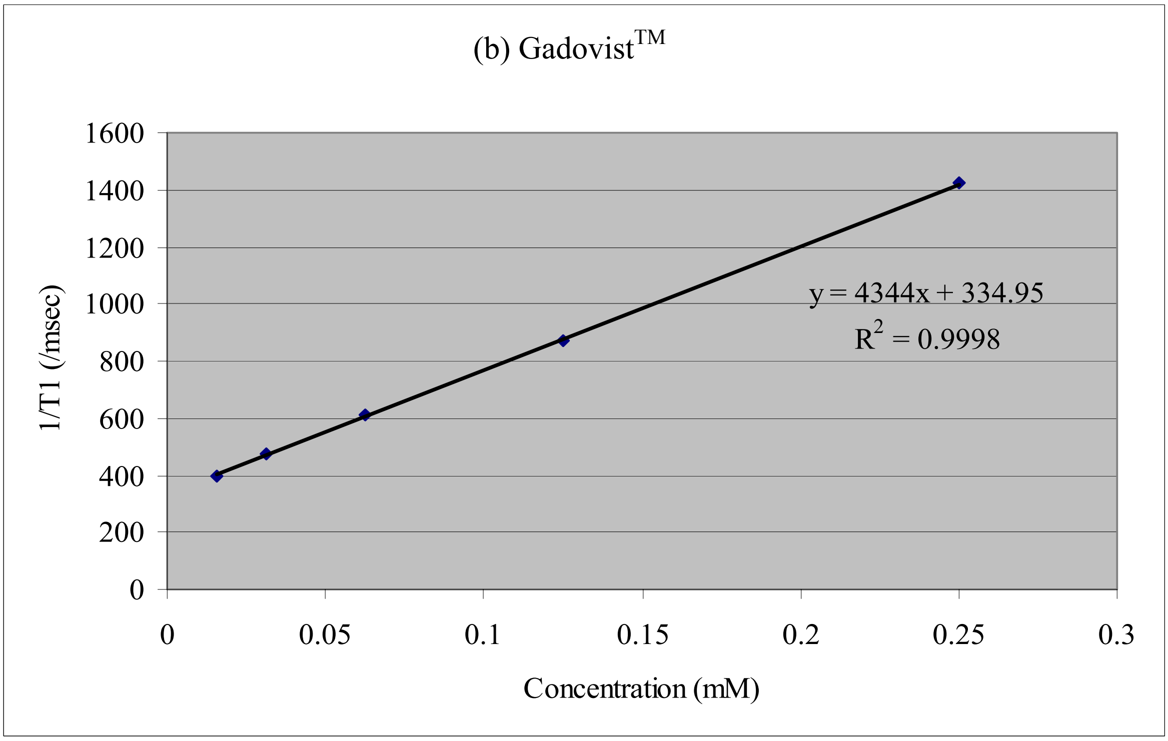

(b) Gadovist^{TM}

Figure 6.13 The relaxivity (r_1) curves obtained using various concentrations of (a) $Gd_2O_3:Yb^{3+},Er^{3+}$ nanorods, (b) Gadovist^{TM} in 1% agarose gel.

6.4 Conclusion

In summary, a facile synthetic strategy has been developed to produce single-phase bifunctional RE^{3+}-doped Gd_2O_3 and Dy_2O_3 nanocrystals and nanorods with tunable optical (down- or up-conversion luminescence), and magnetic (paramagnetism) properties. More importantly, the Yb^{3+}/Er^{3+}-codoped Gd_2O_3 nanorods exhibit good T_1-weighted MRI contrast, comparable to the commercial product. The general synthesis strategy obtained for RE^{3+}-doped Y_2O_3, Gd_2O_3 and Dy_2O_3 nanorods also suggest that the synthesis method could be generalized to other types of RE oxide hosts and dopants. The simplicity and ease of the methodology to fabricate single-phase magnetic-fluorescent rare earth nanomaterials could potentially lead to the realization of a range of bifunctional architectures, as well as contrast agents in integrated imaging technologies, whereby MRI and florescence microscopy can be combined to provide higher resolution and contrast in tissue and cellular imaging.

CHAPTER 7

in vitro Cytotoxicity Evaluation of the Nanoparticles and Their Extracts

7.1 Introduction

The development of nanotechnology has resulted in a wide array of nanomaterials. Many of these nanomaterials have been proposed for biomedical applications and have drawn enormous attention in recent years.[10, 273-274] Assessment of their potential toxicity is a key concern in bioapplications since exposure to toxic nanomaterials may lead to detrimental consequences. Although the type of nanoparticle and their proposed applications continues to increase, studies to characterize their effects after exposure and to address their potential cytotoxicity are few in comparison.[156-158, 275] Currently, there is no uniform way of assessing nanoparticle cytotoxicity *in vitro*. The development of a standard protocol for nanoparticle toxicity evaluation is an urgent need.

Nanoparticles used in bio-imaging and drug delivery are often bioconjugated to target specific cells. Since nanoparticles are engineered to interact with cells, it is important to ensure that they do not cause any adverse effects. For example, nanoparticles may accumulate within cells and lead to intracellular changes such as disruption of organelle integrity or gene alterations.[157] Semiconductor nanocrystal quantum dots (QDs) have shown promise in biological labelling for their robustness and bright emission.[11, 44] Most of the studies regarding potential cytotoxicity of QDs revealed that the core metal constituents of QDs are toxic.[163] If the QDs are exposed to conditions promoting

---

Much of this chapter has published in *Journal of Biomedical Materials Research* 2010, 93A, 337-346. Reproduced with permission. Copyright 2010 John Wiley & Sons, Inc.

degradation, such as an oxidative environment, free metal ions are leached out and released from the core, causing toxicity. One of the strategies to reduce QDs toxicity is to protect the core from degradation by surface-coatings – a layer of ZnS or a silica shell. However, the coating might only be a partial solution since the release of Cd over prolonged period of time has not been studied comprehensively.[11] Superparamagnetic iron oxide nanoparticles with tailored surface chemistry have been used in numerous applications such as magnetic resonance imaging (MRI) contrast enhancer, hyperthermia, drug delivery, cell separation etc.[13] as discussed in chapter 4. In terms of cytotoxicity, bare iron oxide nanoparticles exert some toxic effects while surface coated nanoparticles, especially PEG coated nanoparticles, have been found to be relatively nontoxic.[29] In recent years, rare earth (RE) doped nanomaterials has gained attention as a potential bioimaging probes. One of the reasons is due to its up-conversion ability which is a nice window for deep tissue imaging.[276] However, to the best of our knowledge, there are limited studies on the investigation of the cytotoxicity of the RE-doped inorganic nanocrystals.

In this chapter, we present a new approach of evaluating the toxicity of nanoparticles by *in vitro* cell viability testing. This method is based on American National Standard ISO 10993-5 which describes test methods to assess *in vitro* cytotoxicity of medical devices through extracts and direct contact of the device. Hepatoma HepG2 and fibroblast NIH3T3 cell lines were incubated with nanoparticles and their associated extracts derived at 70 and 121 °C. Nanoparticles proposed as potential biomedical imaging probes were evaluated based on the detection of metabolic activities and cell morphology changes. The Alamar Blue assay was selected to measure quantitatively the proliferation and cytotoxicity of nanoparticles-treated human cell line. This is because Alamar Blue is non-toxic and therefore less likely to interfere with normal metabolism. In addition, the one-step Alamar Blue assay is simple to use. Alamar Blue can be reduced by $FMNH_2$, $FADH_2$, NADH, NADPH, and cytochromes, where the most commonly used tetrazolium salt (MTT) assay can be reduced by all the above substance except cytochromes. Innate metabolic activity of cells results in a chemical reduction of Alarmar Blue, and causes this redox indicator to change from its blue color oxidized form to reduced form in red color.[277] Cells exposed to compounds that induce cytotoxcity will rapidly lose metabolic capacity, and do not reduce this REDOX indicator. Therefore, the absorbance from Alamar Blue is proportional to the number of viable cells. We believe that this new approach could contribute towards the goal of a generalized and systematic evaluation of toxicity of nanomaterials for biomedical application. Here, we have chosen nanoparticles that have been proposed as bioimaging probes as model samples such as semiconductor nanocrystals (CdSe and CdSe@ZnS quantum dots), γ-Fe_2O_3:Tb^{3+}, and Y_2O_3:Er^{3+}, Y_2O_3:Yb^{3+},Er^{3+} nanocrystals. These nanoparticles were amine-functionalized to render them dispersible in water, since it has been reported that QDs surface functionalized with amine groups were less cytotoxic.[242] It should be noted that Y_2O_3:RE^{3+} (RE = Er, Yb/Er) nanocrystals were taken as the representative samples from the three doped RE oxides (i.e. Y_2O_3, Gd_2O_3, Dy_2O_3), and hence we will compare the cell viability results of the QDs, and the Tb^{3+}-doped iron oxides with Er^{3+}, and Yb^{3+}/Er^{3+} doped Y_2O_3 nanocrystals. Cytotoxicity studies for Gd_2O_3:RE^{3+} and Dy_2O_3:RE^{3+} nanocrystals will be reported in the future.

7.2 Experimental Section

7.2.1 Chemicals

Ytterbium (III) chloride hexahydrate (99.99%), erbium (III) chloride hexahydrate (99.9%), tetramethylammoniumhydroxide (TMAH; 25 wt% in methanol), 1-octadecane (tech., 90%), Igepal CO-520 (Polyoxyethylene(5)nonylphenylether), diethylzinc (1.0M solution in hexanes), trioctylphosphine oxide (TOPO; 99%), and oleylamine (tech., 70%), were purchased from Aldrich. Yttrium oxide (99.99%), Iron (III) chloride hexahydrate (98%), selenium powder (99%), HNO_3 (analytical reagents, 70%), n-octadecylphosphonic acid, and oleic acid (tech., 90%) were purchased from Alfa Aesar. 3-aminopropyltrimethoxysilane (APS; 97%), NaOH (reagent grade, 97%, beads), trioctylphosphine (TOP; 90%), hexamethyl disilthiane were purchased from Fluka. Cadmium oxide (99%) was purchased from Hayashi Pure Chemicals Ind. Ltd. Dulbecco's Modified Eagle's medium (DMEM) and penicillin were purchased from Biochrom AG. l-glutamine was purchased from JRH Biosciences, Inc. Phosphate-Buffered Saline (PBS) (1x, containing 144 mg/L KH_2PO_4, 9000 mg/L NaCl and 795 mg/L $Na_2HPO_4.7H_2O$) and Fetal Bovine Serum (FBS) were purchased from Invitrogen Corporation. Ethanol, hexane, cyclohexane and chloroform were of analytical reagent grade and were used as received. Unless stated otherwise, reagents are used as received.

7.2.2 Synthesis and Functionalization of Nanoparticles

Red emitting CdSe and CdSe@ZnS QDs nanocrystals were synthesized based on the methods described in the literature.[252, 278] Single-phase magnetic-fluorescent Tb^{3+}-doped γ-Fe_2O_3 nanocrystals were synthesized based on a method developed by Park *et al.*[218] as described in chapter 5. Er^{3+}-doped and Yb^{3+}/Er^{3+}-codoped Y_2O_3 were prepared by reacting yttrium oxide powder, oleic acid, sodium hydroxide and RE-salts as described in the chapter 4. In every case, the as-synthesized nanoparticles were washed extensively 4-5 times using ethanol to obtain clean particles. Amine functionalization of the nanoparticles was conducted according to the process described by Selvan *et al.*[30]

7.2.3 Samples Preparation

Nanoparticle dosages of 0.0625, 0.10 and 0.25 mg/ml, which are typically used in *in vitro* experimentation, were used to prepare extracts at 37, 50, 70 and 121 °C. A dosage of 0.25 mg/ml is approximately double that used by Jaiswal *et al.*[184] for the labeling of HeLa cells, and roughly 60 times higher than the concentrations used by Wu *et al.*[279] for targeting Her2 epitopes on breast cancer cells. However, it is 4 times less than that used by Derfus *et al.*[163] Three types of nanoparticle sample solutions at the three different sample dosages were prepared with the synthesized nanoparticles: (1) Direct dispersion in PBS, (2) formation of nanoparticles extract at 70 ˚C for 24 h in PBS, and (3) formation of nanoparticles extract at 121˚C for 1 h in PBS. Samples from (1) were used in the direct contact method (DC) of which the nanoparticles were incubated directly with the cells at 37 °C. Samples from (2) and (3) were extract samples and were prepared according to the American National Standard ISO 10993-5. It should be noted that the Standard proposes 4 extraction conditions at 37, 50, 70 and 121 ˚C. The higher temperature conditions at 50, 70 and 121 ˚C are accelerated test conditions used to determine what might be expected at longer time periods at a body temperature of 37 ˚C. However, we have only found ions present at 70 and 121 ˚C and hence have only reported results based on these extraction conditions. The cells (HepG2 and NIH3T3) were then exposed to the above described extracts and nanoparticles for different exposure times (24, 48, and 72 h).

7.2.4 Cell Culture and Viability

Human hepatocellular liver carcinoma (HepG2), and mouse embryonic fibroblast (NIH3T3) cells were used for cell viability tests. Cells were cultured in DMEM, supplemented with 10% FBS, and 1% penicillin/streptomycin at 37 °C in a humidified incubator with 5% CO_2. The cells were seeded in 96-well plates with a concentration of 10,000 cells/well. Twenty-four hours after seeding, spent media was removed and replaced with fresh media. The nanoparticle samples prepared as described in section 7.2.3 were then added, followed by incubation for 24, 48 or 72 h. Control experiments of which no nanoparticle samples were added were also prepared for comparison purposes. Cell viability tests were performed using Alamar Blue^{TM} assays (Biosource, USA) to evaluate cell proliferation based on detection of metabolic activities. The tests were repeated three times for each experimental condition to ensure reproducibility.

7.2.5 Characterization

Transmission electron microscope (TEM) images were obtained on a JEOL 3010 electron microscope operating on 200 kV. Photoluminescence (PL) spectra were collected on a Shimadzu RF-5301 PC Spectrofluorophotometer using 150 W Xenon lamp as an excitation source. Cell morphologies were observed with a Motic AE21 microscope. The concentrations of Cd, Se, Zn, Fe, Tb, Yb and Er ions in the extract solutions were determined using High Dispersion Induction Coupled Plasma-Atomic Emission Spectroscopy (ICP-AES) (Teledyne Prodigy). For analysis using ICP-AES, the samples were dispersed in a 2% nitric acid solution.

To reduce any possible influence of the nanoparticles size and morphology on cytotoxicity, monodisperse and similar size spherical nanocrystals were taken. The size of the Y_2O_3:RE^{3+}, CdSe QDs, and γ-Fe_2O_3:Tb^{3+} measured to be around 3, 6, and 7 nm respectively. TEM images and luminescence properties of the Y_2O_3:RE^{3+} (RE = Er, Yb/Er) nanoparticles have been shown in chapter 4, while the TEM image and photoluminescence spectra of the CdSe nanocrystals are shown in Figure 7.1. Figure 7.1c shows the as-synthesized 7 nm bifunctional γ-Fe_2O_3:Tb^{3+} nanocrystals for cytotoxicity study.

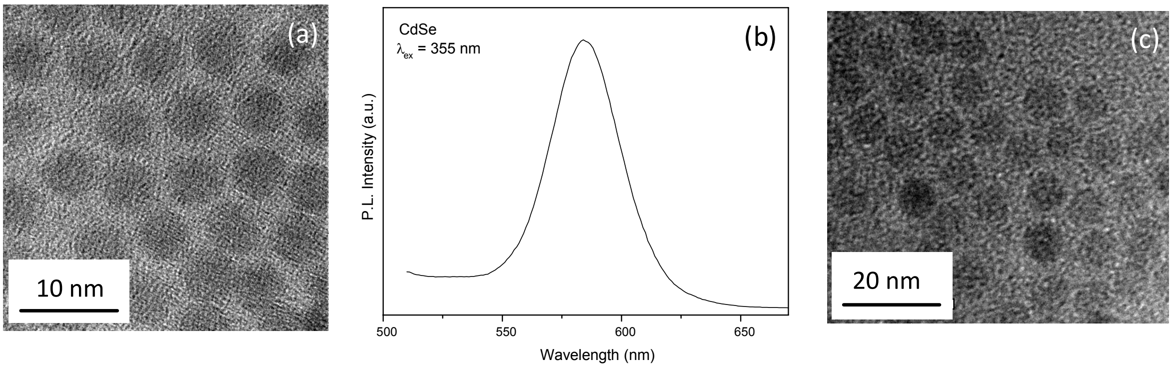

Figure 7.1 (a) TEM image of CdSe quantum dots synthesized for cytotoxicity study. Inset shows a single quantum dot; (b) PL spectra of the quantum dots emitting at 585 nm; (c) TEM image of Tb^{3+}-doped γ-Fe_2O_3 nanocrystals for the cytotoxicity study.

7.2.6 Statistical Analysis

The results are presented as means ± standard deviation (SD). Responses of the cells to the nanoparticles were statistically analyzed using one-way analysis of variance (ANOVA). In all cases P values lower than 0.05 were considered statistically significant. Significant changes induced by samples are marked by asterisks in the figures.

7.3 Results

7.3.1 Nanoparticles Extracts

The ion concentration from the cell media exposed directly to the nanoparticles for 72 h, and the extracts formed at 70 and 121 °C is presented in Table 7.1. Extractions at 37 and 50 °C for 72 h, which were described in the standard, were also investigated. However, no ions could be detected in these extracts. For CdSe, CdSe@ZnS and γ-Fe_2O_3:Tb^{3+} nanoparticles, the highest ion concentration was found when the nanoparticles were exposed directly to the cells for 72 h. However, the concentration of RE ions was not significantly higher for the DC method. It is suggested that the harsher conditions at 121 °C resulted in more rare-earth ions leaching out compared to the DC method of which

Table 7.1 Ion concentrations of samples prepared under different conditions.

		Ion concentrations (ppm)			
		Cell medium (Direct contact method, 72 h after incubation at 37°C)			
Nanoparticle Samples	Ion Released	HepG2	NIH3T3	70 °C Extract	121 °C Extract
CdSe@ZnS	Cd	4.21	5.93	0.51	1.51
	Se	5.34	4.72	ND	3.32
	Zn	4.77	6.20	1.01	1.75
CdSe	Cd	8.41	10.53	2.11	5.11
	Se	9.22	8.87	ND	7.31
γ- Fe_2O_3:Tb^{3+}	Fe	5.23	6.41	1.89	4.48
	Tb	0.59	1.63	ND	1.42
Y_2O_3:Er^{3+}	Y	2.46	4.23	2.34	5.24
	Er	0.12	0.65	ND	1.92
Y_2O_3:Yb^{3+},Er^{3+}	Y	2.07	3.78	2.01	3.43
	Er	0.43	ND	ND	1.12
	Yb	ND	ND	ND	0.90

ND: Non-detectable (detection limit at 10 ppb).

the incubation took place at 37 °C. It is also notable that the amount of ions was generally higher in the NIH3T3 cell media.

7.3.2 *in vitro* Cytotoxicity Studies using HepG2 Cells

The exposure of the HepG2 cells at a concentration of 0.25 mg/ml with exposure duration of 72 h is the highest concentration and longest exposure time used respectively in the current study. This condition is referred to as the extreme condition. The HepG2 cells exposed to the extreme condition are shown in Figure 7.2. Out of the five types of nanoparticles, γ-Fe_2O_3:Tb^{3+}, Y_2O_3:Er^{3+}, and Y_2O_3:Yb^{3+},Er^{3+} studied via the DC method and their associated extracts produced minimal cytotoxicity, with cell viabilities observed to be almost 100%. The results obtained here are consistent with other studies where iron oxide was reported to be of little or no toxicity at low Fe concentration.[13, 180, 280] The presence of these nanoparticles, and the ions (Fe, Tb, Yb, Y, and Er) seem to pose minimal toxicity to HepG2 cells. The results obtained for cell viability were found to be statistically significant with respect to control and marked by asterisks in Figure 7.2. The data show different level of statistical significance categorized on the basis of their P value lower than 0.05, 0.01, and 0.001. CdSe and CdSe@ZnS QDs showed toxicity in the extreme condition with low cell viability using the DC method and with the 121 °C extract. Cells subjected to 70 °C extracts have shown comparatively higher cell viability. CdSe and CdSe@ZnS QDs showed toxicity in the extreme condition with cell viability as low as 19.2% ($P < 0.01$) and 23.1% ($P < 0.01$) respectively using DC method, and 57.5% ($P < 0.05$) and 62.5% ($P < 0.001$) respectively when subjected to their 121°C leachate. Cells subjected to 70 °C leachates have shown comparatively higher cell viability at 85.1% ($P < 0.05$) and 91.9% ($P < 0.06$) for CdSe and CdSe@ZnS respectively.

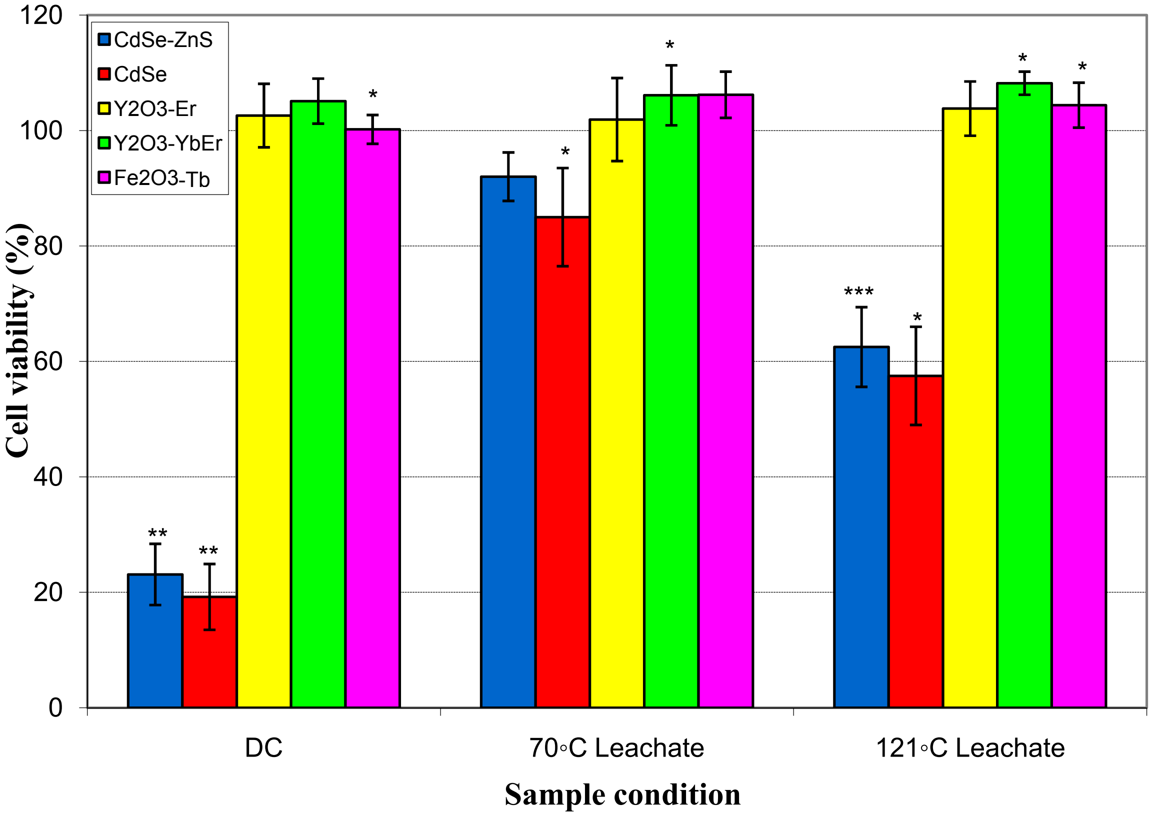

Figure 7.2 Cell viability of HepG2 cells at 0.25 mg/ml and 72 h exposure. Data are presented as mean ± SD for at least three independent experiments. Value statistically significant compared to control (ANOVA), $*P< 0.05$; $**P< 0.01$; $***P< 0.001$.

The observed changes of the cell morphology in Figure 7.3 are indicative of cytotoxicity. Figure 7.3a shows the confluency of HepG2 control cells. Hepatoma cells generally exhibited spindle-shape morphology. The morphology of the viable cells was similar to control cells when exposed to relatively non-toxic nanoparticles like $Y_2O_3:Er^{3+}$, $Y_2O_3:Yb^{3+},Er^{3+}$, and γ-$Fe_2O_3:Tb^{3+}$. However, changes in cell morphology were observed when low cell viability was encountered in the cases of DC method and 121 °C extract. For the case of

DC method subjected to CdSe@ZnS QDs, there were evidence of significant cell disruption and ubiquitous cell debris as shown in Figure 7.3b. For the case of cells subjected to 121 °C CdSe@ZnS extract, cell membranes showed "blebbling", cell volume was reduced, and cells were found to be sparsely packed Figure 7.3c.

We have further investigated the effects of higher nanoparticle concentration and longer exposure time using DC method and 121 °C extracts (Figure 7.4). Figure 7.4 indicates higher nanoparticles concentration and longer exposure time result in decrease in cell viability. For example, using DC method at 72 h incubation time, the cell viability decreased from 61.4% to 23.2% for increase in CdSe@ZnS nanoparticle concentration from 0.0625 mg/ml to 0.25 mg/ml (Figure 6.4a). Yet, longer exposure time also lead to decrease in cell viability. For instance, using DC method cell viability drops from 55.9% to 23.2% at exposure time of 24, and 72 h respectively for CdSe@ZnS nanoparticles (Figure 7.4a). Cells exposed to 121°C leachates shown similar results as well. For example, an increment of CdSe@ZnS dosage from 0.0625 to 0.25 mg/ml caused the cell viability declined from 79.2 to 62.5% (Figure 7.4b), corresponding to an increase of Cd ions concentration from 0.89 ppm to 1.51 ppm and indicating dose-dependent cytotoxicity.

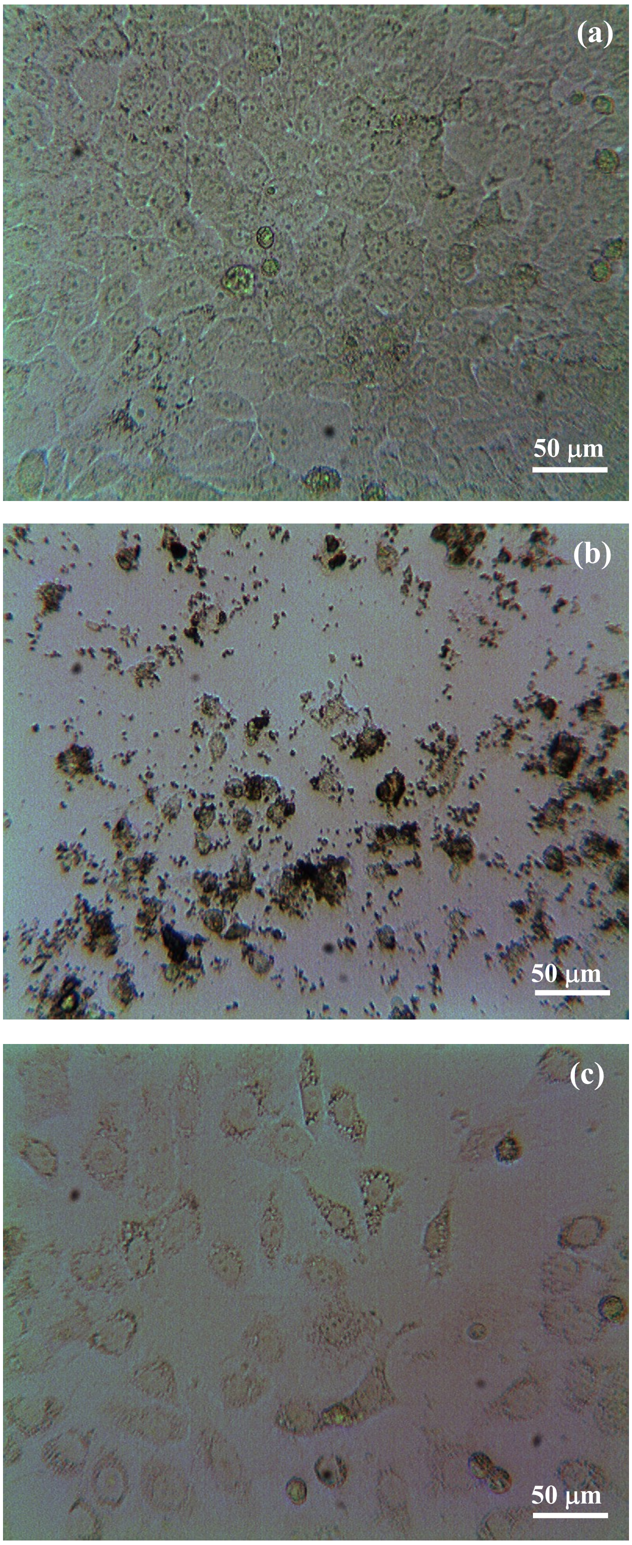

Figure 7.3 Morphology of HepG2 cells at 0.25 mg/ml and 72 h exposure observed under microscope: (a) control , (b) cells subjected to DC method with CdSe@ZnS, (c) cells subjected to 121 °C of CdSe@ZnS leachate.

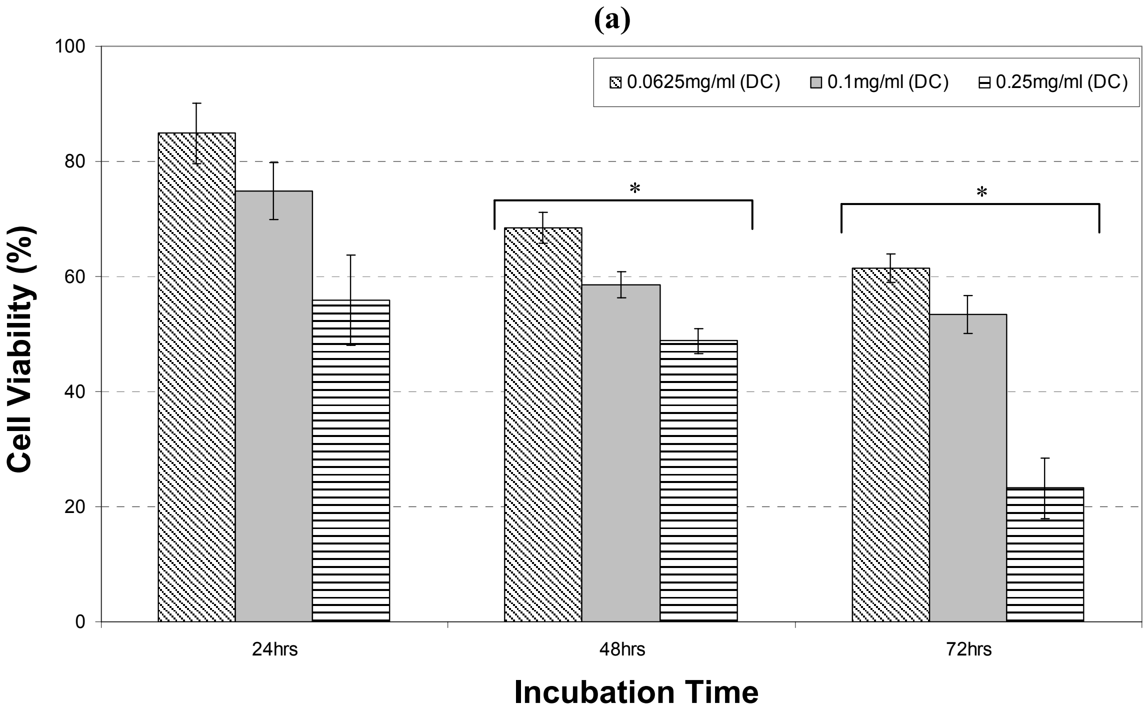

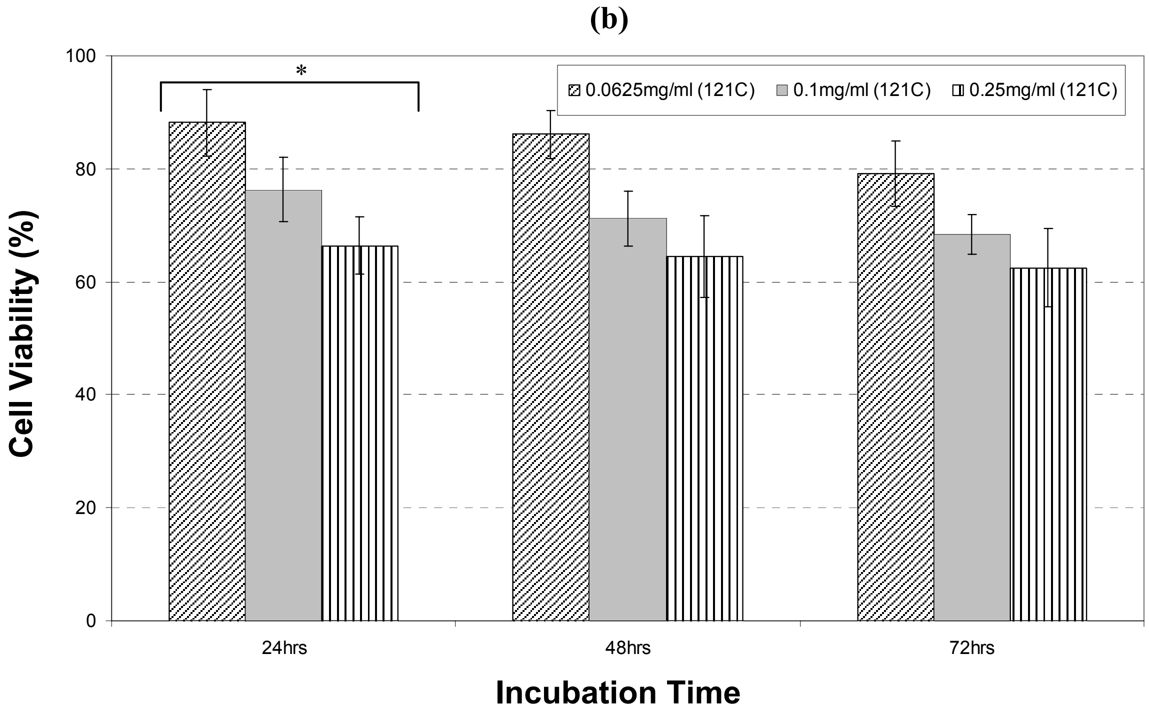

Figure 7.4 Effects of concentrations and exposure time of CdSe@ZnS nanoparticles on cell viability of HepG2 cells: (a) DC method, (b) 121 °C leachate. Data are presented as mean ± SD for at least three independent experiments. *$P < 0.05$; one way ANOVA for repeated measures.

7.3.3 *in vitro* Cytotoxicity Studies using NIH3T3 Cells

The cell viability of NIH3T3 cells in response to these nanoparticles and their extracts was investigated. Similarly, we started with exposing the NIH3T3 cells to the nanoparticles at the extreme condition. The response of the NIH3T3 cells to the nanoparticles is shown in Figure 7.5. γ-Fe_2O_3:Tb^{3+} nanoparticles and its associated extracts showed minimal cytotoxicity. NIH3T3 cell viability was found to be depressed in the presence of CdSe and CdSe@ZnS nanoparticles and their extracts and in fact, the viability was lower compared to that of HepG2 cells. The cell viability was found to be lowest in the DC method, followed by the extracts obtained at 121 °C and then 70 °C. The cell viability was well-correlated to the concentration of toxic Cd ions. Low cell viability was observed at high Cd ion concentration. Revisiting Table 7.1, the highest Cd ion concentration was found in the DC method. Higher Cd ions concentration was found in the CdSe cell media and leachates as compared to that of the CdSe@ZnS nanoparticles, again indicating that ZnS may provide a protective layer to retard, but not totally inhibit, the oxidation of CdSe to Cd ions.

Contrary to results from HepG2 cell viability studies, Y_2O_3:Yb^{3+}:Er^{3+} and Y_2O_3:Er^{3+} nanoparticles and their extracts at 70 and 121 °C showed lower cell viability. As shown in Figure 6.5, the cell viability is lowered to 71.4% when incubated with nanoparticles directly, and to approximately 85.2% for the extracts for Y_2O_3:Er^{3+} samples. Small amounts of rare-earth ions were found in the extracts and cell media (Table 7.1). This finding indicates NIH3T3 cells were more sensitive to the rare-earth ions than HepG2 cells. The presence of rare-earth ions, though present in small concentration, caused aggregation and deformation of the NIH3T3 cells (Figure 7.6b). When exposed to the

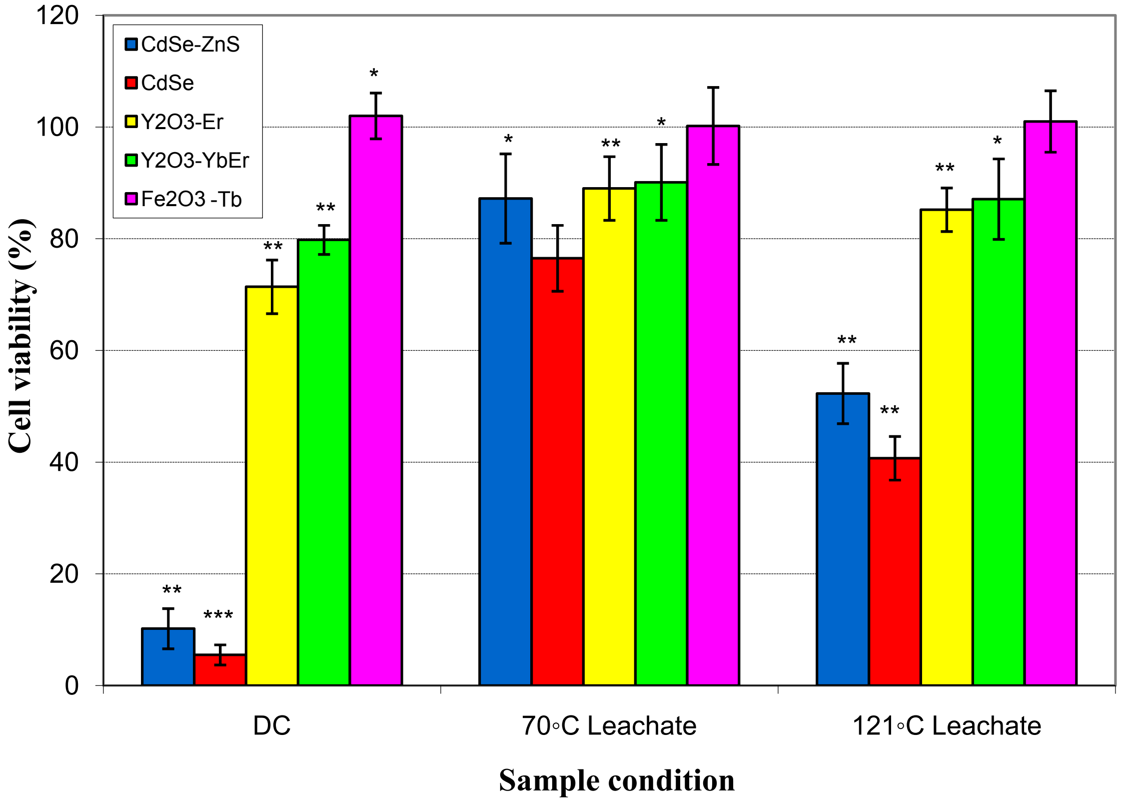

Figure 7.5 Cell viability of NIH3T3 cells at 0.25 mg/ml and 72 h exposure. Data are presented as mean ± SD for at least three independent experiments. Value statistically significant compared to control (ANOVA), $^*P< 0.05$; $^{**}P< 0.01$; $^{***}P< 0.001$.

121 °C extracts of CdSe@ZnS nanoparticles, the cells were sparsely-spaced, and numerous cell debris were observed, indicating more severe toxicity compared to the rare earth oxides (Figure 7.6c).

Figure 7.7 shows the effect of dosage concentration and exposure time of $Y_2O_3:Er^{3+}$ nanoparticles via the DC method. We found that the concentration changes in Y ions were minimal (3.98, 3.79 and 4.23 ppm) with increasing exposure time. These results indicate that the main contribution to decrease in cell viability is the presence of the rare-earth nanoparticles.

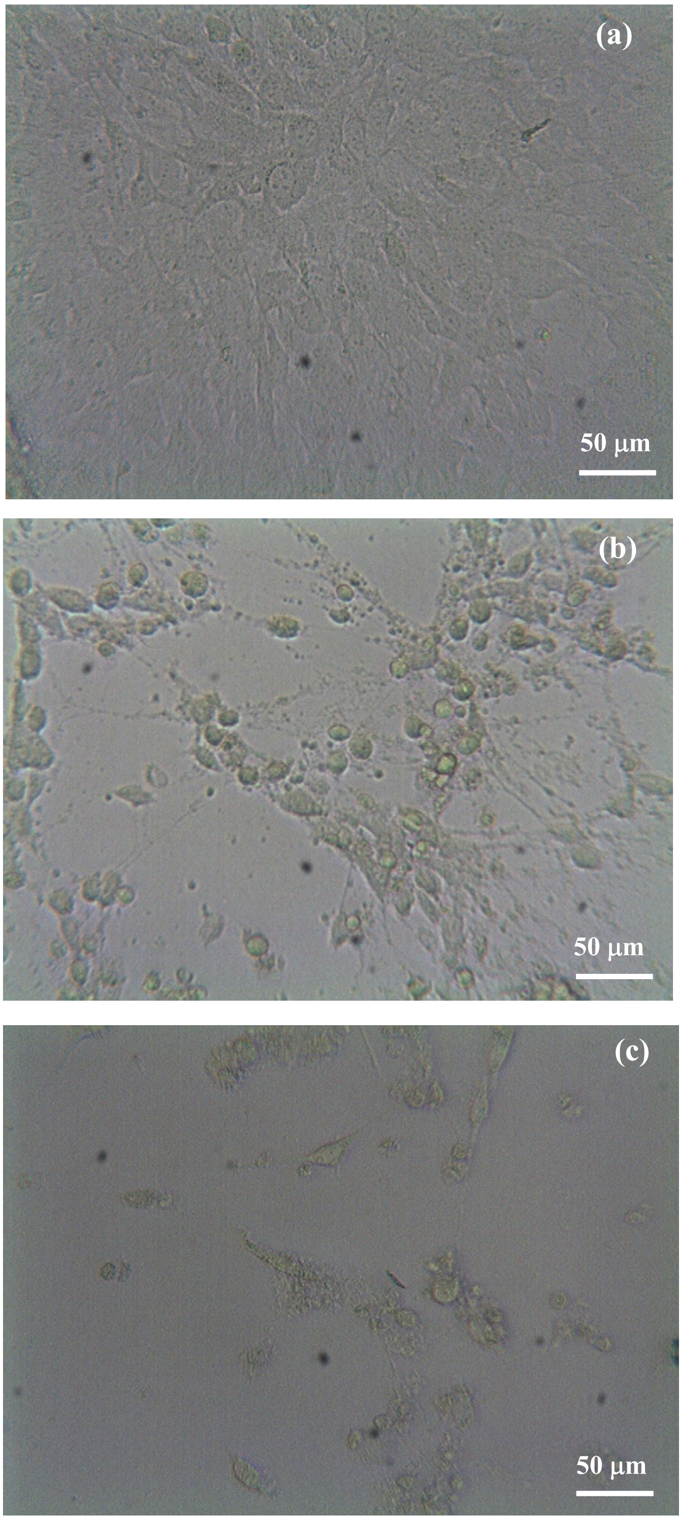

Figure 7.6 Morphologies of NIH 3T3 cells at 0.25 mg/ml and 72 h exposure: (a) control, subjected to (b) 121 °C leachate of $Y_2O_3:Er^{3+}$ nanoparticles, and (c) 121 °C leachate of CdSe@ZnSe nanoparticles.

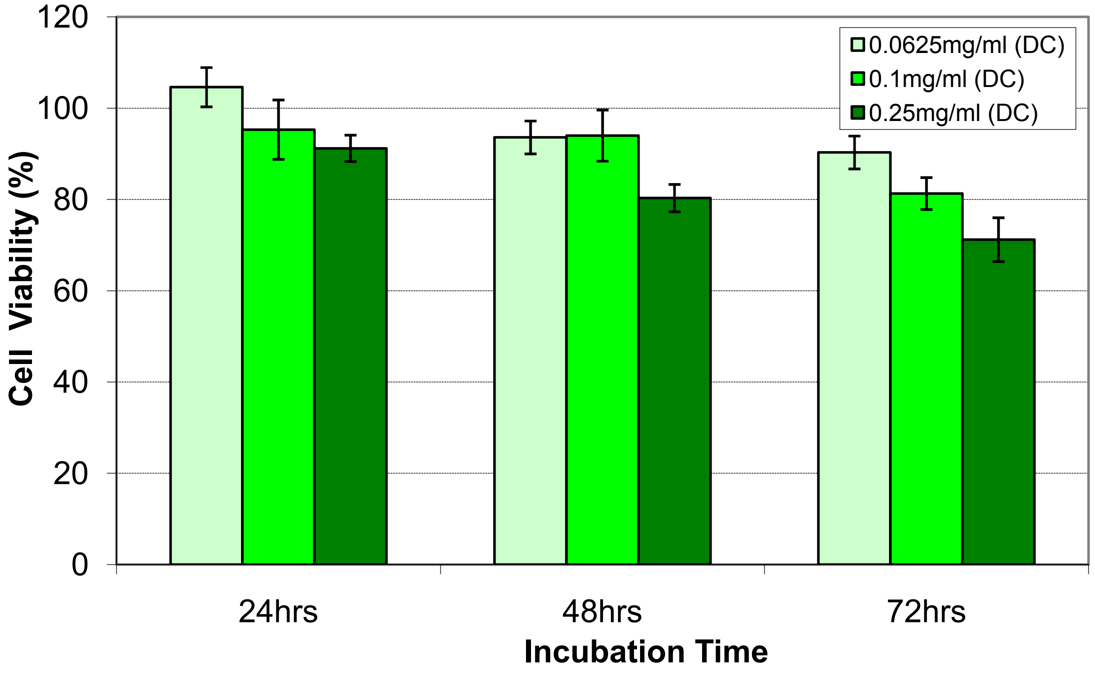

Figure 7.7 Effects of concentrations and exposure time on cell viability of NIH 3T3 cells via DC method using Y_2O_3:Er^{3+} nanoparticles. Data are presented as mean ± SD for at least three independent experiments.

7.4 Discussion

7.4.1 Effects of Nanoparticles and Their Extracts on Cell Viabilities

Based on the results obtained from the extreme condition, it is apparent that the QDs were toxic under conditions of DC method and 121 °C extract. However, as suggested by Figure 7.2, Figure 7.5 and the cell morphology observations, nanoparticles incubated directly with cells (DC method) were more cytotoxic than their respective extracts. The higher cytotoxicity can be attributed to the presence of both the nanoparticle itself and the toxic Cd ions. For HepG2 cells, only the quantum dots and their associated extracts showed cytotoxic effects. The presence of the other nanoparticles, and their ions (Fe, Tb, Yb, Y, and Er) produce minimal toxicity to HepG2 cells. However, for NIH3T3 cells, QDs and rare-earth oxides nanoparticles and their extracts showed cytotoxicity.

Few mechanisms have been proposed to explain the cytotoxicity of CdSe QDs. Oxidation of the QDs can cause decomposition of CdSe nanocrystals leading to release of Cd ions and/or CdSe complex from the core.[281] In addition, QDs can induce reactive oxygen species (ROS) generation through energy or electron transfer to molecular oxygen.[282] Moreover, the nanoparticles could be internalized by the cells, disrupting the cell membrane leading to leakage of cellular content, or affecting the functions of cell organelles and nucleus.[157] In our study, high concentrations of Cd and Se ions were found in the cell media after the CdSe and CdSe@ZnS nanoparticles were incubated with the cells for 72 hrs. The lower cytotoxicity of the CdSe@ZnS is attributed to its ZnS coating which offers a barrier to the leaching of Cd ions (Table 7.1). The cell viability correlates strongly to the Cd ion concentrations found in the cell media (via DC method) and extracts.

Even though rare earth oxides are temperature resistant,[283] the presence of small amount of rare earth ions in the extracts suggest that ions have leached out from the nanoparticle surface, the most probable reason being the high surface area. Very few studies report the toxicity of rare-earth ions at low concentrations. Hopp *et al.*[284] tested cytotoxicity of neodymium (Nd) and samarium (Sm) alloy compounds in NIH 3T3 cells and found that Sm alloy was significantly more toxic than Nd. In an earlier effort, Palmer *et al.*[285] tested cerium (Ce), lanthanum (La), and Nd metal cytotoxicity in rat pulmonary alveolar macrophages and reported low toxicity of these metal ions. Duchen et al[286] reports that the radii of RE ions are very similar to that of Ca^{2+} (0.099 nm), hence they may mimic Ca^{2+} ions in the cellular environment. High uptake of calcium causes mitochondrial dysfunction and cell death.

Figure 7.4 and Figure 7.7 indicate that higher nanoparticles dosage results in more ions in the media, resulting in lower cell viability. Longer exposure time also depresses cell viability. The presence of the nanoparticles also contributes to higher cytotoxicity. A number of studies have reported similar findings on nanoparticles dosage dependent cytotoxic behavior. [163, 287-288] Besides the toxic effects of Cd ions, internalization of the nanoparticles could induce cell death, and the number of nanoparticles internalized correlates to cytotoxicity as reported.[289] A higher amount of internalized nanoparticles could induce a greater extent of cell damage or death by disrupting the cell membranes or destroying the cell organelles,[287] as inferred by Figure 7.3b. In summary, the cell viability of HepG2 is nanoparticle dosage dependent and ion concentration dependent. Toxic ion concentration increases with longer exposure time and higher nanoparticle dosage.

7.4.2 Sensitivity of Cells to Different Nanoparticles

The comparison of the sensitivity of the different cell lines to the CdSe@ZnS and $Y_2O_3:Er^{3+}$ nanoparticles and their extracts at 121 °C is presented in Figure 7.8. It was found that the cell viability in the DC method is lower than in the extraction method. Both cell lines were sensitive to CdSe@ZnS nanoparticles. However, NIH3T3 cells show lower viability. This is indicative that different cell lines respond differently to different nanoparticles. Being a liver cell, HepG2 is capable of the production of metallothionein, a metal sequestering protein, which binds to toxic metal ions forming inert complexes.[290] This could explain the higher tolerance of HepG2 cells towards Cd ion toxicity in all the cases presented in the current study. We also propose that metallothionein is capable of sequestering rare-earth ions, in particular Y ions. The interaction of metallothionein with metal ions takes place via the thiol groups in the cysteine moieties, which are nucleophiles.[291-292] Therefore, it is possible that the metallothionein can form complexes with electrophiles such as metal ions. However, studies have shown that the electronic configuration of the metal ions plays a crucial role in forming stable metal complexes.[293] The metal ions may induce the production of metallothionein, but may not be able to bind to the protein.[290] Metal ions with d10 electronic configuration such as Cd^{2+} andY^{3+} ions are suited for complex formation with the multiple cysteine moieties in metallothionein. This could explain why the HepG2 cells were more resilient towards the metal ions, manifesting higher cell viability.

In addition to the sequestering of toxic metal ions, smaller nanoparticles size plays a vital role in inducing higher cell toxicity. A study by Lovric *et al.*[294] shows that cytotoxicity is more significant with smaller QDs (2.2 nm) than with larger ones (5.2 nm) at the same concentration. They proposed that the smaller QDs could end up in the nucleus, subsequently causing DNA damage and inducing apoptosis. The rare-earth oxide

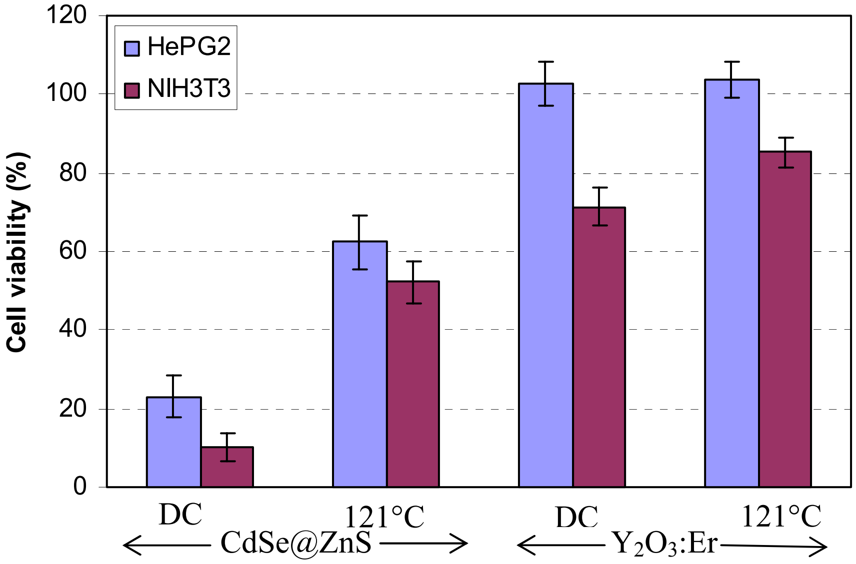

Figure 7.8 Comparison of HepG2 and NIH3T3 cells sensitivity to different nanoparticles under different experimental conditions.

nanoparticles used in the current studies are about 3 nm. This is smaller than the quantum dots nanoparticles (~6 nm) and magnetic nanoparticles (~7 nm). Comparing the results of the DC methods and leachates for the rare-earth oxides, the cell viability is lower in the presence of nanoparticles compared to in the presence of the 121°C leachates, even though the rare earth ion concentrations were lower in the cell medium (Table 7.1). This suggests that the presence of smaller size rare-earth oxide nanoparticles causes lower cell viability.

7.5 Conclusion

We herein propose a new approach for evaluating the *in vitro* cytotoxicity of nanoparticles by analyses of their extracts obtained at different extraction conditions. This approach contributes towards the goal of a generalized and systematic evaluation of toxicity of nanomaterials. From the current study, metal (Cd, Zn, Y, Fe, Yb, Er) ions were only found in extracts obtained at 70 and 121 °C extraction conditions, as well as in the cell media incubated directly with the nanoparticles. The dosage concentration was found to be a critical factor affecting the cell viability. Cells viability was found to decrease in higher concentrations of Cd ions found in extracts obtained at 121 °C and cell media charged with nanoparticles. Such decrease in cell viability is principally due to the toxic Cd ions leached out into the cell media. Particle-induced cell death attributed to internalization of the nanoparticles was also suggested. Cd ion was identified as the most toxic metal ion in the scope of our investigation (cell viability as low as 10.2% ± 3.6 for NIH3T3 cells). HepG2 cell viability appeared unaffected in the presence of rare earth ions. NIH 3T3 cells viability was affected in the presence of both Cd and rare earth ions, showing lower cell viability than HepG2 cells. In addition, our study has shown that different cell lines have different sensitivity to nanoparticles and metal ions toxicity.

In summary, the presence of ions in the extracts suggested that the current proposed method of evaluating cytotoxicity is necessary for nanomaterials intended for biomedical application. As nanoparticulates have increased surface area compared to bulk material, it is expected that more surface ions can be leached out, of which higher concentration could result in dosage dependent toxicity. In order to undertake a comprehensive evaluation of *in vitro* cytotoxicity, a range of cell lines, representative of various mode of contact with the nanoparticles and their associated ions, should be used. Finally, the doped and codoped rare earth oxide nanoparticles studied are found to be less cytotoxic than the Cd-based quantum dots and therefore could be suitable candidates as bioimaging probes.

CHAPTER 8

Conclusions and Recommendations

8.1 Conclusions

The works presented in the preceding chapters of this dissertation show the efforts towards the development of single-phase rare earth doped nanomaterials contrast agents for optical/magnetic resonance imaging. A simple thermal decomposition technique was adopted for the synthesis of the nanomaterials followed by post-synthesis treatment, either by surface functionalization or surface passivation. Different synthesis media, additives, and synthesis conditions have been applied to obtain nanomaterials of different size, morphology, and physiochemical properties. Detail characterizations and analysis were performed to study the properties and investigate the mechanism involved in the fluorescence emission and the growth process of the nanomaterials. The important results and findings of this study are summarized as follows:

(1) Doping and codoping of different rare earth (RE) ions such as terbium (Tb), europium (Eu), erbium (Er), and ytterbium (Yb) in yttrium oxide (Y_2O_3) resulted in down- and up-conversion fluorescent nanomaterials. The morphology of the RE-doped yttrium oxide (Y_2O_3:RE^{3+}) could be selectively controlled from spherical nanocrystals to nanorods. The liganding solvents and synthesis conditions such as reflux time and temperature influenced the nanomaterials morphological evolution, yet the type and amount of dopant showed no influence on nanomaterials morphology. Red and green up-conversion emissions could be selectively tuned by adjusting the concentration

of the codopants. Nanomaterials could be easily surface-functionalized to render them water-dispersible and the ability for further bioconjugation. These nanomaterials have potential in fluorescence optical imaging, especially the up-converting nanomaterials which are promising for deep-tissue imaging.

(2) Highly monodisperse, single-phase bifunctional spherical nanocrystals were synthesized by doping Tb^{3+} ion in superparamagnetic iron oxide (γ-Fe_2O_3) host using a thermal decomposition method. The ~13 nm nanocrystals show superparamagnetism (saturation magnetization strength is 30 emu/g) and down-conversion fluorescence. A fluorescence enhancement technique was applied by passivating the nanocrystal surface with a higher band gap material, ZnS, which resulted in improved PL. The synthesized bifunctional nanomaterial has potential as contrast agents in bimodal imaging, where T_2-weighted MRI and fluorescence microscopy can be combined together. However, the PL obtained from the Tb^{3+}-doped γ-Fe_2O_3 is relatively weak. We believe that the iron oxide host quenches the fluorescence arisen from the 4f→4f intra-transition of the Tb^{3+} ions. Iron oxide has been reported to quench fluorescence of different organic molecules and inorganic nanoparticles.[295-297]

(3) Extending the doping strategy and carefully selecting a paramagnetic host, we have fabricated RE^{3+} (RE = Tb, Yb/Er)-doped Gd_2O_3 and Dy_2O_3 nanomaterials, which showed strong down- and up-conversion fluorescence, and paramagnetism. The RE^{3+}-doped Gd_2O_3 and Dy_2O_3 nanomaterials demonstrated single-phase bifunctionality with a controllable morphology from nanocrystals and nanorods. The evolution mechanism of the nanorods from the spherical

nanocrystals was investigated, where oriented attachment was identified as the mechanism. The RE^{3+}-doped Gd_2O_3 showed both down- and up-conversion luminescence (for Tb^{3+}-doped Gd_2O_3 and Yb^{3+}/Er^{3+}-codoped Gd_2O_3 respectively), and were paramagnetic (magnetization strength of 2.46 emu/g at 10 KOe, 300 K). *in vitro* T_1-weighted MRI for $Gd_2O_3:Yb^{3+},Er^{3+}$ showed close contrast compared to commercial Gd-based contrast agent Gadovist™. The other paramagnetic host Dy_2O_3 (magnetization strength of 2.15 emu/g at 10 KOe, 300 K) showed only down-conversion emission (for Tb^{3+}-doped Dy_2O_3), but no up-conversion emission was observed for Yb^{3+}/Er^{3+}-codoped Dy_2O_3. The presence of Dy ions is believed to act as up-conversion fluorescence quencher in Yb^{3+}/Er^{3+} codopant system as inferred by Auzel.[272] In conclusion, the single-phase up-converting and paramagnetic $Gd_2O_3:Yb^{3+},Er^{3+}$ nanomaterials demonstrate good potential as contrast agent in deep tissue imaging as well as in T_1-weighted MRI in multimodal imaging systems.

(4) *in vitro* cytotoxicity of the RE-doped nanoparticles was evaluated through a new approach based on American National Standard ISO 10993-5. RE^{3+}-doped Y_2O_3 nanomaterials were evaluated as a representative sample of the three RE doped oxides (i.e. $Y_2O_3:RE^{3+}$, $Gd_2O_3:RE^{3+}$, $Dy_2O_3:RE^{3+}$), together with γ-$Fe_2O_3:Tb^{3+}$, and semiconductor quantum dots (QDs). Generally, the type and concentrations of nanomaterials, incubation time, and type of cell subjected to the nanomaterials were found to have influence on cell viability. Cell death was attributed mainly due to leaching of toxic metal ions from the nanomaterials. QDs were shown to be the most toxic while γ-$Fe_2O_3:Tb^{3+}$ the least. $Y_2O_3:RE^{3+}$ (RE =Er, Yb/Er) showed less toxicity in hepatoma HepG2 but revealed relatively greater toxicity

in fibroblast NIH3T3 cell lines. The proposed approach could contribute towards a generalized and systematic evaluation of cytotoxicity of nanomaterials.

8.2 Recommendations

Nanomaterials with novel optical, magnetic, electronic or structural properties are currently under intense research. Among the nanomaterials, rare earth (RE) doped nanomaterials with novel optical and magnetic properties are one of the most promising candidates. In order to exploit their full potential for biomedical applications, the author proposes the following recommendations for improvement of the RE-dope oxide nanomaterials investigated in this dissertation, and future development of RE-doped nanomaterials in general.

(1) *Fundamental studies of* Tb^{3+}*-doped* γ*-*Fe_2O_3*, and* Yb^{3+}/Er^{3+}*-codoped* Dy_2O_3 *nanomaterials*: In the current work, we have suggested that the emission from doped Tb^{3+} ions was quenched by the iron oxide host in γ-Fe_2O_3:Tb^{3+} nanocrystals. The possible explanations are: (a) quenching via electronic coupling and energy transfer; (b) iron oxide may broadly absorb the visible spectrum which could attenuate both the excitation light and fluorescence emission; and (c) the applied crystal field of the iron oxides interacts with excited state electrons of the doped Tb^{3+} ions to promote non-radiative transitions. Also, there was no up-conversion fluorescence observed in Yb^{3+}/Er^{3+}-codoped Dy_2O_3 due to quenching by the energy states in Dy ions, leading to non-radiative relaxation.

A fundamental study is recommended for future work to clearly elucidate how the doped RE ions are spatially distributed in the host materials. Since the crystal field around the doped RE ions greatly influences their emission properties,[105] determination of the spatial distribution of RE ions would provide a better understanding of the dopant-host interaction, which will enable us to fabricate more efficient RE-doped fluorescent materials. Furthermore, a computational study can be done to devise a model to predict such interactions between host and dopants. A qualitative analysis of dopant ion distribution can be done by conducting an etching experiment[298] in which the diameter of the nanocrystals will be reduced in a controlled manner by exposure to hydrofluoric acid (HF) or any suitable reagents. Qualitatively determination of the locations of the dopant ions (whether on the surface or in the core), and the effect of dopant distribution on the luminescent properties can be elucidated by characterizing the reduced-sized nanoparticles.

We believe that by understanding the dopant-host interaction, and therefore the quenching mechanism, nanomaterials with enhanced up-conversion emission efficiency could be fabricated for more effective deep-tissue imaging.

(2) *Investigation of other types of host materials and nanostructures for further enhancement of up-conversion fluorescence, and T_1- and T_2-relaxivities*: We have demonstrated successful synthesis of bifunctional down- and up-conversion fluorescent $Gd_2O_3:RE^{3+}$ nanomaterials, which showed good T_1-weighted MRI contrast property. However, the up-conversion fluorescence efficiency could be improved if a fluoride-based host is used. Fluoride hosts, such as $NaYF_4:RE^{3+}$ and $NaGdF_4:RE^{3+}$, have been reported as some of the best up-conversion hosts.[14] In addition, the problem of up-conversion quenching by Dy ions may be circumvented by adopting a core-shell configuration. Despite advocating a single-phase crystalline system in this work, we realize that such system may not

be favorable for our purpose of incorporating both T_1-, T_2-MRI contrast (Dy ions have been reported to produce T_2-MRI contrast)[54] and up-conversion emission into a single nanocrystal.

Forming a core-shell structure of the same host material such as core-shell $Gd_2O_3:Yb^{3+},Er^{3+}/Gd_2O_3:Dy^{3+}$ would be a possible way to integrate such multifunctionality (up-conversion fluorescent, and T_1- and T_2-MRI contrast). In addition, the formation of a core-shell fluoride structure $NaGdF_4:Yb^{3+},Er^{3+}/NaGdF_4:Dy^{3+}$ could probably produce strong T_1- and T_2-MRI contrast, as well as strong up-conversion emission.

(3) *Long-term cytotoxicity studies*: In the current work, we have proposed a new method of cytotoxicity evaluation of nanomaterials and conducted short-term cell viability studies using the synthesized RE-doped nanoparticles. However, long-term cytotoxicity investigations are needed to ensure the safe application of these nanoparticles in biomedicine. Studies to be undertaken can include the investigation of reactive oxygen species (ROS) generation in cells in the presence of these nanoparticles, biodistribution profiles and metabolic pathways of the RE-doped nanomaterials (all RE oxides in this work, eg. $Y_2O_3:RE^{3+}$, γ-$Fe_2O_3:RE^{3+}$, $GD_2O_3:RE^{3+}$, $Dy_2O_3:RE^{3+}$, as well as the fluoride-based naomaterials). We also recommend comparative studies of poly(ethylene glycol) (PEG)-coated nanomaterials with non-PEG coated ones for such long term studies. PEG-modified nanoparticles have been found to prolong blood-circulation time. The PEG layer prevents the adsorption of plasma proteins (opsonins) that triggers phagocytosis by reticulo-endothelial system (RES).[13]

(4) *To devise an one-pot synthesis method of water-dispersible, uniform, and monodisperse nanoparticle*s: Water-dispersibility of nanoparticles is one of the important requirements for bioapplications. The limitation of many synthesis methods, including the thermal decomposition method used in the current work, is that post-synthesis surface modifications are necessary to render the nanomaterials biocompatible. Hence, it is highly desirable to devise a one-pot synthetic strategy to produce water-dispersible, uniform, and monodisperse multifunctional nanocrystals. Several groups reported fabrication strategy of one-pot water-dispersible nanocrystals with the aid of polymers or surfactants such as PEG-derivatives (e.g. monocarboxyl-terminated poly(ethylene glycol))[61] or amphiphilic surfactants (e.g. polyvinylpyrrolidone).[127] However, uniformity, monodispersity, and stability of these nanoparticles remain as the issues to be addressed. Thus, concerted efforts are needed to devise synthetic strategies for fabrication of water-dispersible nanoparticle with desired surface properties for bioconjugations, or by developing water-dispersible and biocompatible polymer derivatives as strong stabilizing agents in aqueous environment.

(5) *Future development of RE-based nanomaterials for treatment and diagnosis*: A common goal in medicine is to achieve early and accurate diagnosis, so that early treatment can be delivered. A multifunctional nanoparticulate platform with the capability of simultaneous diagnosis (achieved via functional and/or structural bioimaging), targeting (to achieve specificity in treatment) and therapy has been envisioned to achieve this goal. Rare-earth nanomaterials, with their unique fluorescence and magnetic properties, have tremendous potential to achieve this vision. The RE nanomaterial platform can incorporate multimodal contrast agents

(eg. up-conversion optical/T_1-, T_2-MR imaging), together with therapeutic agents (eg. drugs), and targeting moieties (such as folic acid to folate receptors mediated cancer cell targeting) by techniques such as surface functionalization and polymer encapsulation.[185] Such multifunctional nanoparticulate platform could ultimately have the ability to label biomolecules and cells, and image disease organs with high sensitivity in a combinable fashion with magnetic and fluorescent tags, and achieve improved therapeutic efficacy and reduced drug toxicity.

REFERENCES

1. A.P. Alivisatos, Semiconductor Clusters, Nanocrystals, and Quantum Dots. *Science,* **1996**, 271(5251), 933-937.
2. C.B. Murray, D.J. Norris, and M.G. Bawendi, Synthesis and characterization of nearly monodisperse CdE (E = sulfur, selenium, tellurium) semiconductor nanocrystallites. *Journal of the American Chemical Society,* **2002**, 115(19), 8706-8715.
3. S. Link and M.A. El-Sayed, Spectral Properties and Relaxation Dynamics of Surface Plasmon Electronic Oscillations in Gold and Silver Nanodots and Nanorods. *The Journal of Physical Chemistry B,* **1999**, 103(40), 8410-8426.
4. G. Cao and C.J. Brinker, *Annual Review of Nano Research*. Vol. 1 & 2, **2008**, World Scientific Publishing Company
5. L. An-Hui, E.L. Salabas, and S. Ferdi, Magnetic Nanoparticles: Synthesis, Protection, Functionalization, and Application. *Angewandte Chemie International Edition,* **2007**, 46(8), 1222-1244.
6. J. Kim, Y. Piao, and T. Hyeon, Multifunctional Nanostructured Materials for Multimodal Imaging, and Simultaneous Imaging and Therapy. *Chemical Society Reviews,* **2009**, 38(2), 372-390.
7. J. Gao, H. Gu, and B. Xu, Multifunctional Magnetic Nanoparticles: Design, Synthesis, and Biomedical Applications. *Accounts of Chemical Research,* **2009**, DOI:10.1021/ar9000026.

8. M.-C. Daniel and D. Astruc, Gold Nanoparticles: Assembly, Supramolecular Chemistry, Quantum-Size-Related Properties, and Applications toward Biology, Catalysis, and Nanotechnology. *Chemical Reviews,* **2003**, 104(1), 293-346.

9. A. Burns, H. Ow, and U. Wiesner, Fluorescent Core-shell Silica Nanoparticles: Towards "Lab on a Particle" Architectures for Nanobiotechnology. *Chemical Society Reviews,* **2006**, 35(11), 1028-1042.

10. M. Ferrari, Cancer Nanotechnology: Opportunities and Challenges. *Nature Reviews Cancer,* **2005**, 5(3), 161-171.

11. A.P. Alivisatos, W. Gu, and C. Larabell, Quantum dots as cellular probes. *Annual Review of Biomedical Engineering,* **2005**, 7(1), 55-76.

12. R. Duncan, Polymer Conjugates as Anticancer Nanomedicines. *Nature Reviews Cancer,* **2006**, 6(9), 688-701.

13. A.K. Gupta and M. Gupta, Synthesis and surface engineering of iron oxide nanoparticles for biomedical applications. *Biomaterials,* **2005**, 26(18), 3995-4021.

14. F. Wang and X. Liu, Recent Advances in the Chemistry of Lanthanide-doped Upconversion Nanocrystals. *Chemical Society Reviews,* **2009**, 38(4), 976-989.

15. L. Brannon-Peppas and J.O. Blanchette, Nanoparticle and Targeted Systems for Cancer Therapy. *Advanced Drug Delivery Reviews,* **2004**, 56(11), 1649-1659.

16. D. Peer, J.M. Karp, S. Hong, O.C. Farokhzad, R. Margalit, and R. Langer, Nanocarriers as an Emerging Platform for Cancer Therapy. *Nature Nanotechnology,* **2007**, 2(12), 751-760.

17. J. Cheon and J.-H. Lee, Synergistically Integrated Nanoparticles as Multimodal Probes for Nanobiotechnology. *Accounts of Chemical Research,* **2008**, 41(12), 1630-1640.

18. A.K. Salem, P.C. Searson, and K.W. Leong, Multifunctional Nanorods for Gene Delivery. *Nature Materials,* **2003**, 2(10), 668-671.

19. W.S. Seo, J.H. Lee, X. Sun, Y. Suzuki, D. Mann, Z. Liu, M. Terashima, P.C. Yang, M.V. McConnell, D.G. Nishimura, and H. Dai, FeCo/graphitic-shell Nanocrystals as Advanced Magnetic-resonance-imaging and Near-infrared agents. *Nature Materials,* **2006**, 5(12), 971-976.

20. H. Gu, R. Zheng, X. Zhang, and B. Xu, Facile One-Pot Synthesis of Bifunctional Heterodimers of Nanoparticles: A Conjugate of Quantum Dot and Magnetic Nanoparticles. *Journal of the American Chemical Society,* **2004**, 126(18), 5664-5665.

21. J. Kim, J.E. Lee, J. Lee, J.H. Yu, B.C. Kim, K. An, Y. Hwang, C.-H. Shin, J.-G. Park, J. Kim, and T. Hyeon, Magnetic Fluorescent Delivery Vehicle Using Uniform Mesoporous Silica Spheres Embedded with Monodisperse Magnetic and Semiconductor Nanocrystals. *Journal of the American Chemical Society,* **2005**, 128(3), 688-689.

22. J.-s. Choi, Y.-w. Jun, S.-I. Yeon, H.C. Kim, J.-S. Shin, and J. Cheon, Biocompatible Heterostructured Nanoparticles for Multimodal Biological Detection. *Journal of the American Chemical Society,* **2006**, 128(50), 15982-15983.

23. Y.-S. Lin, S.-H. Wu, Y. Hung, Y.-H. Chou, C. Chang, M.-L. Lin, C.-P. Tsai, and C.-Y. Mou, Multifunctional Composite Nanoparticles: Magnetic, Luminescent, and Mesoporous. *Chemistry of Materials,* **2006**, 18(22), 5170-5172.

24. D.K. Yi, S.T. Selvan, S.S. Lee, G.C. Papaefthymiou, D. Kundaliya, and J.Y. Ying, Silica-Coated Nanocomposites of Magnetic Nanoparticles and Quantum Dots. *Journal of the American Chemical Society,* **2005**, 127(14), 4990-4991.

25. J. Kim, J.E. Lee, S.H. Lee, J.H. Yu, J.H. Lee, T.G. Park, and T. Hyeon, Designed Fabrication of a Multifunctional Polymer Nanomedical Platform for Simultaneous Cancer- Targeted Imaging and Magnetically Guided Drug Delivery. *Advanced Materials,* **2008**, 20(3), 478-483.

26. H. Kim, M. Achermann, L.P. Balet, J.A. Hollingsworth, and V.I. Klimov, Synthesis and Characterization of Co/CdSe Core/Shell Nanocomposites: Bifunctional Magnetic-Optical Nanocrystals. *Journal of the American Chemical Society,* **2004**, 127(2), 544-546.

27. S. Donglu, C. Hoon Sung, C. Yan, X. Hong, G. Hongchen, L. Jie, W. Wei, L. Guokui, H. Christopher, W. Lumin, C.E. Rodney, B. Sergei, M.P. Giovanni, and D. Zhongyun, Fluorescent Polystyrene-Fe_3O_4 Composite Nanospheres for *in vivo* Imaging and Hyperthermia. *Advanced Materials,* **2009**, 21(21), 2170-2173.

28. V. Salgueiriño-Maceira, M.A. Correa-Duarte, M. Spasova, L.M. Liz-Marzán, and M. Farle, Composite Silica Spheres with Magnetic and Luminescent Functionalities. *Advanced Functional Materials,* **2006**, 16(4), 509-514.

29. K. Jaeyun, P. Sungjin, L. Ji Eun, J. Seung Min, L. Jung Hee, L. In Su, Y. Ilseung, K. Jun-Sung, K. Seong Keun, C. Myung-Haing, and H. Taeghwan, Designed Fabrication of Multifunctional Magnetic Gold Nanoshells and Their Application to Magnetic Resonance Imaging and Photothermal Therapy. *Angewandte Chemie International Edition,* **2006**, 45(46), 7754-7758.

30. S.T. Selvan, P.K. Patra, C.Y. Ang, and J.Y. Ying, Synthesis of Silica-Coated Semiconductor and Magnetic Quantum Dots and Their Use in the Imaging of Live Cells. *Angewandte Chemie International Edition,* **2007**, 46(14), 2448-2452.

31. X. Hai-Yan, Z. Chao, L. Yi, Z. Zhi-Ling, P. Dai-Wen, L. Xiao-Lan, G. Jian-Ping, D. Calum, and Z. Wuzong, Cell-Targeting Multifunctional Nanospheres with both Fluorescence and Magnetism. *Small,* **2005**, 1(5), 506-509.

32. H. Lu, G. Yi, S. Zhao, D. Chen, L.-H. Guo, and J. Cheng, Synthesis and Characterization of Multi-functional Nanoparticles Possessing Magnetic, Up-conversion Fluorescence and Bio-affinity Properties. *Journal of Materials Chemistry,* **2004**, 14(8), 1336-1341.

33. F. Grasset, F. Dorson, Y. Molard, S. Cordier, V. Demange, C. Perrin, V. Marchi-Artzner, and H. Haneda, One-pot Synthesis and Characterizations of Bi-functional Phosphor-magnetic@SiO_2 Nanoparticles: Controlled and Structured Association of Mo_6 cluster units and γ-Fe_2O_3 nanocrystals. *Chemical Communications,* **2008**(39), 4729-4731.

34. M.F. Kircher, U. Mahmood, R.S. King, R. Weissleder, and L. Josephson, A Multimodal Nanoparticle for Preoperative Magnetic Resonance Imaging and Intraoperative Optical Brain Tumor Delineation. *Cancer Research,* **2003**, 63(23), 8122-8125.

35. S. Corr, Y. Rakovich, and Y. Gun'ko, Multifunctional Magnetic-fluorescent Nanocomposites for Biomedical Applications. *Nanoscale Research Letters,* **2008**, 3(3), 87-104.

36. M. Nahrendorf, H. Zhang, S. Hembrador, P. Panizzi, D.E. Sosnovik, E. Aikawa, P. Libby, F.K. Swirski, and R. Weissleder, Nanoparticle PET-CT Imaging of Macrophages in Inflammatory Atherosclerosis. *Circulation,* **2008**, 117(3), 379-387.

37. T.F. Massoud and S.S. Gambhir, Molecular Imaging in living Subjects: Seeing Fundamental Biological Processes in a New Light. *Genes & Development,* **2003**, 17(5), 545-580.

38. P. Caravan, Strategies for Increasing the Sensitivity of Gadolinium Based MRI Contrast Agents. *Chemical Society Reviews,* **2006**, 35(6), 512-523.

39. W.M.B. Jeff and L.K. Dara, Iron Oxide MR Contrast Agents for Molecular and Cellular Imaging. *NMR in Biomedicine,* **2004**, 17(7), 484-499.

40. Hyon B. Na, Jung H. Lee, K. An, Yong I. Park, M. Park, In S. Lee, D.-H. Nam, Sung T. Kim, S.-H. Kim, S.-W. Kim, K.-H. Lim, K.-S. Kim, S.-O. Kim, and T. Hyeon, Development of a T_1 Contrast Agent for Magnetic Resonance Imaging Using MnO Nanoparticles. *Angewandte Chemie International Edition,* **2007**, 46(28), 5397-5401.

41. R.P. Haugland, *The Handbook: A Guide to Fluorescent Probes and Labeling Technologies*. 10 ed, **2005**, Molecular Probes, Eugene, OR.

42. B. Dubertret, P. Skourides, D.J. Norris, V. Noireaux, A.H. Brivanlou, and A. Libchaber, In Vivo Imaging of Quantum Dots Encapsulated in Phospholipid Micelles. *Science,* **2002**, 298(5599), 1759-1762.

43. X. Gao, Y. Cui, R.M. Levenson, L.W.K. Chung, and S. Nie, *in vivo* Cancer Targeting and Imaging with Semiconductor Quantum Dots. *Nature Biotechnology,* **2004**, 22(8), 969-976.

44. S.T. Selvan, T.T. Tan, and J.Y. Ying, Robust, Non-Cytotoxic, Silica-Coated CdSe Quantum Dots with Efficient Photoluminescence. *Advanced Materials,* **2005**, 17(13), 1620-1625.

45. D. Dosev, M. Nichkova, and I.M. Kennedy, Inorganic Lanthanide Nanophosphors in Biotechnology *Journal of Nanoscience and Nanotechnology,* **2008**, 8(3), 1052-1067.

46. E.I. Altinoglu, T.J. Russin, J.M. Kaiser, B.M. Barth, P.C. Eklund, M. Kester, and J.H. Adair, Near-Infrared Emitting Fluorophore-Doped Calcium Phosphate Nanoparticles for In Vivo Imaging of Human Breast Cancer. *ACS Nano,* **2008**, 2(10), 2075-2084.

47. J. Gao, W. Zhang, P. Huang, B. Zhang, X. Zhang, and B. Xu, Intracellular Spatial Control of Fluorescent Magnetic Nanoparticles. *Journal of the American Chemical Society,* **2008**, 130(12), 3710-3711.

48. J. Shen, L.-D. Sun, and C.-H. Yan, Luminescent Rare Earth Nanomaterials for Bioprobe Applications. *Dalton Transactions,* **2008**, 42(14), 5687–5697

49. E.M. Goldys, K. Drozdowicz-Tomsia, S. Jinjun, D. Dosev, I.M. Kennedy, S. Yatsunenko, and M. Godlewski, Optical Characterization of Eu-Doped and Undoped Gd_2O_3 Nanoparticles Synthesized by the Hydrogen Flame Pyrolysis Method. *Journal of the American Chemical Society,* **2006**, 128(45), 14498-14505.

50. J.-L. Bridot, A.-C. Faure, S. Laurent, C. Riviere, C. Billotey, B. Hiba, M. Janier, V. Josserand, J.-L. Coll, L. Vander Elst, R. Muller, S. Roux, P. Perriat, and O. Tillement, Hybrid Gadolinium Oxide Nanoparticles: Multimodal Contrast Agents for in Vivo Imaging. *Journal of the American Chemical Society,* **2007**, 129(16), 5076-5084.

51. H. Hifumi, S. Yamaoka, A. Tanimoto, T. Akatsu, Y. Shindo, A. Honda, D. Citterio, K. Oka, S. Kuribayashi, and K. Suzuki, Dextran Coated Gadolinium

Phosphate Nanoparticles for Magnetic Resonance Tumor Imaging. *Journal of Materials Chemistry,* **2009**, 19(35), 6393-6399.

52. C.-C. Huang, T.-Y. Liu, C.-H. Su, Y.-W. Lo, J.-H. Chen, and C.-S. Yeh, Superparamagnetic Hollow and Paramagnetic Porous Gd_2O_3 Particles. *Chemistry of Materials,* **2008**, 20(12), 3840-3848.

53. H. Hifumi, S. Yamaoka, A. Tanimoto, D. Citterio, and K. Suzuki, Gadolinium-Based Hybrid Nanoparticles as a Positive MR Contrast Agent. *Journal of the American Chemical Society,* **2006**, 128(47), 15090-15091.

54. M.g. Norek, E. Kampert, U. Zeitler, and J.A. Peters, Tuning of the Size of Dy_2O_3 Nanoparticles for Optimal Performance as an MRI Contrast Agent. *Journal of the American Chemical Society,* **2008**, 130(15), 5335-5340.

55. R. Weissleder, Molecular Imaging in Cancer. *Science,* **2006**, 312(5777), 1168-1171.

56. W.J.M. Mulder, R. Koole, R.J. Brandwijk, G. Storm, P.T.K. Chin, G.J. Strijkers, C. de Mello Donega, K. Nicolay, and A.W. Griffioen, Quantum Dots with a Paramagnetic Coating as a Bimodal Molecular Imaging Probe. *Nano Letters,* **2005**, 6(1), 1-6.

57. T. Beyer, D.W. Townsend, T. Brun, P.E. Kinahan, M. Charron, R. Roddy, J. Jerin, J. Young, L. Byars, and R. Nutt, A Combined PET/CT Scanner for Clinical Oncology. *The Journal of Nuclear Medicine,* **2000**, 41(8), 1369-1379.

58. L. An-Hui, S. Wolfgang, M. Nina, B. Helmut, S. Bernd, T. Bernd, B. Eckhard, K. Wolfgang, and S. Ferdi, Nanoengineering of a Magnetically Separable Hydrogenation Catalyst. *Angewandte Chemie International Edition,* **2004**, 43(33), 4303-4306.

59. T. Shik Chi, C. Valérie, P. Ioannis, C. David, and T. David, Magnetically Separable, Carbon-Supported Nanocatalysts for the Manufacture of Fine Chemicals. *Angewandte Chemie International Edition,* **2004**, 43(42), 5645-5649.

60. S. Mornet, S. Vasseur, F. Grasset, P. Veverka, G. Goglio, A. Demourgues, J. Portier, E. Pollert, and E. Duguet, Magnetic Nanoparticle Design for Medical Applications. *Progress in Solid State Chemistry,* **2006**, 34(2-4), 237-247.

61. Z. Li, L. Wei, M.Y. Gao, and H. Lei, One-Pot Reaction to Synthesize Biocompatible Magnetite Nanoparticles. *Advanced Materials,* **2005**, 17(8), 1001-1005.

62. T. Hyeon, Chemical synthesis of magnetic nanoparticles. *Chemical Communications,* **2003**(8), 927-934.

63. M. Takafuji, S. Ide, H. Ihara, and Z. Xu, Preparation of Poly(1-vinylimidazole)-Grafted Magnetic Nanoparticles and Their Application for Removal of Metal Ions. *Chemistry of Materials,* **2004**, 16(10), 1977-1983.

64. D.W. Elliott and W.-x. Zhang, Field Assessment of Nanoscale Bimetallic Particles for Groundwater Treatment. *Environmental Science & Technology,* **2001**, 35(24), 4922-4926.

65. P. Tartaj, M.d.P. Morales, S. Veintemillas-Verdaguer, T. Gonz´alez-Carre, and C.J. Serna, The Preparation of Magnetic Nanoparticles for Applications in Biomedicine. *Journal of Physics D: Applied Physics,* **2003**, 36(13), R182.

66. F. Wang, W.B. Tan, Y. Zhang, X. Fan, and M. Wang, Luminescent Nanomaterials for Biological Labelling. *Nanotechnology,* **2006**, 17(1), R1-R13.

67. F. Auzel, Upconversion and Anti-Stokes Processes with f and d Ions in Solids. *Chemical Reviews,* **2003**, 104(1), 139-174.

68. R. Weissleder, A Clearer Vision for in vivo Imaging. *Nature Biotechnology,* **2001**, 19(4), 316-317.

69. R. Weissleder and V. Ntziachristos, Shedding Light onto Live Molecular Targets. *Nature Medicine,* **2003**, 9(1), 123-128.

70. Y.A. Labas, N.G. Gurskaya, Y.G. Yanushevich, A.F. Fradkov, K.A. Lukyanov, S.A. Lukyanov, and M.V. Matz, Diversity and Evolution of the Green Fluorescent Protein Family. *Proceedings of the National Academy of Sciences of the United States of America,* **2002**, 99(7), 4256-4261.

71. K.A. Lukyanov, D.M. Chudakov, S. Lukyanov, and V.V. Verkhusha, Photoactivatable Fluorescent Proteins. *Nature Reviews Molecular Cell Biology,* **2005**, 6(11), 885-890.

72. P. Anna, R. Oliver, and I.H.B. Philippe, Imaging Activation of Two Ras Isoforms Simultaneously in a Single Cell. *ChemBioChem,* **2005**, 6(1), 78-85.

73. P.T. Tran, A. Paoletti, and F. Chang, Imaging Green Fluorescent Protein Fusions in Living Fission Yeast Cells. *Methods,* **2004**, 33(3), 220-225.

74. P. Sharma, S. Brown, G. Walter, S. Santra, and B. Moudgil, Nanoparticles for Bioimaging. *Advances in Colloid and Interface Science,* **2006**, 123-126, 471-485.

75. H.J. Weinmann, M. Laniado, and W. Mutzel, Pharmacokinetics of GdDTPA/dimeglumine after Intravenous Injection into Healthy Volunteers. *Physiological Chemistry & Physics & Medical NMR,* **1984**, 16, 167-172.

76. S.R. Cherry, Multimodality in vivo Imaging Systems: Twice the Power or Double the Trouble? *Annual Review of Biomedical Engineering,* **2006**, 8(1), 35-62.

77. E.M.C. Hillman and A. Moore, All-optical Anatomical Co-registration for Molecular Imaging of Small Animals Using Dynamic Contrast. *Nature Photonics,* **2007**, 1(9), 526-530.

78. http://www.biotechsystems.com.

79. V. Ntziachristos, A.G. Yodh, M. Schnall, and B. Chance, Concurrent MRI and Diffuse Optical Tomography of Breast after Indocyanine Green Enhancement. *Proceedings of the National Academy of Sciences of the United States of America,* **2000**, 97(6), 2767-2772.

80. L. Josephson, M.F. Kircher, U. Mahmood, Y. Tang, and R. Weissleder, Near-Infrared Fluorescent Nanoparticles as Combined MR/Optical Imaging Probes. *Bioconjugate Chemistry,* **2002**, 13(3), 554-560.

81. A. Moore, Z. Medarova, A. Potthast, and G. Dai, In Vivo Targeting of Underglycosylated MUC-1 Tumor Antigen Using a Multimodal Imaging Probe. *Cancer Res,* **2004**, 64(5), 1821-1827.

82. O. Veiseh, C. Sun, J. Gunn, N. Kohler, P. Gabikian, D. Lee, N. Bhattarai, R. Ellenbogen, R. Sze, A. Hallahan, J. Olson, and M. Zhang, Optical and MRI Multifunctional Nanoprobe for Targeting Gliomas. *Nano Letters,* **2005**, 5(6), 1003-1008.

83. H. Lee, M.K. Yu, S. Park, S. Moon, J.J. Min, Y.Y. Jeong, H.-W. Kang, and S. Jon, Thermally Cross-Linked Superparamagnetic Iron Oxide Nanoparticles: Synthesis and Application as a Dual Imaging Probe for Cancer in Vivo. *Journal of the American Chemical Society,* **2007**, 129(42), 12739-12745.

84. T.-J. Yoon, Kyeong N. Yu, E. Kim, Jun S. Kim, Byung G. Kim, S.-H. Yun, B.-H. Sohn, M.-H. Cho, J.-K. Lee, and Seung B. Park, Specific Targeting, Cell Sorting,

and Bioimaging with Smart Magnetic Silica Core-Shell Nanomaterials13. *Small,* **2006**, 2(2), 209-215.

85. C.-W. Lu, Y. Hung, J.-K. Hsiao, M. Yao, T.-H. Chung, Y.-S. Lin, S.-H. Wu, S.-C. Hsu, H.-M. Liu, C.-Y. Mou, C.-S. Yang, D.-M. Huang, and Y.-C. Chen, Bifunctional Magnetic Silica Nanoparticles for Highly Efficient Human Stem Cell Labeling. *Nano Letters,* **2007**, 7(1), 149-154.

86. J.-H. Lee, Y.-w. Jun, S.-I. Yeon, J.-S. Shin, and J. Cheon, Dual-Mode Nanoparticle Probes for High-Performance Magnetic Resonance and Fluorescence Imaging of Neuroblastoma. *Angewandte Chemie International Edition,* **2006**, 45(48), 8160-8162.

87. C. Xu, J. Xie, D. Ho, C. Wang, N. Kohler, Edward G. Walsh, Jeffrey R. Morgan, Y.E. Chin, and S. Sun, Au-Fe_3O_4 Dumbbell Nanoparticles as Dual-Functional Probes. *Angewandte Chemie International Edition,* **2008**, 47(1), 173-176.

88. J.H. Choi, F.T. Nguyen, P.W. Barone, D.A. Heller, A.E. Moll, D. Patel, S.A. Boppart, and M.S. Strano, Multimodal Biomedical Imaging with Asymmetric Single-Walled Carbon Nanotube/Iron Oxide Nanoparticle Complexes. *Nano Letters,* **2007**, 7(4), 861-867.

89. W.J.M. Mulder, R. Koole, R.J. Brandwijk, G. Storm, P.T.K. Chin, G.J. Strijkers, C. de Mello Donega, K. Nicolay, and A.W. Griffioen, Quantum Dots with a Paramagnetic Coating as a Bimodal Molecular Imaging Probe. *Nano Letters,* **2006**, 6(1), 1-6.

90. H. Yang, S. Santra, G.A. Walter, and P.H. Holloway, Gd^{III}-Functionalized Fluorescent Quantum Dots as Multimodal Imaging Probes. *Advanced Materials,* **2006**, 18(21), 2890-2894.

91. S. Santra, R.P. Bagwe, D. Dutta, J.T. Stanley, G.A. Walter, W. Tan, B.M. Moudgil, and R.A. Mericle, Synthesis and Characterization of Fluorescent, Radio-Opaque, and Paramagnetic Silica Nanoparticles for Multimodal Bioimaging Applications. *Advanced Materials,* **2005**, 17(18), 2165-2169.

92. V.S. Talanov, C.A.S. Regino, H. Kobayashi, M. Bernardo, P.L. Choyke, and M.W. Brechbiel, Dendrimer-Based Nanoprobe for Dual Modality Magnetic Resonance and Fluorescence Imaging. *Nano Letters,* **2006**, 6(7), 1459-1463.

93. William J. Rieter, Jason S. Kim, Kathryn M.L. Taylor, H. An, W. Lin, T. Tarrant, and W. Lin, Hybrid Silica Nanoparticles for Multimodal Imaging13. *Angewandte Chemie International Edition,* **2007**, 46(20), 3680-3682.

94. J.S. Kim, W.J. Rieter, K.M.L. Taylor, H. An, W. Lin, and W. Lin, Self-Assembled Hybrid Nanoparticles for Cancer-Specific Multimodal Imaging. *Journal of the American Chemical Society,* **2007**, 129(29), 8962-8963.

95. K.M.L. Taylor, J.S. Kim, W.J. Rieter, H. An, W. Lin, and W. Lin, Mesoporous Silica Nanospheres as Highly Efficient MRI Contrast Agents. *Journal of the American Chemical Society,* **2008**, 130(7), 2154-2155.

96. C.-P. Tsai, Y. Hung, Y.-H. Chou, D.-M. Huang, J.-K. Hsiao, C. Chang, Y.-C. Chen, and C.-Y. Mou, High-Contrast Paramagnetic Fluorescent Mesoporous Silica Nanorods as a Multifunctional Cell-Imaging Probe13. *Small,* **2008**, 4(2), 186-191.

97. D.G. Mitchell, *MRI Principles*, **1999**, Philadelphia, PA, W. B. Saunders Company.

98. S. Demos, H. Radousky, and R. Alfano, Deep Subsurface Imaging in Tissues using Spectral and Polarization Filtering. *Optics Express,* **2000**, 7(1), 23-28.

99. S. Demos, H. Radousky, and R. Alfano, Deep subsurface imaging in tissues using spectral and polarization filtering. *Opt. Express,* **2000**, 7(1), 23-28.

100. G.J. Tearney, M.E. Brezinski, B.E. Bouma, S.A. Boppart, C. Pitris, J.F. Southern, and J.G. Fujimoto, In Vivo Endoscopic Optical Biopsy with Optical Coherence Tomography. *Science,* **1997**, 276(5321), 2037-2039.

101. I. Vanzetta and A. Grinvald, Increased Cortical Oxidative Metabolism Due to Sensory Stimulation: Implications for Functional Brain Imaging. *Science,* **1999**, 286(5444), 1555-1558.

102. D.L. Farkas and D. Becker, Applications of Spectral Imaging: Detection and Analysis of Human Melanoma and Its Precursors. *Pigment Cell Research,* **2001**, 14(1), 2.

103. A. Villringer and B. Chance, Non-invasive Optical Spectroscopy and Imaging of Human Brain Function. *Trends in Neurosciences,* **1997**, 20(10), 435-442.

104. V. Ntziachristos, A.G. Yodh, M.D. Schnall, and B. Chance, MRI-Guided Diffuse Optical Spectroscopy of Malignant and Benign Breast Lesions. *Neoplasia,* **2002**, 4(4), 347–354.

105. A.J. Kenyon, Recent Developments in Rare-earth Doped Materials for Optoelectronics. *Progress in Quantum Electronics,* **2002**, 26(4-5), 225-284.

106. G.H. Dieke, *Spectra and Energy Levels of Rare Earth Ions in Crystals* **1968**, New York, Interscience Publishers.

107. P.W. Atkins, *Physical Chemistry*. 2nd ed, **1983**, Oxford, Oxford University Press.

108. M. Michael Alexander and L.W. Kenneth, Investigations into the Physicochemical Properties of Dextran Small Particulate Gadolinium Oxide Nanoparticles. *Academic radiology,* **2006**, 13(4), 421-427.

109. M.-A. Fortin, R.M.P. Jr, F. Söderlind, A. Klasson, M. Engström, T. Veres, P.-O. Käll, and K. Uvdal, Polyethylene Glycol-covered Ultra-small Gd_2O_3 Nanoparticles for Positive Contrast at 1.5 T Magnetic Resonance Clinical Scanning. *Nanotechnology,* **2007**, 18(39), 395501.

110. F. Evanics, P.R. Diamente, F.C.J.M. van Veggel, G.J. Stanisz, and R.S. Prosser, Water-Soluble GdF_3 and GdF_3/LaF_3 NanoparticlesPhysical Characterization and NMR Relaxation Properties. *Chemistry of Materials,* **2006**, 18(10), 2499-2505.

111. Y.I. Park, K. Jeong Hyun, L. Kang Taek, J. Ki-Seok, N. Hyon Bin, Y. Jung Ho, K. Hyung Min, L. Nohyun, C. Seung Hong, B. Sung-Il, K. Hyoungsu, P. Seung Pyo, P. Beom-Jin, K. Young Woon, L. Sung Ho, Y. Soo-Young, S. In Chan, M. Woo Kyung, S. Yung Doug, and H. Taeghwan, Nonblinking and Nonbleaching Upconverting Nanoparticles as an Optical Imaging Nanoprobe and T1 Magnetic Resonance Imaging Contrast Agent. *Advanced Materials,* **2009**, 21(44), 4467-4471.

112. D. Deng, S. Xu, R. Bao, S. Zhao, B. Wang, H. Wang, and H. Ju, Blue cooperative upconversion in Yb 3+ -doped glass ceramic containing LiYF 4 nanocrystals. *Journal of Physics D: Applied Physics,* **2009**, 42(10), 105111.

113. E. Nakazawa and S. Shionoya, Cooperative Luminescence in $YbPO_4$. *Physical Review Letters,* **1970**, 25(25), 1710.

114. G. Blasse and B.C. Grabmaier, *Luminescent Materials*, **1994**, Berlin, Springer.

115. S. Heer, K. Kömpe, H.U. Güdel, and M. Haase, Highly Efficient Multicolour Upconversion Emission in Transparent Colloids of Lanthanide-Doped $NaYF_4$ Nanocrystals. *Advanced Materials,* **2004**, 16(23-24), 2102-2105.

116. Z.-G. Yan and C.-H. Yan, Controlled Synthesis of Rare Earth Nanostructures. *Journal of Materials Chemistry,* **2008**, 18(42), 5046-5059.

117. R. Bazzi, M.A. Flores, C. Louis, K. Lebbou, W. Zhang, C. Dujardin, S. Roux, B. Mercier, G. Ledoux, E. Bernstein, P. Perriat, and O. Tillement, Synthesis and Properties of Europium-based Phosphors on the Nanometer Scale: Eu_2O_3, Gd_2O_3:Eu, and Y_2O_3:Eu. *Journal of Colloid and Interface Science,* **2004**, 273(1), 191-197.

118. D. Dosev, B. Guo, and I.M. Kennedy, Photoluminescence of Eu^{3+}:Y_2O_3 as an Indication of Crystal Structure and Particle Size in Nanoparticles Synthesized by Flame Spray Pyrolysis. *Journal of Aerosol Science,* **2006**, 37(3), 402-412.

119. H. Wang, R. Wang, X. Sun, R. Yan, and Y. Li, Synthesis of Red-luminescent Eu^{3+}-doped Lanthanides Compounds Hollow Spheres. *Materials Research Bulletin,* **2005**, 40(6), 911-919.

120. H. Wang, M. Uehara, H. Nakamura, M. Miyazaki, and H. Maeda, Synthesis of Well-Dispersed Y_2O_3:Eu Nanocrystals and Self-Assembled Nanodisks Using a Simple Non-hydrolytic Route. *Advanced Materials,* **2005**, 17(20), 2506-2509.

121. B. Yan and X.-Q. Su, Chemical co-precipitation synthesis of luminescent $Bi_xY_{1-x}VO_4$: RE (RE = Eu^{3+}, Dy^{3+}, E^{r3+}) phosphors from hybrid precursors. *Journal of Non-Crystalline Solids,* **2006**, 352(30-31), 3275-3279.

122. W. Feng, X. Xuejia, and L. Xiaogang, Multicolor Tuning of (Ln, P)-Doped YVO_4 Nanoparticles by Single-Wavelength Excitation. *Angewandte Chemie International Edition,* **2008**, 47(5), 906-909.

123. P. Schuetz and F. Caruso, Electrostatically Assembled Fluorescent Thin Films of Rare-Earth-Doped Lanthanum Phosphate Nanoparticles. *Chemistry of Materials,* **2002**, 14(11), 4509-4516.

124. M. Bottrill, L. Kwok, and N.J. Long, Lanthanides in Magnetic Resonance Imaging. *Chemical Society Reviews,* **2006**, 35(6), 557-571.

125. A.O.G. Dikovska, P.A. Atanasov, M. Jiménez de Castro, A. Perea, J. Gonzalo, C.N. Afonso, and J. García López, Optically Active Er^{3+}-Yb^{3+} Codoped Y_2O_3 Films Produced by Pulsed Laser Deposition. *Thin Solid Films,* **2006**, 500(1-2), 336-340.

126. G.-S. Yi and G.-M. Chow, Colloidal LaF_3:Yb,Er, LaF_3:Yb,Ho and LaF_3:Yb,Tm Nanocrystals with Multicolor Upconversion Fluorescence. *Journal of Materials Chemistry,* **2005**, 15(41), 4460-4464.

127. L. Zhengquan and Z. Yong, Monodisperse Silica-Coated Polyvinylpyrrolidone/$NaYF_4$ Nanocrystals with Multicolor Upconversion Fluorescence Emission. *Angewandte Chemie International Edition,* **2006**, 45(46), 7732-7735.

128. F. Wang and X. Liu, Upconversion Multicolor Fine-Tuning: Visible to Near-Infrared Emission from Lanthanide-Doped $NaYF_4$ Nanoparticles. *Journal of the American Chemical Society,* **2008**, 130(17), 5642-5643.

129. J.W. Stouwdam and F.C.J.M. van Veggel, Near-infrared Emission of Redispersible Er^{3+}, Nd^{3+}, and Ho^{3+} Doped LaF_3 Nanoparticles. *Nano Letters,* **2002**, 2(7), 733-737.

130. H. Stephan, L. Olaf, H. Markus, and G. Hans-Ulrich, Blue, Green, and Red Upconversion Emission from Lanthanide-Doped $LuPO_4$ and $YbPO_4$ Nanocrystals in a Transparent Colloidal Solution. *Angewandte Chemie International Edition,* **2003**, 42(27), 3179-3182.

131. H.-X. Mai, Y.-W. Zhang, R. Si, Z.-G. Yan, L.-d. Sun, L.-P. You, and C.-H. Yan, High-Quality Sodium Rare-Earth Fluoride Nanocrystals: Controlled Synthesis and Optical Properties. *Journal of the American Chemical Society,* **2006**, 128(19), 6426-6436.

132. J.-C. Boyer, L.A. Cuccia, and J.A. Capobianco, Synthesis of Colloidal Upconverting $NaYF_4$: Er^{3+}/Yb^{3+} and Tm^{3+}/Yb^{3+} Monodisperse Nanocrystals. *Nano Letters,* **2007**, 7(3), 847-852.

133. Y.-W. Zhang, X. Sun, R. Si, L.-P. You, and C.-H. Yan, Single-Crystalline and Monodisperse LaF_3 Triangular Nanoplates from a Single-Source Precursor. *Journal of the American Chemical Society,* **2005**, 127(10), 3260-3261.

134. L. Wang and Y. Li, Controlled Synthesis and Luminescence of Lanthanide Doped $NaYF_4$ Nanocrystals. *Chemistry of Materials,* **2007**, 19(4), 727-734.

135. C. Liu and D. Chen, Controlled Synthesis of Hexagon Shaped Lanthanide-doped LaF_3 Nanoplates with Multicolor Upconversion Fluorescence. *Journal of Materials Chemistry,* **2007**, 17(37), 3875-3880.

136. Y. Wei, F. Lu, X. Zhang, and D. Chen, Polyol-mediated Synthesis and Luminescence of Lanthanide-doped $NaYF_4$ Nanocrystal Upconversion Phosphors. *Journal of Alloys and Compounds,* **2008**, 455(1-2), 376-384.

137. V. Venkatramu, D. Falcomer, A. Speghini, M. Bettinelli, and C.K. Jayasankar, Synthesis and Luminescence Properties of Er^{3+}-doped $Lu_3Ga_5O_{12}$ Nanocrystals. *Journal of Luminescence,* **2008**, 128(5-6), 811-813.

138. A. Patra, C.S. Friend, R. Kapoor, and P.N. Prasad, Fluorescence Upconversion Properties of Er^{3+}-Doped TiO_2 and $BaTiO_3$ Nanocrystallites. *Chemistry of Materials,* **2003**, 15(19), 3650-3655.

139. Y. Kuisheng, Z. Fang, W. Rina, L. Hansheng, and Z. Xiyan, Upconversion Luminescent Properties of YVO_4:Yb^{3+}, Er^{3+} Nano-Powder by Sol-Gel Method. *Journal of Rare Earths,* **2006**, 24(1, Supplement 1), 162-166.

140. F. Vetrone, J.-C. Boyer, J.A. Capobianco, A. Speghini, and M. Bettinelli, Significance of Yb^{3+} Concentration on the Upconversion Mechanisms in

Codoped Y_2O_3:Er^{3+},Yb^{3+} Nanocrystals. *Journal of Applied Physics,* **2004**, 96(1), 661-667.

141. J. Semmel, L. Nahle, S. Hofling, and A. Forchel, Edge Emitting Quantum Cascade Microlasers on InP with Deeply Etched One-dimensional Photonic Crystals. *Applied Physics Letters,* **2007**, 91(7), 071104-3.

142. H.-X. Mai, Y.-W. Zhang, L.-D. Sun, and C.-H. Yan, Highly Efficient Multicolor Up-Conversion Emissions and Their Mechanisms of Monodisperse $NaYF_4$:Yb,Er Core and Core/Shell-Structured Nanocrystals. *The Journal of Physical Chemistry C,* **2007**, 111(37), 13721-13729.

143. G.-S. Yi and G.-M. Chow, Water-Soluble NaYF4:Yb,Er(Tm)/NaYF4/Polymer Core/Shell/Shell Nanoparticles with Significant Enhancement of Upconversion Fluorescence. *Chemistry of Materials,* **2006**, 19(3), 341-343.

144. Q. Lu, F. Guo, L. Sun, A. Li, and L. Zhao, Silica-/Titania-coated Y_2O_3:Tm^{3+},Yb^{3+} Nanoparticles with Improvement in Upconversion Luminescence Induced by Different Thickness Shells. *Journal of Applied Physics,* **2008**, 103(12), 123533-10.

145. G.S. Yi and G.M. Chow, Synthesis of Hexagonal-Phase $NaYF_4$:Yb,Er and $NaYF_4$:Yb,Tm Nanocrystals with Efficient Up-Conversion Fluorescence. *Advanced Functional Materials,* **2006**, 16(18), 2324-2329.

146. Z. Chen, H. Chen, H. Hu, M. Yu, F. Li, Q. Zhang, Z. Zhou, T. Yi, and C. Huang, Versatile Synthesis Strategy for Carboxylic Acid Functionalized Upconverting Nanophosphors as Biological Labels. *Journal of the American Chemical Society,* **2008**, 130(10), 3023-3029.

147. H. Hu, M. Yu, F. Li, Z. Chen, X. Gao, L. Xiong, and C. Huang, Facile Epoxidation Strategy for Producing Amphiphilic Up-Converting Rare-Earth

Nanophosphors as Biological Labels. *Chemistry of Materials,* **2008**, 20(22), 7003-7009.

148. G.-S. Yi and G.-M. Chow, Water-Soluble $NaYF_4$:Yb,Er(Tm)/$NaYF_4$/Polymer Core/Shell/Shell Nanoparticles with Significant Enhancement of Upconversion Fluorescence. *Chemistry of Materials,* **2007**, 19(3), 341-343.

149. L. Wang, Y. Ruoxue, H. Ziyang, W. Lun, Z. Jinghui, B. Jie, W. Xun, P. Qing, and L. Yadong, Fluorescence Resonant Energy Transfer Biosensor Based on Upconversion-Luminescent Nanoparticles. *Angewandte Chemie International Edition,* **2005**, 44(37), 6054-6057.

150. W. Stöber, A. Fink, and E. Bohn, Controlled Growth of Monodisperse Silica Spheres in the Micron Size Range. *Journal of Colloid and Interface Science,* **1968**, 26(1), 62-69.

151. Z. Liu, G. Yi, H. Zhang, J. Ding, Y. Zhang, and J. Xue, Monodisperse Silica Nanoparticles Encapsulating Upconversion Fluorescent and Superparamagnetic Nanocrystals. *Chemical Communications,* **2008**(6), 694-696.

152. X. Younan, Y. Xiong, L. Byungkwon, and E.S. Sara Shape-Controlled Synthesis of Metal Nanocrystals: Simple Chemistry Meets Complex Physics? *Angewandte Chemie International Edition,* **2009**, 48(1), 60-103.

153. J. Young-wook, C. Jin-sil, and C. Jinwoo, Shape Control of Semiconductor and Metal Oxide Nanocrystals through Nonhydrolytic Colloidal Routes. *Angewandte Chemie International Edition,* **2006**, 45(21), 3414-3439.

154. R.T. Andrea, H. Susan, and Y. Peidong, Shape Control of Colloidal Metal Nanocrystals. *Small,* **2008**, 4(3), 310-325.

155. V.F. Puntes, K.M. Krishnan, and A.P. Alivisatos, Colloidal Nanocrystal Shape and Size Control: The Case of Cobalt. *Science,* **2001**, 291(5511), 2115-2117.

156. A. Nel, T. Xia, L. Madler, and N. Li, Toxic Potential of Materials at the Nanolevel. *Science,* **2006**, 311(5761), 622-627.

157. N. Lewinski, V. Colvin, and R. Drezek, Cytotoxicity of Nanoparticles. *Small,* **2008**, 4(1), 26-49.

158. M.R. Gwinn and V. Vallyathan, Nanoparticles: Health Effects—Pros and Cons. *Environmental Health Perspectives,* **2006**, 114(12), 1818-1825.

159. Y. Zhao and H.S. Nalwa, *Nanotoxicology*, **2007**, California, American Scientific Publlishers.

160. H. Kimura, T. Sawada, S. Oshima, K. Kozawa, T. Ishioka, and M. Kato, Toxicity and Roles of Reactive Oxygen Species. *Current Drug Targets - Inflammation & Allergy,* **2005**, 4, 489-495.

161. K.D. Pickering and M.R. Wiesner, Fullerol-Sensitized Production of Reactive Oxygen Species in Aqueous Solution. *Environmental Science & Technology,* **2005**, 39(5), 1359-1365.

162. H. Zhou, X. Gan, T. Liu, Q. Yang, and G. Li, Electrochemical Study of Photovoltaic Effect of Nano Titanium Dioxide on Hemoglobin. *Bioelectrochemistry,* **2006**, 69(1), 34-40.

163. A.M. Derfus, W.C.W. Chan, and S.N. Bhatia, Probing the Cytotoxicity of Semiconductor Quantum Dots. *Nano Letters,* **2004**, 4(1), 11-18.

164. A.C.S. Samia, X. Chen, and C. Burda, Semiconductor Quantum Dots for Photodynamic Therapy. *Journal of the American Chemical Society,* **2003**, 125(51), 15736-15737.

165. I. Binil Itty, L. Manfred, and M.N. Christof On the Generation of Free Radical Species from Quantum Dots. *Small,* **2005**, 1(7), 706-709.

166. M. Green and E. Howman, Semiconductor Quantum Dots and Free Radical Induced DNA Nicking. *Chemical Communications,* **2005**(1), 121-123.

167. A.A. Shvedova, V. Castranova, E.R. Kisin, D. Schwegler-Berry, A.R. Murray, V.Z. Gandelsman, A. Maynard, and P. Baron, Exposure to Carbon Nanotube Material: Assessment of Nanotube Cytotoxicity using Human Keratinocyte Cells. *Journal of Toxicology & Environmental Health: Part A,* **2003**, 66(20), 1909.

168. S.M. Hussain, K.L. Hess, J.M. Gearhart, K.T. Geiss, and J.J. Schlager, In vitro Toxicity of Nanoparticles in BRL 3A Rat Liver Cells. *Toxicology in Vitro,* **2005**, 19(7), 975-983.

169. C. Krieger and M.R. Duchen, Mitochondria, Ca^{2+} and Neurodegenerative Disease. *European Journal of Pharmacology,* **2002**, 447(2-3), 177-188.

170. R. Savic, L. Luo, A. Eisenberg, and D. Maysinger, Micellar Nanocontainers Distribute to Defined Cytoplasmic Organelles. *Science,* **2003**, 300(5619), 615-618.

171. S. Foley, C. Crowley, M. Smaihi, C. Bonfils, B.F. Erlanger, P. Seta, and C. Larroque, Cellular Localisation of a Water-Soluble Fullerene Derivative. *Biochemical and Biophysical Research Communications,* **2002**, 294(1), 116-119.

172. J.G. Rouse, J. Yang, A.R. Barron, and N.A. Monteiro-Riviere, Fullerene-based Amino Acid Nanoparticle Interactions with Human Epidermal Keratinocytes. *Toxicology in Vitro,* **2006**, 20(8), 1313-1320.

173. K. Pulskamp, S. Diabaté, and H.F. Krug, Carbon Nanotubes Show No Sign of Acute Toxicity but Induce Intracellular Reactive Oxygen Species in Dependence on Contaminants. *Toxicology Letters,* **2007**, 168(1), 58-74.

174. P. Wick, P. Manser, L.K. Limbach, U. Dettlaff-Weglikowska, F. Krumeich, S. Roth, W.J. Stark, and A. Bruinink, The Degree and Kind of Agglomeration

Affect Carbon Nanotube Cytotoxicity. *Toxicology Letters,* **2007**, 168(2), 121-131.

175. S.K. Manna, S. Sarkar, J. Barr, K. Wise, E.V. Barrera, O. Jejelowo, A.C. Rice-Ficht, and G.T. Ramesh, Single-Walled Carbon Nanotube Induces Oxidative Stress and Activates Nuclear Transcription Factor-Î°B in Human Keratinocytes. *Nano Letters,* **2005**, 5(9), 1676-1684.

176. A.G. Tkachenko, H. Xie, Y. Liu, D. Coleman, J. Ryan, W.R. Glomm, M.K. Shipton, S. Franzen, and D.L. Feldheim, Cellular Trajectories of Peptide-Modified Gold Particle Complexes: Comparison of Nuclear Localization Signals and Peptide Transduction Domains. *Bioconjugate Chemistry,* **2004**, 15(3), 482-490.

177. C.-H. Su, H.-S. Sheu, C.-Y. Lin, C.-C. Huang, Y.-W. Lo, Y.-C. Pu, J.-C. Weng, D.-B. Shieh, J.-H. Chen, and C.-S. Yeh, Nanoshell Magnetic Resonance Imaging Contrast Agents. *Journal of the American Chemical Society,* **2007**, 129(7), 2139-2146.

178. T.B. Huff, M.N. Hansen, Y. Zhao, J.-X. Cheng, and A. Wei, Controlling the Cellular Uptake of Gold Nanorods. *Langmuir,* **2007**, 23(4), 1596-1599.

179. T. Niidome, M. Yamagata, Y. Okamoto, Y. Akiyama, H. Takahashi, T. Kawano, Y. Katayama, and Y. Niidome, PEG-modified Gold Nanorods with a Stealth Character for in vivo Applications. *Journal of Controlled Release,* **2006**, 114(3), 343-347.

180. A. Petri-Fink, M. Chastellain, L. Juillerat-Jeanneret, A. Ferrari, and H. Hofmann, Development of Functionalized Superparamagnetic Iron Oxide Nanoparticles for Interaction with Human Cancer Cells. *Biomaterials,* **2005**, 26(15), 2685-2694.

181. W. Shourong, H. Junsheng, G. Miao, Z. Hongkai, C. Youjia, Y. Husheng, and L. Keliang, Biocompatible superparamagnetic iron oxide nanoparticle dispersions stabilized with poly(ethylene glycol)-oligo(aspartic acid) hybrids. *Journal of Biomedical Materials Research Part A,* **2007**, 80A(4), 946-954.

182. H. Duan and S. Nie, Cell-Penetrating Quantum Dots Based on Multivalent and Endosome-Disrupting Surface Coatings. *Journal of the American Chemical Society,* **2007**, 129(11), 3333-3338.

183. C. Emmanuel, T. Nadhi, W.Y. William , L.C. Vicki , and D. Rebekah, Evaluation of Quantum Dot Cytotoxicity Based on Intracellular Uptake. *Small,* **2006**, 2(12), 1412-1417.

184. J.K. Jaiswal, H. Mattoussi, J.M. Mauro, and S.M. Simon, Long-term Multiple Color Imaging of Live Cells Using Quantum Dot Bioconjugates. *Nature Biotechnology,* **2003**, 21(1), 47-51.

185. S. Nie, Y. Xing, G.J. Kim, and J.W. Simons, Nanotechnology Applications in Cancer. *Annual Review of Biomedical Engineering,* **2007**, 9(1), 257-288.

186. D.B. Williams and B.C. Carter, *Electron Microscopy: A Textbook for Materials Science*, **1996**, New York, Plenum Press.

187. R.F. Egerton, *Electron Energy Loss Spectroscopy in the Electron Microscope*, **1996**, New York, Plenum Press.

188. G.J. Shugar, J.A. Dean, and R.A. Shugar, *The Chemist's Ready Reference Handbook*, **1990**, New York, McGraw-Hill Inc.

189. A.L. Patterson, The Scherrer Formula for X-Ray Particle Size Determination. *Physical Review,* **1939**, 56(10), 978-982.

190. J.F. Moulder, W.F. Stickle, P.E. Sobol, and K.D. Bomben, *Handbook of X-ray Photoelectron Spectroscopy*, **1992**, Eden Prairie, Perkin Elmer.

191. B.H. Stuart, *Infrared Spectroscopy: Fundamentals and Applications*, **2004**, New York, John Wiley & Sons, Ltd.

192. G.W. Ewing, *Instrumental Methods of Chemical Analysis*. 5th ed, **1985**, Singapore, McGraw-Hill Book Co.

193. R.J. Hunter, *Foundations of Colloid Science*. 2nd ed, **2001**, New York, Oxford University Press, Inc.

194. A. Agresti and B. Finlay, *Statistical Methods for the Social Sciences*. 2nd ed, **1986**, San Francisco, Dellen Publishing Company.

195. W. Mendenhall and T. Sincich, *Statistics for Engineering and the Sciences*, **2007**, New Jersey, Pearson Prentice Hall.

196. S. Coe, W.-K. Woo, M. Bawendi, and V. Bulovic, Electroluminescence from Single Monolayers of Nanocrystals in Molecular Organic Devices. *Nature,* **2002**, 420(6917), 800-803.

197. M. Bruchez, Jr., M. Moronne, P. Gin, S. Weiss, and A.P. Alivisatos, Semiconductor Nanocrystals as Fluorescent Biological Labels. *Science,* **1998**, 281(5385), 2013-2016.

198. W.C. Chan, nbsp, W, and S. Nie, Quantum Dot Bioconjugates for Ultrasensitive Nonisotopic Detection. *Science,* **1998**, 281(5385), 2016-2018.

199. H. Mattoussi, J.M. Mauro, E.R. Goldman, G.P. Anderson, V.C. Sundar, F.V. Mikulec, and M.G. Bawendi, Self-Assembly of CdSe-ZnS Quantum Dot Bioconjugates Using an Engineered Recombinant Protein. *Journal of the American Chemical Society,* **2000**, 122(49), 12142-12150.

200. T.T. Tan, S.T. Selvan, L. Zhao, S. Gao, and J.Y. Ying, Size Control, Shape Evolution, and Silica Coating of Near-Infrared-Emitting PbSe Quantum Dots. *Chemistry of Materials,* **2007**, 19(13), 3112-3117.

201. J. Liang, Z. He, S. Zhang, S. Huang, X. Ai, H. Yang, and H. Han, Study on DNA Damage Induced by CdSe Quantum Dots using Nucleic Acid Molecular "light switches" as Probe. *Talanta,* **2007**, 71(4), 1675-1678.

202. G. Guo, W. Liu, J. Liang, Z. He, H. Xu, and X. Yang, Probing the Cytotoxicity of CdSe Quantum Dots with Surface Modification. *Materials Letters,* **2007**, 61(8-9), 1641-1644.

203. W.O. Gordon, J.A. Carter, and B.M. Tissue, Long-lifetime Luminescence of Lanthanide-doped Gadolinium Oxide Nanoparticles for Immunoassays. *Journal of Luminescence,* **2004**, 108(1-4), 339-342.

204. M. Nichkova, D. Dosev, S.J. Gee, B.D. Hammock, and I.M. Kennedy, Microarray Immunoassay for Phenoxybenzoic Acid Using Polymer Encapsulated Eu:Gd_2O_3 Nanoparticles as Fluorescent Labels. *Analytical Chemistry,* **2005**, 77(21), 6864-6873.

205. G. Yi, H. Lu, S. Zhao, Y. Ge, W. Yang, D. Chen, and L.-H. Guo, Synthesis, Characterization, and Biological Application of Size-Controlled Nanocrystalline $NaYF_4$:Yb,Er Infrared-to-Visible Up-Conversion Phosphors. *Nano Letters,* **2004**, 4(11), 2191-2196.

206. F. Vetrone, J.C. Boyer, J.A. Capobianco, A. Speghini, and M. Bettinelli, Effect of Yb^{3+} Codoping on the Upconversion Emission in Nanocrystalline Y_2O3:Er^{3+}. *The Journal of Physical Chemistry B,* **2003**, 107(5), 1107-1112.

207. R.E. Muenchausen, L.G. Jacobsohn, B.L. Bennett, E.A. McKigney, J.F. Smith, J.A. Valdez, and D.W. Cooke, Effects of Tb doping on the photoluminescence of Y2O3:Tb nanophosphors. *Journal of Luminescence,* **2007**, 126(2), 838-842.

208. A. Camenzind, R. Strobel, and S.E. Pratsinis, Cubic or Monoclinic Y_2O_3:Eu^{3+} Nanoparticles by One Step Flame Spray Pyrolysis. *Chemical Physics Letters,* **2005**, 415(4-6), 193-197.

209. R. Si, Y.-W. Zhang, H.-P. Zhou, L.-D. Sun, and C.-H. Yan, Controlled-Synthesis, Self-Assembly Behavior, and Surface-Dependent Optical Properties of High-Quality Rare-Earth Oxide Nanocrystals. *Chemistry of Materials,* **2007**, 19(1), 18-27.

210. S. Zeng, K. Tang, T. Li, and Z. Liang, 3D flower-like Y_2O_3:Eu^{3+} nanostructures: Template-free Synthesis and Its Luminescence Properties. *Journal of Colloid and Interface Science,* **2007**, 316(2), 921-929.

211. S. Yin, M. Shinozaki, and T. Sato, Synthesis and Characterization of Wire-like and Near-spherical Eu_2O_3-doped Y_2O_3 Phosphors by Solvothermal Reaction. *Journal of Luminescence,* **2007**, 126(2), 427-433.

212. S. Polizzi, M. Battagliarin, M. Bettinelli, A. Speghini, and G. Fagherazzi, Investigation on Lanthanide-doped Y_2O_3 Nanopowders Obtained by Wet Chemical Synthesis. *Journal of Materials Chemistry,* **2002**, 12(3), 742-747.

213. R.L. Penn and J.F. Banfield, Imperfect Oriented Attachment: Dislocation Generation in Defect-Free Nanocrystals. *Science,* **1998**, 281(5379), 969-971.

214. J.F. Banfield, S.A. Welch, H. Zhang, T.T. Ebert, and R.L. Penn, Aggregation-Based Crystal Growth and Microstructure Development in Natural Iron Oxyhydroxide Biomineralization Products. *Science,* **2000**, 289(5480), 751-754.

215. K.-S. Cho, D.V. Talapin, W. Gaschler, and C.B. Murray, Designing PbSe Nanowires and Nanorings through Oriented Attachment of Nanoparticles. *Journal of the American Chemical Society,* **2005**, 127(19), 7140-7147.

216. R. Si, Y.-W. Zhang, L.-P. You, and C.-H. Yan, Rare-Earth Oxide Nanopolyhedra, Nanoplates, and Nanodisks. *Angewandte Chemie International Edition,* **2005**, 44(21), 3256-3260.

217. P.T.K. Chin, J.W. Stouwdam, and R.A.J. Janssen, Highly Luminescent Ultranarrow Mn Doped ZnSe Nanowires. *Nano Letters,* **2009**, 9(2), 745-750.

218. J. Park, K. An, Y. Hwang, J.G. Park, H.J. Noh, J.Y. Kim, J.H. Park, N.M. Hwang, and T. Hyeon, Ultra-large-scale Syntheses of Monodisperse Nanocrystals. *Nature Materials,* **2004**, 3(12), 891-895.

219. Y.C. Cao, Synthesis of Square Gadolinium-Oxide Nanoplates. *Journal of the American Chemical Society,* **2004**, 126(24), 7456-7457.

220. L. Manna, E.C. Scher, and A.P. Alivisatos, Synthesis of Soluble and Processable Rod-, Arrow-, Teardrop-, and Tetrapod-Shaped CdSe Nanocrystals. *Journal of the American Chemical Society,* **2000**, 122(51), 12700-12706.

221. E.T. Goldburt, B. Kulkarni, R.N. Bhargava, J. Taylor, and M. Libera, Size Dependent Efficiency in Tb Doped Y_2O_3 Nanocrystalline Phosphor. *Journal of Luminescence,* **1997**, 72-74, 190-192.

222. G. Yi, B. Sun, F. Yang, D. Chen, Y. Zhou, and J. Cheng, Synthesis and Characterization of High-Efficiency Nanocrystal Up-Conversion Phosphors: Ytterbium and Erbium Codoped Lanthanum Molybdate. *Chemistry of Materials,* **2002**, 14(7), 2910-2914.

223. J.-H. Park, N.G. Back, M.-G. Kwak, B.-E. Jun, B.-C. Choi, B.-K. Moon, J.-H. Jeong, S.-S. Yi, and J.-B. Kim, Synthesis and Properties of Luminescent Y_2O_3:Tb^{3+} (5, 8, 12 wt.%) nanocrystals. *Materials Science and Engineering: C,* **2007**, 27(5-8), 998-1001.

224. Q. Pang, J. Shi, Y. Liu, D. Xing, M. Gong, and N. Xu, A Novel Approach for Preparation of Y_2O_3:Eu^{3+} Nanoparticles by Microemulsion-Microwave Heating. *Materials Science and Engineering B,* **2003**, 103(1), 57-61.

225. P.K. Sharma, M.H. Jilavi, R. Nass, and H. Schmidt, Tailoring the Particle Size from um-->nm Scale by Using a Surface Modifier and Their Size Effect on the Fluorescence Properties of Europium Doped Yttria. *Journal of Luminescence,* **1999**, 82(3), 187-193.

226. A. Pires, S. Heer, H. Güdel, and O. Serra, Er, Yb Doped Yttrium Based Nanosized Phosphors: Particle Size, “Host Lattice” and Doping Ion Concentration Effects on Upconversion Efficiency. *Journal of Fluorescence,* **2006**, 16(3), 461-468.

227. Z. Liu, X. Sun, S. Xu, J. Lian, X. Li, Z. Xiu, Q. Li, D. Huo, and J.-G. Li, Tb^{3+}- and Eu^{3+}-Doped Lanthanum Oxysulfide Nanocrystals. Gelatin-Templated Synthesis and Luminescence Properties. *The Journal of Physical Chemistry C,* **2008**, 112(7), 2353-2358.

228. C. Wu and Y. Wang, Hydrothermal Synthesis and Luminescent Properties of (La,Gd)PO_4:Tb Phosphors under VUV Excitation. *Materials Letters,* **2007**, 61(11-12), 2416-2418.

229. C.-S. Park, M.-G. Kwak, S.-S. Choi, Y.-S. Song, S.-J. Hong, J.-I. Han, and D.Y. Lee, Influence of Eu^{3+} Doping Content on Photoluminescence of Gd_2O_3:Eu^{3+} Phosphors Prepared by Liquid-phase Reaction Method. *Journal of Luminescence,* **2006**, 118(2), 199-204.

230. X. Liu and X. Wang, Preparation and Luminescence Properties of $BaZrO_3$:Eu Phosphor Powders. *Optical Materials,* **2007**, 30(4), 626-629.

231. H. Lei, Q. Yang, H. Ou, B. Chen, J. Yu, Q. Wang, D. Xie, J. Wu, D.-F. Xu, and G.-X. Xu, *Preparation and characterization of erbium-doped sol-gel silica glasses*, in *Rare-Earth-Doped Materials and Devices III.* 1999, SPIE: San Jose, CA, USA. p. 74-80.

232. B.-C. Hwang, S. Jiang, T. Luo, J. Watson, G. Sorbello, and N. Peyghambarian, Cooperative Upconversion and Energy Transfer of New High Er^{3+}- and Yb^{3+}/Er^{3+}-doped Phosphate Glasses. *Journal of the Optical Society of America B,* **2000**, 17(5), 833-839.

233. S.F. Wuister, A.V. Houselt, C.d.M. Donegá, D. Vanmaekelbergh, and A. Meijerink, Temperature Antiquenching of the Luminescence from Capped CdSe Quantum Dots. *Angewandte Chemie International Edition,* **2004**, 43(23), 3029-3033.

234. D.V. Talapin, A.L. Rogach, A. Kornowski, M. Haase, and H. Weller, Highly Luminescent Monodisperse CdSe and CdSe/ZnS Nanocrystals Synthesized in a Hexadecylamine-Trioctylphosphine Oxide-Trioctylphospine Mixture. *Nano Letters,* **2001**, 1(4), 207-211.

235. C. de Mello Donega, S.G. Hickey, S.F. Wuister, D. Vanmaekelbergh, and A. Meijerink, Single-Step Synthesis to Control the Photoluminescence Quantum Yield and Size Dispersion of CdSe Nanocrystals. *The Journal of Physical Chemistry B,* **2002**, 107(2), 489-496.

236. G.M. Salley, R. Valiente, and H.U. Guedel, Luminescence Upconversion Mechanisms in Yb^{3+}-Tb^{3+} Systems. *Journal of Luminescence,* **2001**, 94-95, 305-309.

237. H. Guo, N. Dong, M. Yin, W. Zhang, L. Lou, and S. Xia, Visible Upconversion in Rare Earth Ion-Doped Gd_2O_3 Nanocrystals. *The Journal of Physical Chemistry B,* **2004**, 108(50), 19205-19209.

238. H. Lin, G. Meredith, S. Jiang, X. Peng, T. Luo, N. Peyghambarian, and E.Y.-B. Pun, Optical Transitions and Visible Upconversion in Er^{3+} Doped Niobic Tellurite Glass. *Journal of Applied Physics,* **2003**, 93(1), 186-191.

239. A. Nayak, R. Sahoo, and R. Debnath, Hydration-induced Coupling of the Excitonic State of Y_2O_3 with its Phonon: Negative Effect on the Luminescence Efficiency of $Y_2O_3:Eu^{+3}$ Nanophosphor. *Journal of Materials Research,* **2007**, 22(1), 35-39.

240. A.S. Maria Chong and X.S. Zhao, Functionalization of SBA-15 with APTES and Characterization of Functionalized Materials. *The Journal of Physical Chemistry B,* **2003**, 107(46), 12650-12657.

241. L.D. White and C.P. Tripp, Reaction of (3-Aminopropyl)dimethylethoxysilane with Amine Catalysts on Silica Surfaces. *Journal of Colloid and Interface Science,* **2000**, 232(2), 400-407.

242. A. Hoshino, K. Fujioka, T. Oku, M. Suga, Y.F. Sasaki, T. Ohta, M. Yasuhara, K. Suzuki, and K. Yamamoto, Physicochemical Properties and Cellular Toxicity of Nanocrystal Quantum Dots Depend on Their Surface Modification. *Nano Letters,* **2004**, 4(11), 2163-2169.

243. J.-W. Choi, T.M. Liakopoulos, and C.H. Ahn, An On-chip Magnetic Bead Separator using Spiral Electromagnets with Semi-encapsulated Permalloy. *Biosensors and Bioelectronics,* **2001**, 16(6), 409-416.

244. C. Bergemann, D. Müller-Schulte, J. Oster, L. à Brassard, and A.S. Lübbe, Magnetic Ion-exchange Nano- and Microparticles for Medical, Biochemical and

Molecular Biological Applications. *Journal of Magnetism and Magnetic Materials,* **1999**, 194(1-3), 45-52.

245. R. Weissleder, A. Moore, U. Mahmood, R. Bhorade, H. Benveniste, E.A. Chiocca, and J.P. Basilion, In vivo Magnetic Resonance Imaging of Transgene Expression. *Nature Medicine,* **2000**, 6(3), 351-354.

246. W.S. Enochs, H. Griffith, H. Fred, and W. Ralph, Improved Delineation of Human Brain Tumors on MR Images Using a Long-circulating, Superparamagnetic Iron Oxide Agent. *Journal of Magnetic Resonance Imaging,* **1999**, 9(2), 228-232.

247. Y. Zhang, N. Kohler, and M. Zhang, Surface Modification of Superparamagnetic Magnetite Nanoparticles and Their Intracellular Uptake. *Biomaterials,* **2002**, 23(7), 1553-1561.

248. O.S. Nielsen, M. Horsman, and J. Overgaard, A Future for Hyperthermia in Cancer Treatment? *European Journal of Cancer,* **2001**, 37(13), 1587-1589.

249. C.F.C. Daniel, B.K. Dmitri, and A.B.J. Paul, Synthesis and Evaluation of Colloidal Magnetic Iron Oxides for the Site-specific Radiofrequency-induced Hyperthermia of Cancer. *Journal of Magnetism and Magnetic Materials,* **1993**, 122(1-3), 374-378.

250. D.R. Baselt, G.U. Lee, M. Natesan, S.W. Metzger, P.E. Sheehan, and R.J. Colton, A Biosensor Based on Magnetoresistance Technology. *Biosensors and Bioelectronics,* **1998**, 13(7-8), 731-739.

251. W.J.M. Mulder, A.W. Griffioen, G.J. Strijkers, D.P. Cormode, K. Nicolay, and Z.A. Fayad, Magnetic and Fluorescent Nanoparticles for Multimodality Imaging. *Nanomedicine,* **2007**, 2(3), 307-324.

252. D. Wang, J. He, N. Rosenzweig, and Z. Rosenzweig, Superparamagnetic Fe_2O_3 Beads-CdSe/ZnS Quantum Dots Core-Shell Nanocomposite Particles for Cell Separation. *Nano Letters,* **2004**, 4(3), 409-413.

253. B.O. Dabbousi, J. Rodriguez-Viejo, F.V. Mikulec, J.R. Heine, H. Mattoussi, R. Ober, K.F. Jensen, and M.G. Bawendi, (CdSe)ZnS Core-Shell Quantum Dots: Synthesis and Characterization of a Size Series of Highly Luminescent Nanocrystallites. *The Journal of Physical Chemistry B,* **1997**, 101(46), 9463-9475.

254. M.A. Hines and P. Guyot-Sionnest, Synthesis and Characterization of Strongly Luminescing ZnS-Capped CdSe Nanocrystals. *The Journal of Physical Chemistry,* **1996**, 100(2), 468-471.

255. H.P. Klug and L.E. Alexander, *X-ray Diffraction Procedures*, **1959**, New York, John Wiley.

256. X. Teng, D. Black, N.J. Watkins, Y. Gao, and H. Yang, Platinum-Maghemite Core-Shell Nanoparticles Using a Sequential Synthesis. *Nano Letters,* **2003**, 3(2), 261-264.

257. B.H. Sohn and R.E. Cohen, Processible Optically Transparent Block Copolymer Films Containing Superparamagnetic Iron Oxide Nanoclusters. *Chemistry of Materials,* **1997**, 9(1), 264-269.

258. K.I. Gnanasekar, P. Selvam, H.V. Keer, R. Pinto, S.C. Purandare, A.S. Tamhane, L.C. Gupta, and R. Vijayaraghavan, Superconductivity and Valence State of Tb in $Lu_{1-x}Tb_xBa_2Cu_3O_{7-X}$ ($0 <= x <= 0.7$). *Applied Physics Letters,* **1994**, 65(10), 1296-1298.

259. A.S. Pereira, M. Peres, M.J. Soares, E. Alves, A. Neves, T. Monteiro, and T. Trindade, Synthesis, Surface Modification and Optical Properties of Tb^{3+}-doped ZnO Nanocrystals. *Nanotechnology,* **2006**, 17(3), 834.

260. I. prigogine and S.A. Rice, *Advances in Chemical Physics*. Vol. 98, **1997**, New York, John Willey & Sons Inc.

261. S. Sun and H. Zeng, Size-Controlled Synthesis of Magnetite Nanoparticles. *Journal of the American Chemical Society,* **2002**, 124(28), 8204-8205.

262. R.H. Kodama, A.E. Berkowitz, J.E.J. McNiff, and S. Foner, Surface Spin Disorder in $NiFe_2O_4$ Nanoparticles. *Physical Review Letters,* **1996**, 77(2), 394.

263. C. Sun, J.S.H. Lee, and M. Zhang, Magnetic nanoparticles in MR imaging and drug delivery. *Advanced Drug Delivery Reviews,* **2008**, 60(11), 1252-1265.

264. D.E. Sosnovik and R. Weissleder, Emerging concepts in molecular MRI. *Current Opinion in Biotechnology,* **2007**, 18(1), 4-10.

265. D. Sosnovik, M. Nahrendorf, and R. Weissleder, Magnetic nanoparticles for MR imaging: agents, techniques and cardiovascular applications. *Basic Research in Cardiology,* **2008**, 103(2), 122-130.

266. J.W.M. Bulte and D.L. Kraitchman, Iron Oxide MR Contrast Agents for Molecular and Cellular Imaging. *NMR in Biomedicine,* **2004**, 17(7), 484-499.

267. H.-J. Weinmann, W. Ebert, B. Misselwitz, and H. Schmitt-Willich, Tissue-specific MR Contrast Agents. *European Journal of Radiology,* **2003**, 46(1), 33-44.

268. A.M. Morawski, G.A. Lanza, and S.A. Wickline, Targeted Contrast Agents for Magnetic Resonance Imaging and Ultrasound. *Current Opinion in Biotechnology,* **2005**, 16(1), 89-92.

269. R.L. Penn and J.F. Banfield, Morphology Development and Crystal Growth in Nanocrystalline Aggregates under Hydrothermal Conditions: Insights from Titania. *Geochimica et Cosmochimica Acta,* **1999**, 63(10), 1549-1557.

270. C. Pacholski and A.K.H. Weller, Self-Assembly of ZnO: From Nanodots to Nanorods. *Angewandte Chemie International Edition,* **2002**, 41(7), 1188-1191.

271. M.B. Sigman, A. Ghezelbash, T. Hanrath, A.E. Saunders, F. Lee, and B.A. Korgel, Solventless Synthesis of Monodisperse Cu_2S Nanorods, Nanodisks, and Nanoplatelets. *Journal of the American Chemical Society,* **2003**, 125(51), 16050-16057.

272. F. Auzel, Upconversion and Anti-Stokes Processes with f and d Ions in Solids. *Chemical Reviews,* **2004**, 104(1), 139-174.

273. A. Burns, H. Ow, and U. Wiesner, Fluorescent Core - Shell Silica Nanoparticles: Towards ldquoLab on a Particlerdquo Architectures for Nanobiotechnology. *Chemical Society Reviews,* **2006**, 35, 1028-1042.

274. D.W. Grainger and D.G. Castner, Nanobiomaterials and Nanoanalysis: Opportunities for Improving the Science to Benefit Biomedical Technologies. *Advanced Materials,* **2008**, 20(5), 867-877.

275. V.L. Colvin, The Potential Environmental Impact of Engineered Nanomaterials. *Nature Biotechnology,* **2003**, 21(10), 1166-1170.

276. D.K. Chatterjee, A.J. Rufaihah, and Y. Zhang, Upconversion fluorescence imaging of cells and small animals using lanthanide doped nanocrystals. *Biomaterials,* **2008**, 29(7), 937-943.

277. E. Henriksson, E. Kjellén, P. Wahlberg, J. Wennerberg, and J. Kjellström, Differences in estimates of cisplatin-induced cell kill in vitro between

colorimetric and cell count/colony assays. *In Vitro Cellular & Developmental Biology - Animal,* **2006**, 42(10), 320-323.

278. Z.A. Peng and X. Peng, Formation of High-Quality CdTe, CdSe, and CdS Nanocrystals Using CdO as Precursor. *Journal of the American Chemical Society,* **2001**, 123(1), 183-184.

279. X. Wu, H. Liu, J. Liu, K.N. Haley, J.A. Treadway, J.P. Larson, N. Ge, F. Peale, and M.P. Bruchez, Immunofluorescent Labeling of Cancer Marker Her2 and Other Cellular Targets with Semiconductor Quantum Dots. *Nature Biotechnology,* **2003**, 21(1), 41-46.

280. S. Wan, J. Huang, M. Guo, H. Zhang, Y. Cao, H. Yan, and K. Liu, Biocompatible superparamagnetic iron oxide nanoparticle dispersions stabilized with poly(ethylene glycol)-oligo(aspartic acid) hybrids. *Journal of Biomedical Materials Research Part A,* **2007**, 80A(4), 946-954.

281. A.P. Alivisatos, Perspectives on the Physical Chemistry of Semiconductor Nanocrystals. *Journal of Physical Chemistry,* **1996**, 100(31), 13226-13239.

282. D. Maysinger, J. Lovric, A. Eisenberg, and R. Savic, Fate of micelles and quantum dots in cells. *European Journal of Pharmaceutics and Biopharmaceutics,* **2007**, 65(3), 270-281.

283. L. Ramanathan, M. Pillis, and S. Fernandes, Role of rare earth oxide coatings on oxidation resistance of chromia-forming alloys. *Journal of Materials Science,* **2008**, 43(2), 530-535.

284. M. Hopp, S. Rogaschewski, and T. Groth, Testing the cytotoxicity of metal alloys used as magnetic prosthetic devices. *Journal of Materials Science: Materials in Medicine,* **2003**, 14(4), 335-345.

285. R.J. Palmer, J.L. Butenhoff, and J.B. Stevens, Cytotoxicity of the rare earth metals cerium, lanthanum, and neodymium in vitro: Comparisons with cadmium in a pulmonary macrophage primary culture system. *Environmental Research,* **1987**, 43(1), 142-156.

286. M.R. Duchen, Roles of mitochondria in health and disease. *Diabetes,* **2004**, 53, S96-S102.

287. H. Yin, H.P. Too, and G.M. Chow, The effects of particle size and surface coating on the cytotoxicity of nickel ferrite. *Biomaterials,* **2005**, 26(29), 5818-5826.

288. C. Kirchner, T. Liedl, S. Kudera, T. Pellegrino, A. MunozJavier, H.E. Gaub, S. Stolzle, N. Fertig, and W.J. Parak, Cytotoxicity of Colloidal CdSe and CdSe/ZnS Nanoparticles. *Nano Letters,* **2005**, 5(2), 331-338.

289. E. Chang, N. Thekkek, William W. Yu, Vicki L. Colvin, and R. Drezek, Evaluation of Quantum Dot Cytotoxicity Based on Intracellular Uptake. *Small,* **2006**, 2(12), 1412-1417.

290. K. Kobayashi, R. Shida, T. Hasegawa, M. Satoh, Y. Seko, C. Tohyama, J. Kuroda, N. Shibata, N. Imura, and S. Himeno, Induction of Hepatic Metallothionein by Trivalent Cerium: Role of Interleukin 6. *Biological & Pharmaceutical Bulletin,* **2005**, 28(10), 1859-1863.

291. A. Munoz, D.H. Petering, and C.F. Shaw, Structure−Reactivity Relationships among Metallothionein Three-Metal Domains: Role of Non-Cysteine Amino Acid Residues in Lobster Metallothionein and Human Metallothionein-3. *Inorganic Chemistry,* **2000**, 39(26), 6114-6123.

292. F. Denizli, Y. Arica, and A. Denizli, Removal of Cadmium(II) Ions from Human Plasma by Thionein Modified pHEMA Based Membranes. *Reactive and Functional Polymers,* **2000**, 44(3), 207-217.

293. M. Vašák, Application of 113Cd NMR to metallothioneins. *Biodegradation,* **1998**, 9(6), 501-512.

294. J. Lovrić, H.S. Bazzi, Y. Cuie, G.R.A. Fortin, F.M. Winnik, and D. Maysinger, Differences in Subcellular Distribution and Toxicity of Green and Red Emitting CdTe Quantum Dots. *Journal of Molecular Medicine,* **2005**, 83(5), 377-385.

295. T.R. Sathe, A. Agrawal, and S. Nie, Mesoporous Silica Beads Embedded with Semiconductor Quantum Dots and Iron Oxide Nanocrystals: Dual-Function Microcarriers for Optical Encoding and Magnetic Separation. *Analytical Chemistry,* **2006**, 78(16), 5627-5632.

296. N.J. Turro, P.H. Lakshminarasimhan, S. Jockusch, S.P. O'Brien, S.G. Grancharov, and F.X. Redl, Spectroscopic Probe of the Surface of Iron Oxide Nanocrystals. *Nano Letters,* **2002**, 2(4), 325-328.

297. A. Manciulea, A. Baker, and J.R. Lead, A Fluorescence Quenching Study of the Interaction of Suwannee River Fulvic Acid with Iron Oxide Nanoparticles. *Chemosphere,* **2009**, 76(8), 1023-1027.

298. R. Li, J. Lee, B. Yang, D.N. Horspool, M. Aindow, and F. Papadimitrakopoulos, Amine-Assisted Facetted Etching of CdSe Nanocrystals. *Journal of the American Chemical Society,* **2005**, 127(8), 2524-2532.